



Contribution à l'étude du phénomène d'oscillation argumentaire

Daniel Cintra

► To cite this version:

Daniel Cintra. Contribution à l'étude du phénomène d'oscillation argumentaire. Génie mécanique [physics.class-ph]. Université Paris-Est, 2017. Français. NNT : 2017PESC1220 . tel-02398198

HAL Id: tel-02398198

<https://pastel.hal.science/tel-02398198>

Submitted on 7 Dec 2019

HAL is a multi-disciplinary open access archive for the deposit and dissemination of scientific research documents, whether they are published or not. The documents may come from teaching and research institutions in France or abroad, or from public or private research centers.

L'archive ouverte pluridisciplinaire **HAL**, est destinée au dépôt et à la diffusion de documents scientifiques de niveau recherche, publiés ou non, émanant des établissements d'enseignement et de recherche français ou étrangers, des laboratoires publics ou privés.



THESE

(version provisoire)

présentée pour l'obtention du diplôme de :

Docteur de l'Ecole Nationale des Ponts et Chaussées

Spécialité : Mécanique

Ecole doctorale : Sciences, Ingénierie et Environnement

par

Daniel CINTRA

Contribution à l'étude du phénomène d'oscillation argumentaire

Soutenue le 6 décembre 2017 à l'Ecole des Ponts ParisTech
devant le jury composé de :

Rapporteurs

Thien-Phu LE
Jean-Jacques SINOU (président du jury)

Examineurs

Alain EHRLACHER
Jean-Claude GOLINVAL
Roger SERRA

Directeur de thèse

Pierre Argoul

Contribution à l'étude du phénomène
d'oscillation argumentaire
Présentation générale de la thèse

Daniel Cintra
Université Paris-Est,
Laboratoire Navier (UMR 8205), CNRS, ENPC, IFSTTAR

Directeur de thèse :
Pierre Argoul
IFSTTAR, Laboratoire MAST-SDOA

16 octobre 2017

1 Introduction.

L'oscillateur argumentaire a un mouvement stable périodique, à une fréquence proche de sa fréquence fondamentale, lorsqu'il est soumis à une excitation provenant d'une source de type harmonique, à une fréquence qui est un multiple de ladite fréquence fondamentale, et agissant de manière telle que son interaction avec le système dépend des coordonnées d'espace du système.

Pour un système à un degré de liberté (DDL), une équation du second ordre typique est la suivante :

$$\ddot{x} + 2\beta\omega_0\dot{x} + \omega_0^2x = g_1(x) + g_2(x)\cos(\nu t) \quad (1)$$

où x est la coordonnée d'espace, β est le facteur d'amortissement, ω_0 est la pulsation fondamentale de l'oscillateur, g_1 et g_2 sont des fonctions de x , and ν est la pulsation de l'excitation.

Un oscillateur présentant ces caractéristiques a été décrit par Béthenod en 1928 [1]. Le mot "argumentaire" a été créé par Penner [15]. D'autres développements ont été faits par Doubochinski [13, 14], notamment en ce qui concerne la résonance multiple et l'"effet quantique macroscopique". Des oscillations argumentaires ont été décrites dans [12, 16]. Le phénomène a aussi été étudié dans [6–11].

2 La démarche.

La présente thèse étudie quelques systèmes argumentaires et essaie de mettre en évidence des relations symboliques entre les paramètres de ces systèmes et leur comportement observé ou calculé. C'est la représentation de Van der Pol qui a été utilisée la plupart du temps pour représenter l'état du système, car c'est la plus naturelle qui soit adaptée à la méthode de centrage, puisque dans cette dernière, on cherche une solution sous forme d'un signal de type sinusoïdal d'amplitude et de phase lentement variables. L'originalité de la présente thèse vis-à-vis des publications antérieures est dans la modélisation, plus proche des systèmes physiques réels, dans les développements symboliques qui donnent des représentations inédites, dans les expériences, qui utilisent toutes une visualisation de Van der Pol en temps réel, et dans l'expérience elle-même de la poutre excitée axialement de manière argumentaire.

Au cours de cette thèse, des systèmes simples à un DDL ont été modélisés, construits et expérimentés [11]. Des relations symboliques, notamment concernant les probabilités de capture par des attracteurs [9], ainsi que des critères de stabilité et une solution approchée [10], ont été mis en évidence. Un système continu constitué d'une poutre élastique excitée axialement a ensuite été modélisé à l'aide de deux modèles [8] et expérimenté [6] ; toujours dans le domaine symbolique, des propriétés ont été étudiées, notamment concernant des combinaisons

de plages de paramètres permettant au phénomène argumentaire d'exister [7].

En outre, des exposés ont été faits dans quatre conférences :

- Dynolin 2013 [2] Présentation du phénomène argumentaire à l'aide du cas du pendule.
- Dynolin 2014 [4] Présentation de six modèles d'oscillateurs argumentaires.
- VISHNO 2014 [3] Etude de la probabilité de capture par un attracteur.
- Dynolin 2015 [5] Vibration argumentaire transverse d'une poutre excitée axialement.

3 Les articles composant la thèse.

La présente thèse est une compilation de six articles dont les trois premiers sont publiés, le quatrième et le cinquième sont en cours de finalisation, et le sixième est en construction.

3.1 Premier article [11]

Intitulé “Oscillateurs argumentaires non-linéaires : quelques exemples de modulation via la position spatiale”, cet article décrit six modèles de pendule, qui sont modélisés et expérimentés. Les résultats expérimentaux sont comparés aux simulations numériques basées sur les modèles. Pour chaque type de pendule, c'est l'interaction électromagnétique qui sert d'intermédiaire entre la source d'excitation, spatialement localisée, et le système dynamique étudié, c'est-à-dire le pendule. Selon que l'extrémité du pendule recevant l'action extérieure est un aimant ou une bille d'acier, selon l'orientation de l'aimant, et selon le type et l'orientation de la bobine excitatrice, on obtient six types de pendule différents. Les pendules sont modélisés comme des oscillateurs de Duffing, et la localisation spatiale de la source d'énergie introduit une non-linéarité supplémentaire. Un système de commande permet une représentation de type Van der Pol en temps réel. Des attracteurs sont mis en évidence à partir des résultats expérimentaux.

3.2 Deuxième article [10]

Intitulé “Oscillateurs argumentaires non-linéaires : critère de stabilité et solution analytique approchée”, cet article étudie un oscillateur argumentaire de type pendule, et donne une expression analytique d'un critère de stabilité. En utilisant la méthode de centrage et un facteur intégrant, on obtient une solution analytique exacte pour le cas où l'amortissement est nul, et une solution analytique approchée lorsqu'il y a amortissement. Une représentation de Van der Pol dans l'espace (amplitude, phase) est utilisée, et un attracteur est identifié.

3.3 Troisième article [9]

Intitulé “Probabilité de capture par un attracteur dans des oscillateurs argumentaires non-linéaires”, cet article étudie le comportement d'un oscillateur

argumentaire de type “Duffing”. A partir d’une solution analytique implicite approchée, et en utilisant une représentation de Van der pol dans l’espace (amplitude, phase), la forme et la répartition des bassins amont des attracteurs sont étudiées, et différentes probabilités de capture par les attracteurs sont évaluées sous forme symbolique. Les expressions obtenues peuvent être utiles lors de la conception de structures en génie mécanique, où en général on cherche à éviter l’apparition de phénomènes vibratoires.

3.4 Quatrième article [8]

Intitulé “Modélisation et résultats numériques concernant la vibration argumentaire transverse d’une poutre excitée via un contact élastique permanent ou intermittent par un mouvement axial harmonique”, cet article montre que, dans certaines circonstances, l’excitation axiale d’une poutre peut entraîner une vibration transverse argumentaire, c’est-à-dire à la fréquence propre de la poutre, alors que l’excitation a une fréquence qui est un multiple pair (au moins égal à 4) de ladite fréquence propre. Deux cas sont étudiés : le cas articulé-(articulé-guidé) et le cas encastré-(encastré-guidé). Un modèle “naturel” est donné. Un modèle “lissé” en est déduit, qui permet l’application de la méthode de centrage. L’état stationnaire est étudié et représenté dans le plan (amplitude de l’oscillateur, amplitude de l’excitation). La stabilité est étudiée sous forme symbolique, et un critère de stabilité, généralisant celui donné dans le deuxième article ci-dessus, est mis en évidence. Des simulations numériques permettent de comparer le modèle naturel et le modèle lissé dans le plan de Van der Pol.

3.5 Cinquième article [6]

Intitulé “Résultats expérimentaux concernant la vibration argumentaire transverse d’une poutre excitée via un contact élastique intermittent par un mouvement axial harmonique”, cet article étudie expérimentalement une poutre telle que décrite dans le quatrième article ci-dessus. La configuration est encastré-(encastré-guidé). Deux cas sont étudiés : le rapport de fréquence entre l’excitation axiale et la vibration transverse de la poutre est de quatre dans le premier cas, et de six dans le second. Les résultats expérimentaux sont comparés aux modèles naturel et lissé.

3.6 Sixième article [7]

Intitulé “Quelques propriétés sous forme symbolique concernant la vibration argumentaire transverse d’une poutre excitée via un contact élastique intermittent par un mouvement axial harmonique”, cet article met en évidence, sous forme symbolique, les conditions d’apparition du régime stationnaire et des propriétés du seuil d’excitation.

4 Les principales difficultés rencontrées.

4.1 La multiplicité des paramètres.

Ces systèmes ont souvent un nombre de paramètres suffisant pour introduire un risque de redondance au fil du temps. Il a fallu bien identifier les paramètres physiques statiques du système au repos, les paramètres dynamiques, et les paramètres purement liés aux modes de calcul. Il a aussi fallu réduire le plus possible le nombre de paramètres en éliminant les paramètres dépendant d'un ou plusieurs autres paramètres, ce qui n'est pas toujours visible immédiatement. Une difficulté vient du fait qu'au fur et à mesure que la recherche progresse, on est amené à voir les choses différemment, et à changer de paramètres. Il faut alors revoir tout ce qui a déjà été fait pour mettre à jour les changements quand c'est encore possible, c'est-à-dire pour les textes non encore publiés, et établir des liens avec ce qui a été publié et n'est plus modifiable.

Une difficulté est dans le paramètre ρ , proche de 1, égal à $\frac{f_{excitation}}{nf_{00}}$, avec n égal au rapport de fréquence et f_{00} égal à la fréquence fondamentale de la poutre sans force axiale appliquée. On trouve dans la littérature que ce paramètre est "à déterminer". C'est au moment d'examiner le système standard à centrer que l'on s'aperçoit que, selon le choix de ce paramètre, on obtient soit un système standard centré pouvant aboutir à une solution stationnaire stable non nulle, soit un système donnant une solution qui tend vers zéro. Il y a alors une contradiction apparente : en choisissant deux valeurs voisines de ρ , on obtient deux systèmes différentiels donnant deux solutions différentes. La démarche est alors la suivante : comme $f_{excitation}$ est connu, c'est en fait n qu'on choisit pour obtenir un ρ le plus proche possible de 1, puis on examine le système standard obtenu, et on regarde s'il y a possibilité de solution stationnaire. Ce type de solution dépend des conditions initiales. Dans certains cas, il y a plusieurs valeurs possibles pour n ; ainsi, si n est grand, par exemple de l'ordre de la centaine, on aura aisément plusieurs valeurs possibles pour ρ , proches les unes des autres, chacune donnant un système centré différent, avec ses propres critères d'existence de solutions stationnaires. Même si une seule de ces valeurs est celle qui est la plus proche possible de 1, d'autres valeurs voisines sont possibles, car la fréquence à laquelle le système oscille peut varier légèrement en fonction de l'amplitude du mouvement. Ainsi, le système peut s'ajuster sur un des sous-multiples de la fréquence d'excitation, en faisant varier son amplitude. Il faut explorer plusieurs valeurs de n pour savoir si le phénomène argumentaire a des chances de se produire et faire l'inventaire des solutions obtenues.

4.2 Les difficultés expérimentales.

Les pendules. La réalisation des pendules n'a pas présenté de problème majeur, mais la mise au point des algorithmes d'extraction de l'amplitude et de la phase en temps réel a demandé du temps. Ces algorithmes permettent à l'opérateur de voir très rapidement si un mouvement de l'oscillateur est capturé par

un attracteur. Ceci est un avantage important permettant de gagner du temps, car, lorsqu'on cherche à obtenir une capture, on peut relancer l'oscillateur si on s'aperçoit qu'il ne sera pas capturé, sans avoir à attendre qu'il atteigne une amplitude quasi nulle. Les zones de capture apparaissent assez rapidement, après que l'on a obtenu quelques courbes complètes capturées et non capturées. Dans le cas où on cherche à obtenir un ensemble de courbes couvrant l'ensemble des possibles, on peut aussi relancer l'oscillateur si la courbe qu'il suit est proche d'une courbe déjà obtenue. Les algorithmes mis au point pour l'étude des pendules ont servi ensuite pour les expériences sur la poutre.

L'étalonnage des forces magnétiques a été délicat dans certains cas, en raison de la limitation en amplitude des forces mises en jeu, due à l'échauffement des bobines créant le champ magnétique. Certaines expériences ont dû être limitées en durée pour éviter la détérioration définitive des bobines.

La poutre. La réalisation de l'expérience de la poutre a, au contraire, été difficile. Au début, c'est le modèle articulé-(articulé-guidé) qui avait été choisi, dans l'espoir que l'amortissement serait facile à diminuer. Mais c'est au contraire le modèle encastré-(encastré-guidé) qui s'est révélé le moins amorti. En effet, les roulements à billes ont toujours un petit jeu, qui est néfaste pour qui veut limiter les pertes d'énergie par dissipation. Ensuite, est apparu le problème des résonances du pot vibrant. Au début, celui-ci avait été placé dans l'axe de la poutre, en bout. La liaison se faisait par un ressort de 5 mm fixé au pot vibrant et venant directement au contact de la poutre sur sa tranche. Deux difficultés sont alors apparues :

- La première est que le pot vibrant entraînait en résonance au contact intermittent de la poutre, sur des fréquences perturbant totalement l'expérience.
- La deuxième est que le ressort s'écrouissait en quelques minutes et finissait par se désintégrer.

Pour éviter que le mouvement de la poutre perturbe le pot vibrant, il a fallu démultiplier l'effort exercé par ce dernier sur la poutre. En effet, le pot est conçu pour produire une force maximale de 20 N avec des déplacements de ± 5 mm. Or il faut pour la poutre des forces de l'ordre de 30 N avec des déplacements de l'ordre du dixième de mm. La solution trouvée a été d'utiliser une deuxième poutre, dite poutre de commande, dans l'alignement de la poutre principale, et d'induire une flexion dans cette poutre de commande. Ainsi, on a pu également remplacer le ressort par l'élasticité de flexion de la poutre de commande. Au début, il était tentant de placer la poutre de commande de façon à ce que sa position de repos soit rectiligne dans le prolongement de la poutre principale. Mais cette disposition s'est révélée peu pratique, car il fallait imposer au centre de la poutre de commande un débattement trop grand pour les capacités du pot vibrant. C'est donc une position de repos décalée qui a été adoptée, en utilisant un roulement à billes qui excentrait l'extrémité de la poutre de commande située à l'opposé de la poutre principale. L'utilisation d'un roulement à billes pour la poutre de commande n'a pas entraîné de difficultés liées à la dissipation, car cette dernière est négligeable dans le contexte d'une commande.

Le contact entre les deux poutres a été amélioré grâce à une demi-sphère fixée au bout de la poutre principale, sur la tranche. De plus, un feillard d'acier, d'épaisseur 0,1 à 0,3 mm, pouvait être placé entre la poutre de commande et la demi-sphère pour ajuster le contact au repos et ajouter de l'élasticité.

Enfin, il a été nécessaire d'inclure le pot vibrant dans une boucle de contrôle-commande pour s'assurer que le pot n'introduisait pas de fréquences indésirables dans la poutre principale, et en particulier qu'il n'y avait pas d'injection de fréquences correspondant à la résonance fondamentale de la poutre principale, ce qui aurait entraîné une résonance classique. En effet, lorsque le pot vibrant était utilisé sans boucle de contrôle-commande, il était piloté soit en tension, soit en courant. Le pilotage en courant est un pilotage en force, puisque la force magnétique est proportionnelle au courant, alors que le pilotage en tension est plus complexe à analyser, car il fait intervenir des termes dépendant de la réaction du bobinage aux variations de tension. Il se trouve que le pilotage en tension donnait des résultats un peu meilleurs que le pilotage en courant, peut-être parce qu'il mettait en jeu une impédance non nulle de la bobine, et une sorte de contre-réaction qui permettait au pot de réagir moins brusquement aux chocs provenant du contact avec la poutre principale. Pour ce qui est de la chaîne de mesure, elle est analogue à celle utilisée pour les pendules, seuls les capteurs de position de la poutre principale et de la poutre de commande étant par nature différents du capteur angulaire des pendules.

4.3 La complexité des calculs symboliques.

Il est bien connu que les calculs purement symboliques deviennent très rapidement complexes, voire impossibles à réaliser. Néanmoins, on a essayé d'aller toujours le plus loin possible sans passer en numérique ni faire d'approximation. Cependant, les approximations symboliques ont très souvent été inévitables, ce qui a nécessité des tests de validité par des calculs numériques.

5 Conclusion.

5.1 Concernant la poutre.

Concernant la poutre, les voies d'exploration suivantes semblent intéressantes.

Evaluation de l'erreur maximale commise en considérant que le point de tangence de la “ β -curve” et de la “Solution curve” est le minimum de cette dernière. Les premières investigations dans ce domaine, tant en symbolique qu'en numérique, semblent montrer que ladite erreur maximale est de l'ordre de quelques pourcents. Il serait intéressant, autant qu'important, de faire l'analyse complète dans le domaine symbolique.

Un nouveau modèle lissé. Comme la méthode de centrage est basée sur un calcul de moyenne temporelle, il semble naturel de chercher à faire cette moyenne directement sur le modèle naturel, au lieu de commencer par lisser le modèle naturel avant d'appliquer le centrage. Si cette voie est praticable, le résultat pourrait être un modèle lissé plus proche de la réalité que celui utilisé dans la présente thèse.

Rétro-ajustement du modèle lissé. Pour le modèle lissé, il serait intéressant de chercher à modifier les fonctions g_1 et g_2 de façon à obtenir, après centrage, des fonctions G et H plus simples. Et ceci, même si on doit aboutir à des fonctions g_1 et g_2 complexes à exprimer. En effet, pour l'ensemble des calculs symboliques, ce ne sont pas les expressions de g_1 et g_2 qui sont utilisées, mais toujours celles de G et H . Il suffit donc de trouver de nouvelles fonctions g_1 et g_2 à partir de fonctions G et H simplifiées a priori, et de regarder si ces fonctions g_1 et g_2 sont au moins aussi représentatives du modèle naturel que le sont les fonctions g_1 et g_2 utilisées dans la présente thèse. Partant de fonctions G et H simplifiées, on obtient g_1 et g_2 à l'aide d'équations intégrales. Même s'il s'avère que ces dernières ne peuvent être résolues explicitement, on peut espérer pouvoir tester si elles représentent bien le système.

Stabilité dans le cas $a_A > a_{Acrit}$. Le quatrième article ci-dessus [8] étudie un critère de stabilité dans le cas $a_A < a_{Acrit}$. Il serait intéressant d'étudier les régions de stabilité dans le cas $a_A > a_{Acrit}$. Il y a quelques calculs à faire dans cette région où G dépend de a_A , et non plus seulement de a , ce qui signifie que les calculs symboliques seront sans doute un tant soit peu plus compliqués.

5.2 Concernant les systèmes argumentaires en général.

Propriétés générales du système argumentaire centré. A partir des propriétés de la fonction de répartition spatiale de l'interaction, il est possible d'établir quelques propriétés des fonctions déduites de cette dernière. Il serait intéressant d'aller plus loin et de chercher s'il est possible de trouver une méthode symbolique générale permettant, à partir de ces fonctions, de dire si le phénomène argumentaire a des chances de se produire.

Références

- [1] M.J. Béthenod. Sur l’entretien du mouvement d’un pendule au moyen d’un courant alternatif de fréquence élevée par rapport à sa fréquence propre. *Comptes rendus hebdomadaires de l’Académie des sciences*, 207(19) :847–849, November 1938. (in French).
- [2] D. Cintra and P. Argoul. Argumentary oscillation phenomenon. In *(online publication)*, Lille, France, October 2013. Dynolin conference.
- [3] D. Cintra and P. Argoul. Argumentary Duffing oscillators - Stable-regime probability. In *(online publication)*, Aix-en-Provence (France), June 2014. XIX th Vishno symposium.
- [4] D. Cintra and P. Argoul. Six models of argumental oscillators - Experimental results. In *(online publication)*, Paris, France, October 2014. Dynolin conference.
- [5] D. Cintra and P. Argoul. Argumental transverse vibration of an axially-excited beam. In *(online publication)*, Paris, France, October 2015. Dynolin conference.
- [6] D. Cintra, G. Cumunel, and P. Argoul. Experimental study of the argumental transverse vibration of a beam excited through permanent or intermittent elastic contact by a harmonic axial motion. *Journal to be determined*, 2017.
- [7] D. Cintra, G. Cumunel, and P. Argoul. A few properties in symbolic form for the argumental transverse vibration of a beam excited through permanent or intermittent elastic contact by a harmonic axial motion. *Journal to be determined*, 2017.
- [8] D. Cintra, G. Cumunel, and P. Argoul. Modeling and numerical results for the argumental transverse vibration of a beam excited through permanent or intermittent elastic contact by a harmonic axial motion. *Journal to be determined*, 2017.
- [9] Daniel Cintra and Pierre Argoul. Attractor’s capture probability in non-linear argumental oscillators. *Communications in Nonlinear Science and Numerical Simulation*, 48(Supplement C) :150 – 169, 2017.
- [10] Daniel Cintra and Pierre Argoul. Non-linear argumental oscillators : Stability criterion and approximate implicit analytic solution. *International Journal of Non-Linear Mechanics*, 94(Supplement C) :109 – 124, 2017. A Conspectus of Nonlinear Mechanics : A Tribute to the Oeuvres of Professors G. Rega and F. Vestroni.
- [11] Daniel Cintra and Pierre Argoul. Nonlinear argumental oscillators : A few examples of modulation via spatial position. *Journal of Vibration and Control*, 23(18) :2888–2911, 2017.
- [12] B. Cretin and D. Vernier. Quantized amplitudes in a nonlinear resonant electrical circuit. In *2009 Joint Meeting of the European Frequency and Time Forum and the IEEE International Frequency Control Symposium*,

- vols 1 and 2*, volume 1 & 2, pages 797–800, Besançon, France, April 2009. Joint Meeting of the 23rd European Frequency and Time Forum/IEEE International Frequency Control Symposium.
- [13] D. Doubochinski. *Argumental oscillations. Macroscopic quantum effects*. SciTech Library, August 2015.
 - [14] D.B. Doubochinski and J.B. Doubochinski. Amorçage argumentaire d’oscillations entretenues avec une série discrète d’amplitudes stables. *E.D.F. Bulletin de la direction des études et recherches, série C mathématiques, informatique*, 3 :11–20, 1991. (in French).
 - [15] D. I. Penner, D. B. Duboshinskii, M. I. Kozakov, A. S. Vermel, and Yu. V. Galkin. Asynchronous excitation of undamped oscillations. *Phys. Usp.*, 16(1) :158–160, 1973.
 - [16] J.P. Treilhou, J. Coutelier, J.J. Thocaven, and C. Jacquez. Payload motions detected by balloon-borne fluxgate-type magnetometers. *Advances in Space Research*, 26(9) :1423–1426, 2000.

Nonlinear argumental oscillators: A few examples of modulation via spatial position

Daniel Cintra (corresponding author), Gwendal Cumunel
Université Paris-Est,
Laboratoire Navier (UMR 8205), CNRS, ENPC, IFSTTAR,
6 et 8, avenue Blaise Pascal,
Cité Descartes, Champs-sur-Marne,
F-77455 Marne La Vallée Cedex 2, France.
email: daniel.cintra@enpc.fr, gwendal.cumunel@enpc.fr
and

Pierre Argoul
IFSTTAR, Laboratoire MAST-SDOA,
F-77455 Marne La Vallée, Cedex 2, France
email: pierre.argoul@ifsttar.fr

Abstract

Under certain conditions, an oscillator can enter a stable regime when submitted to an external harmonic force whose frequency is far from the natural frequency of the oscillator. This may happen when the external force acts on the oscillator in a way which depends on the oscillator's spatial position. This phenomenon is called “argumental oscillation”. In this paper, six argumental oscillators are described and modelled; experimental results are given and compared to numerical simulations based on the models. A polar Van der Pol representation, with embedded time indications, is used to allow a precise comparison. The pendulums are modelled as Duffing oscillators. The six models are based on various pendulums excited by spatially-localized magnetic-field sources consisting of wire coils. Each pendulum receives the excitation via a steel element or via a permanent magnet, fitted at the tip of the pendulum's rod. The spatial localization induces another nonlinearity besides the Duffing nonlinearity. A control system allowing a real-time Van der Pol representation of the motion is presented. Attractors are brought out from experimental results.

Keywords— argumental, Duffing, oscillator, pendulum, nonlinear, Van der Pol representation, spatial modulation, experimental

Contents

1	Introduction	4
1.1	Aim of this paper	5
2	Statement of the problem	5
2.1	Equation of motion	5
2.2	General description of the pendulum	5
3	Geometry of the physical devices: pendulum, sources and receptors	5
3.1	The pendulum	6
3.2	The source of magnetic field	7
3.3	The receptor	8
4	Modelling	9
4.1	Notations	9
4.2	Simplifying hypothesis	10
4.3	The Type I Source	10
4.4	The Type II Source	10
4.5	The Type 1 Receptor	11
4.6	The Type 2- and Type 3 receptors	11
5	The six forms of the H-function	11
6	Equation of motion	12
6.1	Type 1 Receptor	12
6.2	Types 2 and 3 receptors	14
7	Numerical ODE resolution and Van der Pol representation	14
8	Description of the physical devices used in the experiments	15
8.1	The pendulum	15
8.2	The source of magnetic field	16
8.3	The receptor	16
8.4	Synoptic diagram of the control system	17
9	Experimental results	20
9.1	Static torque measurements	20
9.2	Motion measurements	20
9.3	Experimental results for the Type 1 Receptor	22
9.4	Experimental results for the Type 2 Receptor	22
9.5	Experimental results for the Type 3 Receptor	24
10	Discussion	26
10.1	Simulation quality	26
10.2	Predictability	26
10.3	Attractors. Capture probability	26
10.4	Robustness versus the form of the H-function.	26

10.5 Robustness versus the source's frequency.	27
10.6 Robustness versus transient energy perturbations	27
11 Future	29
12 Appendices	35
12.1 Introduction to the Appendices.	35
12.2 Appendix A: Type 1 Receptor with a Type I source.	35
12.3 Appendix B: Type 1 Receptor with a Type II source (Béthenod's pendulum).	35
12.4 Appendix C: Type 2 Receptor with a Type I source (Doubochinski's pendulum).	36
12.5 Appendix D: Type 2 Receptor with a Type II source.	37
12.6 Appendix E: Type 3 Receptor with a Type I source.	38
12.7 Appendix F: Type 3 Receptor with a Type II source.	39

1 Introduction

In the 1920s, physicists were searching for a device to divide the mains current frequency in order to manufacture mains-driven clocks. As no electronics were available, they studied various inherently frequency-dividing oscillators. Among them was a pendulum designed by Béthenod in 1929 [1], that oscillated at a low frequency, typically 1 Hz, when driven by the mains at 50 Hz. This design was inspired by a remark made by Soulier [7] in 1928 about an oscillating bar. Before, Cornu [5] and Féry [11] had designed pendulums based on magnetic forces, aimed at the synchronization of clocks, but with a pendulum frequency equal to the excitation frequency. Béthenod’s oscillator was a pendulum fitted with a steel sphere at the tip of the rod. The sphere could sense the external electromagnetic force only when it was near the lower equilibrium position of the pendulum. Thus, there was a spatial modulation of the force. The force was due to a magnetic field created by a solenoid with vertical axis, carrying an alternating current. The force could only be attractive. Béthenod presented observations and calculation using a perturbation method. He did not go deeper into this phenomenon. In this paper, this type of oscillator is referred to as “Béthenod’s pendulum” or “Type II-1 oscillator”.

In the 1960s, Russian researchers studied an oscillator subjected to a spatially-localized external force; the oscillator operated at a frequency much lower than that of the external force. D. I. Penner et al. coined the term “argumental oscillations” [13, 12] from the fact that the interaction between the oscillator and the excitation depends on the “argument” of a space-localization function, which we call the H-function hereinafter. The oscillator was a pendulum fitted with a permanent electric charge at the tip of the rod. The charge crossed a parallel-plate capacitor connected to an harmonic voltage, and could sense a force only when passing through the capacitor. From that time on, Doubouchinski [8] studied this type of oscillator, as well as other related types. He used a pendulum fitted with a permanent magnet at the tip of the rod, whose magnetic moment was aligned with the rod. In this set-up, the magnet can sense the external electromagnetic force only when it is near the lower equilibrium position. The force is due to a magnetic field created by a coil with horizontal axis perpendicular to the plane of displacement of the rod and the tip. This force can be attractive or repulsive, depending on the polarity of the current producing the magnetic field. In this paper, this type of oscillator is referred to as “Doubouchinski’s pendulum” or “Type I-2 oscillator”. Doubouchinski modelled this phenomenon and produced mathematical results regarding the resolution of the system [9]. He modelled the spatial localization of the interaction zone by means of a gate function. He also designed physical models and carried out a vast number of measurements. He also built many devices using this phenomenon.

Motion of oscillators at a frequency lower than the excitation frequency has been studied: energy transfer from high-frequency to low-frequency modes, with a frequency ratio up to 100, observed in [14]; argumental oscillations, observed in [15]; subharmonic resonance, observed and modelled in [10]. An electronic argumental oscillator with a gate function used as dependent-variable localization function has been studied in [6]. A new formula about the magnetic interaction between an external force and an argumental oscillator is given in [2]. Preliminary experimental results about six argumental oscillators are given in [4]. A symbolic formula giving the stable-regime establishment probability of an argumental oscillator is exposed in [3].

1.1 Aim of this paper

In this paper, our goal is to show numerically and experimentally that the argumental phenomenon can arise for a diversity of oscillators and excitations. Six argumental oscillators are presented, then modelled. The models are closer to physical reality than in previous articles. For each type of oscillator, the equation of motion is built. Experimental results are given and compared to numerical simulations based on the models.

2 Statement of the problem

In this section, the generic equation of a simple argumental Duffing oscillator and the implementation of this oscillator as a simple pendulum are presented.

2.1 Equation of motion

This equation can be expressed as follows:

$$\ddot{\alpha} + 2\beta\omega_0\dot{\alpha} + \omega_0^2(\alpha + \mu\alpha^3) = A H(\alpha) K(t) \quad (1)$$

where the dot notation is used to represent the derivation with respect to time, α is the time-dependent dimensionless variable, β represents the damping of the system, ω_0 is the angular velocity of a small motion of the oscillator, μ represents the Duffing coefficient, corresponding to the non-linearity of the restoring force, A is a constant, and K is a periodic function of the time t ; the H function characterizes the spatial localization of the interaction between the excitation source and the oscillator and must be non-constant. Usually, the modulus of the right member of equation (1) is small compared to ω_0^2 . This condition generally allows to use the averaging method to approach symbolic results regarding the solution (see [9]).

In this paper, the oscillators which are modelled are pendulums, for which α is an angle characterizing the spatial position; in this case, we have $\mu = -1/6$ for $|\alpha| \leq 1$, and $K(t) = \sin(\nu t)$ or $K(t) = \sin^2(\nu t)$, ν being the angular velocity of the external excitation source.

2.2 General description of the pendulum

The pendulum (see Figure 1) consists of a rod articulated around a fixed point S. At the tip of the rod is a “receptor”, which is submitted to an external excitation originating in a “source” located under the bottom point of the receptor’s course. A detailed description is given below. The six argumental oscillators presented herein are each built with one (among two) source of harmonic magnetic field and one (among three) receptor. The interaction between sources and receptors constitutes the external excitation of the oscillator.

3 Geometry of the physical devices: pendulum, sources and receptors

In this section, the elements which are used in the modelling are described from a geometrical point of view. The physical elements will be described in an other section below.

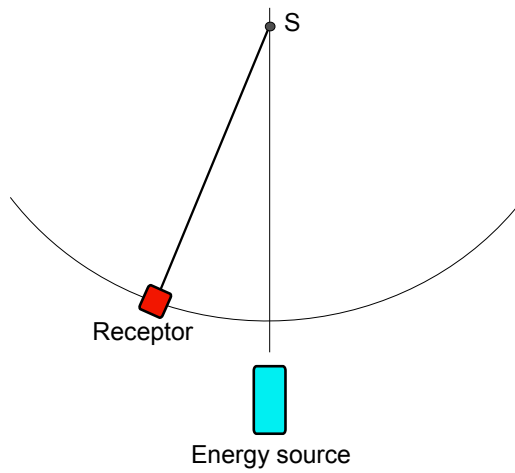


Figure 1: Pendulum with receptor and source

The pendulum is fitted with a magnet or a steel piece, called a “receptor”, at the tip of its rod. The external excitation, called the “source”, consists of a magnetic-field generator, located near the bottom point of the receptor’s path.

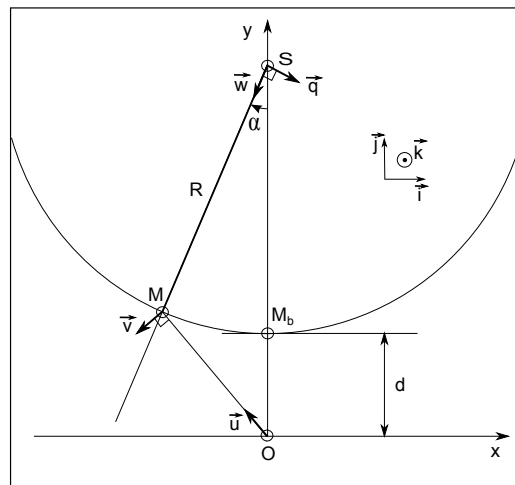


Figure 2: Pendulum part of the physical set-up

3.1 The pendulum

The pendulum (see Figure 2) is described in a Cartesian coordinate system $(Oxyz)$ with unitary vectors \mathbf{i} , \mathbf{j} , \mathbf{k} . The pendulum is articulated at point S . The rod is SM , of length R , and carries a unitary vector \mathbf{w} oriented from S to M . Let M_b be the lowest point reachable by M . Let d

be the distance OM_b . The segment OM carries a unitary vector \mathbf{u} oriented from O to M . Let $\alpha = (\mathbf{SO}, \mathbf{SM})$. In the polar coordinate system based at S , let \mathbf{q} be the unit vector resulting of a rotation of angle $\pi/2$ applied to \mathbf{w} , and let $\mathbf{k} = \mathbf{w} \times \mathbf{q}$. Let \mathbf{v} be the unitary vector resulting of a rotation of angle $\pi/2$ applied to \mathbf{u} .

3.2 The source of magnetic field

A source of magnetic field is located at point O . This source can be one of the two following types. Type I is a wire parallel to \mathbf{k} , conveying a current oriented like \mathbf{k} (see Figure 3). The wire is part of a rectangular current loop having an horizontal axis parallel to \mathbf{i} . The loop is large enough so that the return path of the wire is considered having a negligible contribution to the creation of the magnetic field at M . In practice, the loop consists of a plurality of parallel wires, grouped in a sufficiently narrow region, so as to be considered a unique thick wire going through point O . Those wires form a coil as depicted in Figure 3. The useful wire length of the coil perpendicular to the Ox axis is denoted by L .

Type II is a solenoid (see Figure 4) whose axis is parallel to \mathbf{j} ; its upper tip is at O , and its length is large enough to allow to consider that the other end of the solenoid does not have a significant role in the creation of the magnetic field around O . This solenoid is considered a magnetic dipole, whose north pole is at O . Let B_0 be the modulus of the magnetic field at M_b .

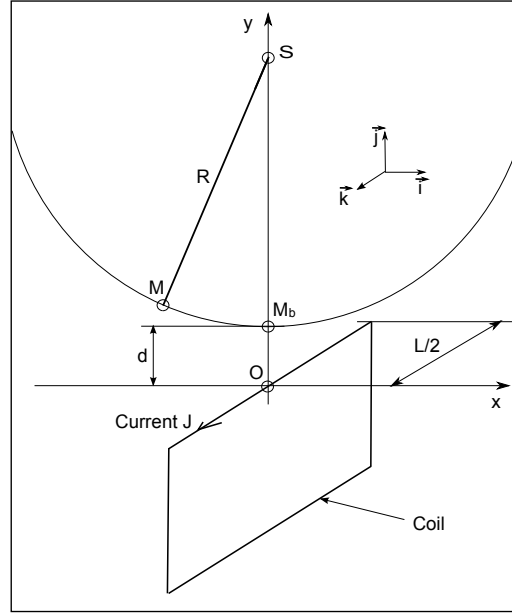


Figure 3: Type I Source

In either case, the electric circuit carries a current which is produced by a current generator. So, we control the magnetic field without having to consider retro-actions of the field onto the circuit.

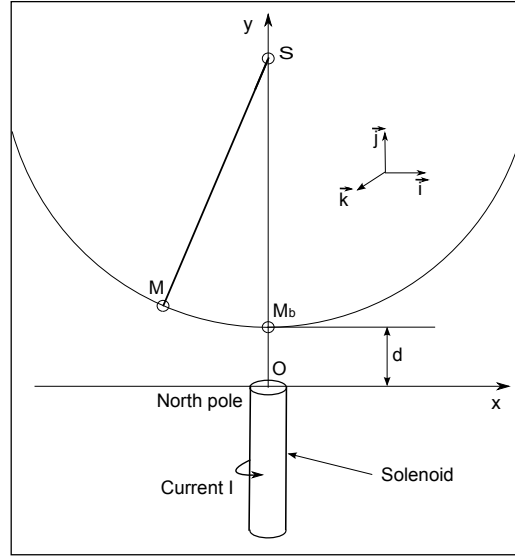


Figure 4: Type II Source

3.3 The receptor

At M is a “receptor”, which interacts with the magnetic field to produce a force or a torque on the rod (see Figure 5). The receptor is one of the three following types. Type 1 is a steel sphere or a steel parallelepiped, which in a magnetic field acquires a magnetic moment aligned with the field. Type 2 is a permanent magnet whose magnetic moment is aligned with the pendulum’s rod. Type 3 is permanent magnet whose magnetic moment is perpendicular to the pendulum’s rod. When placed in a non-uniform magnetic field, the steel sphere or parallelepiped is subjected to a force, which is translated into a torque on the rod.

When placed in a magnetic field, the magnet is subjected to a torque; if the field is non-uniform, it is also subjected to a force. Said torque and force are translated into torques on the rod.

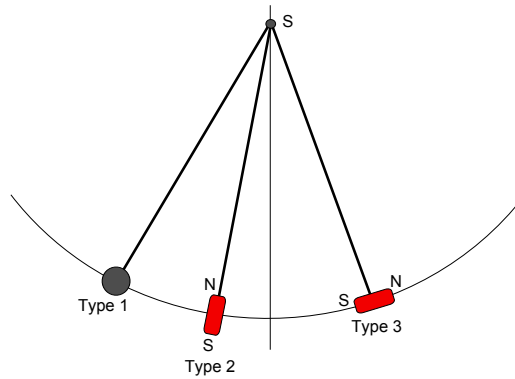


Figure 5: The three types of receptors

4 Modelling

All six combinations from two types of source and three types of receptor are studied. Firstly, at point M, the magnetic field produced by the source is calculated. Then, the magnetic field is applied to the receptor. This field applies a force and a torque to the receptor. This results in a torque applied to the pendulum's rod. This torque arises, in each case, from the combination of one source and one receptor. The expression of $\nabla(\|\mathbf{B}\|^2)$ is also calculated; it is used in the calculation of the magnetic interaction when the Type 1 Receptor is involved.

4.1 Notations

In the calculations given hereafter and in the appendices, we denote by:

- α the oscillator's space coordinate;
- Points S , M and M_b , vectors \mathbf{u} , \mathbf{v} , \mathbf{w} and \mathbf{q} , lengths d and R are as of Figure 2;
- \mathbf{B} the magnetic field produced in M by the source;
- B_0 the amplitude of \mathbf{B} at point M_b ;
- \mathbf{T}' the torque transmitted to the receptor due to the magnetic interaction with the source;
- \mathbf{F}' the force transmitted to the receptor due to the magnetic interaction with the source;
- \mathbf{T}'' the torque transmitted to the pendulum's rod due to the magnetic force \mathbf{F}' transmitted to the receptor;
- \mathbf{T} the total torque transmitted to the pendulum's rod due to the magnetic interaction between the receptor and the source;
- T the coordinate of \mathbf{T} along \mathbf{k} ;
- \mathbf{M}_n the magnetic moment of Source II (with $\|\mathbf{M}_n\| = \mu_0 N S I$);
- \mathbf{m} is the magnetic moment of the permanent magnet at M (for the Type 2 and Type 3 receptors);
- m_0 is the projection of this moment along \mathbf{w} ;
- κ the relative magnetic susceptibility of steel;
- μ_0 the permeability of void;
- N the number of turns in the coil;
- S the area of one turn;
- L the useful wire length of the coil perpendicular to the Ox axis.
- I the current in the coil;
- ν is the angular velocity of the source's signal;

- $\gamma = \frac{R}{d}$;
- $\eta = \sqrt{\gamma(1 + \gamma)}$.

4.2 Simplifying hypothesis

We consider that α is small wherever T has a significant value. Hence we can, in first approximation, replace $\sin(\alpha)$ by α and $\sin(\alpha/2)$ by $\alpha/2$ in this region. In the other regions, we still use these replacements, because T is so small that even a large relative error on the expression of T has no significance on the physical result. We call this hypothesis the “simplifying hypothesis”.

4.3 The Type I Source

The magnetic field created by a Type I Source is given by the following classical result :

$$\mathbf{B} = \frac{B_0 d}{OM} \mathbf{v} \quad (2)$$

where $B_0 = \frac{\mu_0 N I}{2\pi} \frac{L}{\sqrt{L^2 + d^2}}$, μ_0 is the permeability of void, N is the number of turns in the coil, I is the value of the current in the coil, L is the length of the coil in the direction of \mathbf{k} .

The electric circuits are arranged so as to be able to assume that $L \gg d$, so that $B_0 \approx \frac{\mu_0 N I}{2\pi}$.

In order to calculate the expression of $\nabla(\|\mathbf{B}\|^2)$, we start from the equation $\|\mathbf{B}\|^2 = \frac{B_0^2 d^2}{OM^2}$; considering, in the polar system coordinates based on the origin S and the angle α , a point M having the coordinates (r, α) , we have: $OM^2 = (R + d - r)^2 + 4r(R + d) \sin^2 \frac{\alpha}{2}$, and therefore,

$$\|\mathbf{B}\|^2 = B_0^2 d^2 P_I(r, \alpha)$$

with

$$P_I(r, \alpha) = \frac{1}{(R + d - r)^2 + 4r(R + d) \sin^2 \frac{\alpha}{2}} \quad (3)$$

Hence:

$$\nabla(\|\mathbf{B}\|^2) = B_0^2 d^2 \left(\frac{\partial}{\partial r} P_I(r, \alpha) \mathbf{w} + \frac{1}{r} \frac{\partial}{\partial \alpha} P_I(r, \alpha) \mathbf{q} \right) \quad (4)$$

4.4 The Type II Source

The vertical solenoid placed at O is considered a magnetic dipole having its north pole at O, and a magnetic moment \mathbf{M}_n , whose value $M_n = NSI$, where N is the number of turns, S is the surface embraced by one turn, and I is the current in the solenoid. Considering that the magnetic moment is caused predominantly by the north magnetic pole of the solenoid, placed at point O on Figure 4, we have at M a magnetic potential $V = \frac{M_n}{4\pi\rho}$, where $\rho = OM$.

Hence the magnetic field at M is:

$$\mathbf{B} = -\mu_0 \nabla V = \frac{B_0}{\rho^2} \mathbf{u} \quad (5)$$

where $B_0 = \frac{\mu_0 M_n}{4\pi d^2}$, ρ is the distance between M and the upper tip of the solenoid, and d is the minimum distance between M and the solenoid.

In the same way as in previous paragraph, we get:

$$\|\mathbf{B}\|^2 = B_0^2 d^4 P_{II}(r, \alpha)$$

with

$$P_{II}(r, \alpha) = \frac{1}{((R + d - r)^2 + 4r(R + d) \sin^2 \frac{\alpha}{2})^2} \quad (6)$$

Hence:

$$\nabla(\|\mathbf{B}\|^2) = B_0^2 d^4 \left(\frac{\partial}{\partial r} P_{II}(r, \alpha) \mathbf{w} + \frac{1}{r} \frac{\partial}{\partial \alpha} P_{II}(r, \alpha) \mathbf{q} \right) \quad (7)$$

4.5 The Type 1 Receptor

This receptor consists of a steel sphere or parallelepiped, as described above. Starting from a general formula related to the torque in the case of this receptor, we study the torque applied to the pendulum's rod due to a Type I- and to a Type II source.

General formula of the torque applied to the pendulum's rod. Due to the magnetic field \mathbf{B}_M at point M, the sphere becomes a magnetic doublet with a magnetic moment \mathbf{m} aligned with \mathbf{B}_M , i.e.: $\mathbf{m} = \kappa \mathbf{B}_M$, where κ is the magnetic susceptibility of the sphere's steel (around 10^4 m.N/T). The force applied to the sphere by the magnetic field is $\mathbf{F} = \nabla(\mathbf{m} \cdot \mathbf{B}) = \nabla(\kappa \mathbf{B}_M \cdot \mathbf{B})$ calculated with \mathbf{m} taken as a constant, so that $\mathbf{F} = \frac{1}{2} \kappa \nabla(\|\mathbf{B}\|^2)$. This force applies in turn a torque \mathbf{T} on the rod, and thus we have:

$$\mathbf{T} = \mathbf{SM} \times \mathbf{F} = \frac{\kappa}{2} R \mathbf{w} \times \nabla(\|\mathbf{B}\|^2) \quad (8)$$

4.6 The Type 2- and Type 3 receptors

General formula of the torque applied to the pendulum's rod. For these receptors, due to the magnetic field at M, the permanent magnet at M is submitted to a torque $\mathbf{T}' = \mathbf{m} \times \mathbf{B}$ and to a force \mathbf{F}' . \mathbf{T}' and \mathbf{F}' in turn respectively apply torques \mathbf{T}' and $\mathbf{T}'' = \mathbf{SM} \times \mathbf{F}'$ to the rod. We call \mathbf{T} the total torque applied, with $\mathbf{T} = \mathbf{T}' + \mathbf{T}''$. For the Type 2 Receptor, the tip of the pendulum's rod is fitted with a permanent magnet with a moment \mathbf{m} aligned with the rod, while for the Type 3 Receptor, the magnet's moment \mathbf{m} is perpendicular to the rod.

5 The six forms of the H-function

In Table 1, we summarize the six configurations, with their respective H-functions (with $|\alpha| < 1$ and $\gamma \gg 1$) and the indication of the Appendix giving the calculus details. We also include the shapes of the H-function plots. In this table, H_{max} refers to the maximum value of $|H|$, α_e is the value of α for H_{max} , and $L_{0.5}$ =width of the H-function's plot at half-height.

Four of the oscillator models have an odd-parity space-modulating H-function, and two have an even-parity one.

For the I-1 combination, we have:

$$H_{max} = \frac{3\sqrt{3}}{16} \frac{1}{\eta} \approx 0.325 \frac{1}{\eta} \text{ at } \alpha_e = -\frac{1}{\eta\sqrt{3}}, \text{ and } L_{0.5} \approx \frac{1.214}{\eta}.$$

For the II-1 combination, we have:

$$H_{max} = \frac{1}{\sqrt{5}} \left(\frac{5}{6}\right)^3 \frac{1}{\eta} \approx \frac{0.259}{\eta} \text{ at } \alpha_e = -\frac{1}{\eta\sqrt{5}}, \text{ and } L_{0.5} \approx \frac{0.8458}{\eta}.$$

For the I-2 combination, we have: $H_{max} = 1$ at $\alpha_e = 0$, and $L_{0.5} \approx \frac{0.972}{\eta}$.

For the II-2 combination, we have:

$$H_{max} = \frac{16}{25\sqrt{5}} \frac{1}{\eta} \approx \frac{0.286}{\eta} \text{ at } \alpha_e = -\frac{1}{2\eta}, \text{ and } L_{0.5} \approx \frac{0.984}{\eta}.$$

For the I-3 combination, we have:

$$H_{max} = \frac{3\sqrt{3}}{16} \frac{1}{\eta} \approx \frac{0.325}{\eta} \text{ at } \alpha_e = \frac{1}{\eta\sqrt{3}}, \text{ and } L_{0.5} \approx \frac{1.214}{\eta}.$$

For the II-3 combination, we have: $H_{max} = 1$ at $\alpha_e = 0$, and $L_{0.5} \approx \frac{0.768}{\eta}$.

6 Equation of motion

Now that we have modeled the interaction between sources and receptors, we can derive the corresponding equations of motion. The Type 1 Receptor has its own type of equation, and will be studied first. The Type 2 and Type 3 receptors have the same type of equation, and will be studied afterwards.

6.1 Type 1 Receptor

We have seen above that the torque value can be expressed as $T = T_1 B_0^2 H(\alpha)$, where T_1 is a constant depending only of the geometrical configuration of the system, and B_0 is the value of the static magnetic field in M_b . We now replace the constant field produced by the source by a time-harmonic field. The field B_0 is now: $B_0(t) = B_{0M} \sin \nu t$, where B_{0M} is the amplitude of B_0 , and we have:

$$T = T_1 B_{0M}^2 H(\alpha) \sin^2 \nu t$$

The equation of motion is then:

$$\begin{aligned} \ddot{\alpha} + 2\beta\omega_0\dot{\alpha} + \omega_0^2(\alpha + \mu\alpha^3) = \\ \frac{T}{J} = \frac{T_1 B_{0M}^2 H(\alpha) \sin^2 \nu t}{J} = E H(\alpha) \sin^2 \nu t \end{aligned} \quad (9)$$

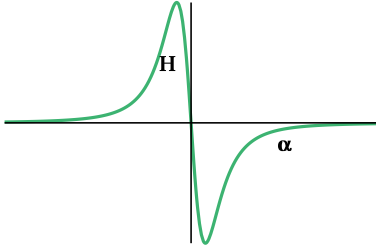
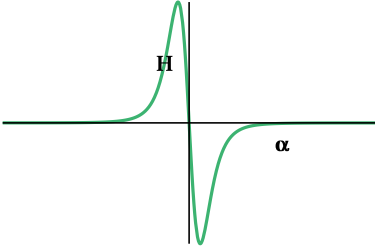
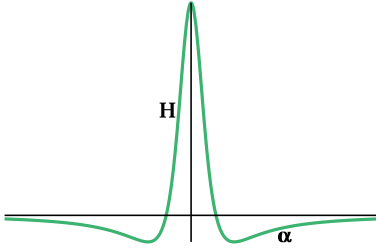
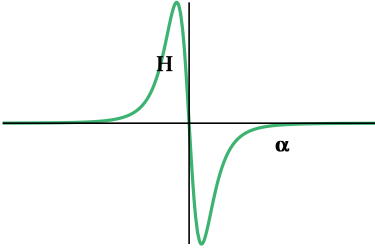
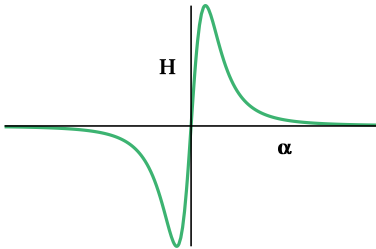
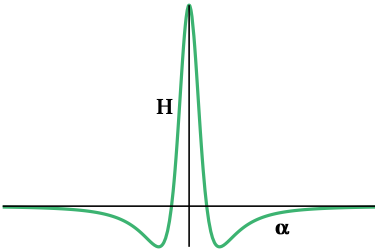
with J =inertial moment of the pendulum, as seen from point S.

To simplify the expression of the system behaviour, one can use the classic reduced time $\tau = \omega_0 t$. Equation (9) becomes:

$$\frac{d^2\alpha}{d\tau^2} + 2\beta\frac{d\alpha}{d\tau} + \alpha + \mu\alpha^3 = A H(\alpha) \sin^2 \frac{\nu\tau}{\omega_0} \quad (10)$$

with $A = \frac{E}{\omega_0^2}$.

Table 1: The six H-functions.

	Type I Source: Wire along Oz	Type II Source: Solenoid along axis y'y
Type 1	$H(\alpha) = -\frac{\alpha}{(1 + \eta^2 \alpha^2)^2}$ (Appendix A)	$H(\alpha) = -\frac{\alpha}{(1 + \eta^2 \alpha^2)^3}$ (Appendix B)
Receptor	 $H_{max} = \frac{0.325}{\eta}$ at $\alpha = -\frac{1}{\eta\sqrt{3}}$; $L_{0.5} \approx \frac{1.214}{\eta}$	 (Béthenod's pendulum) $H_{max} = \frac{0.259}{\eta}$ at $\alpha = -\frac{1}{\eta\sqrt{5}}$; $L_{0.5} \approx \frac{0.8458}{\eta}$
Type 2	$H(\alpha) = \frac{1 - \eta^2 \alpha^2}{(1 + \eta^2 \alpha^2)^2}$ (Appendix C)	$H(\alpha) = -\frac{1 - \frac{\eta}{6} \alpha^2}{(1 + \eta^2 \alpha^2)^{\frac{5}{2}}} \alpha$ (Appendix D)
Receptor	 (Doubochinski's pendulum) $H_{max} = 1$ at $\alpha = 0$; $L_{0.5} \approx \frac{0.972}{\eta}$	 $H_{max} = \frac{0.286}{\eta}$ at $\alpha = -\frac{1}{2\eta}$; $L_{0.5} \approx \frac{0.984}{\eta}$
Type 3	$H(\alpha) = \frac{\alpha}{(1 + \eta^2 \alpha^2)^2}$ (Appendix E)	$H(\alpha) = \frac{1 - 2\eta^2 \alpha^2}{(1 + \eta^2 \alpha^2)^{\frac{5}{2}}}$ (Appendix F)
Receptor	 $H_{max} = \frac{0.325}{\eta}$ at $\alpha = \frac{1}{\eta\sqrt{3}}$; $L_{0.5} \approx \frac{1.214}{\eta}$	 $H_{max} = 1$ at $\alpha = 0$; $L_{0.5} \approx \frac{0.768}{\eta}$

6.2 Types 2 and 3 receptors

We have seen above that the torque value can be expressed as $T = T_1 B_0 H(\alpha)$, where T_1 is a constant depending on the geometrical configuration of the system, B_0 is the value of the static magnetic field in M_b , and $H(\alpha)$ is a function of α whose parameters depend only on the geometrical configuration of the system. Replacing the constant field produced by the source by a time-harmonic field, we obtain for the field B_0 : $B_0(t) = B_{0M} \sin(\nu t)$, where B_{0M} is the amplitude of B_0 , and we have $T = T_1 B_{0M} H(\alpha) \sin(\nu t)$.

The equation of motion is then:

$$\begin{aligned} \ddot{\alpha} + 2\beta\omega_0\dot{\alpha} + \omega_0^2(\alpha + \mu\alpha^3) &= \frac{T}{J} = \\ &= \frac{T_1 B_{0M} H(\alpha) \sin(\nu t)}{J} = E H(\alpha) \sin(\nu t) \end{aligned} \quad (11)$$

which defines E , and where J =inertial moment of the pendulum, as seen from point S.

To simplify the expression of the system's behaviour, one can use the classic reduced time $\tau = \omega_0 t$. Equation (11) becomes:

$$\frac{d^2\alpha}{d\tau^2} + 2\beta\frac{d\alpha}{d\tau} + \alpha + \mu\alpha^3 = A H(\alpha) \sin \frac{\nu\tau}{\omega_0} \quad (12)$$

with $A = \frac{E}{\omega_0^2}$.

7 Numerical ODE resolution and Van der Pol representation

After obtaining a numerical solution to second-order ordinary differential equation (ODE) (10) or (12), noting the reduced time by τ , with $\tau = \omega_0 t$, one classically notices by physical experiment and by numerical simulation that $\alpha(\tau)$ is close to a sinusoid whose amplitude $a(\tau)$ and phase $\varphi(\tau)$ are slowly-varying functions. One is therefore led to do a change of variables by putting:

$$\alpha(\tau) = a(\tau) \sin(\rho\tau + \varphi(\tau)) \quad (13)$$

with $\rho = \text{constant}$. Moreover, to complete said change of variables, moving from variables $(\alpha, \dot{\alpha})$ to variables (a, φ) , one puts:

$$\frac{d\alpha}{d\tau}(\tau) = \rho a(\tau) \cos(\rho\tau + \varphi(\tau)) \quad (14)$$

Equations (13) and (14) define said change of variables.

An analysis using the averaging method (see [9]) shows that a stable oscillation can take place when $\rho = \frac{1}{n} \frac{\nu}{\omega_0}$, where n is an integer, which may have to be odd or even, depending on system parameters. Moreover, the form of the averaged equations shows that the problem is invariant by a transformation $\varphi \mapsto \varphi + \frac{2\pi}{n}$.

To plot, in the (a, φ) space, an integral curve obtained from numerical resolution of equation (10) or (12), we must obtain a and φ directly from α and $\frac{d\alpha}{d\tau}$. From equations (13) and (14), which we

note, for sake of clarity:

$$\begin{cases} \alpha &= a \sin(\rho\tau + \varphi) \\ \frac{d\alpha}{d\tau} &= \rho a \cos(\rho\tau + \varphi) \end{cases} \quad (15)$$

we obtain:

$$\begin{cases} a &= \sqrt{\alpha^2 + \frac{1}{\rho^2} \left(\frac{d\alpha}{d\tau} \right)^2} \\ \varphi &= -\rho\tau + \arctan \left(\frac{\rho\alpha}{\frac{d\alpha}{d\tau}} \right) \end{cases} \quad (16)$$

Once the numerical solution is obtained as $\alpha(\tau)$, we first evaluate $\frac{d\alpha}{d\tau}(\tau)$ in every point, then calculate $a(\tau)$ and $\varphi(\tau)$ using equations (16). At this point, variables a and φ are not yet averaged. To complete the numerical averaging, we smooth them by using a moving-average extending over one pendulum period and centred on the current time. Integral curves according to the averaged variables can then be represented in a Cartesian diagram giving $a(\tau)$ versus $\varphi(\tau)$, which is the classical Van der Pol representation. Knowing that the problem is invariant by an addition of $2k\pi/n$ to phase $\varphi(\tau)$ (where k is an integer), we are led to use a polar form of this representation, where the modulus is $a(\tau)$ and the argument is $\varphi(\tau)$. The plots obtained can be duplicated by $2k\pi/n$ rotations to obtain the complete representation of the motion possibilities. In this way, one can obtain the images of all the possible attractors (for a given set of experimental conditions) once one has obtained one of these images.

8 Description of the physical devices used in the experiments

In this section, the physical elements which are used in the experiments are described. The pendulum is fitted with a magnet or a steel piece, called a “receptor”, at the tip of its rod. The external excitation, called the “source”, consists of a magnetic-field generator, located near the bottom point of the receptor’s path.

8.1 The pendulum

The pendulum is depicted in Figure 6. At point S is a ball bearing, brand SKF model 6004. The axis is fitted with an angular sensor having 100,000 points per turn (see close-up in Figure 7). R varies between 49 and 52.5 cm, and we have $d \geq 3$ mm. The value of d is difficult to assess directly, because we do not know exactly where the centre of a magnetic dipole resides. During the modelling process, we had to consider d as a parameter to be adjusted by pragmatically trying different values so as to obtain a model which can correctly represent the experimental results.

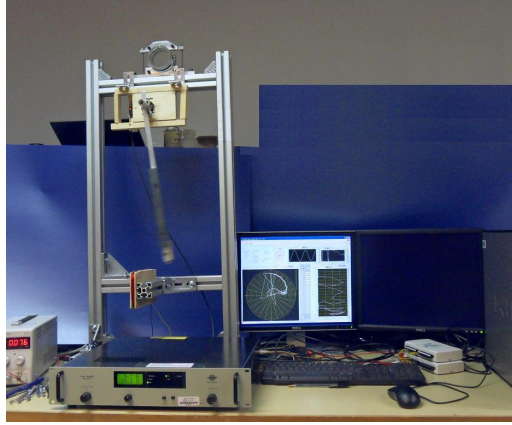


Figure 6: Experimental set-up

8.2 The source of magnetic field

The Type I source used in the experiments is depicted in Figure 8. The coil's height is 10 cm, and the depth L is 18 cm. The cross-section of the wire-winded region is 10 mm high and 9 mm wide. The wire is made of enamelled copper, and its diameter is 0.4 mm.

The Type II source used in the experiments is depicted in Figure 9. The coil has an inside diameter of 20 mm, an outside diameter of 50 mm, a total length of 60 mm. The wire is made of enamelled copper, and its diameter is 1 mm. When this solenoid is associated with a Type-1 Receptor (see below), a soft-iron core is added to the coil to increase the magnetic field.

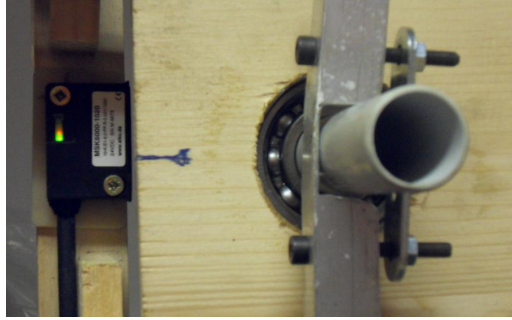


Figure 7: Shaft close-up

8.3 The receptor

The various physical receptors used in the experiments are depicted in Figure 10.

Type 1 is a steel sphere or a steel parallelepiped. In Figure 10, the sphere is marked "1a", while the parallelepiped is marked "1b". The sphere's diameter is 10 mm; the dimensions of the parallelepiped are 20 mm (direction aligned with the rod), 42 mm (direction perpendicular to the rod, in the plane

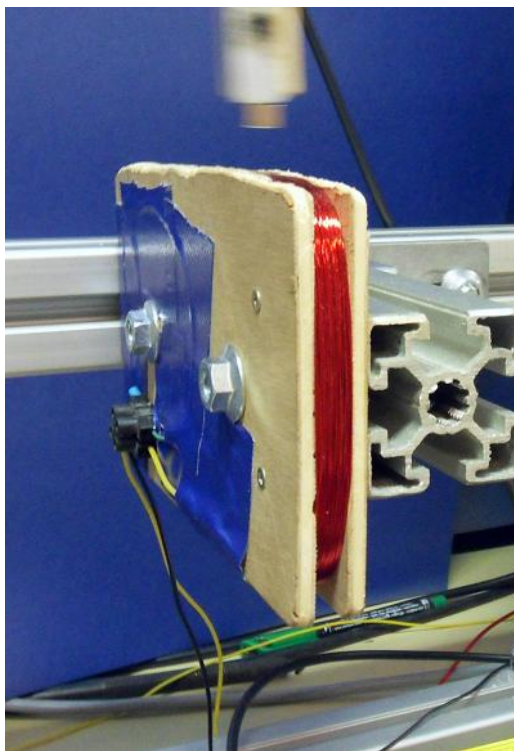


Figure 8: Type I Source

of displacement of the rod's tip), 20 mm (direction perpendicular to said plane).

Type 2 consists of two Neodymium magnets (grade N42, pull strength 1.6 kg) in contact with each other in a serial fashion, south pole of first magnet against north pole of second one; each magnet is a cube with an edge of 7 mm. The Type 2 Receptor is marked "R2" in Figure 10. Type 3 is a magnet physically identical to one of the magnets constituting the Type 2 Receptor. The Type 3 Receptor is marked "R3" in Figure 10.

The data regarding the masses of the elements used in the experiments are given in Table 2.

8.4 Synoptic diagram of the control system

To visualize the Van der Pol diagram in real-time, we use a control system as described hereafter. On Figure 11, we can see a system consisting of a number of components: a Personal Computer (PC), an Interface, a Current Generator, a Hardware Frequency Divider, a Peak Detector, a Phase Comparator, an Angular Sensor, a Source, and a Receptor. In our system, the Peak Detector and the Phase Comparator are implemented in software. The Frequency Divider is implemented in hardware.

The PC runs a software under LabVIEW to control the system, via the Interface, which receives the numerical control informations from the PC, sends numerical informations to the PC, and handles analog and digital signals to and from the other components of the system.



Figure 9: Type II Source

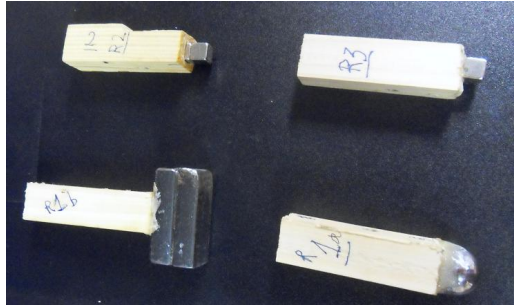


Figure 10: Receptors

The PC asks the Interface to produce a sine signal at frequency f to the current generator, which in turn produces a sinusoidal excitation current to the Source. The current generator sends informations to the Interface about the actual current and voltage at its output. We use a current generator instead of a voltage generator, because the magnetic field is proportional to the current in the wires of the coils. Had we used a voltage generator, we would have had to consider the feedback effects due to the variations of current induced by the interactions between the Source and the Receptor. We used a generator whose maximum power was much greater than the power of the phenomenons involved in the interaction between the excitation source and the oscillator. Therefore, we considered the system as an ideal vibrating system, allowing us not to take into account

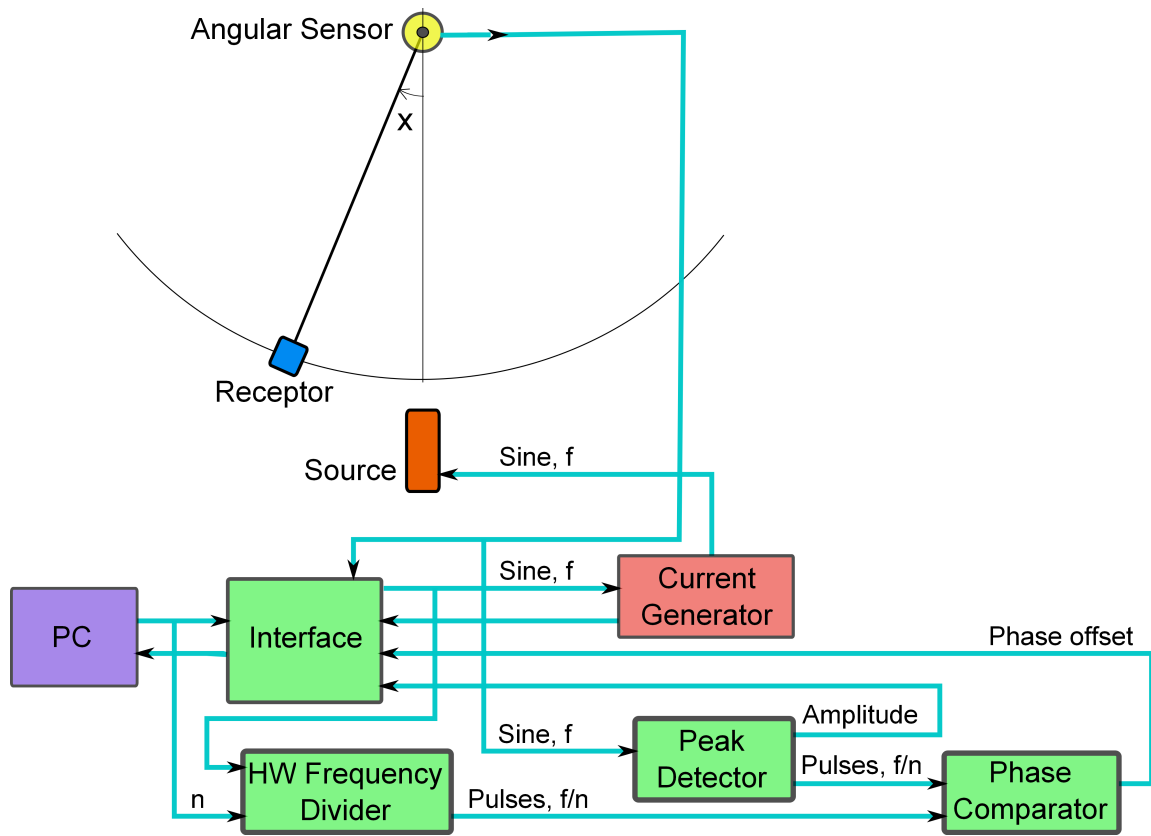


Figure 11: Control system. f is the frequency of the source; n is the expected frequency ratio of the source to the pendulum.

an action of the oscillator onto the excitation source. In contrast, [1] made a study encompassing the action of the oscillator onto the source, because he used a voltage generator having a significant output impedance.

The Hardware Frequency Divider receives an integer n from the PC and the sine wave produced by the interface. It creates pulses at a frequency equal to f/n and sends them to the Phase Comparator. We call these pulses the “reference signal”. This signal is phase-locked to the excitation signal sent to the Source. We use a hardware device to ensure that not one period of the sine signal sent to the Source is lost.

The signal from the Angular Sensor goes to the Interface and to the Peak Detector, which extracts the amplitude of the signal, and generates one pulse at each extremum detected. The detected amplitude is sent to the Interface, and the pulses are sent to the Phase Comparator.

The Phase Comparator measures the phase offset between its two inputs, that is between the pendulum’s angular position and the reference signal, and sends this offset to the Interface.

So, the Interface has two informations available: the amplitude and the phase offset. Those informations are enough to draw a Van der Pol diagram in real-time, which is done by the control

software in the PC.

This possibility to see the Van der Pol diagram in real-time allows the operator to adjust the parameters in real-time or to stop the experiment. This is useful, because, depending on the initial conditions, the movement doesn't "hook on" every time the pendulum is dropped from an initial position. The Van der Pol diagram allows to see very quickly if the movement will hook on or if it will be damped to zero.

Instead of the group "Hardware Frequency Divider + Peak Detector + Phase Comparator", we could use only software with equations (16), but in this case, it is necessary to smooth the resulting Van der Pol curve; we prefer anticipating future experiments with higher-frequency source signals, where a software-only process could be too slow.

The Generator is used as a blackbox. Its output current is controlled (inside the Generator) to be equal to a given input signal to the Generator (an harmonic signal in our experiments). In our experimental setup, everything outside the Generator works in open-loop mode. More specifically, the Peak Detector output and the Phase Comparator output, which are often used as feedback parameters in this kind of setups, are used here only for display purposes. The Current Generator is given an input which consists of a constant-amplitude, constant-phase (vs absolute time) sinusoidal waveform, and is independent of the oscillator's motion.

9 Experimental results

9.1 Static torque measurements

We first carried out torque measurements using a direct-current excitation in the coil, to check that the actual torque (as a function of α , the pendulum's rod angular position versus vertical) applied to the pendulum's rod fits the model of magnetic interaction. Except for the combination Source I - Receptor 1, we present in each figure (e.g. in Figure 14a) a first plot called " I/I_0 vs α " showing the direct current I required in the coil to have the rod undergo a given angle α ; the ordinate is noted I/I_0 , where I_0 is a reference current with a value of 2 A. A model of the current I necessary to obtain a given angle α is derived from the torque model, by substituting $B_{ref}I/I_{ref}$ for B_0 in the equation giving the torque model, where I_{ref} is a reference current and B_{ref} is the corresponding magnetic field at the bottom of the pendulum's trajectory when the reference current I_{ref} is applied to the coil. The experimental results are represented by circles, while the model is represented by a solid line.

We then present a second plot called " T/T_0 vs α " (e.g. in Figure 14b), giving (versus α) the ratio of the torque T to a reference torque T_0 , which is the T_0 found in the expression of our torque model. The experimental results are represented by circles, while the model is represented by a solid line. The model is determined by the value which is given to parameter η . Except for combination Source I - Receptor 1, the optimum value which we find for η is then used in the numerical simulation. For combination Source I - Receptor 1, the value of η is determined by the best fit we could obtain between experimental motion data and numerical simulations based upon the torque model.

9.2 Motion measurements

In agreement with previous results presented in the literature, we observe that the movement can "hook on" and stabilize in a stationary quasi-sinusoidal movement, if the pendulum's actual frequency is a sub-multiple n of the excitation frequency. We call n the "expected frequency

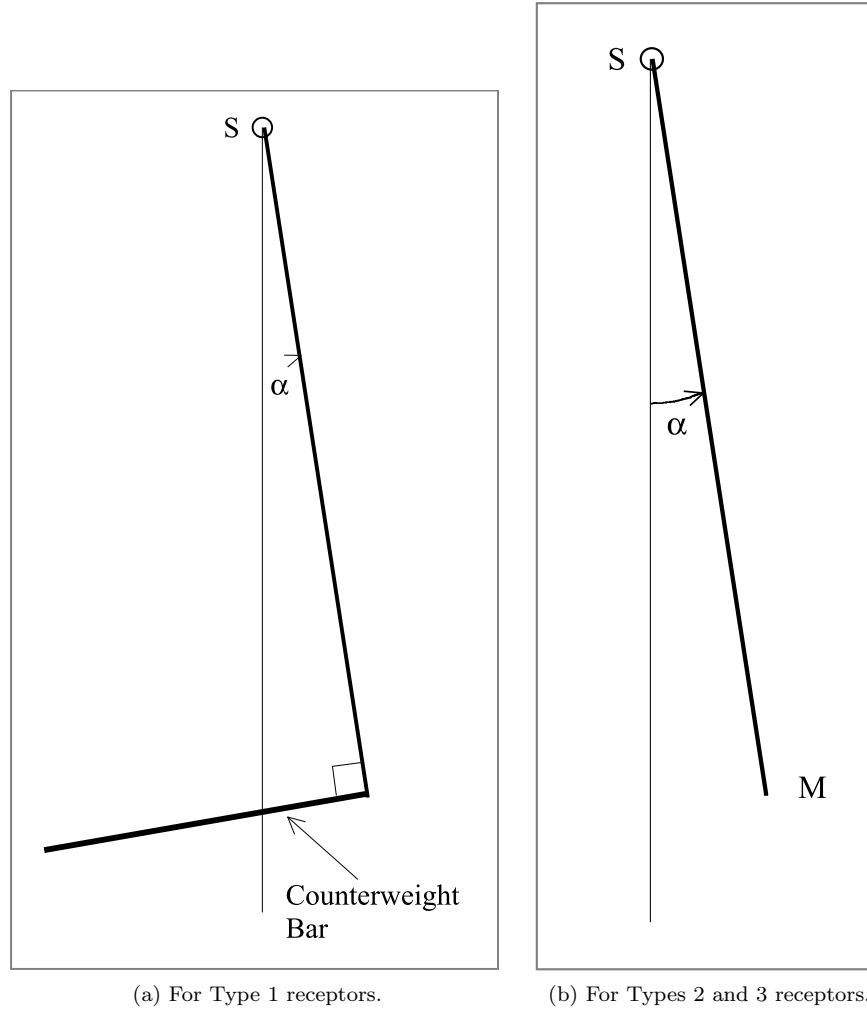


Figure 12: Experimental set-ups for static torque measurements

ratio". Depending on the H-function and the source and receptor types, an additional condition can be that n be odd or even. The pendulum's actual frequency is very close to the frequency the pendulum would exhibit if it were dropped at the stationary amplitude without damping nor external excitation.

We present experimental results under two forms: angle-versus-time plots and Van der Pol plots. In the Van der Pol plots, we represent dots (along the curves) which are inter-spaced by four periods of the expected stationary movement. Those dots allow to be aware of the time flow inside a Van der Pol representation, which is, by construction, an integral curve in which time is not explicitly apparent. It also allows to better compare experimental and numerical results.

The parameter “A” mentioned in the data relative to each numerical simulation refers to reduced-time equations (10) or (12).

To establish the experimental Van der Pol representation, we use the control system introduced above (see Figure 11). We first evaluate the amplitude over every 1-period set of data from the angle-vs-time data. Then we localize (vs time) the positions of the extremums, and then measure the phase offset between each extremum and a reference periodic signal. This reference signal is derived from the harmonic excitation current via frequency division by a ratio equal to the expected frequency ratio between the external force and the pendulum. This means that if the movement stabilizes, said phase offset moves towards a constant. This is indeed what we observe in the experiments whenever a movement becomes stationary.

9.3 Experimental results for the Type 1 Receptor

Static torque measurements. For the torque measurements of this receptor, we had to use a counterweight bar to establish an off-vertical no-current stable position, because the force can only be attractive, so that the stable position without counterweight can only be vertical. The experimental set-up is as of Figure 12a. Only Type II Source could give usable measurement values; the Type I Source gave too weak torques to be measurable with a current that the coil could admit. So for the combination Source I - Receptor 1, we could only infer from the other five oscillator types that the torque should be in fair accordance with the model. The measurements results (current and torque) for the Type II Source are in Figures 14a and 14b.

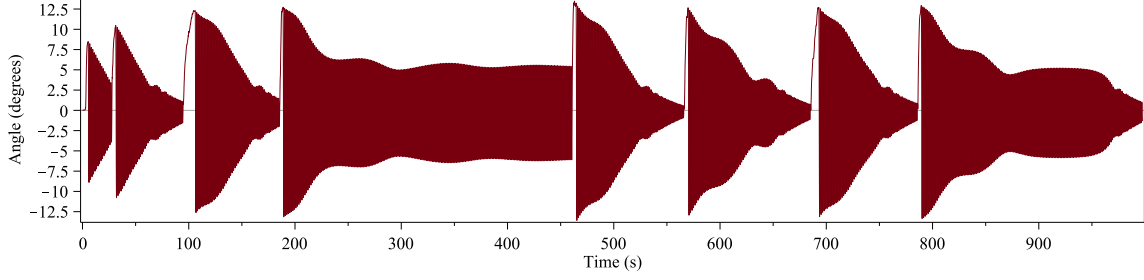
Motion measurements. We carried out experiments with a type I source and a type II source. The results are presented on Figures 13 and 14. On Figures 13a and 14c, giving Cartesian pendulum-angle-versus-time, we can see that a few attempts may be necessary before being able to initiate a stable motion of the pendulum. This is due to the system’s sensitivity to initial conditions and to the fact that the motion is captured by the attractor with a probability different from 1. Figures 13b and 14d give the Van der Pol plots of the experimental measurements. Figures 13c and 14e give the Van der Pol plots of the numerical simulations.

Receptor 1 with Source I. The data relative to the numerical simulations of Figure 13c are given in Table 3.

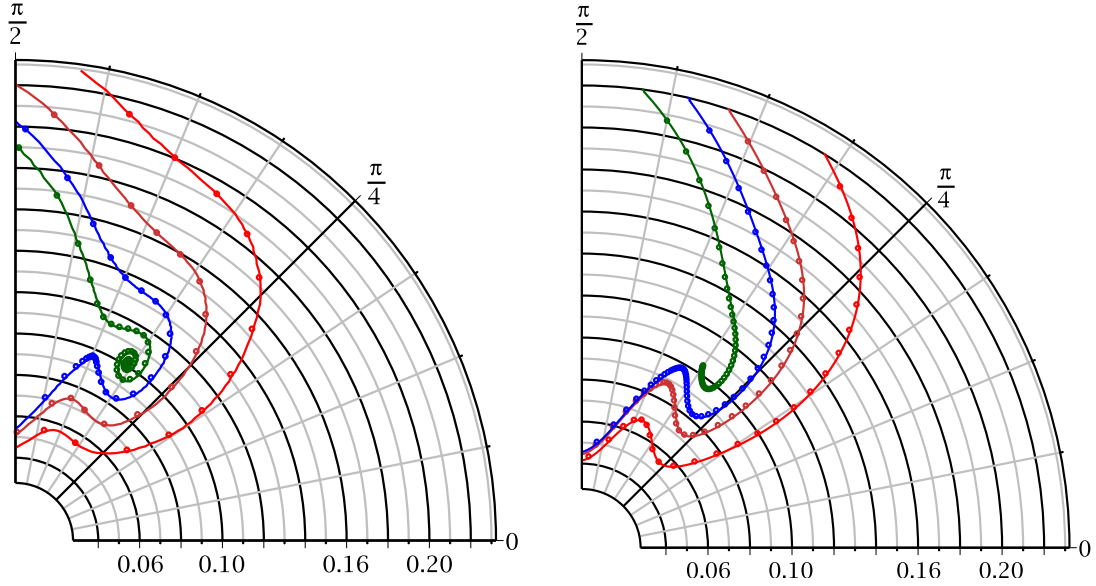
Receptor 1 with Source II. The data relative to the numerical simulations of Figure 14e are given in Table 4.

9.4 Experimental results for the Type 2 Receptor

Static torque measurements. For the torque measurements of this receptor, we carried out measurements without a counterweight bar (as of Figure 12b), for various values of the current I . For the central position of the rod ($\alpha = 0$), we had to use a counterweight bar, because without a counterweight, the current is too weak to measure the small angles α , and the torques are too weak too, and get lost into Coulomb damping. The experimental set-up is as of Figure 12b. The measurements results (current and torque) are in Figures 15a and 15b for the Type I Source, and in Figures 16a and 16b for the Type II Source.



(a) Angle vs time. The fourth attempt corresponds to the spiral-shaped plot in the Van der Pol representation below.



(b) Experimental results (Van der Pol representation). (c) Numerical simulations (Van der Pol representation).

Figure 13: Type 1 Receptor with Type I Source, frequency ratio=4, plots designated from 1 (spiral-shaped, innermost) to 4 (outermost). Along the curves, one dot every four periods of the pendulum.

Motion measurements. We carried out experiments with a type I- and a type II source. The results, given in dependent-coordinate-versus-time and Van der Pol plots, are presented on Figures 15 and 16. In the same way as for Figures 13a and 14c, we left on Figures 15c and 16c a few attempts visible.

Receptor 2 with Source I. The data relative to the numerical simulations of Figure 15e are given in Table 3.

Table 2: Masses and usage of the elements (the screws are not all the same mass). G is the gravity centre of the equipped rod.

Element	Mass (g)	Distance SG (cm)	Measurements the element is used in
Rod+Screw+Receptor 1 (sphere)	103.43	27.05	Static
Rod+Screw+Receptor 1 (parallel.)	213.37	39.85	Dynamic
Rod+Screw+Receptor 2	83.51	21.60	Static
Rod+Screw+Receptor 3	82.71	21.30	Static
Weighted rod+Receptor 1 (sphere)	382.94	31.2	Dynamic
Weighted rod+Screw+Receptor 2	363.01	30.20	Dynamic
Weighted rod+Screw+Receptor 3	362.22	30.00	Dynamic
Counterweight bar	26.80	-	Static
Receptor 1 (sphere)	34.23	-	-
Receptor 1 (parallelepiped)	143.26	-	-
Receptor 2	15.66	-	-
Receptor 3	13.53	-	-
Angular-position cylinder	426.31	-	All

Receptor 2 with Source II. The data relative to the numerical simulations of Figure 16e are given in Table 4.

9.5 Experimental results for the Type 3 Receptor

Static torque measurements. For the torque measurements of this receptor, we carried out measurements with the same principles as for the Type 2 Receptor. The experimental set-up is as of Figure 12b. The measurements results (current and torque) are in Figures 17a and 17b for the Type I Source, and in Figures 18a and 18b for the Type II Source.

Motion measurements. We carried out experiments with a type I- and a type II source. The results, given in dependent-coordinate-versus-time and Van der Pol plots, are presented on Figures 17 and 18. As above, we left on Figures 17c and 18c a few attempts visible.

Receptor 3 with Source I. The data relative to the numerical simulations of Figure 17e are given in Table 3.

Receptor 3 with Source II. The data relative to the numerical simulations of Figure 18e are given in Table 4.

Table 3: Numerical simulations: initial conditions and other parameters, Source I.

Combination	I-1	I-2	I-3
Initial amplitude	0.22	0.58	0.60
Initial phase 1	1.440796 (#1, innermost)	0.728 (#1, innermost)	1.630 (#1, innermost)
Initial phase 2	1.340796 (#2)	0.692 (#2)	1.585 (#2)
Initial phase 3	1.250796 (#3)	0.665 (#3, outermost)	1.560 (#3)
Initial phase 4	1.020796 (#4, outermost)	-	1.490 (#4, outermost)
Initial phase 5	-	-	-
Frequency ratio	4	21	20
Stationary amplitude	0.1	0.41	0.362
Excitation frequency (Hz)	2.836880	17.196905	16.447368
β	0.002	0.002332	0.0024
η	80.0	42.0	60.0
A	1.6	0.230	16.0
ω_0	4.456272	5.199630	5.209892
Coil current amplitude (A)	0.9	1	0.5

Table 4: Numerical simulations: initial conditions and other parameters, Source II.

Combination	II-1	II-2	II-3
Initial amplitude	0.60	0.63	0.64
Initial phase 1	1.076 (#1, innermost)	1.098 (#1, innermost)	0.973 (#1, innermost)
Initial phase 2	1.018 (#2)	1.087 (#2)	0.845 (#2)
Initial phase 3	0.985 (#3)	1.067 (#3, outermost)	0.740 (#3)
Initial phase 4	0.929 (#4, outermost)	-	0.635 (#4, outermost)
Initial phase 5	-	-	-
Frequency ratio	12	24	11
Stationary amplitude	0.4385	0.425	0.44
Excitation frequency (Hz)	9.708738	19.436346	9.00900
β	0.002	0.0030	0.003405
η	20.0	17.49	18.0
A	0.18	0.18	0.105
ω_0	5.142472	5.142472	5.205311
Coil current amplitude (A)	3	3	3

10 Discussion

10.1 Simulation quality

The models allowed us to make very good simulations, compared to the experimental results, except for the Type 1 Receptor with Type I Source, where the simulation is only fair. In all remaining five models, the dots representing time in the Van der Pol representations showed only small time offsets between the experimental results and the simulations. We found only a few degrees difference in the angular data in the Van der Pol representations. Knowing that even a $\pi/8$ offset represents 1/16 of an oscillator period over a typical 100-periods global time, we can see that the angular offsets are very small.

One hypothesis about the case of the Type 1 Receptor with Type I Source is that in this case, the receptor's size was not negligible compared to the distance between the source and the receptor. This size was necessary, because the magnetic effect was too weak with a small steel sphere. A more elaborate model could be built, considering the spatial extent of the receptor and integrating the magnetic interaction over the whole receptor's body. This would result in a more complicated H-function. It would also be feasible to build a stronger coil and to use a very high-susceptibility steel to try to be able to measure the actual torque along the pendulum's trajectory. Nevertheless, we notice that the torque model is the same between the combinations Source I-Receptor 1 and Source I-Receptor 3. Hence to experiment and model the interaction with the associated H-function, we rely on the combination Source I-Receptor 3.

10.2 Predictability

We noticed a sensitivity to initial conditions which was not beyond usual values for predictable motions. The Van der Pol representations of the averaged amplitude and phase were smooth, and any initial condition comprised between two flows next to each other produced a flow which stayed between said two flows, both via numerical simulations and by experimental measurements. We conclude that the argumental phenomenon, considered in terms of averaged amplitude and phase, and as far as we investigated it numerically and experimentally in this paper, is not of chaotic nature.

10.3 Attractors. Capture probability

Attractors, linked to stable motion, appear in the Van der Pol diagrams. The sizes of the attractors, in the simulations as well as in the experimental results, show that the capture probability is not negligible in typical cases. Experimentally, we noticed that the stable argumental regime is easily obtained, except for the Source I-Receptor 1 case; the order of magnitude of the experimental capture probability with our parameters is 0.1.

10.4 Robustness versus the form of the H-function.

It can be seen that the argumental phenomenon arises with various forms of the space-distribution function H and of the excitation. Table 1 characterizes the six forms by both their parity and their widths at half-height.

The shapes of the spirals converging towards stable regimes are remarkably similar in all our experiments, although the H-functions involved are quite different from each other. These shapes outline

attractors which also are similar in the various experiments. In every case, once the movement is captured by an attractor, the stable regime is reached in the same way, by following a clockwise spiral and getting around adjacent attractors. This suggests that the argumental phenomenon is robust versus the form of the H-function.

10.5 Robustness versus the source's frequency.

Although we did not systematically investigate this robustness, we could note incidentally, during our experiments, that, depending on the way the source's frequency varies, the oscillator having a negative μ Duffing parameter can adapt to a source-frequency increase by decreasing its average amplitude and vice versa, if the phase variation between the source and the oscillator happens in such a way that the representative point in the Van der Pol diagram lands, after a perturbation in the source's frequency, in one of the attractor basins corresponding to the frequency ratio between the new source frequency and the new (after perturbation) actual stable-regime oscillator frequency, and provided the source frequency variation is not too fast. This kind of robustness appears subjected to complex conditions, and seems to be comprehensively assessable only by a study in the analytic domain.

10.6 Robustness versus transient energy perturbations

Once the oscillator has entered an attractor's basin (in the Van der Pol representation), it gets "captured", and its representative point moves towards the "center" of that basin, which represents the final stable regime. But if the oscillator undergoes a small variation of energy from an external cause, for instance a small bump from an external object, or a transient friction, one can wonder if this movement towards stability will be disrupted.

We can assess the energy which is necessary to disrupt the movement towards stability: it is the energy which is necessary to go from inside the attractor's basin to just outside this basin. We mention "just" outside, because if the energy variation is big enough, the representative point can "jump" directly from one attractor's basin to another attractor's basin, and the oscillator's motion will keep going towards stability, but with a different final phase.

Using the notations of Equation (12), and considering the damping, as well as the action of the external force, as involving a negligible energy variation during the perturbation, and using the equation of the free-running undamped Duffing oscillator: $\frac{d^2\alpha}{d\tau^2} + \alpha + \mu\alpha^3 = 0$, we have the expression of the potential (W_p) and total (W) energies: $W_p = \frac{1}{2}\alpha^2 + \frac{\mu}{4}\alpha^4$ and $W = W_k + W_p$, where W_k is the kinetic energy. When $|\alpha|$ is maximum, we have $|\alpha| \approx a$ and $\frac{d\alpha}{d\tau} = 0$, and therefore,

$$W = W_p = \frac{1}{2}a^2 + \frac{\mu}{4}a^4 \quad (17)$$

In case of a small variation Δa of a , we have $\Delta W = (a + \mu a^3)\Delta a$.

In our experiments and simulations, relation $|\mu|a^3 \ll a$ holds, so that

$$\frac{\Delta W}{W} \approx 2 \frac{\Delta a}{a} \quad (18)$$

Now let us consider a point A in the Van der Pol representation (see Figure 16d), corresponding to a given total energy W_A . Assuming that the total energy is approximately constant over one period of

the oscillator (because the oscillator loses energy due to damping, but gains energy via the external source), we can see that the total energy of the oscillator is characterized by a function, given by Equation (17), of only its averaged amplitude a . Therefore, the total energy of the oscillator is a function of only point A 's radius. Now, if we investigate the robustness of the oscillator's motion, we see that if point A is at the centre of an attractor, i.e. the oscillator has reached a stable motion (A is in A_1), and if a perturbation pushes point A out of the attractor, we can make an assessment of the energy variation due to the perturbation by observing the displacement of point A . We shall study two elementary cases, the first one being when the amplitude remains constant, and the second one being where the phase remains constant.

Perturbation with no amplitude variation We can see that if the averaged amplitude is the same before and after the perturbation event, point A 's radius is invariant, and the energy variation is null. This is illustrated by point A_1 moving to point A_2 in Figure 16d. In this case, a very small amount of energy can theoretically induce an average phase variation big enough to disrupt the march towards stable motion. This could be realized by carrying out a phase shift by inducing a delay in the oscillator's motion while it is at its extreme position. If done with a frictionless device (like, for instance, a gate whose course would be perpendicular to the pendulum's course), this would yield a phase shift with theoretically no external energy consumption, because the kinetic energy amounts to 0 in this position, and the position (and hence, the potential energy) does not change during this kind of perturbation. However, this procedure involves a carefully-controlled process, which seems to have a low occurrence probability in nature, where perturbations are most often of dissipative kind.

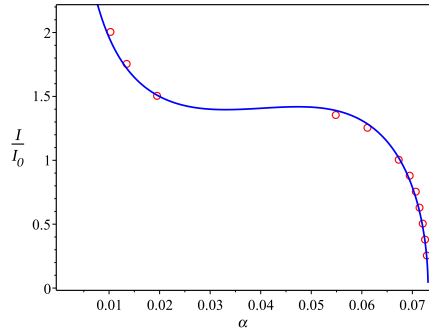
Perturbation with no phase shift In this case, where only the amplitude is altered, we can assess the energy which is necessary to disrupt the stable motion. In the Van der Pol representation, this kind of perturbation is represented by a radial segment. We can see that if the perturbation arises while the representative point is near the external border of said basin, a very small amount of energy will be sufficient to disrupt the march to stability (this is illustrated by point A_4 moving to point A_3). On the other hand, if said perturbation arises while the representative point is near the center of the basin, the energy to push it out of the basin will correspond to the basin's radius along the radial direction of the Van der Pol representation (this is illustrated by point A_1 moving to point A_3). This kind of perturbation could be realized by temporarily (for instance, over one period of the oscillator) varying the amplitude of the external excitation source, and seems more likely to happen in nature than the previous case (phase shift with no amplitude variation). As it can be seen that, in our experiments, the diameters of the attractors' basins are from 10 to 30% of the final stable amplitude, and due to Equation (18), we can state that in our experiments, when the oscillator is in a stable regime, the energy required to irreversibly destabilize it with no phase shift is about 20 to 60% the average energy of the oscillator in said stable regime, which amounts to a large energy variation. Experimentally, we never observed a disruption of the march towards stable motion (once engaged), whatever the form of the H-function, and despite all the imperfections of our experimental setup.

In conclusion, the robustness of the oscillator's motion versus natural perturbations seems overall good.

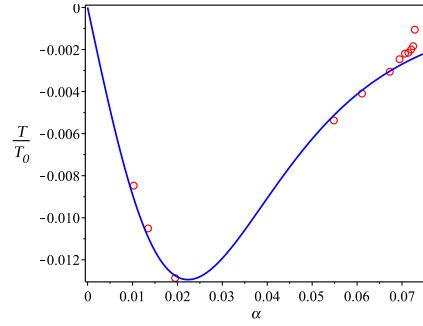
11 Future

In upcoming papers, we shall study the equations of motion symbolically to understand how the oscillator enters a stable motion, and to indicate symbolic expressions regarding the stability, the robustness and the capture probabilities of the attractors.

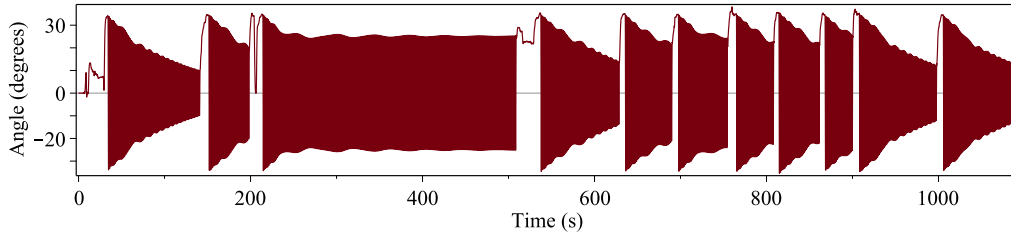
Acknowledgments The authors wish to thank Mr Gwendal Cumunel for his advice and suggestions about the form of this article.



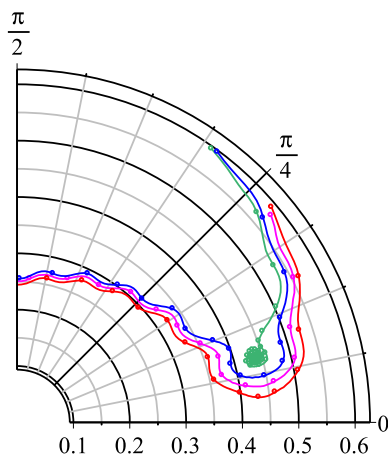
(a) Currents ratio I/I_0 vs angle α : measurements (circles), model (line).



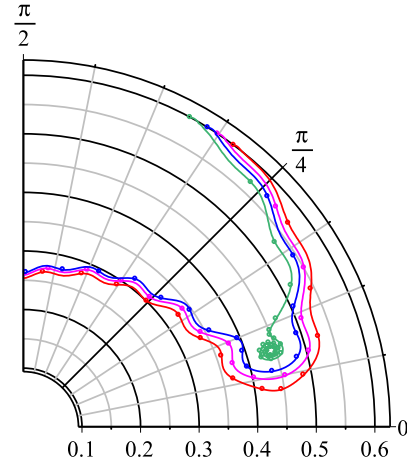
(b) Torques ratio T/T_0 vs α : measurements (circles), model (line).



(c) Angle vs time. The third attempt corresponds to the spiral-shaped plot in the Van der Pol representation below.

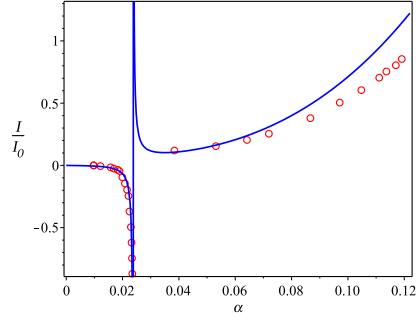


(d) Experimental results (Van der Pol representation).

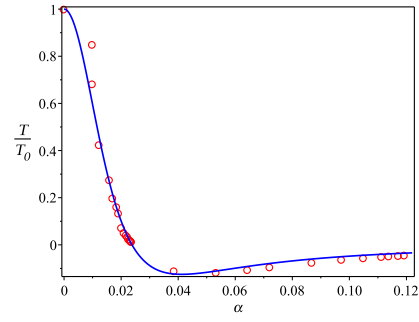


(e) Numerical simulations (Van der Pol representation).

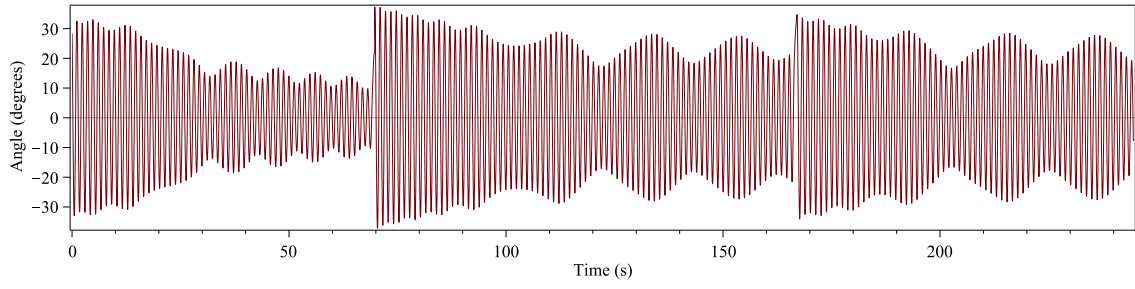
Figure 14: Type 1 Receptor with Type II Source, frequency ratio=12, plots designated from 1 (spiral-shaped, innermost) to 4 (outermost). Along the curves, one dot every four periods of the pendulum.



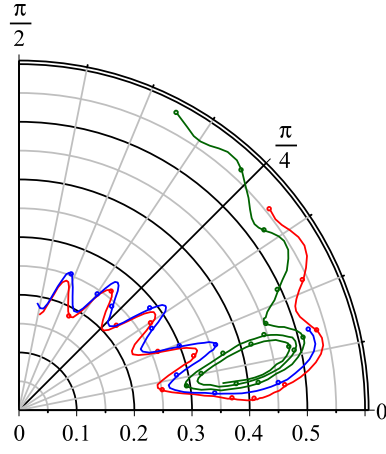
(a) Currents ratio I/I_0 vs angle α : measurements (circles), model (line).



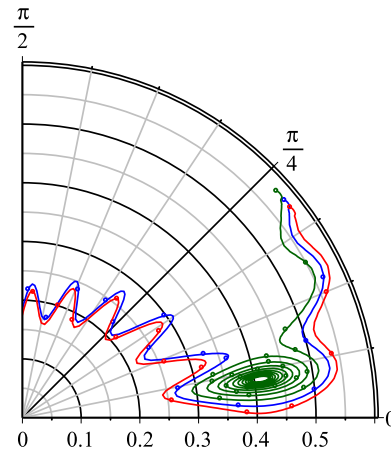
(b) Torques ratio T/T_0 vs angle α : measurements (circles), model (line).



(c) Angle vs time. The second attempt corresponds to the spiral-shaped plot in the Van der Pol representation below.

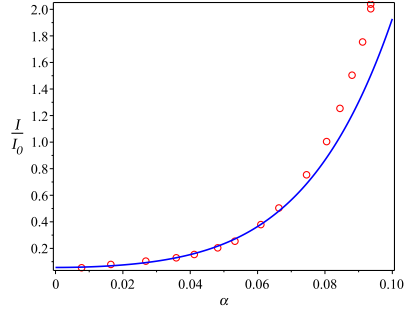


(d) Experimental results (Van der Pol representation).

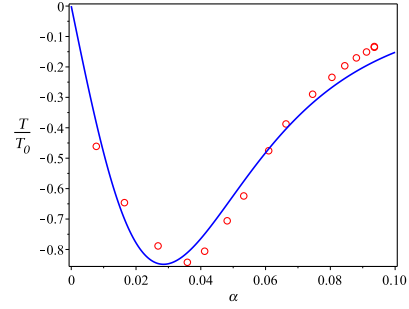


(e) Numerical simulation results (Van der Pol representation).

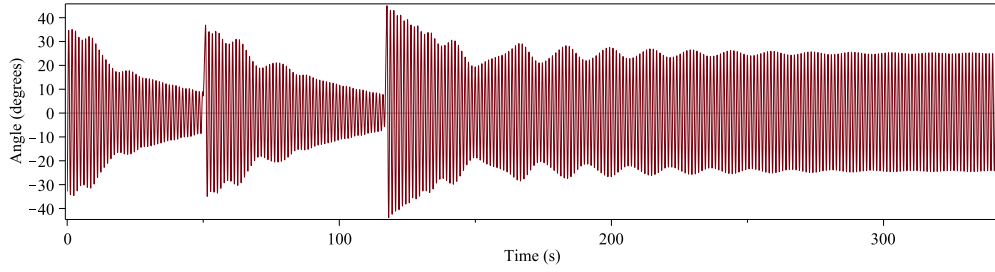
Figure 15: Type 2 Receptor with Type I Source, frequency ratio=21, plots designated from 1 (spiral-shaped, innermost) to 3 (outermost). Along the curves, one dot every four periods of the pendulum.



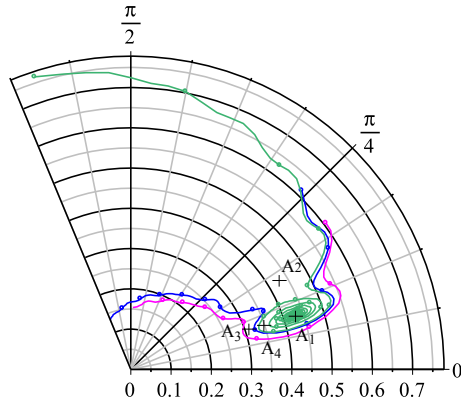
(a) Currents ratio I/I_0 vs angle α : measurements (circles), model (line).



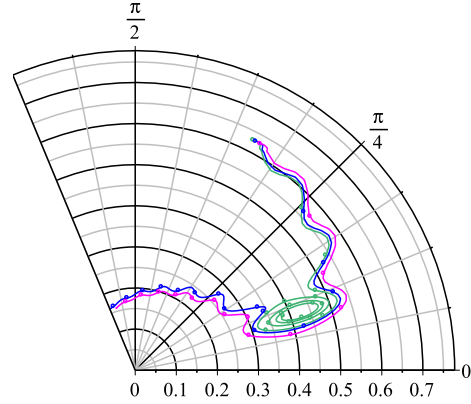
(b) Torques ratio T/T_0 vs angle α : measurements (circles), model (line).



(c) Angle vs time. The third attempt corresponds to the spiral-shaped plot in the Van der Pol representation below.

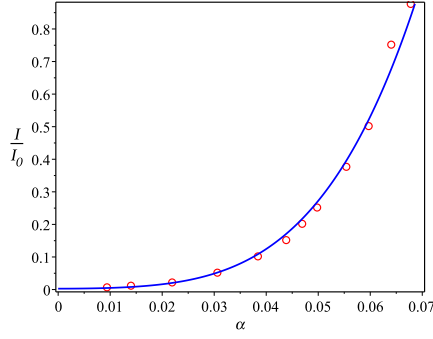


(d) Experimental results (Van der Pol representation). Points A_i are referred to in the text.

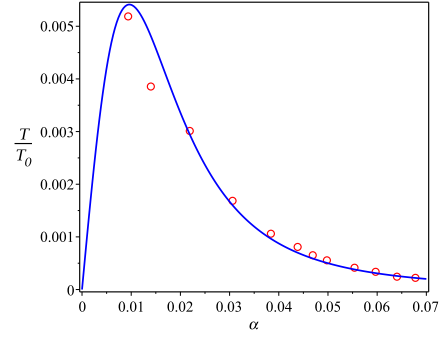


(e) Numerical simulations (Van der Pol representation).

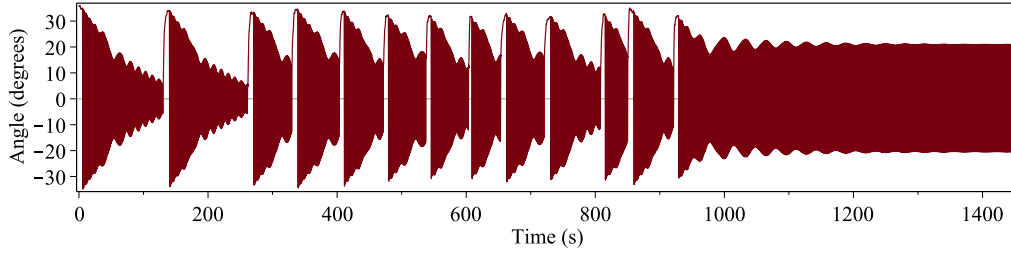
Figure 16: Type 2 Receptor with Type II Source, frequency ratio=24, plots designated from 1 (spiral-shaped, innermost) to 3 (outermost). Along the curves, one dot every four periods of the pendulum.



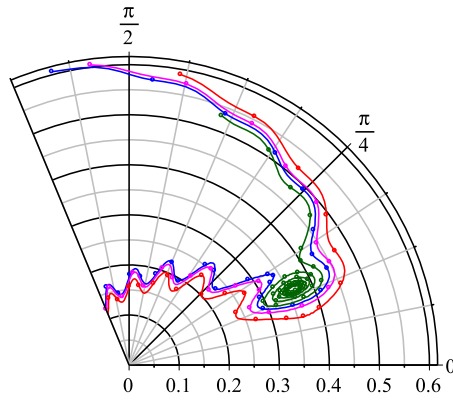
(a) Currents ratio I/I_0 vs angle α : measurements (circles), model (line).



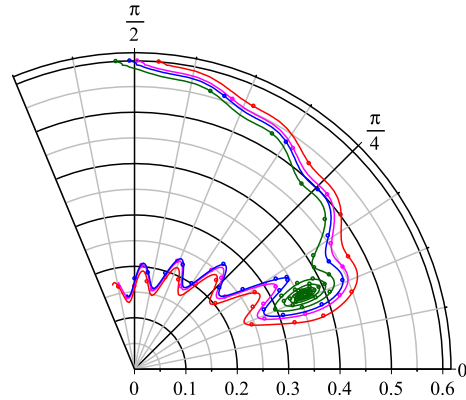
(b) Torques ratio T/T_0 vs angle α : measurements (circles), model (line).



(c) Angle vs time. The last attempt corresponds to the spiral-shaped plot in the Van der Pol representation below.

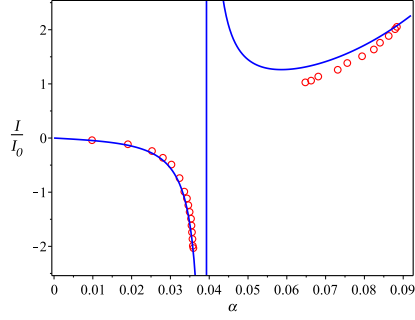


(d) Experimental results (Van der Pol representation).

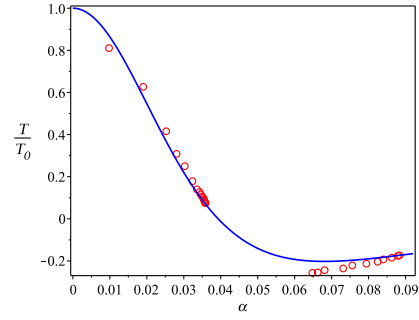


(e) Numerical simulations (Van der Pol representation).

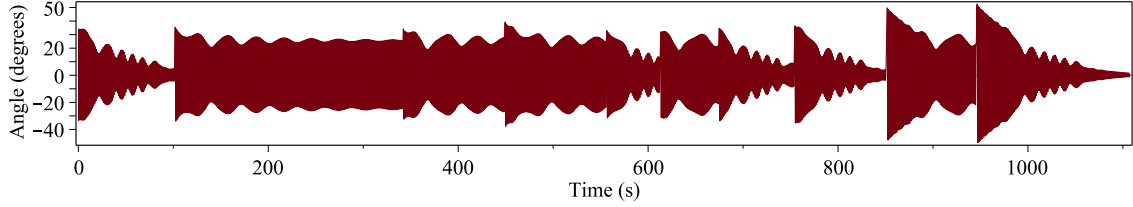
Figure 17: Type 3 Receptor with Type I Source, frequency ratio=20, plots designated from 1 (spiral-shaped, innermost) to 4 (outermost). Along the curves, one dot every four periods of the pendulum.



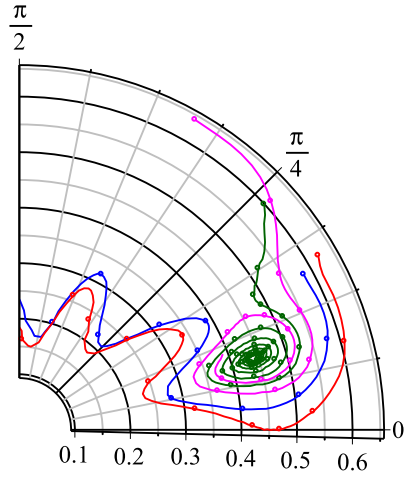
(a) Currents ratio I/I_0 vs angle α : measurements (circles), model (line).



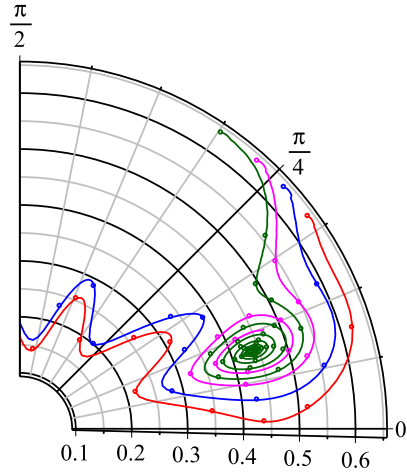
(b) Torques ratio T/T_0 vs angle α : measurements (circles), model (line).



(c) Angle vs time. The second attempt corresponds to the spiral-shaped plot in the Van der Pol representation below.



(d) Experimental results (Van der Pol representation).



(e) Numerical simulations (Van der Pol representation).

Figure 18: Type 3 Receptor with Type II Source, frequency ratio=11, plots designated from 1 (spiral-shaped, innermost) to 4 (outermost). Along the curves, one dot every four periods of the pendulum.

12 Appendices

12.1 Introduction to the Appendices.

The aim of each of the six following Appendices, is to calculate the H-function as defined by

$$T \approx T_0 H(\alpha)$$

where T =coordinate of \mathbf{T} along \mathbf{k} , and T_0 is a constant.

12.2 Appendix A: Type 1 Receptor with a Type I source.

Using equations (4) and (8), we obtain:

$$\begin{aligned} \mathbf{T} &= B_0^2 d^2 \frac{\kappa}{2} R \mathbf{w} \times \left(\frac{\partial}{\partial r} P_I(r, \alpha) \mathbf{w} + \frac{1}{r} \frac{\partial}{\partial \alpha} P_I(r, \alpha) \mathbf{q} \right) \\ &= B_0^2 d^2 \frac{\kappa}{2} R \frac{1}{r} \frac{\partial}{\partial \alpha} P_I(r, \alpha) \mathbf{k} \end{aligned} \quad (19)$$

Calculating $\frac{\partial}{\partial \alpha} P_I(r, \alpha)$ from equation (3) and then substituting R for r in the result (because point M must now move along the circle centred at S), we get:

$$\begin{aligned} \frac{\partial}{\partial \alpha} P_I(r, \alpha) &= \\ &- 2R \sin \alpha (R + d) \left(d^2 + 4R(R + d) \sin^2 \frac{\alpha}{2} \right)^{-2} \end{aligned}$$

Substituting this value into equation (19), we finally obtain:

$$T = -T_0 \frac{\sin(\alpha)}{\left(1 + 4 \gamma (1 + \gamma) \sin^2 \frac{\alpha}{2} \right)^2}$$

with $T_0 = \kappa \gamma (1 + \gamma) B_0^2$ and $B_0 = \frac{\mu_0 M_n}{4\pi d^2}$.

Here, we finally get, using the simplifying hypothesis: $H(\alpha) = -\frac{\alpha}{(1 + \eta^2 \alpha^2)^2}$ and $T_0 = \kappa \eta^2 B_0^2$.

12.3 Appendix B: Type 1 Receptor with a Type II source (Béthenod's pendulum).

In the same way as for the Type 1 Receptor with a Type I Source, and using equations (7) and (8), we obtain: $T = \frac{1}{2} \kappa B_0^2 d^4 \frac{R}{r} \frac{\partial P_{II}}{\partial \alpha}$. Then, from equation (6):

$$\begin{aligned} \frac{\partial}{\partial \alpha} P_{II}(r, \alpha) &= \\ &- 4R \sin \alpha (R + d) \left(d^2 + 4R(R + d) \sin^2 \frac{\alpha}{2} \right)^{-3} \end{aligned}$$

Hence: $T = -T_0 \frac{\sin \alpha}{(1 + 4\gamma(1 + \gamma) \sin^2 \frac{\alpha}{2})^3}$ with $T_0 = 2\kappa\gamma(1 + \gamma)B_0^2$.

Finally, using the simplifying hypothesis, we obtain: $H(\alpha) = -\frac{\alpha}{(1 + \eta^2 \alpha^2)^3}$ and $T_0 = \kappa\eta^2 B_0^2$.

12.4 Appendix C: Type 2 Receptor with a Type I source (Doubochinski's pendulum).

We first calculate the \mathbf{T}' torque. Using equation (2), we have:

$$\mathbf{T}' = \mathbf{m} \times \mathbf{B} = m_0 \mathbf{w} \times \frac{B_0 d}{OM} \mathbf{v} = \frac{m_0 B_0 d}{OM} \mathbf{w} \times \mathbf{v}.$$

After some transformations, we find:

$$\mathbf{T}' = -T'_0 \frac{1 - 2(1 + \gamma) \sin^2 \frac{\alpha}{2}}{1 + 4\gamma(1 + \gamma) \sin^2 \frac{\alpha}{2}} \mathbf{k}$$

with $T'_0 = m_0 B_0$, $B_0 = \frac{\mu_0 N I}{2\pi} \frac{L}{\sqrt{L^2 + d^2}}$, and $\gamma = \frac{R}{d}$.

We then calculate the \mathbf{T}'' torque. Let M be a fixed point of polar coordinates (r_M, α_M) and N a variable point of coordinates (r, α) , in the vicinity of M. Let \mathbf{m}_M be the magnetic moment of the magnet located at M, and \mathbf{B} the magnetic field at point N. While point N moves for the calculation of the gradient hereafter, we must consider that the magnetic moment in N is constant and equal to \mathbf{m}_M . The force \mathbf{F}' applied to the magnet by the magnetic field is: $\mathbf{F} = \nabla(\mathbf{m}_M \cdot \mathbf{B})$, taken with N at M, \mathbf{m}_M being considered constant. We find that, while point N is not at M, it holds: $\mathbf{m}_M \cdot \mathbf{B} = -m_0 B_0 d E(r, \alpha)$, with

$$E(r, \alpha) = \frac{(R + d) \sin \alpha_M + r \sin(\alpha - \alpha_M)}{(R + d - r)^2 + 2r(R + d)(1 - \cos \alpha)}$$

Hence

$$\mathbf{F} = -m_0 B_0 d \left(\frac{\partial}{\partial r} E(r, \alpha) \mathbf{w} + \frac{1}{r} \frac{\partial}{\partial \alpha} E(r, \alpha) \mathbf{q} \right)$$

This force applies a torque \mathbf{T}'' to the rod, and we have

$$\begin{aligned} \mathbf{T}'' &= R \mathbf{w} \times \mathbf{F} \\ &= -m_0 B_0 d \frac{R}{r} \frac{\partial}{\partial \alpha} E(r, \alpha) \mathbf{k} \end{aligned} \tag{20}$$

Calculating $\frac{\partial}{\partial \alpha} E(r, \alpha)$ and substituting in the result R for r and α for α_M , we find:

$$\begin{aligned} \frac{\partial}{\partial \alpha} E(r, \alpha) &= \\ &= R \frac{d^2 + 2R(R + d)(1 - \cos \alpha) - 2(R + d)^2 \sin^2 \alpha}{(d^2 + 2R(R + d)(1 - \cos \alpha))^2} \end{aligned}$$

After some transformations, and putting T'' =coordinate of \mathbf{T}'' along \mathbf{k} , we find:

$$T'' = -T''_0 \frac{1 + 4\gamma(1 + \gamma) \sin^2 \frac{\alpha}{2} - 2(1 + \gamma)^2 \sin^2 \alpha}{(1 + 4\gamma(1 + \gamma) \sin^2 \frac{\alpha}{2})^2}$$

with $T_0'' = -m_0 B_0 \gamma$ and $B_0 = \frac{\mu_0 N I}{2\pi} \frac{L}{\sqrt{L^2 + d^2}}$.

Then, putting $\mathbf{T} = \mathbf{T}' + \mathbf{T}''$, we obtain:

$$\mathbf{T} = T_0(1 + \gamma) \frac{1 - 2(1 + 2\eta^2) \sin^2 \frac{\alpha}{2}}{(1 + 4\eta^2 \sin^2 \frac{\alpha}{2})^2} \mathbf{k}$$

Then, using the simplifying hypothesis, and putting T =coordinate of \mathbf{T} along \mathbf{k} , we have, considering that $|\eta^2| \gg 1$: $H(\alpha) = \frac{1 - \eta^2 \alpha^2}{(1 + \eta^2 \alpha^2)^2}$ and $T_0 = -(1 + \gamma)m_0 B_0$.

12.5 Appendix D: Type 2 Receptor with a Type II source.

We first calculate the \mathbf{T}' torque. Using equation (5), we have:

$$\mathbf{T}' = \mathbf{m} \times \mathbf{B} = m_0 \mathbf{w} \times \frac{B_0 d^2}{OM^2} \mathbf{u} = \frac{m_0 B_0 d^2}{OM^2} \mathbf{w} \times \mathbf{u}$$

After some transformations, we find:

$$\mathbf{T}' = T_0' \frac{\sin \alpha}{(1 + 4\gamma(1 + \gamma) \sin^2 \frac{\alpha}{2})^{\frac{3}{2}}} \mathbf{k}$$

with $T_0' = m_0 B_0(1 + \gamma)$ and $B_0 = \frac{\mu_0 N I}{2\pi} \frac{L}{\sqrt{L^2 + d^2}}$.

We then calculate the \mathbf{T}'' torque. In the same way as for the Type I Source above, the force \mathbf{F}' applied to the magnet by the magnetic field is: $\mathbf{F} = \nabla(\mathbf{m}_M \cdot \mathbf{B})$. We find

$$\mathbf{m}_M \cdot \mathbf{B} = m_0 B_0 d^2 E(r, \alpha)$$

with

$$E(r, \alpha) = \frac{r \cos(\alpha_M - \alpha) - (R + d) \cos \alpha_M}{((R + d - r)^2 + 4r(R + d) \sin^2 \frac{\alpha}{2})^{\frac{3}{2}}}$$

Hence

$$\mathbf{F} = m_0 B_0 d^2 \left(\frac{\partial}{\partial r} E(r, \alpha) \mathbf{w} + \frac{\partial}{\partial \alpha} E(r, \alpha) \mathbf{q} \right)$$

This force applies a torque \mathbf{T}'' to the rod, and we have

$$\begin{aligned} \mathbf{T}'' &= R \mathbf{w} \times \mathbf{F} \\ &= -m_0 B_0 d^2 R \frac{\partial}{\partial \alpha} E(r, \alpha) \mathbf{k} \end{aligned}$$

Calculating $\frac{\partial}{\partial \alpha} E(r, \alpha)$ and substituting in the result R for r and α for α_M , we find:

$$\begin{aligned} \frac{\partial}{\partial \alpha} E(r, \alpha) &= \\ &- 3R(R + d) \frac{-d + 2(R + d) \sin^2 \frac{\alpha}{2}}{(d^2 + 4R(R + d) \sin^2 \frac{\alpha}{2})^{\frac{5}{2}}} \sin \alpha \end{aligned}$$

After some transformations, and putting T'' =coordinate of \mathbf{T}'' along \mathbf{k} , we find:

$$T'' = -T_0'' \frac{1 - 2(1 + \gamma) \sin^2 \frac{\alpha}{2}}{(1 + 4\gamma(1 + \gamma) \sin^2 \frac{\alpha}{2})^{\frac{5}{2}}}$$

with $\gamma = \frac{R}{d}$, $T_0'' = -3\gamma(\gamma + 1)m_0B_0$,

and $B_0 = \frac{\mu_0 NI}{2\pi} \frac{L}{\sqrt{L^2 + d^2}}$.

Then, putting $\mathbf{T} = \mathbf{T}' + \mathbf{T}''$ and T =coordinate of \mathbf{T} along \mathbf{k} , we obtain:

$$T = T_0' \frac{3\gamma + 1 - 2\eta^2 \sin^2 \frac{\alpha}{2}}{(1 + 4\eta^2 \sin^2 \frac{\alpha}{2})^{\frac{5}{2}}} \sin \alpha$$

with $T_0' = -m_0B_0(\gamma + 1)$ and $B_0 = \frac{\mu_0 NI}{2\pi} \frac{L}{\sqrt{L^2 + d^2}}$.

Then, using the simplifying hypothesis, and considering that $|\gamma| \gg 1$, we obtain:

$$H(\alpha) = -\frac{1 - \frac{\eta}{6}\alpha^2}{(1 + \eta^2\alpha^2)^{\frac{5}{2}}} \alpha \quad \text{and} \quad T_0 = 3\eta^2 m_0 B_0.$$

12.6 Appendix E: Type 3 Receptor with a Type I source.

Following the same calculus path as for the Type 2 Receptor with a Type I source, and with the same notations (unless otherwise specified), we first calculate the \mathbf{T}' torque. Using equation (2), we have:

$$\mathbf{T}' = \mathbf{m} \times \mathbf{B} = m_0 \mathbf{q} \times \frac{B_0 d}{OM} \mathbf{v} = \frac{m_0 B_0 d}{OM} \mathbf{q} \times \mathbf{v}$$

After some transformations, we find:

$$\mathbf{T}' = T_0' \frac{\sin \alpha}{1 + 4\gamma(1 + \gamma) \sin^2 \frac{\alpha}{2}} \mathbf{k}$$

with $T_0' = m_0 B_0(1 + \gamma)$.

Calculating the \mathbf{T}'' torque, we find:

$$E(r, \alpha) = \frac{-(R + d) \cos \alpha_M + r \cos(\alpha - \alpha_M)}{(R + d - r)^2 + 4r(R + d) \sin^2 \frac{\alpha}{2}}$$

Then, calculating $\frac{\partial}{\partial \alpha} E(r, \alpha)$ and substituting in the result R for r and α for α_M , we find:

$$\frac{\partial}{\partial \alpha} E(r, \alpha) = 2R(R + d) \frac{d - 2(R + d) \sin^2 \frac{\alpha}{2}}{(d^2 + 4R(R + d) \sin^2 \frac{\alpha}{2})^2} \sin \alpha$$

Applying equation (20), and carrying out some transformations, we find:

$$\mathbf{T}'' = 2\gamma T_0' \frac{1 - 2(1 + \gamma) \sin^2 \frac{\alpha}{2}}{(1 + 4\gamma(1 + \gamma) \sin^2 \frac{\alpha}{2})^2} \sin \alpha \mathbf{k}$$

with $T'_0 = m_0 B_0 (1 + \gamma)$.

Then, putting $\mathbf{T} = \mathbf{T}' + \mathbf{T}''$ and T =coordinate of \mathbf{T} along \mathbf{k} , we obtain:

$$T = T_0 \frac{\sin \alpha}{(1 + 4\eta^2 \sin^2 \frac{\alpha}{2})^2} \quad \text{with } T_0 = m_0 B_0 (1 + \gamma)(1 + 2\gamma).$$

Finally, using the simplifying hypothesis, we get: $H(\alpha) = \frac{\alpha}{(1 + \eta^2 \alpha^2)^2}$.

12.7 Appendix F: Type 3 Receptor with a Type II source.

Following the same calculus path as for the Type 2 Receptor with a Type II source, and with the same notations (unless otherwise specified), we first calculate the \mathbf{T}' torque. Using equation (5), we have:

$$\mathbf{T}' = \mathbf{m} \times \mathbf{B} = m_0 \mathbf{q} \times \frac{B_0 d^2}{OM^2} \mathbf{v} = \frac{m_0 B_0 d^2}{OM^2} \mathbf{q} \times \mathbf{v}$$

After some transformations, we find:

$$\mathbf{T}' = T'_0 \frac{1 - 2(1 + \gamma) \sin^2 \frac{\alpha}{2}}{1 + 4\gamma(1 + \gamma) \sin^2 \frac{\alpha}{2}} \mathbf{k}$$

with $T'_0 = m_0 B_0$.

We now calculate the \mathbf{T}'' torque. We find here:

$$E(r, \alpha) = \frac{(R + d) \sin \alpha_M + r \sin(\alpha - \alpha_M)}{((R + d - r)^2 + 4r(R + d) \sin^2 \frac{\alpha}{2})^{\frac{5}{2}}}$$

Then, calculating $\frac{\partial}{\partial \alpha} E(r, \alpha)$ and substituting in the result R for r and α for α_M , we find:

$$\begin{aligned} \frac{\partial}{\partial \alpha} E(r, \alpha) = \\ R \frac{d^2 + 4R(R + d) \sin^2 \frac{\alpha}{2} - 3(R + d)^2 \sin^2 \alpha}{(d^2 + 4R(R + d) \sin^2 \frac{\alpha}{2})^{\frac{5}{2}}} \end{aligned}$$

Applying equation (20), and carrying out some transformations, we find:

$$\begin{aligned} \mathbf{T}'' = \\ \gamma T'_0 \frac{1 + 4\gamma(1 + \gamma) \sin^2 \frac{\alpha}{2} - 3(\gamma + 1)^2 \sin^2 \alpha}{(1 + 4\gamma(1 + \gamma) \sin^2 \frac{\alpha}{2})^2} \sin \alpha \mathbf{k} \end{aligned}$$

Then, putting $\mathbf{T} = \mathbf{T}' + \mathbf{T}''$ and T =coordinate of \mathbf{T} along \mathbf{k} , we obtain:

$$T = T_0 \frac{1 - 2(4\eta^2 - 1) \sin^2 \frac{\alpha}{2} + 4\eta^2 \sin^4 \frac{\alpha}{2}}{(1 + 4\eta^2 \sin^2 \frac{\alpha}{2})^{\frac{5}{2}}}$$

with $T_0 = m_0 B_0 (1 + \gamma)$.

Then, using the simplifying hypothesis, and considering that $|\gamma| \gg 1$, we obtain:

$$H(\alpha) = \frac{1 - 2\eta^2 \alpha^2}{(1 + \eta^2 \alpha^2)^{\frac{5}{2}}}.$$

References

- [1] M.J. Béthenod. Sur l’entretien du mouvement d’un pendule au moyen d’un courant alternatif de fréquence élevée par rapport à sa fréquence propre. *Comptes rendus hebdomadaires de l’Académie des sciences*, 207(19):847, November 1938. (in French).
- [2] D. Cintra and P. Argoul. Argumentary oscillation phenomenon. In *(online publication)*, Lille, France, October 2013. Dynolin conference.
- [3] D. Cintra and P. Argoul. Argumentary Duffing oscillators - Stable-regime probability. In *(online publication)*, Aix-en-Provence (France), June 2014. XIX th Vishno symposium.
- [4] D. Cintra and P. Argoul. Six models of argumental oscillators - Experimental results. In *(online publication)*, Paris, France, October 2014. Dynolin conference.
- [5] A. Cornu. Sur la synchronisation des horloges de précision et la distribution de l’heure. *Journal de Physique Théorique et Appliquée*, 7(1):231–239, 1888. (in French).
- [6] B. Cretin and D. Vernier. Quantized amplitudes in a nonlinear resonant electrical circuit. In *2009 Joint Meeting of the European Frequency and Time Forum and the IEEE International Frequency Control Symposium, vols 1 and 2*, volume 1 & 2, pages 797–800, Besançon, France, April 2009. Joint Meeting of the 23rd European Frequency and Time Forum/IEEE International Frequency Control Symposium.
- [7] G. Darrieus. Joseph Béthenod - Sa vie, son oeuvre - Présentation à la Société française des Electriciens le 2 décembre 1944. *Technica*, 67:8, June-July 1945. The presentation by A. Soulier is cited in this article about Béthenod (in French).
- [8] D. Doubochinski and J. Tennenbaum. On the general nature of physical objects and their interactions, as suggested by the properties of argumentally-coupled oscillating systems. *arXiv:0808.1205 [physics.gen-ph]*, 2008.
- [9] D.B. Doubochinski and J.B. Doubochinski. Amorçage argumentaire d’oscillations entretenues avec une série discrète d’amplitudes stables. *E.D.F. Bulletin de la direction des études et recherches, série C mathématiques, informatique*, 3:11–20, 1991. (in French).
- [10] H. Onur Ekici and Hakan Boyaci. Effects of non-ideal boundary conditions on vibrations of microbeams. *Journal of Vibration and Control*, 13(9-10):1369–1378, September 2007.
- [11] Ch. Féry. Sur quelques modes électriques d’entretien du pendule. Pendule sans lien matériel. *Journal de Physique Théorique et Appliquée*, 7(1):520–530, 1908. (in French).
- [12] D. I. Penner, D. B. Doubochinski, M. I. Kozakov, A. S. Vermel, and Yu. V. Galkin. Asynchronous excitation of undamped oscillations. *Soviet Physics Uspekhi*, 16(1), July-August 1973.
- [13] D. I. Penner, Ya. B. Doubochinski, D. B. Doubochinski, and M. I. Kozakov. Oscillations with self-regulating interaction time. *Soviet Physics Doklady*, 17:541, December 1972.
- [14] Pavol Popovic, Ali H. Nayfeh, Kyoyul Oh, and Samir A. Nayfeh. An experimental investigation of energy transfer from a high- frequency mode to a low-frequency mode in a flexible structure. *Journal of Vibration and Control*, 1(1):115–128, January 1995.

- [15] J.P. Treilhou, J. Coutelier, J.J. Thocaven, and C. Jacquez. Payload motions detected by balloon-borne fluxgate-type magnetometers. *Advances in Space Research*, 26(9):1423–1426, 2000.

Non-linear argumental oscillators: Stability criterion and approximate implicit analytic solution

Daniel Cintra (corresponding author)
Université Paris-Est, Laboratoire Navier (UMR 8205),
CNRS, Ecole des Ponts ParisTech, IFSTTAR,
F-77455 Marne La Vallée, France.
email: daniel.cintra@enpc.fr

and
Pierre Argoul
Université Paris-Est, MAST, SDOA, IFSTTAR,
F-77447 Marne La Vallée, France
email: pierre.argoul@ifsttar.fr

Abstract

The behaviour of a space-modulated, so-called “argumental” oscillator, is studied. The oscillator is submitted to an external harmonic force, which is amplitude-modulated by the oscillator’s position in space. An analytic expression of a stability criterion is given. Using the averaging method, an integrating factor and a Van der Pol representation in the (amplitude, phase)-space, an exact implicit analytic solution is given when there is no damping, and an approximate implicit analytic solution is given when there is damping, allowing the plotting of the separatrix curve. An attractor is identified.

Keywords— non-linear; argumental oscillator; spatial modulation; analytic solution; stability criterion; Van der Pol representation.

Contents

1	Introduction	3
2	Canonical second-order equation of motion.	3
3	Calculus workflow.	4
4	First step: building the standard system of equations.	5
5	Second step: averaging the standard system of equations.	6
5.1	Type B oscillators.	6
5.1.1	Averaging Eq.(10).	6
5.1.2	Averaging Eq.(12).	7
5.1.3	Averaged system for Type B oscillators.	8
	The possible values of n . Critical value of n	8
5.2	Type A oscillators.	9
5.3	Symbolic expressions of the $S(a)$ and $D(a)$ functions.	10
5.3.1	Type A.	10
5.3.2	Type B1.	11
5.3.3	Type B2.	11
5.4	Equilibrium.	12
5.4.1	Stability condition.	12
5.4.2	Stability criterion.	13
	First inequality	13
	Second inequality	14
	Application to Type B2 systems	14
5.4.3	The $A(a_S)$ function for Type B2 systems.	15
5.4.4	Bifurcations for Type B2 systems.	17
5.5	The rectangular Van der Pol representation.	19
5.6	The polar Van der Pol representation.	19
5.7	Quality of the averaging method in the present context.	19
	Discussion	21
6	Third step: approximate analytical solution for the argumental Duffing oscillator.	22
6.1	Integrating factor.	22
	Special case $\beta = 0$	28
	General case: $\beta \neq 0$	30
6.2	Implicit equation of the integral curves.	31
6.3	Quality of the approximated symbolic solution to the averaged system.	31
	Results	32
7	Conclusion	32

1 Introduction

In the 1920s, physicists were searching for a device to divide the mains current frequency in order to manufacture mains-driven clocks. As no electronics were available, they studied various inherently frequency-dividing oscillators. Among them was a pendulum designed by Béthenod in 1929 [1], that oscillated at a low frequency, typically 1 Hz, when driven by the mains at 50 Hz. Béthenod's pendulum was fitted with a steel sphere at the tip of the rod. The force, which could only be attractive, was due to a magnetic field created by a solenoid with vertical axis, carrying an alternating current. The sphere could sense this force only when it was near the lower equilibrium position of the pendulum. Thus, there was a spatial modulation of the force.

An oscillator subjected to a spatially-localized external harmonic force is presented in [9], where the term “argumental oscillations” is coined from the fact that the interaction between the oscillator and the excitation depends on the “argument” of a space-localization function, which is called the H -function hereinafter.

A pendulum fitted with a permanent magnet at the tip of the rod, which can sense the external electromagnetic force only when it is near a coil located at the lower equilibrium position, is presented in [6]. Here the force can be both attractive or repulsive. A model of the spatial localization of the interaction is built, and mathematical elements regarding the system are given.

Argumental oscillations are presented in [11]. An electronic argumental oscillator with a Π function used as dependent-variable localization function is presented in [5].

Modeling and experimental results about six argumental oscillators are given in [3]. Capture probability by an attractor in argumental oscillators is studied in [4].

A system with a second-order equation exhibiting a cubic and a quadratic nonlinearities with an excitation frequency two or three times the system's natural frequency is studied in [10].

The purpose of this article is to study symbolically some aspects of the argumental oscillators, namely a stability criterion and an approximate implicit equation of the integral curves, to be able to draw separatrix lines and assess some areas around the attractors in the (amplitude, phase)-space.

2 Canonical second-order equation of motion.

To simplify the expression of the system behaviour, the reduced time $\tau = \omega_0 t$ is classically introduced, where ω_0 is the natural angular frequency of the oscillator. Using from now on the dot notation to refer to the derivatives with respect to τ , we shall distinguish three types of oscillator, which we call “Type A”, “Type B1” and “Type B2”. The general second-order equation of motion for these oscillators is:

$$\ddot{\alpha} + 2\beta\dot{\alpha} + \alpha + \mu\alpha^3 = AH(\alpha)E(\tau) \quad (1)$$

where β is the dissipation coefficient, μ is the Duffing coefficient, A is a constant, H is a function of α , and $E(\tau)$ is a periodic function of time τ , with frequency components located above the

oscillator's fundamental frequency.

With ν being the angular frequency of the external excitation:

- For Type A oscillators, H is an odd function of α , and E is the function $\sin^2\left(\frac{\nu}{\omega_0}\tau\right)$.
- For Type B oscillators, H is an even function of α , and E is the function $\sin\left(\frac{\nu}{\omega_0}\tau\right)$.

An example of a Type-A H -function is

$$H(\alpha) = \frac{\alpha}{(1 + \gamma\alpha^2)^3}, \quad (2)$$

where γ is a constant.

An example of a Type-B H -function is

$$H(\alpha) = \Pi\left(\frac{\alpha}{2h}\right), \quad (3)$$

where h is a constant, and Π denotes the Pi function, i.e. $\Pi(x) = 1$ if $|x| < \frac{1}{2}$ and $\Pi(x) = 0$ otherwise. In this paper, this example is called a Type B1 oscillator.

Another example of a Type-B H -function is

$$H(\alpha) = \frac{1 - \gamma\alpha^2}{(1 + \gamma\alpha^2)^2}, \quad (4)$$

with γ being a constant. In this paper, this example is called a Type B2 oscillator.

The “Type A” oscillator in this paper is a Béthenod’s pendulum, or Type II-1 oscillator as discussed in [3]. The Type B1 is a Doubochinski’s pendulum, as discussed in [6]. The “Type B2” oscillator is analogous to a Doubochinski’s pendulum, but with a smoother H -function. [6] used a coarser approximation to the H -function, as shown by Eq.(3). This approximation was sufficient to elaborate averaged equations and to derive an expression of the amplitude of the external force as a function of the oscillator’s amplitude, leading to an explanation of a discrete set of stable amplitudes. We use herein our smoother and more precise Type-B2 H -function, as shown by Eq.(4), with the advantage of handling a H -function which is C^∞ : this will allow to eliminate artefacts in a function relative to the Type-B1 model, and to derive an approximate symbolic solution.

It will be shown later on that after the averaging process, the systems of equations of Types A, B1 and B2 are formally similar.

3 Calculus workflow.

Having available the reduced-time second-order differential equation of motion for both oscillators, it is classically considered that a perturbation method could be an appropriate approach, because the oscillator is almost always in a free-run mode. Only at certain narrow locations in space will it “feel” the external force. Moreover, this force is of small amplitude. Keeping the expressions under symbolic form, we shall go through three steps to get to an analytic approximation of the solution to Eq.(1).

The averaging method used in the first and second steps is classical, and has been described in [2], and used in [6]. So only the implementation of the method will be outlined for these two steps. Our contribution to the second step is the symbolic expression of the Fourier series for the H -functions of the Type-A and Type-B oscillators, the symbolic expression of the stability criterion in the general case, and the Van der Pol polar representation of the averaged amplitude and phase. Our contribution further consists of the third step, which will be detailed hereinafter.

- The first step of the calculus is to replace the second-order differential equation of motion by two first-order equations to get the classical standard system of equations.
- The second step is to form a Fourier series of the H -function and to apply the averaging method to obtain an averaged system of equations. As the external force is periodic, simplifications can be expected.
- The third step is to find an integrating factor to approximately solve the averaged system, while keeping the symbolic form of the equations.

4 First step: building the standard system of equations.

Starting from the equation of motion under its general form as shown by Eq.(1), define a function X by:

$$X(\tau, \alpha, \dot{\alpha}) = -2\beta \frac{d\alpha}{d\tau} - \mu\alpha^3 + AH(\alpha)E(\tau). \quad (5)$$

Thus Eq.(1) can be rewritten:

$$\frac{d^2\alpha}{d\tau^2} + \alpha = X(\tau, \alpha, \dot{\alpha}). \quad (6)$$

By observing the experimental oscillators [3] and corresponding numerical simulations, one concludes that the motion is close to that of a free-running oscillator, with slowly varying amplitude and phase. Hence the slow-varying amplitude $a(\tau)$ and phase $\varphi(\tau)$ are introduced as two new independent variables, which will replace the variables α and $\dot{\alpha}$. The motion, expressed as a function of t or τ , will be $\alpha(t) = a(t) \sin(\omega t + \varphi(t)) = a(\tau) \sin(\rho\tau + \varphi(\tau))$, where ω is a parameter close to ω_0 , and $\rho = \frac{\omega}{\omega_0}$. As these two new independent variables are chosen, we found it natural to introduce a Van der Pol representation, with a as abscissae and φ as ordinates. Alternatively, a polar Van der Pol representation will also be used, i.e. a as radius and φ as angle.

Define the change of variables by putting:

$$\alpha(\tau) = a(\tau) \sin(\rho\tau + \varphi(\tau)), \quad (7)$$

$$\dot{\alpha}(\tau) = a(\tau)\rho \cos(\rho\tau + \varphi(\tau)). \quad (8)$$

This is natural, because Eq.(8) is obtained by differentiating Eq.(7) with a and φ taken as constant. This is simply the implementation of the physical observation [3] that a and φ vary slowly with respect to the period of the free-running oscillator.

Differentiating Eq.(7) and comparing the result with Eq.(8) yields:

$$\dot{a} \sin(\rho\tau + \varphi) + a\dot{\varphi} \cos(\rho\tau + \varphi) = 0 \quad (9)$$

Differentiating Eq.(8) and putting the result into Eq.(6) yields:

$$\dot{a} = \frac{\cos(\theta)}{\rho} (X(\tau, a \sin(\theta), a\rho \cos(\theta)) + a \sin(\theta)(\rho^2 - 1)), \quad (10)$$

where $\theta = \rho\tau + \varphi$. This is the first differential equation involving only the two new variables a and φ .

In Eq.(10), replacing $X(\tau, a \sin(\theta), a\rho \cos(\theta))$ by its expression given in Eq.(5) yields, taking into account Eq.(7) and Eq.(8):

$$\begin{aligned} \dot{a} &= \frac{\cos(\theta)}{\rho} \left(-2\beta\dot{\alpha} - \mu\alpha^3 + AH(\alpha) \sin\left(\frac{\nu}{\omega_0}\tau\right) + a \sin(\theta)(\rho^2 - 1) \right) \\ &= \frac{\cos(\theta)}{\rho} \left(-2\beta a\rho \cos(\theta) - \mu a^3 \sin^3(\theta) + AH(a \sin(\theta)) \sin\left(\frac{\nu}{\omega_0}\tau\right) + a \sin(\theta)(\rho^2 - 1) \right). \end{aligned} \quad (11)$$

Substituting in Eq.(9) the expression (10) for \dot{a} yields:

$$\dot{\varphi} = -\frac{1}{a\rho} (a \sin(\theta)(\rho^2 - 1) + X(\tau, a \sin(\theta), a\rho \cos(\theta))) \sin(\theta) \quad (12)$$

which is the second differential equation involving only the two new variables a and φ . From Eq.(12), it is obtained, in the same way as for Eq.(11):

$$\begin{aligned} \dot{\varphi} &= -\frac{1}{a\rho} (a \sin(\theta)(\rho^2 - 1) - 2\beta\dot{\alpha} - \mu\alpha^3 + AH(\alpha) \sin\left(\frac{\nu}{\omega_0}\tau\right)) \sin(\theta) \\ &= \frac{\sin(\theta)}{a\rho} \left(-a \sin(\theta)(\rho^2 - 1) + 2\beta a\rho \cos(\theta) + \mu a^3 \sin^3(\theta) - AH(a \sin(\theta)) \sin\left(\frac{\nu}{\omega_0}\tau\right) \right). \end{aligned} \quad (13)$$

So far, no approximation has been made, and the system consisting of Eqs.(11) and (13) is equivalent to Eq.(6).

5 Second step: averaging the standard system of equations.

5.1 Type B oscillators.

In this section, use the variable $\theta = \rho\tau + \varphi$ as defined in the previous section, and suppose that $H(\alpha)$ is an even function of α . That is, focus will be put on oscillators of Type B. The oscillators of Type A will be studied thereafter.

Eqs.(10) and (12) have to be averaged with respect to θ . To do so, form the Fourier series of $H(\alpha) = H(a \sin(\theta))$.

5.1.1 Averaging Eq.(10).

Knowing that $\overline{\cos^2(\theta)} = \frac{1}{2}$, $\overline{\cos(\theta) \sin^3(\theta)} = 0$, and $\overline{\cos(\theta) \sin(\theta)} = 0$, obtain:

$$\bar{a} = -\beta a + \frac{A}{\rho} \overline{H(a \sin(\theta)) \cos(\theta) \sin\left(\frac{\nu}{\omega_0}\tau\right)}$$

Knowing that H is an even function of α , introduce the Fourier series of $H(a \sin(\theta))$, namely

$$H(a \sin(\theta)) = \sum_{q=0}^{+\infty} c_q(a) \cos(2q\theta)$$

with

$$c_q(a) = \frac{2}{\pi} \int_0^\pi H(a \sin(\eta)) \cos(2q\eta) d\eta.$$

At this point, define a real number n by $n = \frac{\nu}{\omega} = \frac{\nu}{\rho\omega_0}$. It holds:

$$\begin{aligned} \overline{H(a \sin(\theta)) \cos(\theta) \sin\left(\frac{\nu}{\omega_0}\tau\right)} &= \sum_{q=0}^{+\infty} c_q(a) \cos(2q\theta) \cos(\theta) \sin\left(\frac{\nu}{\omega_0}\tau\right) \\ &= \sum_{q=0}^{+\infty} c_q(a) \overline{\cos(2q\theta) \cos(\theta) \sin\left(\frac{\nu}{\omega_0}\tau\right)} \\ &= \begin{cases} -\frac{1}{4} \sin(n\varphi)(c_m(a) + c_p(a)) & \text{if } n \text{ is an odd integer,} \\ 0 & \text{otherwise,} \end{cases} \end{aligned}$$

with $m = \frac{n-1}{2}$ and $p = \frac{n+1}{2}$.

Consequently, if n is an odd integer, the first averaged equation is obtained:

$$\dot{a} = -\frac{A}{4\rho} S(a) \sin(n\varphi) - \beta a, \quad (14)$$

with $m = \frac{n-1}{2}$, $p = \frac{n+1}{2}$, and $S(a) = c_m(a) + c_p(a)$.

and otherwise, it holds:

$$\ddot{a} = -\beta a. \quad (15)$$

That is, if n is not an odd integer, the averaged equation is the same as for n odd integer, except that it holds here $A = 0$.

The various possible values of n will be discussed hereafter.

5.1.2 Averaging Eq.(12).

In the same way as for the averaging of Eq.(10), it holds:

$$\overline{H(a \sin(\theta)) \sin(\theta) \sin\left(\frac{\nu}{\omega_0}\tau\right)} = \begin{cases} \frac{1}{4}(c_m(a) + c_p(a)) \cos(n\varphi) & \text{if } n \text{ is an odd integer,} \\ 0 & \text{otherwise.} \end{cases}$$

Hence, knowing that $\overline{\sin^2(\theta)} = \frac{1}{2}$, $\overline{\sin^4(\theta)} = \frac{3\pi}{8}$, and $\overline{\cos(\theta) \sin(\theta)} = 0$, write that, if n is an odd integer:

$$\ddot{\varphi} = \frac{1-\rho^2}{2\rho} + \frac{3\pi}{8} \frac{\mu a^2}{\rho} - \frac{A}{4a\rho} \cos(n\varphi)(c_m(a) - c_p(a)), \quad (16)$$

and otherwise:

$$\bar{\varphi} = \frac{1 - \rho^2}{2\rho} + \frac{3\pi}{8} \frac{\mu a^2}{\rho}.$$

That is, here again, in the same way as for the averaging of Eq.(10), if n is not an odd integer, the averaged equation is the same as for n odd integer, except that it holds here $A = 0$.

Define a_n by:

$$\rho^2 = \left(\frac{1}{n} \frac{\nu}{\omega_0} \right)^2 = \frac{3\mu a_n^2}{4} + 1. \quad (17)$$

Then $\frac{1 - \rho^2}{2\rho} = -\frac{3\mu a_n^2}{8}$, and Eq.(16) can be written as follows:

$$\dot{\varphi} = \frac{3\mu}{8\rho}(a^2 - a_n^2) - \frac{A}{4a\rho} \cos(n\varphi)D(a). \quad (18)$$

with $m = \frac{n-1}{2}$, $p = \frac{n+1}{2}$, and $D(a) = c_m(a) - c_p(a)$.

And if n is not an odd integer, it holds, putting $A = 0$ in Eq.(18):

$$\dot{\varphi} = \frac{3\mu}{8\rho}(a^2 - a_n^2). \quad (19)$$

5.1.3 Averaged system for Type B oscillators.

The averaged system can now be established, consisting of Eqs.(14) and (18):

$$\begin{cases} \dot{a} &= -\frac{A}{4\rho_n} S(a) \sin(n\varphi) - \beta a \\ \dot{\varphi} &= \frac{3\mu}{8\rho_n}(a^2 - a_n^2) - \frac{A}{4a\rho_n} \cos(n\varphi)D(a). \end{cases} \quad (20)$$

The possible values of n . Critical value of n In this paragraph, the link between ν , ω_0 , n , and the amplitudes of the free oscillator will be studied. This will enable us to give a physical sense to ρ .

Recall the system of Eqs.(15) and (19), where the external force is null ($A = 0$):

$$\begin{cases} \dot{a} &= -\beta a \\ \dot{\varphi} &= \frac{3\mu}{8\rho}(a^2 - a_n^2). \end{cases} \quad (21)$$

Now consider the case of the free undamped oscillator, looking for the stable regime condition. It holds $\beta = 0$ and therefore, the system (21) resolves to $a = a_0$ and $\dot{\varphi} = \frac{3\mu}{8\rho}(a_0^2 - a_n^2)$, where a_0 is the initial value of a . The regime will be stable if $\dot{\varphi}$ is null, that is, if $a_0 = a_n$. Thus, the value a_n which appears in Eq.(17) is the amplitude of the free undamped oscillator. This equation shows that the case $\mu > 0$ (hardening) and the case $\mu < 0$ (softening) must be distinguished.

Introduce an integer critical value for n : $n_{crit} = \left\lceil \frac{\nu}{\omega_0} \right\rceil$, where the square bracket notation means

here: “integer part of”. Define a real ε by $\frac{\nu}{\omega_0} = \left\lfloor \frac{\nu}{\omega_0} \right\rfloor + \varepsilon$; it holds $0 \leq \varepsilon < 1$. From Eq.(17),

obtain $a_n^2 = \frac{4}{3\mu} \left(\left(\frac{1}{n} \frac{\nu}{\omega_0} \right)^2 - 1 \right)$. Thus if μ is negative, it must hold $\left(\frac{1}{n} \frac{\nu}{\omega_0} \right)^2 - 1 < 0$, i.e.

$n > \frac{\nu}{\omega_0} = n_{crit} + \varepsilon$, which reduces to $n \geq n_{crit} + 1$. n can be taken as large as desired, provided one stays in the validity domain of the averaging method. The energy of the oscillator increases as n increases.

Conversely, if μ is positive, the condition $n < \frac{\nu}{\omega_0} = n_{crit} + \varepsilon$ must hold, which reduces to $n \leq n_{crit}$; $n \geq 3$ must also hold, because n is odd and must be greater than 1 (otherwise, the system is in a classical forced-oscillations condition). There are a finite number of possible stable amplitudes, and the energy increases as n decreases.

From Eq.(17), it is possible to get the physical sense of ρ : this value gives an indication of the energy of the system, and takes a discrete set of values. This is why from now on, ρ_n will be written instead of ρ , because to each value of n is associated a value of ρ .

This discrete series of stable amplitudes and energy levels has been discussed in [6].

5.2 Type A oscillators.

In this section, it is supposed that $H(\alpha)$ is an odd function of α . That is, focus on oscillators of Type A, and apply the same method as for Section 5.1.

The main difference between those three types of oscillator, A, B1 and B2, lies in the Fourier series of the function $H(a \sin(\theta))$. Because for this oscillator, the function of θ is odd, it holds:

$$H(a \sin(\theta)) = \sum_{q=0}^{+\infty} c_q(a) \sin((2q+1)\theta)$$

with

$$c_q(a) = \frac{1}{\pi} \int_0^{2\pi} H(a \sin(\eta)) \sin((2q+1)\eta) d\eta,$$

and therefore:

$$\overline{H(a \sin(\theta)) \cos(\theta) \sin^2\left(\frac{\nu}{\omega_0} \tau\right)} = \begin{cases} -\frac{1}{8}(c_m(a) + c_p(a)) \sin(n\varphi) & \text{if } n \text{ is an even integer,} \\ 0 & \text{otherwise,} \end{cases}$$

with $n = \frac{2\nu}{\omega} = \frac{2\nu}{\rho_n \omega_0}$, $m = \frac{n}{2} - 1$ and $p = \frac{n}{2}$. Hence, in the same way as for the Type B oscillator, the following system of two averaged equations is obtained:

If $n = \frac{2\nu}{\omega} = \frac{2\nu}{\rho_n \omega_0}$ is an even integer:

$$\begin{cases} \dot{a} &= -\frac{A}{8\rho_n} S(a) \sin(n\varphi) - \beta a \\ \dot{\varphi} &= \frac{3\mu}{8\rho_n} (a^2 - a_n^2) - \frac{A}{8a\rho_n} \cos(n\varphi) D(a), \end{cases} \quad (22)$$

with $S(a) = c_m(a) + c_p(a)$, $D(a) = c_m(a) - c_p(a)$, $m = \frac{n}{2} - 1$ and $p = \frac{n}{2}$.

If n is not an even integer:

$$\begin{cases} \dot{a} &= -\beta a \\ \dot{\varphi} &= \frac{3\mu}{8\rho_n}(a^2 - a_n^2). \end{cases}$$

It can be seen that this averaged system is formally similar to the averaged system (20) of the Type B2 oscillator, in which $A/2$ would substituted for A . The difference lies in the expression of the functions $S(a)$ and $D(a)$. Therefore, from now on only the averaged system of the Type B2 oscillator will be discussed.

5.3 Symbolic expressions of the $S(a)$ and $D(a)$ functions.

In order to be able to go further into the symbolic calculus and to draw plots for given examples, it is necessary to know the explicit expressions of the S and D functions for a given oscillator. Therefore, the $c_q(a)$ coefficients of the H -function for the Type A oscillator and the Type B oscillators will be calculated. From these coefficients, it will be possible to express the S and D functions.

5.3.1 Type A.

As an example of Type A oscillator, take the original Béthenod pendulum and our H -function as shown by Eq.(2). Calculate the generic r -th term of the Fourier series of $H(asin(\theta))$, namely:

$$\begin{aligned} c_r(a) &= \frac{1}{\pi} \int_0^{2\pi} H(a \sin(\eta)) \sin((2r+1)\eta) d\eta \\ &= \frac{1}{\pi} \int_0^{2\pi} \frac{a \sin(\eta)}{(1 + \gamma a^2 \sin^2(\eta))^3} \sin((2r+1)\eta) d\eta \end{aligned}$$

Define $L(b, q, m)$ as:

$$L(b, q, m) = \int_0^{2\pi} \frac{\sin(\eta) \sin(q\eta)}{(1 + b \sin^2(\eta))^m} d\eta.$$

Hence:

$$c_r(a) = \frac{a}{\pi} L(\gamma a^2, 2r+1, 3).$$

and

$$\begin{aligned} S(a) &= c_{n-1} + c_{n+1} = \frac{a}{\pi} (L(\gamma a^2, 2n-1, 3) + L(\gamma a^2, 2n+3, 3)) \\ D(a) &= c_{n-1} - c_{n+1} = \frac{a}{\pi} (L(\gamma a^2, 2n-1, 3) - L(\gamma a^2, 2n+3, 3)) \end{aligned}$$

Then, using [7, §3.616-7]:

$$L(b, q, m) = \frac{1}{2} \frac{1}{\left(1 + \frac{b}{2}\right)^m} (M(q-1, g, m) - M(q+1, g, m)), \text{ with}$$

$$M(s, g, m) = \int_0^{2\pi} \frac{\cos(s\eta)}{1 - g \cos(2\eta))^m} d\eta$$

$$= \frac{2^{m+1}}{g^m} \frac{\pi}{f^{n-m}(f^2 - 1)^{2m-1}} \sum_{k=0}^{m-1} \binom{m+n-1}{k} \binom{2m-k-2}{m-1} (f^2 - 1)^k$$

with $n = \frac{s}{2}$, $g = \frac{b}{2+b}$ and $f = \frac{1}{g} + \sqrt{\frac{1}{g^2} - 1}$.

Finally, it is found that some approximations are possible. If $q \gg 5$ and $\sqrt{1+b} \gg 1$, it holds:

$$L(b, q, 3) \approx \frac{\pi}{8\sqrt{b}} \left(6 + 4\frac{q}{b} + 36\frac{q^2}{b^2} \left(1 + \frac{106}{36b} + \frac{308}{36b^2} + \frac{32}{36b^3} \right) \right).$$

And if $q < b$ and $b \gg \frac{106}{36}$, it holds:

$$L(b, q, 3) \approx \frac{\pi}{8\sqrt{b}} \left(6 + 4\frac{q}{b} + 36\frac{q^2}{b^2} \right).$$

5.3.2 Type B1.

As shown by Eq.(3), it holds $H(\alpha) = \Pi(\frac{\alpha}{2h})$, and $H(a \sin(\theta)) = \sum_0^{+\infty} c_q \cos(2q\theta)$. Putting $\alpha = \arcsin\left(\frac{h}{a}\right)$ if $a \geq h$ and $\alpha = \frac{\pi}{2}$ if $a < h$, obtain $c_q(a) = \frac{4}{\pi q} \sin(q\alpha)$. It follows that, with $S = c_{\frac{n-1}{2}} + c_{\frac{n+1}{2}}$ and $D = c_{\frac{n-1}{2}} - c_{\frac{n+1}{2}}$:

$$S(\alpha) = \frac{4}{\pi} \left(\frac{\sin\left(\frac{n-1}{2}\alpha\right)}{\frac{n-1}{2}} + \frac{\sin\left(\frac{n+1}{2}\alpha\right)}{\frac{n+1}{2}} \right)$$

$$D(\alpha) = \frac{4}{\pi} \left(\frac{\sin\left(\frac{n-1}{2}\alpha\right)}{\frac{n-1}{2}} - \frac{\sin\left(\frac{n+1}{2}\alpha\right)}{\frac{n+1}{2}} \right)$$

$$\frac{D(\alpha)}{S(\alpha)} = \frac{\tan\left(\frac{n\alpha}{2}\right) - n \tan\left(\frac{\alpha}{2}\right)}{n \tan\left(\frac{n\alpha}{2}\right) - \tan\left(\frac{\alpha}{2}\right)}$$

5.3.3 Type B2.

As shown by Eq.(4), it holds $H(\alpha) = \frac{1 - \gamma\alpha^2}{(1 + \gamma\alpha^2)^2}$ and $H(a \sin(\theta)) = \sum_0^{+\infty} c_q \cos(2q\theta)$, and therefore:

$$c_q = \frac{1}{\pi} \int_0^{2\pi} \frac{1 - \gamma a^2 \sin^2(\eta)}{(1 + \gamma a^2 \sin^2(\eta))^2} \cos(2q\eta) d\eta,$$

and then, using [7, §3.613] and after a few manipulations:

$$c_q(a) = 2 \frac{1 + 2q\sqrt{1 + \gamma a^2}}{(1 + \gamma a^2)^{3/2}} \left(\frac{1 - \sqrt{1 + \gamma a^2}}{a\sqrt{\gamma}} \right)^{2q}.$$

Hence, with $S = c_{\frac{n-1}{2}} + c_{\frac{n+1}{2}}$ and $D = c_{\frac{n-1}{2}} - c_{\frac{n+1}{2}}$:

$$S(a) = \frac{4n}{a\sqrt{\gamma}\sqrt{1 + \gamma a^2}} \left(\frac{\sqrt{1 + \gamma a^2} - 1}{a\sqrt{\gamma}} \right)^n \quad (23)$$

$$D(a) = \frac{4}{a\sqrt{\gamma}(1 + \gamma a^2)^{3/2}} \left(\frac{\sqrt{1 + \gamma a^2} - 1}{a\sqrt{\gamma}} \right)^n (n\sqrt{1 + \gamma a^2} - \gamma a^2) \quad (24)$$

$$\frac{D(a)}{S(a)} = \frac{1}{\sqrt{1 + \gamma a^2}} - \frac{1}{n} \frac{\gamma a^2}{1 + \gamma a^2}. \quad (25)$$

5.4 Equilibrium.

It will be discussed herein the averaged system of Type B. There is no loss of generality, knowing that the Type A is formally similar, as is showed above about Eq.(22).

5.4.1 Stability condition.

Recall the averaged system of Type B2, given in System (20):

$$\begin{cases} \dot{a} = -\frac{A}{4\rho_n} S(a) \sin(n\varphi) - \beta a \\ \dot{\varphi} = \frac{3\mu}{8\rho_n} (a^2 - a_n^2) - \frac{A}{4a\rho_n} \cos(n\varphi) D(a) \end{cases}$$

Write this system in a more general fashion, as follows:

$$\begin{cases} \dot{a} = Af(a) \sin(n\varphi) + g(a) = F(a, \varphi) \\ \dot{\varphi} = Aj(a) \cos(n\varphi) + h(a) = G(a, \varphi) \end{cases} \quad (26)$$

with $f(a) = -\frac{S(a)}{4\rho_n}$, $g(a) = -\beta a$, $j(a) = -\frac{D(a)}{4a\rho_n}$, and $h(a) = \frac{3\mu}{8\rho_n} (a^2 - a_n^2)$. Write the equilibrium condition for this averaged system. Call a_S and φ_S the values of a and φ at an equilibrium point. Putting $\dot{a} = 0$ and $\dot{\varphi} = 0$ for $a = a_S$ and $\varphi = \varphi_S$ yields:

$$\begin{cases} Af(a_S) \sin(n\varphi_S) + g(a_S) = 0 \\ Aj(a_S) \cos(n\varphi_S) + h(a_S) = 0 \end{cases} \quad (27)$$

Hence:

$$\begin{cases} A^2 = \frac{g^2(a_S)}{f^2(a_S)} + \frac{h^2(a_S)}{j^2(a_S)} \\ \tan(n\varphi_S) = \frac{g(a_S)j(a_S)}{f(a_S)h(a_S)} \end{cases} \quad (28)$$

For instance, for the system of Type B2, it holds:

$$\begin{cases} A = \frac{4a_S}{S(a_S)} \sqrt{(\rho_n \beta)^2 + \frac{9}{64} \mu^2 \frac{S(a_S)^2}{D(a_S)^2} (a_S^2 - a_n^2)^2} \\ \tan(n\varphi_S) = -\frac{8}{3\mu} \frac{\rho_n}{a_S^2 - a_n^2} \frac{D(a_S)}{S(a_S)} \end{cases} \quad (29)$$

5.4.2 Stability criterion.

Having written the equilibrium condition, we shall now give a simple expression of the stability criterion. Use the general form as shown by Eq.(26) of the equilibrium condition. To simplify the notations, put

$$F'_a = \left. \frac{dF}{da} \right|_{a=a_S}, F'_\varphi = \left. \frac{dF}{d\varphi} \right|_{a=a_S}, G'_a = \left. \frac{dG}{da} \right|_{a=a_S}, \text{ and } G'_\varphi = \left. \frac{dG}{d\varphi} \right|_{a=a_S}.$$

To express the stability criterion, use the classical method of the first-order expansion of the tangent system around the equilibrium point. It holds, noting a_S and φ_S the values taken by a and φ at the equilibrium point:

$$\begin{cases} \dot{a} &= (a - a_S)F'_a + (\varphi - \varphi_S)F'_\varphi \\ \dot{\varphi} &= (a - a_S)G'_a + (\varphi - \varphi_S)G'_\varphi \end{cases}$$

The characteristic equation of this system is:

$$\begin{vmatrix} F'_a - \lambda & F'_\varphi \\ G'_a & G'_\varphi - \lambda \end{vmatrix} = 0$$

that is, $\lambda^2 - (F'_a + G'_\varphi)\lambda + F'_a G'_\varphi - F'_\varphi G'_a = 0$. The classical condition for this system to have a stable stationary solution is that the roots of the characteristic equation have negative real parts and that their product be positive, i.e., knowing that the roots are complex conjugates, that:

$$\begin{cases} \text{the sum of the real parts be negative, that is, } F'_a + G'_\varphi < 0 \\ \text{the product of the roots be positive, that is, } F'_a G'_\varphi - F'_\varphi G'_a > 0 \end{cases} \quad (30)$$

In order to transform the first and second inequalities constituting the stability criterion in Eq.(30), use the form as shown by Equation (26) and, to simplify the notations, put

$$f = f(a_S), g = g(a_S), f' = \left. \frac{df(a)}{da} \right|_{a=a_S}, g' = \left. \frac{dg(a)}{da} \right|_{a=a_S},$$

First inequality It has been shown in Eqs.(30) that the first inequality linked to the stability criterion is:

$$F'_a + G'_\varphi < 0, \quad (31)$$

which gives here: $A \sin(n\varphi_S)(f' - nj) + g' < 0$. Replacing, in this expression, $A \sin(n\varphi_S)$ by its value deduced from Eq.(27), yields: $-\frac{g}{f}(f' - nj) + g' < 0$, which can be written:

$$f \left. \frac{d}{da} \left(\frac{g}{f} \right) \right|_{a=a_S, \varphi=\varphi_S} + nj \frac{g}{f} < 0. \quad (32)$$

Given the definition of the averaged system (26), this form will be much easier to manipulate than the original form as given by system (31). It can be noticed that the function h is not part of this inequality.

Second inequality It has been shown in Eqs.(30) that the second inequality linked to the stability criterion is:

$$F'_a G'_\varphi - F'_\varphi G'_a > 0, \quad (33)$$

Substituting in Eq.(33) the developed values of F'_a , F'_φ , G'_a and G'_φ by their expressions as deduced from Eq.(26) yields:

$$F'_a G'_\varphi - F'_\varphi G'_a = -(Af' \sin(n\varphi_S) + g')nAjsin(n\varphi_S) - nAf \cos(n\varphi_S)(Aj' \cos(n\varphi_S) + h').$$

Being in a stationary condition, it is possible to replace, in this expression, $Asin(n\varphi_S)$ and $Acos(n\varphi_S)$ by their expressions as deduced from Equation (27), thus obtaining:

$$F'_a G'_\varphi - F'_\varphi G'_a = n \left(-f'j \frac{g^2}{f^2} + g'j \frac{g}{f} - j'f \frac{h^2}{j^2} + h'f \frac{h}{j} \right) \quad (34)$$

Now, from Eq.(28), expressing the derivative of A^2 with respect to a_S , obtain:

$$\frac{1}{2} \frac{dA^2}{da_S} = \frac{gg'f - g^2f'}{f^3} + \frac{hh'j - h^2j'}{j^3}.$$

Therefore, by taking Eq.(34) into account:

$$\begin{aligned} \frac{1}{2} jf \frac{dA^2}{da_S} &= \frac{gg'jf^2 - g^2f'jf}{f^3} + \frac{hh'j^2f - h^2jj'f}{j^3} \\ &= \frac{gg'j}{f} - \frac{g^2f'j}{f^2} + \frac{hh'f}{j} - \frac{h^2j'f}{j^2} \\ &= \frac{1}{n} (F'_a G'_\varphi - F'_\varphi G'_a). \end{aligned}$$

And, because n is always positive, the second inequality of the stability criterion can be written as follows:

$$jf \frac{dA^2}{da} > 0. \quad (35)$$

Because A is always positive by definition, A could be used instead of A^2 , but the expression of A and its derivatives is much more intricate than that of A^2 , and thus, the form given in inequality (35) will be preferred.

Application to Type B2 systems For illustrative purpose, the symbolic expression of the stability criterion for the Type B2 systems will be given. The calculus for Type-A and Type-B1 systems is analogous. In inequalities (32) and (35), substitute the expressions of f , g and j corresponding to the system of Type B2, i.e.:

$$f(a) = -\frac{S(a)}{4\rho_n}, \quad g(a) = -\beta a \quad \text{and} \quad j(a) = -\frac{D(a)}{4a\rho_n}.$$

The first inequality (32) becomes:

$$\frac{a}{S(a)} \frac{dS(a)}{da} - n \frac{D(a)}{S} - 1 < 0 \quad (36)$$

while the second inequality (35) becomes: $S(a)D(a)\frac{dA^2(a)}{da} > 0$. And because $A > 0$, it holds:

$$S(a)D(a)\frac{dA(a)}{da} > 0 \quad (37)$$

Replacing the general expressions $S(a)$ and $D(a)$ by their known particular expressions given in Eqs.(23) and (24), transform the first inequality (36), thus obtaining: $-1 - \frac{1 + \gamma a^2}{1 + \gamma a^2} < 0$, which is always true. Then, using Eq.(25) to transform the second inequality (37), obtain:

$$\left(\gamma a^2 - \left(\frac{2}{n^2 - n\sqrt{n^2 + 4} + 2} - 1 \right) \right) \frac{dA}{da} < 0, \quad (38)$$

knowing that $\frac{dA}{da}$ and $\frac{dA^2}{da}$ are the same sign.

Call a_{flip} the value of a such that $\gamma a_{flip}^2 = \frac{2}{n^2 - n\sqrt{n^2 + 4} + 2} - 1$. In the plots hereafter, when it holds $n = 101$ and $\gamma \approx 10000$, leading to $a_{flip} \approx 1.01$, the domain of interest actually is included in the region $a < a_{flip}$, so that the stability criterion is: $\frac{dA}{da} > 0$, which is easy to locate. The points representing the stable steady-state regimes are located at the intersection of the ascending parts of the $A(a_S)$ curve with the line $A(a_S) = A_{ext}$, where A_{ext} is the amplitude of the external force.

For $n \geq 3$, the expression $\gamma a^2 - \left(\frac{2}{n^2 - n\sqrt{n^2 + 4} + 2} - 1 \right)$ can be approximated by $\gamma a^2 - n^2 - 1$. In conclusion, for the systems of Type B2, the stability criterion is as given by inequality (38), and can be approximated by

$$(\gamma a^2 - n^2 - 1) \frac{dA}{da} < 0. \quad (39)$$

5.4.3 The $A(a_S)$ function for Type B2 systems.

When the stability condition has been studied, it has been found an expression (28) giving A as a function of a_S : the $A(a_S)$ function gives the amplitude of the external force as a function of the oscillator's amplitude at the equilibrium point (a_S, φ_S) , for a given n .

Then, when the stability criterion has been studied, it has been found that, for systems of Type B2, the stability criterion can be expressed very simply as a condition on the $A(a_S)$ function, as given by inequalities (38) and (39).

Thus, the variation of the $A(a_S)$ function is worth being discussed.

First, it can be seen that when $a_S \rightarrow 0$ and when $a_S \rightarrow +\infty$, $\frac{a_S}{S(a_S)} \rightarrow +\infty$, and therefore $A(a_S) \rightarrow +\infty$. So the $A(a_S)$ function has at least one minimum over \mathbb{R}^+ .

Second, it can reasonably be guessed that there can exist a local minimum around $a_S = a_n$.

To give an idea of the shape of the plot of $A(a_S)$, take an example: the case of the Type B2 system (29), where it holds:

$$A(a_S) = \frac{4a_S}{S(a_S)} \sqrt{(\rho_n \beta)^2 + \frac{9}{64} \mu^2 \frac{S(a_S)^2}{D(a_S)^2} (a_S^2 - a_n^2)^2}. \quad (40)$$

Being in the case of a system of Type B2, one knows the symbolic expressions of $S(a_S)$ and $D(a_S)$, given in Eq.(25). By substitution of these expressions in Eq.(40), the function $A(a_S)$ can be plotted for any numeric instance of the system parameters. It must be kept in mind that the averaging calculus is only valid for small values of A , say $A < 10$. Moreover, in some cases, the $A(a_S)$ function may exhibit more than one minimum.

Consider a case analogous to those studied in [3], where $\gamma = 10100$, $\mu = -\frac{1}{6}$ (pendulum case), $\nu = 6.26 * 101$, $\omega_0 = 6.28$, $n = 101$ and $\beta = 0.001$. Consequently, it holds $\rho_n = 6.26/6.28$. Fig. 1 is relative to a Type B1 system with h chosen so that $h = 1/\sqrt{\gamma}$. In this model, it can be seen that the use of a H -function which is discontinuous introduces many minima in the curve: many attractors may be expected in the numerical simulations based on this model. However, in our experiments [3] reconstituting this material configuration, we could not bring out this multiplicity of attractors. Only the attractor located at an amplitude near a_n could be found. A more realistic model, based on the intensity of the magnetic field [3], yields an $A(a_S)$ -curve having only one local minimum which coincides with the minimum of the $A(a_S)$ -curve of the B1 model around $a_S = 0.22$.

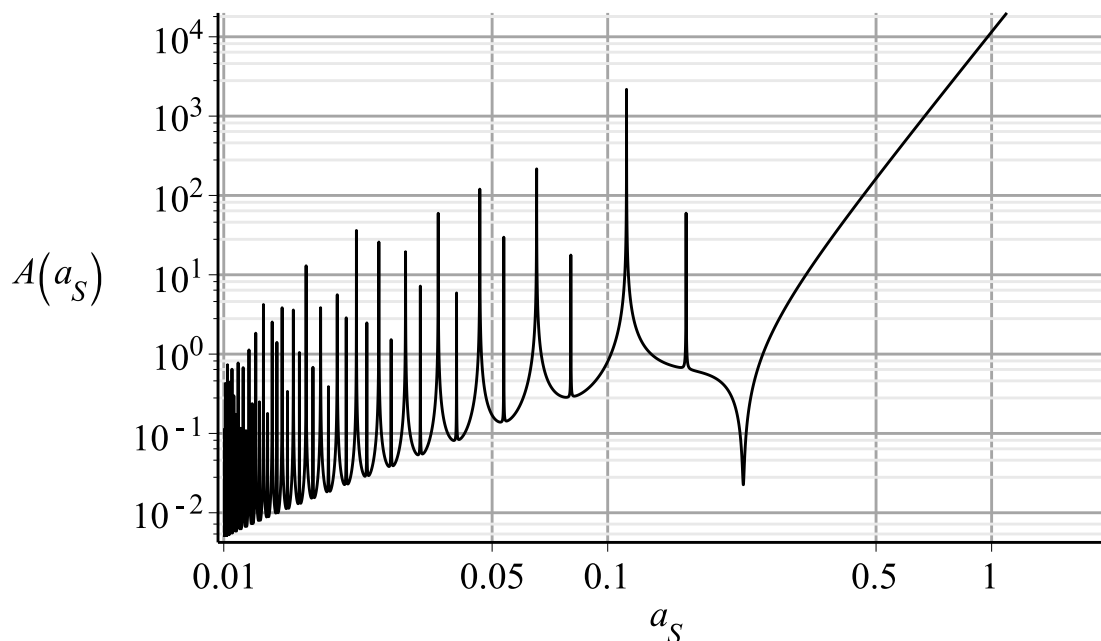


Figure 1: $A(a_S)$ for a Type B1 system. Parameter values: $n = 101$, $\mu = -1/6$, $\rho = 6.26/6.28$, $\gamma = 10100$, $\beta = 0.001$.

Fig. 2 is relative to a Type B2 system, with the same parameters as in case B1 above. In this model, the curve for $A(a_S)$ is smooth, because a smooth function has been used for our H -function. The numerical integration of the system, whose solution is represented in Fig. 8, shows that in

Fig. 2, the minimum of the curve is close to point S, which is the intersection of the $A(as)$ curve with the horizontal dotted line having a given ordinate A representing the chosen amplitude of the external force for said numerical integration, and corresponds to the point S in Fig. 8, which is an attractor. When the amplitude of the external force is lowered, points T and S come closer to the curve's minimum, while the attractor's radius in the Van der Pol representation comes closer to the minimum's abscissa in the $A(a_S)$ curve.

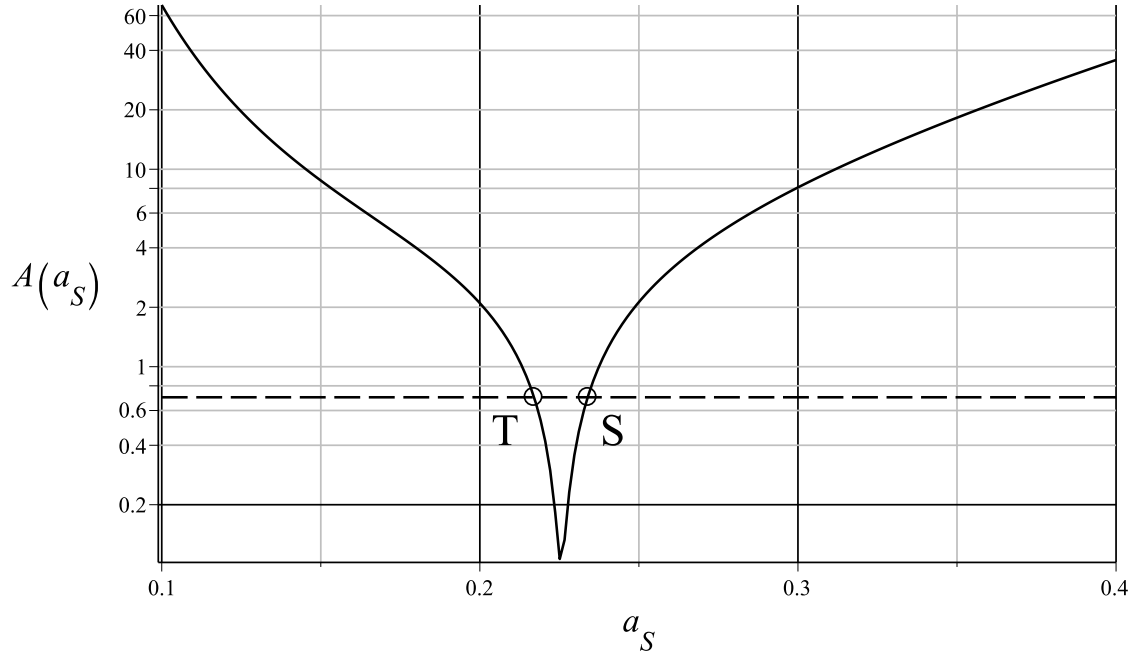


Figure 2: $A(a_S)$ for a Type B2 system. Parameter values: same as for Fig.1, plus $A = 0.7$. Points T and S will be described in the third section, about Fig. 8.

5.4.4 Bifurcations for Type B2 systems.

Until now, the averaged system has been discussed on the basis of only one averaging calculus, based on one value of n . However, in the reality, it must be taken into account the fact that there is a plurality of values possible for n [6], each one corresponding to a value of the amplitude of the free oscillator, to an averaging calculus, and to an integral solution curve $U_n(a, \varphi) = 0$. This way, a plurality of solutions are obtained, in the form of a plurality of integral curves $U_n(a, \varphi) = 0$. These curves will overlap in the Van der Pol representations, and it will have to be decided which curve is the effective solution in a given domain of the Van der Pol plane.

For illustrative purpose, take the same case than for the representation of the $A(a_S)$ curve of Type B2 in Fig. 2.

As μ has been chosen negative, one has to take $n > n_{crit} + 1 = 100$, i.e. $n \geq 101$. Plot the $A(a_S)$

curves for $n = 101, 103, \dots, 119$. A series of overlapped curves are obtained (see Fig. 3). Denote the local minimums by letters $M_{101} \dots M_{111}$, and the ordinate of M_n by A_n . From Eq.(40), it holds:

$$A_n = A(a_n) = \frac{4a_n}{S(a_n)} \rho_n \beta.$$

As showed above, the stable solutions to the averaged system of equations are on the increasing parts of the curve $A(a_S)$.

Because the averaged method gives better results when the perturbation is small, keep (in a first approach) the parts of the overlapped curves which are the lowest in ordinates, i.e. corresponding to the lowest values of A , the intensity of the perturbation.

In Fig. 3 are also represented the points J_n , which are the intersections of curves $A(a_S)$ for two consecutive values of n : n and $n + 2$. And as the ordinate of M_n increases as the system parameter A (the external excitation amplitude) increases, it can be seen that the number of stable solutions to the original non-averaged system (10) and (12), i.e. the number of $A(a_S)$ curves intersected by a given line $A = \text{Const}$, increases as A increases, constituting the phenomenon of bifurcation.

Considering that an upper bound of the limits (in abscissa a) of the region where the averaging

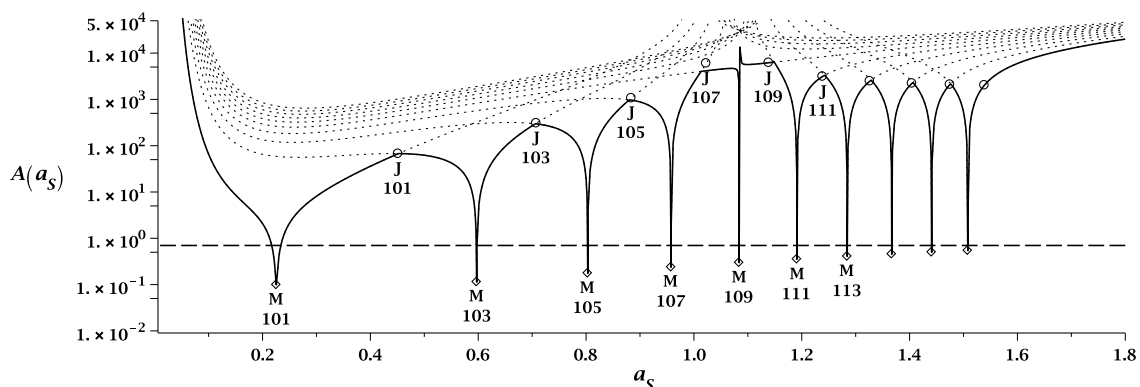


Figure 3: $A(a_S)$ for a Type B2 system, with multiple values of n . For the sake of clarity, the indices are omitted beyond $n = 113$, as well as the plots beyond $n = 119$. Parameters: $n = 101$, $\beta = 0.001$, $\rho = 6.24/6.28$, $\gamma = 10100$, $\mu = -1/6$, $A = 0.7$ (dashed line). The parts of the plots of $A(a_S)$ which are kept are in solid line, the remaining parts are dotted.

method is valid for a given value of n is delimited by points J_{n-2} and J_n , a symbolic expression has now to be found for the coordinates of the points J_n . Denote by $\overset{q}{A}(a_S)$ the curve representing the function $A(a_S)$ when n has the value q . Then J_n is the intersection of $\overset{n}{A}(a_S)$ and $\overset{n+2}{A}(a_S)$. The abscissa x of J_n satisfies Eq.(40) with n for $\overset{n}{A}(a_S)$ as well as this same equation with $n + 2$ for $\overset{n+2}{A}(a_S)$. After a few transformations, it is obtained:

$$\lambda^2 \beta^2 \left(\frac{1}{n^2} - \frac{1}{(n+2)^2} - 2 \right) = \frac{9}{64} \mu^2 \left(\frac{S(x)}{D(x)} \right)^2 (a_n^2 - a_{n+2}^2)(2x^2 - a_n^2 - a_{n+2}^2),$$

with $\lambda = \frac{\nu}{\omega_0}$.

Replacing a_n and a_{n+2} by their developed expressions as given in Eq.(17) yields:

$$x^2 = \frac{2}{3\mu} \left(\frac{\lambda^2}{n^2} + \frac{\lambda^2}{(n+2)^2} - 2 \right) + \frac{8\beta^2}{3\mu} \left(\frac{D(x)}{S(x)} \right).$$

Assuming that, for x in the interval $[a_n, a_{n+2}]$, $S(x) \approx S(\xi)$ and $D(x) \approx D(\xi)$, with $\xi = \frac{a_n + a_{n+2}}{2}$, and remarking that $a_n^2 + a_{n+2}^2 = \frac{4}{3\mu} \left(\frac{\lambda^2}{n^2} + \frac{\lambda^2}{(n+2)^2} - 2 \right)$, finally yields:

$$a_{n,n+2} = \sqrt{\frac{a_n^2 + a_{n+2}^2}{2} + \frac{8}{3\mu} \lambda^2 \beta^2 \left(\frac{D(\xi)}{S(\xi)} \right)^2},$$

where $a_{n,n+2}$ denotes the abscissa of J_n , intersection of the curves $\overset{n}{A}(a_S)$ and $\overset{n+2}{A}(a_S)$.

5.5 The rectangular Van der Pol representation.

As previously mentioned, we are naturally induced to use a Van der Pol representation, with a as abscissa and φ as ordinate. For instance, with parameters identical to those used about the bifurcations, Fig. 4 is a Van der Pol representation of the integral curve of System (20) computed using a Runge-Kutta-Fehlberg method that produces a fifth-order accurate solution, with initial conditions $a_0 = 0.318$ and $\varphi_0 = 0.390$. The parameters are the same as previously. The integral curve winds up into a spiral leading to a stable equilibrium represented as point S.

5.6 The polar Van der Pol representation.

We also use a polar Van der Pol representation, i.e. a as radius and φ as angle. This polar representation is useful to represent plots having a periodicity with respect to φ , as well as plots in which φ varies globally by more than a given finite interval. In particular, it can be noticed that the averaged system (20) is invariant by the transformation $\varphi \rightarrow \varphi + \frac{\pi}{2n}$. Therefore, in the polar Van der Pol representation, the plot of the integral curves will be invariant by a rotation of angle $\frac{\pi}{2n}$, and the entirety of the plot can be obtained by duplication and rotation of only one set of solution curves, located in a given sector. Fig. 5 is a polar Van der Pol representation of one numerical solution to System (20) with same parameters as for Fig. 4, but initial conditions slightly different, so that the solution winds up around the origin, and cannot be entirely represented in a rectangular plot, because although $a(t)$ remains finite, $\varphi(t)$ becomes large when t increases.

With the same parameters, if the initial conditions $a_0 = 0.318$, $\varphi_0 = 0.392$ are taken, a different behaviour is obtained, as represented in Fig. 6: the movement enters a spiral winding up around a stable solution not located at the origin. The zoomed view in Fig. 6 shows the detail in polar coordinates. This represents the same data as in Fig. 4, which was in rectangular coordinates.

5.7 Quality of the averaging method in the present context.

Because the third step hereafter makes use of the averaged System(20) instead of the original second-order Eq.(1), it is necessary to assess the quality of the averaging method in the present

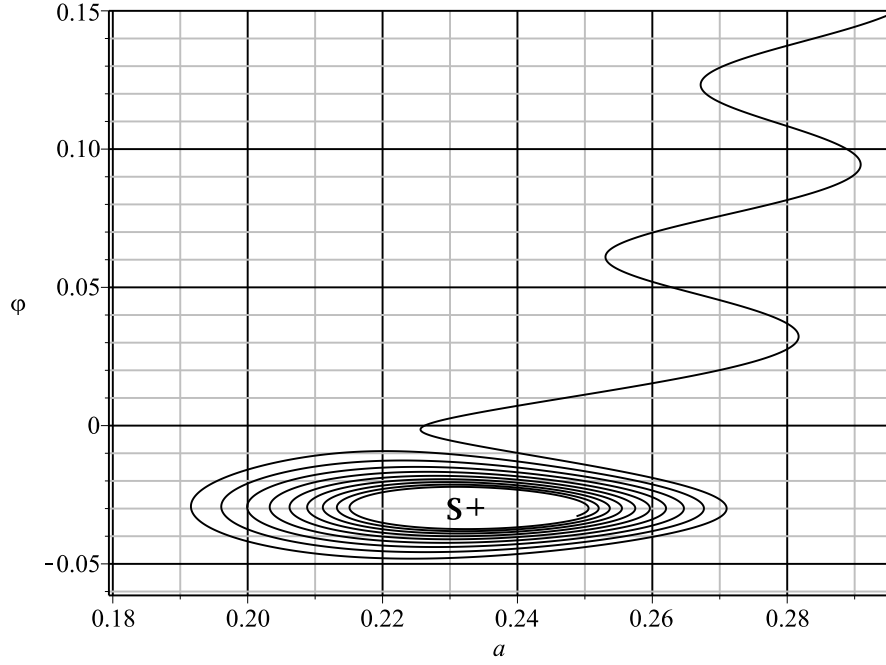


Figure 4: Integral curve with stable equilibrium at point S. Parameters: same as for Fig.2. Initial conditions: $a_0 = 0.318$ (initial value for a), $\varphi_0 = 0.392$ (initial value for φ).

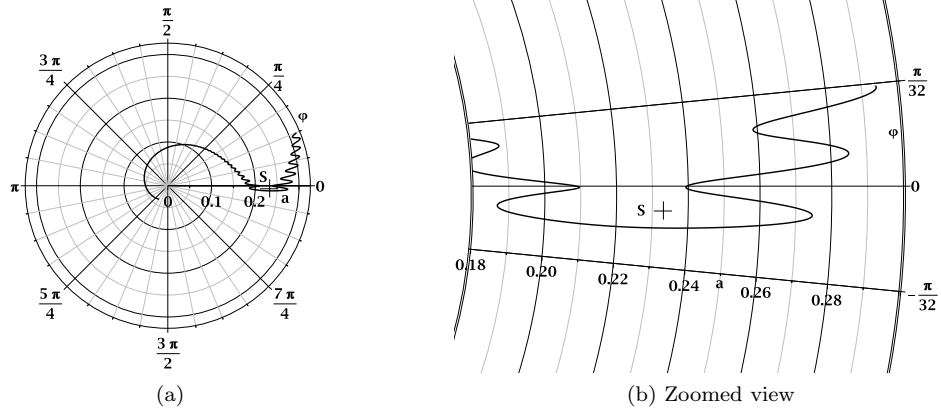


Figure 5: Polar representation: integral curve winding up around the origin. Radius is a , argument is φ . Parameters: same as for Fig.4. Initial conditions: $a_0 = 0.318$ (initial value for a), $\varphi_0 = 0.390$.

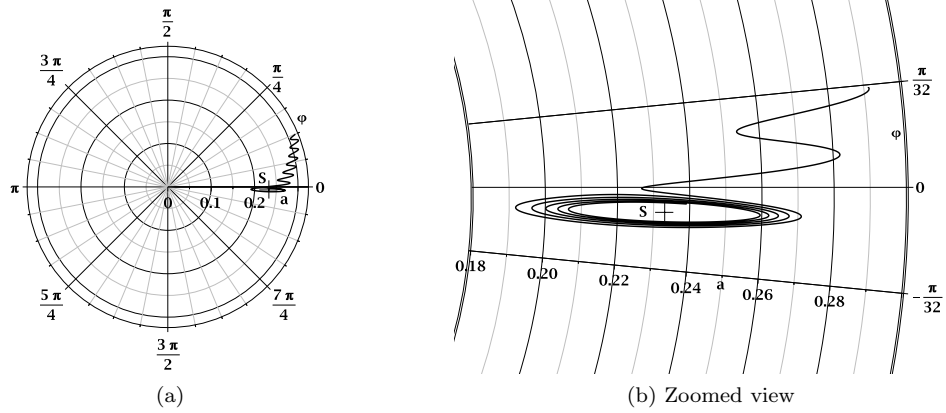


Figure 6: Polar representation: integral curve winding up around a stable solution represented as point S, not located at the origin. Parameters and initial conditions: $a_0 = 0.318$, $\varphi_0 = 0.392$.

context. Take the same example system as for the discussion about Fig. 2. Tables 1, 2 and 3 show the results of the numerical solution to the original second-order Eq.(1) as compared to the results of the numerical solution to the averaged System(20), for various values of the parameters, as described in Table 4. For the sake of clarity, only a part of the plots is represented, to allow for a zoomed view around the attractors; knowing that the solution has a rotational symmetry of $2\pi/n$, each figure can be completed by applying $n - 1$ successive rotations of $2\pi/n$ to the plots represented. The numerically-calculated integral curves are represented for various starting points located at regularly-spaced angular intervals at a same radius. For the plots of the integral curves of the original second-order equation, a smoothing process had to be applied, because the raw curves are very shaky by nature. The smoothing process is a moving average over a full period of the oscillator, centered on the current point. The moving average is carried out on each variable a and φ separately. This is why the beginning and the end of the curves had to be removed in Table 3, because the moving average is not applicable near the extremities of the curves. Then an offset must be added to the phase in the initial conditions of the 2nd-order equation so as to have a good coincidence with the solutions of the averaged system. This offset is denoted $\Delta\varphi$ in Table 4. Finally, a global rotation is applied to the curves of the second-order equation, to align them with those of the averaged system, because there is a slight difference in said global orientation, probably due to the fact that the averaged system supposes that the motion is already effective at $t = 0$, while the average carried out on the solution to the original equation needs some time to establish.

Discussion For the ranges of parameters as given in Table 4, the plots show a very good coincidence between the integral curves of the second-order original equation and those of the averaged system. However, a difference begins to appear for high values of n and β , as shown in Fig. (c) of Table 3. In said figure, the curves for the smoothed second-order equation are shaky, because in this case, the amplitude of the external excitation is very high ($A = 5.5$); the oscillator, when passing nearby the point where the H -function is maximum, can receive a high impulse, depending

on the phase of said force. But this difference does not invalidate the similarity between the two curves, which is still surprisingly good, despite the quite high value of A .

An interesting question is about systems with more than one minimum in the A -function, and therefore with more complicated implicit solutions. Such systems can be seen in Figs. (b) and (c) of Table 1 and in Fig. (c) of Table 2. The presence of two attractors for a same value of n is due to the presence of more than one minimum in the curve giving A against a_S , and therefore, of more than one intersection point (with positive derivative, in this example) between the $A(a_S)$ -curve and the line $A = \text{Const}$. Take the example of case (b) in Table 1. The corresponding A -curve is shown in Fig. 7, to be compared to Fig. 2. Here, an additional stable-equilibrium point S' and an additional unstable-equilibrium point T' are represented. It can be verified that the abscissae of points S and S' in Fig. 7 are the radii of attractors in Fig. (b) of Table 1. Moreover, it can be noticed that the unstable-equilibrium point T' has a very low abscissa in Fig. 7, and that integral curves passing near T' and evolving around the attractor in S' may lead to high-amplitude motion, as can be seen in said Fig. (b). When such integral curves pass near the origin, it can be seen that the argumental motion can be initiated even when the initial conditions are close to $(x = 0, \dot{x} = 0)$, because a small perturbation or, if A is high enough, the forced-vibration regime near the origin, can have an amplitude high enough to engage the system into an argumental regime, via said integral curve. Moreover, once the system is engaged on an integral curve around an attractor and has its amplitude increasing, it can jump (due to a small external perturbation at the right moment) to another integral curve which can drive it to even higher amplitudes, towards another attractor. This can be seen in Fig.(b) of Table 1. These cases are important, because in them, the capture phenomenon can be initiated at surprisingly low amplitudes, and evolve into high-amplitude oscillations, taking advantage of the energy provided by the external periodic excitation source. This kind of argumental oscillations is of interest, for instance in civil engineering, to further delimit the hazardous parameter domains. Switching from one attractor to another is mentioned in [8].

6 Third step: approximate analytical solution for the argumental Duffing oscillator.

In this section, an approximate closed-form solution of the averaged system (20) for the Type B oscillators will be presented. An integrating factor will be used, which will lead to an implicit equation of the integral curves (independent of the reduced time τ). Then, the quality of the approximation will be discussed. Because the averaged systems of the Type-A and Type-B oscillators are similar, this calculus is analogous for the Type A oscillator.

The symbolic expression of the averaged system allows to characterize the separatrix and then the area inside the separatrix, which is the capture region of the attractor.

6.1 Integrating factor.

Recall the averaged system (20):

$$\begin{cases} \dot{a} &= -\frac{A}{4\rho} S(a) \sin(n\varphi) - \beta a \\ \dot{\varphi} &= \frac{3\mu}{8\rho} (a^2 - a_n^2) - \frac{A}{4a\rho_n} \cos(n\varphi) D(a) \end{cases} \quad (41)$$

Table 1: Quality of the averaging method for $n = 3$. The polar plots show φ (angular) and a (radial). Parameter values are given in Table 4.

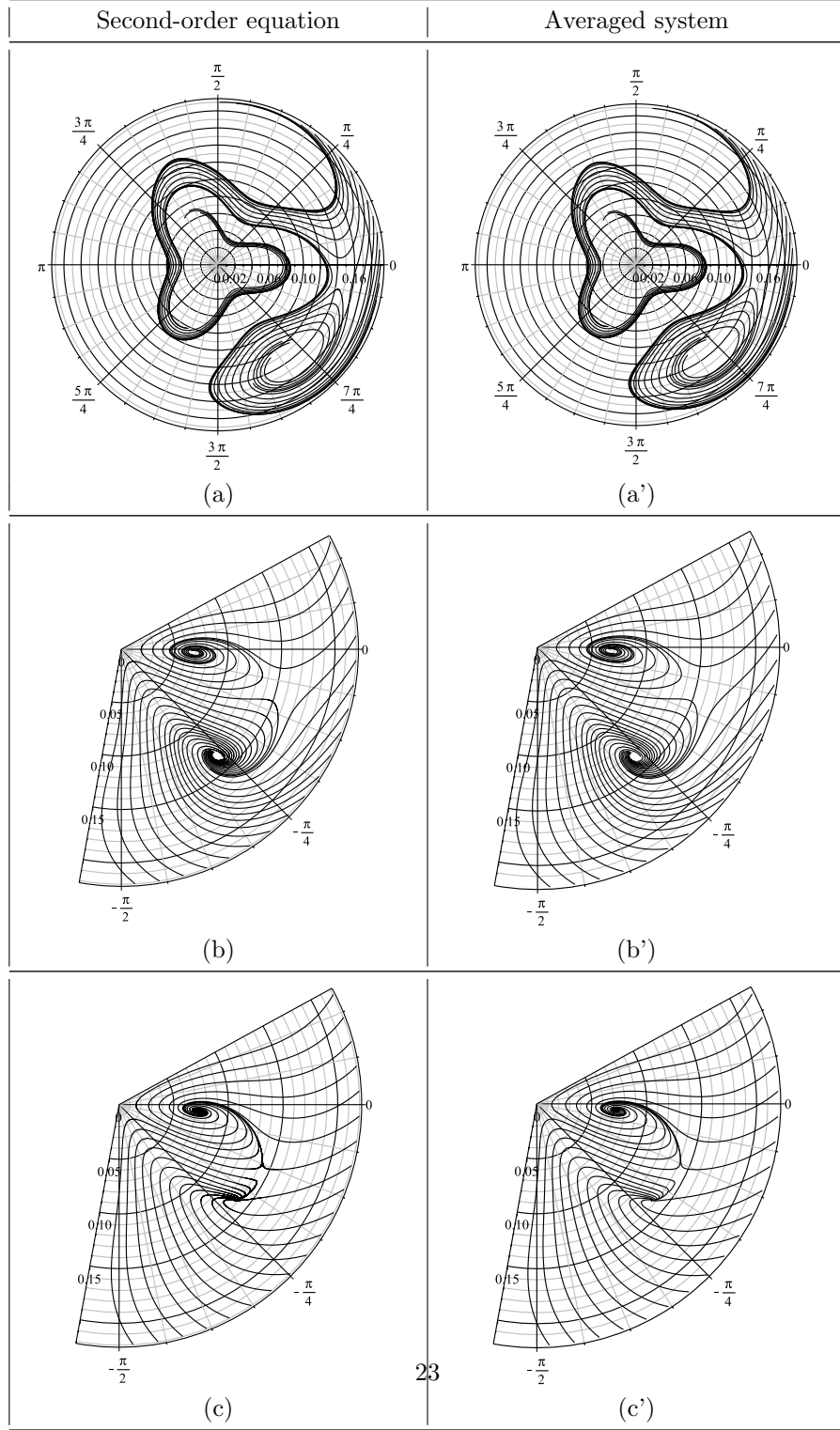


Table 2: Quality of the averaging method for $n = 7$. The polar plots show φ (angular) and a (radial). Parameter values are given in Table 4.

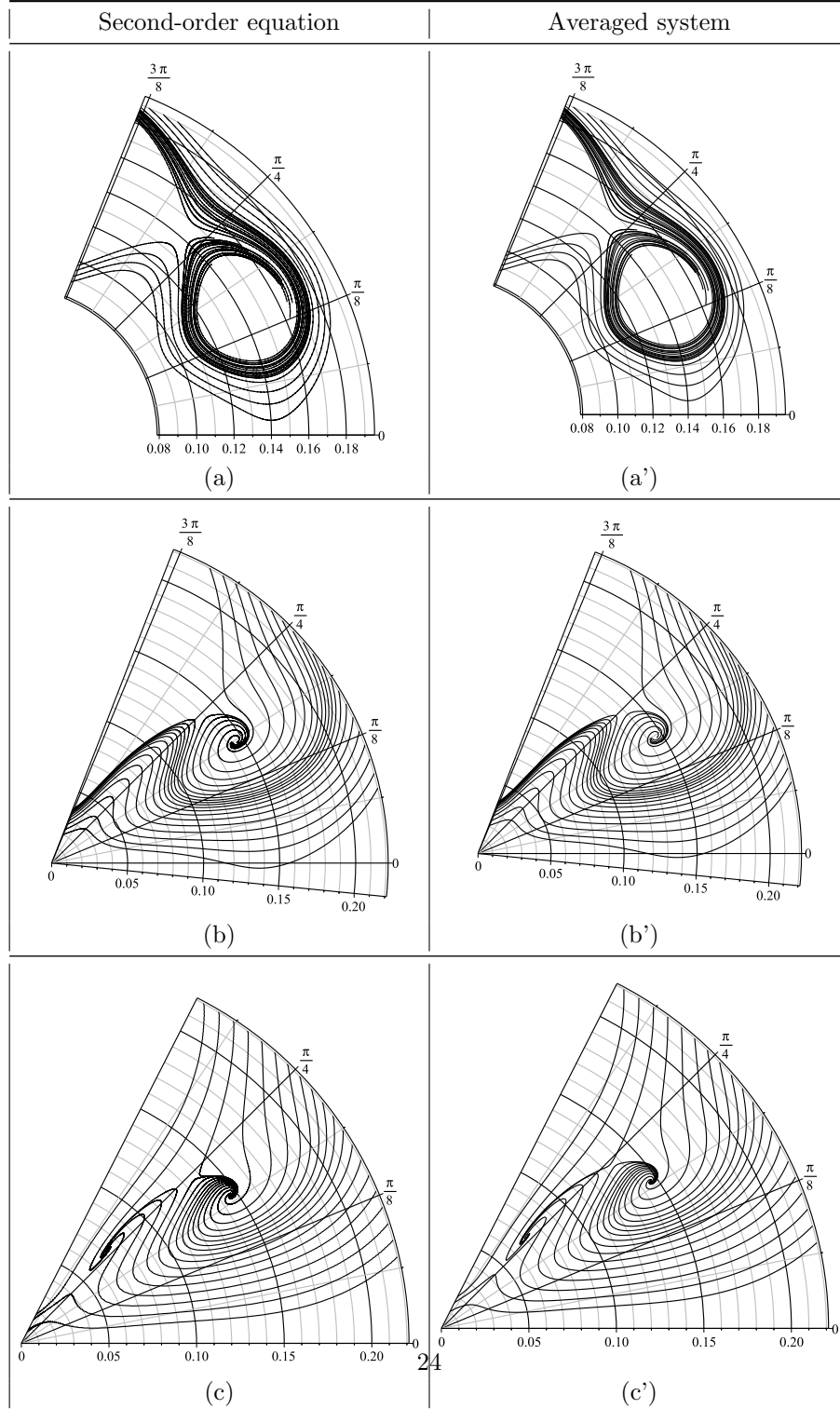
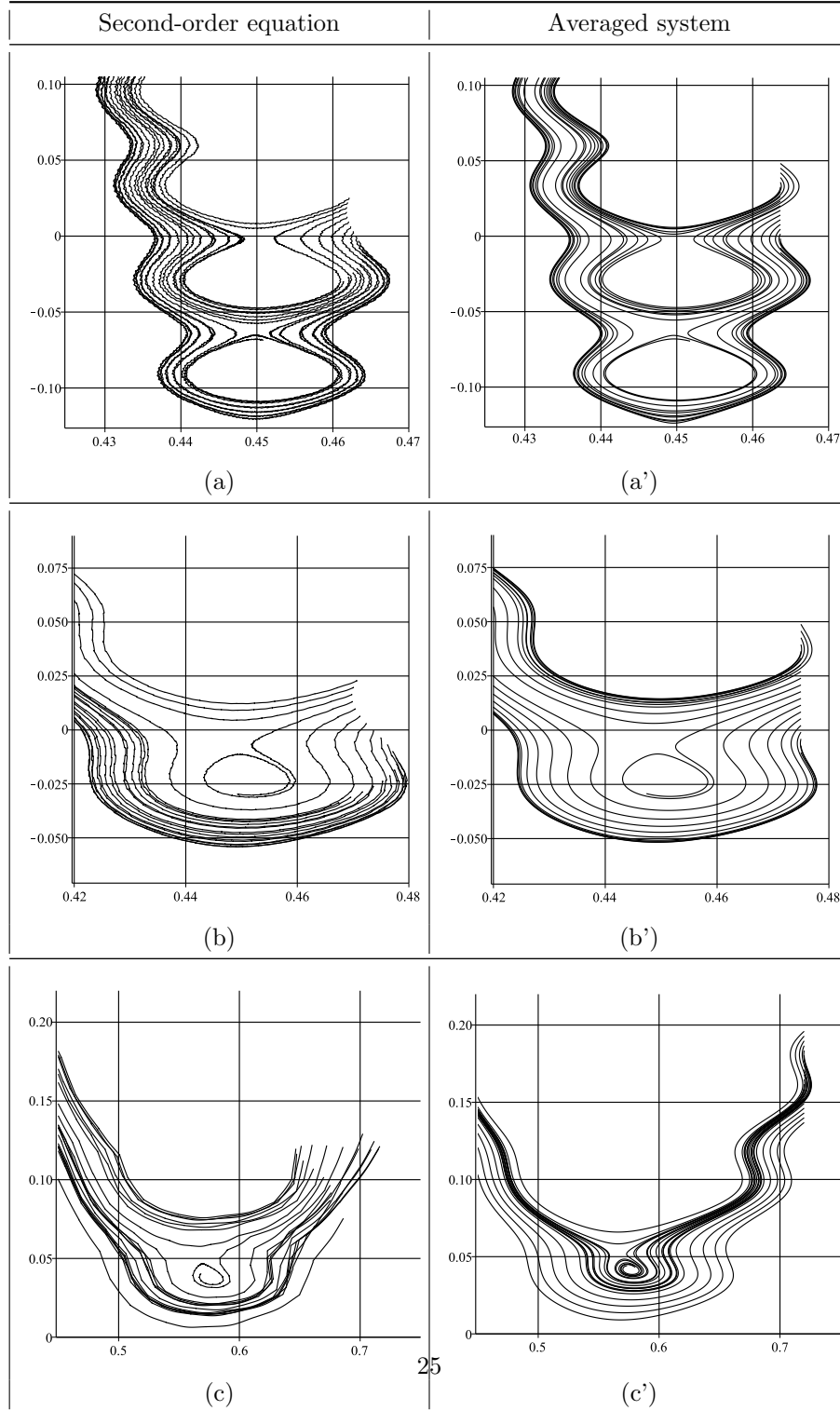


Table 3: Quality of the averaging method for $n = 101$. The Cartesian plots show φ as ordinate and a as abscissa. Parameter values are given in Table 4.



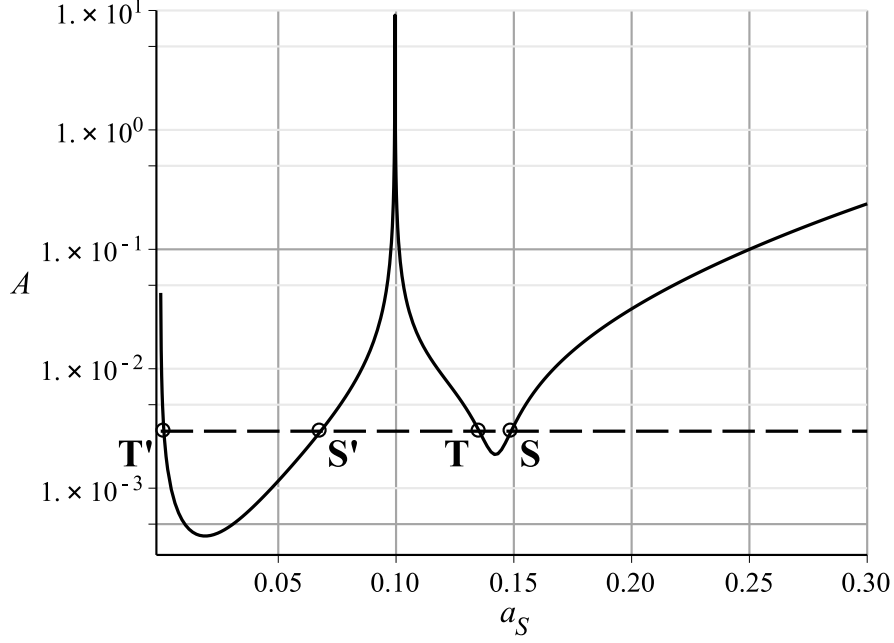


Figure 7: $A(a_S)$ for a Type B2 system. The parameter values are those given for Picture (b) of Table 4 for $n = 3$.

Write the system (41) under a more compact form, by defining two functions F and G of a and φ as follows:

$$\begin{cases} F(a, \varphi) &= -\frac{A}{4\rho} S(a) \sin(n\varphi) - \beta a \\ G(a, \varphi) &= \frac{3\mu}{8\rho} (a^2 - a_n^2) - \frac{A}{4a\rho_n} \cos(n\varphi) D(a) \end{cases} \quad (42)$$

Hence:

$$\begin{cases} \dot{a} &= F(a, \varphi) \\ \dot{\varphi} &= G(a, \varphi) \end{cases}$$

that is,

$$G(a, \varphi) da - F(a, \varphi) d\varphi = 0. \quad (43)$$

This is generally not an exact differential, but multiply the whole equation through by an integrating factor, i.e an appropriate function $I(a, \varphi)$ such that there exists a function $U(a, \varphi)$ such that

$$dU(a, \varphi) = \frac{\partial}{\partial a} (U(a, \varphi)) da + \frac{\partial}{\partial \varphi} (U(a, \varphi)) d\varphi \quad (44)$$

$$= I(a, \varphi) G(a, \varphi) da - I(a, \varphi) F(a, \varphi) d\varphi \quad (45)$$

Table 4: Quality of the averaging method: parameter values for Tables 1, 2 and 3. Common parameter values: $\gamma = 1000$, $\mu : -1/6$. The initial conditions of the first curve are a_0 and φ_0 . The other curves have the same a_0 , and a φ_0 increased by $2\pi/(20n)$ each. The parameter denoted “ $\Delta\varphi$ ” is the offset which must be added to the phase in the initial conditions of the 2nd-order equation so as to have a good coincidence with the solutions to the averaged system.

n	Picture	A	β	ρ	a_0	φ_0	$\Delta\varphi$
3	a, a'	$5 \cdot 10^{-4}$	10^{-4}	0.99873	0.19	0.23753	0.62582
	b, b'	$3 \cdot 10^{-3}$	10^{-3}	0.99873	0.22	-1.5184	0.5236
	c, c'	$4 \cdot 10^{-3}$	$2 \cdot 10^{-3}$	0.99873	0.22	-1.5184	0.5236
7	a, a'	$7 \cdot 10^{-4}$	10^{-4}	0.99873	0.19	1.0771	0.2244
	b, b'	$2.5 \cdot 10^{-3}$	10^{-3}	0.99873	0.22	0.2244	0.2244
	c, c'	$4.5 \cdot 10^{-3}$	$2 \cdot 10^{-3}$	0.99873	0.22	0.2244	0.2244
101	a, a'	0.5	10^{-4}	0.98726	0.46365	-0.01182	-0.0015552
	b, b'	1.5	10^{-3}	0.98726	0.475	-0.010265	-0.0023329
	c, c'	5.5	10^{-2}	0.97930	0.72	0.13686	0.033593

then Eq.(43) becomes $dU(a, \varphi) = 0$, whose solution is $U(a, \varphi) = \text{Const}$. In this case, by identification between Eqs(44) and (45), it holds:

$$\begin{cases} \frac{\partial}{\partial a}(U(a, \varphi) = I(a)G(a, \varphi) \\ \frac{\partial}{\partial \varphi}(U(a, \varphi) = -I(a)F(a, \varphi) \end{cases} \quad (46)$$

The new expression $dU(a, \varphi)$ is an exact differential. A necessary condition for this to be possible is that $\frac{\partial^2 U(a, \varphi)}{\partial a \partial \varphi} = \frac{\partial^2 U(a, \varphi)}{\partial \varphi \partial a}$, i.e.

$$\frac{\partial}{\partial \varphi}(I(a, \varphi)G(a, \varphi)) = \frac{\partial}{\partial a}(-I(a, \varphi)F(a, \varphi))$$

Replacing F and G by their definition expressions from Eq.(42), and developing, this condition translates to:

$$\begin{aligned} & \left(\frac{An}{4a\rho_n} D(a) \sin(n\varphi) - \frac{A}{4\rho_n} \frac{dS(a)}{da} \sin(n\varphi) - \beta \right) I(a, \varphi) = \\ & \left(\frac{A}{4\rho_n} S(a) \sin(n\varphi) + \beta a \right) \frac{\partial}{\partial a} I(a, \varphi) - \left(\frac{3}{8} \frac{\mu}{\rho_n} (a^2 - a_n^2) - \frac{A}{4a\rho_n} D(a) \cos(n\varphi) \right) \frac{\partial}{\partial \varphi} I(a, \varphi) \end{aligned} \quad (47)$$

To search for an integrating factor as a function of a and φ is as difficult a problem as searching for a solution to the original equation. It is more practical to search for I as a function of a only. By so doing, a way can be figured out to an approximate integrating factor in closed-form.

Let $I(a)$ be the unknown integrating factor. For the sake of clarity, the following functions of a : $S(a), D(a), I(a), \frac{dS(a)}{da}, \frac{dD(a)}{da}, \frac{dI(a)}{da}$ will respectively be denoted by S, D, I, S', D', I' . Eq.(47)

becomes:

$$\frac{A}{4\rho_n} \sin(n\varphi) \left(\frac{nD}{a} I - S' I - S I' \right) = \beta (aI' + I)$$

and, due to the fact that a and φ are independent variables, this is possible only if:

$$\begin{cases} I \frac{An}{4a\rho_n} D - I' \frac{A}{4\rho_n} S - I \frac{A}{4\rho_n} S' \equiv 0 \\ I' \beta a + I \beta \equiv 0 \end{cases}$$

that is, the two following equations are obtained:

$$\begin{aligned} \frac{nD}{a} I - I S' - I' S &\equiv 0 \\ (aI' + I) \beta &\equiv 0. \end{aligned}$$

At this point, the special case $\beta = 0$ is of interest.

Special case $\beta = 0$ Here, Eq.(48) classically yields

$$I(a) = \frac{e^{J(a)}}{S(a)}$$

with

$$J(a) = n \int_{a_1}^a \frac{D(u)}{uS(u)} du \quad (48)$$

and a_1 an arbitrary constant. The second Eq.(46) writes, knowing that here, $\beta = 0$:

$$\frac{\partial U(a, \varphi)}{\partial a} = -I(a) F(a, \varphi) = \frac{A}{4\rho_n} \sin(n\varphi) e^{J(a)}.$$

Hence

$$U(a, \varphi) = -\frac{A}{4\rho_n} e^{J(a)} \cos(n\varphi) + L(a), \quad (49)$$

where $L(a)$ is a function of a to be determined.

Substituting this expression into the first Eq.(46) yields:

$$\frac{dL(a)}{da} = \frac{3\mu}{8\rho_n} (a^2 - a_n^2) \frac{e^{J(a)}}{S(a)}$$

and therefore

$$L(a) = \int_{a_2}^a \frac{3\mu}{8\rho_n} (w^2 - a_n^2) \frac{e^{J(w)}}{S(w)} dw$$

where a_2 is an arbitrary constant.

Substituting this expression into Eq.(49) allows to conclude that the exact solution to system (41) when $\beta = 0$ is $V(a, \varphi) = Const$, with

$$V(a, \varphi) = 3\mu n \int_{a_2}^a (w^2 - a_n^2) \frac{e^{J(w)}}{S(w)} dw - 2A e^{J(a)} \cos(n\varphi).$$

Thus the equation of the integral curve passing through point (a_0, φ_0) is

$$V(a, \varphi) = V(a_0, \varphi_0), \quad (50)$$

where the constant a_2 disappears.

In the case $\beta = 0$, it is also possible to find this result by applying the classical “variation of the constant” method to System (20) viewed as a first-order differential equation of variable $y = \cos(n\varphi(a))$ depending on variable a . But the integrating factor approach additionally allows, as studied hereinafter, an approximation of the general solution when $\beta \neq 0$.

As an example, consider the case of a Type-B2 system, with functions $S(a)$ and $D(a)$ as given by Eqs(25).

Applying Eq.(48), it holds:

$$J(a) = n \int_{a_0}^a \frac{1}{u} \left(\frac{1}{\sqrt{1 + \gamma u^2}} + \frac{1}{n} \left(\frac{1}{1 + \gamma u^2} - 1 \right) \right) du$$

A classical calculus yields

$$J(a) = \frac{n}{2} \left(\ln \left(\frac{\sqrt{1 + \gamma a^2} - 1}{\sqrt{1 + \gamma a^2} + 1} \right) - \ln \left(\frac{\sqrt{1 + \gamma a_0^2} - 1}{\sqrt{1 + \gamma a_0^2} + 1} \right) \right) - \ln \left(\frac{\sqrt{1 + \gamma a^2}}{\sqrt{1 + \gamma a_0^2}} \right)$$

Hence

$$e^{J(a)} = \frac{\left(\frac{\sqrt{1 + \gamma a^2} - 1}{\sqrt{1 + \gamma a^2} + 1} \right)^{n/2}}{\left(\frac{\sqrt{1 + \gamma a_0^2} - 1}{\sqrt{1 + \gamma a_0^2} + 1} \right)^{n/2}} \frac{\sqrt{1 + \gamma a_0^2}}{\sqrt{1 + \gamma a^2}}.$$

Notice that expression

$$K(a) = \left(\frac{\sqrt{1 + \gamma a^2} - 1}{\sqrt{1 + \gamma a^2} + 1} \right)^{n/2}$$

can also be written here

$$K(a) = \frac{\sqrt{\gamma}}{4n} \sqrt{1 + \gamma a^2} a S(a),$$

so that

$$e^{J(a)} = \frac{aS(a)}{a_0 S(a_0)}$$

and Eq.(50) writes:

$$3\mu n \int_{a_0}^a (w^2 - a_n^2) \frac{\frac{wS(w)}{a_0 S(a_0)}}{S(w)} dw = 2A \left(\frac{aS(a)}{a_0 S(a_0)} \cos(n\varphi) - \cos(n\varphi_0) \right)$$

hence

$$3\mu \int_{a_0}^a (w^2 - a_n^2) w dw = \frac{2A}{n} (aS(a) \cos(n\varphi) - a_0 S(a_0) \cos(n\varphi_0))$$

giving the exact equation of the curve passing through point (a_0, φ_0) for the Type-B2 oscillator when $\beta = 0$:

$$3\mu \frac{a^2 - a_0^2}{2} \left(\frac{a^2 + a_0^2}{2} - a_n^2 \right) = \frac{2A}{n} (aS(a) \cos(n\varphi) - a_0 S(a_0) \cos(n\varphi_0))$$

General case: $\beta \neq 0$ Here, Eq.(48) yields $I(a) = \frac{k}{a}$, where k is a real constant. And as the result is equivalent for any non-null value of k , as is expressed by $kU(a, \varphi) = 0$, take $k = 1$ to simplify the writing. Substituting this expression of $I(a)$ into Eq.(48) yields: $\frac{n}{a^2}D + \frac{n}{a^2}S - \frac{1}{a}S' \equiv 0$, that is,

$$nD + S - aS' \equiv 0. \quad (51)$$

This equation is not strictly verified by the functions $S(a)$ and $D(a)$, but it can be noticed that generally, $|S| \gg |D|$, so that it may be expected that altering D will introduce less of an error than altering S . So try to use one of the following two methods to replace S or D by another function so as to satisfy Eq.(51):

- Keeping the original definition of $S(a)$, and replacing $D(a)$ by $\frac{aS' - S}{n}$;
- Keeping the original definition of $D(a)$, and replacing $S(a)$ by $na \int \frac{D}{a^2} da + C_1 a$, where C_1 is a constant.

The numerical simulations show that these two methods are approximately equivalent and may lead to satisfactory results for oscillators of Type B2 (examples are given hereafter). Supposing that now an $S(a)$ and a $D(a)$ functions satisfy Eq.(51), it is possible to go on and express the function $U(a, \varphi)$ using one of the two following formulas:

$$\frac{\partial U}{\partial a} = I(a)G(a, \varphi) \quad (52)$$

$$\frac{\partial U}{\partial \varphi} = -I(a)F(a, \varphi). \quad (53)$$

Pick Eq.(53). Replacing $F(a, \varphi)$ by its definition expression from Eq.(42) yields:

$$U(a, \varphi) = -\frac{A}{4\rho_n} \frac{\cos(n\varphi)}{n} \frac{S}{a} + \beta\varphi + L(a), \quad (54)$$

where $L(a)$ is a function of a to be determined using Eq.(53).

Calculating $\frac{\partial U}{\partial a}$ from Eq.(54) and substituting the result into Eq.(53) yields:

$$\frac{A}{4\rho_n} \left(\frac{1}{n}(S - S'a) + D \right) \cos(n\varphi) = \frac{3}{8} \frac{\mu}{\rho_n} a(a^2 - a_n^2) - a^2 L'(a).$$

As a and φ are independent variables, this is possible only if:

$$\begin{cases} S - S'a + nD \equiv 0 \\ \frac{3}{8} \frac{\mu}{\rho_n} (a^2 - a_n^2) - aL'(a) \equiv 0. \end{cases}$$

The first condition has already been encountered and discussed previously as Eq.(51). The second condition gives: $L'(a) = \frac{3}{8} \frac{\mu}{\rho_n} \left(a - \frac{a_n^2}{a} \right)$. Hence $L(a) = \frac{3}{8} \frac{\mu}{\rho_n} \left(\frac{a^2}{2} - a_n^2 \ln(a) \right) + C_2$, where C_2 is a

constant.

Finally, substituting this expression of $L(a)$ into Eq.(54) yields:

$$U(a, \varphi) = -\frac{AS(a) \cos(n\varphi)}{4n\rho_n} + \beta\varphi + \frac{3}{8} \frac{\mu}{\rho_n} \left(\frac{a^2}{2} - a_n^2 \ln(a) \right) + C_3 \quad (55)$$

where C_3 is a constant and with $nD(a) \equiv aS'(a) - S(a)$.

6.2 Implicit equation of the integral curves.

From Eq.(55), deduce the implicit equation of the integral curve beginning at the initial condition ($a = a_0, \varphi = \varphi_0$): $U(a, \varphi) = U(a_0, \varphi_0)$. Developing and eliminating the constant C_3 yields:

$$\begin{aligned} \beta(\varphi - \varphi_0) - \frac{A}{4n\rho_n} \left(\frac{S(a) \cos(n\varphi)}{a} - \frac{S(a_0) \cos(n\varphi_0)}{a_0} \right) + \\ \frac{3}{8} \frac{\mu}{\rho_n} \left(\frac{a^2 - a_0^2}{2} - a_n^2 (\ln(a) - \ln(a_0)) \right) = 0. \end{aligned} \quad (56)$$

In Fig. 8, the implicit Eq.(56) is represented by a solid line, with a set of system parameters as used in Fig. 6. The corresponding numeric solution is represented as a dotted line. On the set of integral curves, dashed lines represent the locus of the condition $\frac{da}{dt} = 0$, and a space-dotted line

represents the locus of the condition $\frac{d\varphi}{dt} = 0$. Depending on the initial conditions, the symbolic approximation is composed of either a single curve surrounding an ovoid region, or two curves, one of which surrounds the ovoid region, the other following the numeric solution before arriving at the ovoid, and then going away from the ovoid.

The ovoid region is an attractor of the system, represented in the (amplitude, phase)-space. Due to the invariance of the averaged system versus a transformation $\varphi \rightarrow \varphi + \frac{2k\pi}{n}$ (with k integer), there is a rotational symmetry of the averaged system as represented in the Van der Pol polar diagram. Therefore, the attractor duplicates by successive rotations by a $\frac{2\pi}{n}$ angle.

In Fig. 8 are also represented four points: S, which represents the stable stationary solution; T, which represents the unstable stationary solution; N, which represents the point with $a = a_n$ as defined about Eq.(17); and Start, which represents the starting point of the numeric simulation. It can be seen here that the amplitude (abscissa) of point T is lower than that of point S. This is clearly visible also in Fig. 2, where point S is located on the increasing part of the $A(a_S)$ curve, while point T is located on a decreasing part.

6.3 Quality of the approximated symbolic solution to the averaged system.

To assess the quality of the approximated solution to the averaged system of equations, Table 5 shows plots of the separatrix calculated with a method based on point T, which is the unstable-equilibrium point studied above. The study is carried out in the neighbourhood of points S and T which are at radii close to a_n as defined by Eq.(17). The parameters n and β are varied over an extended range. The method consists of using two integral curves passing near point T: one

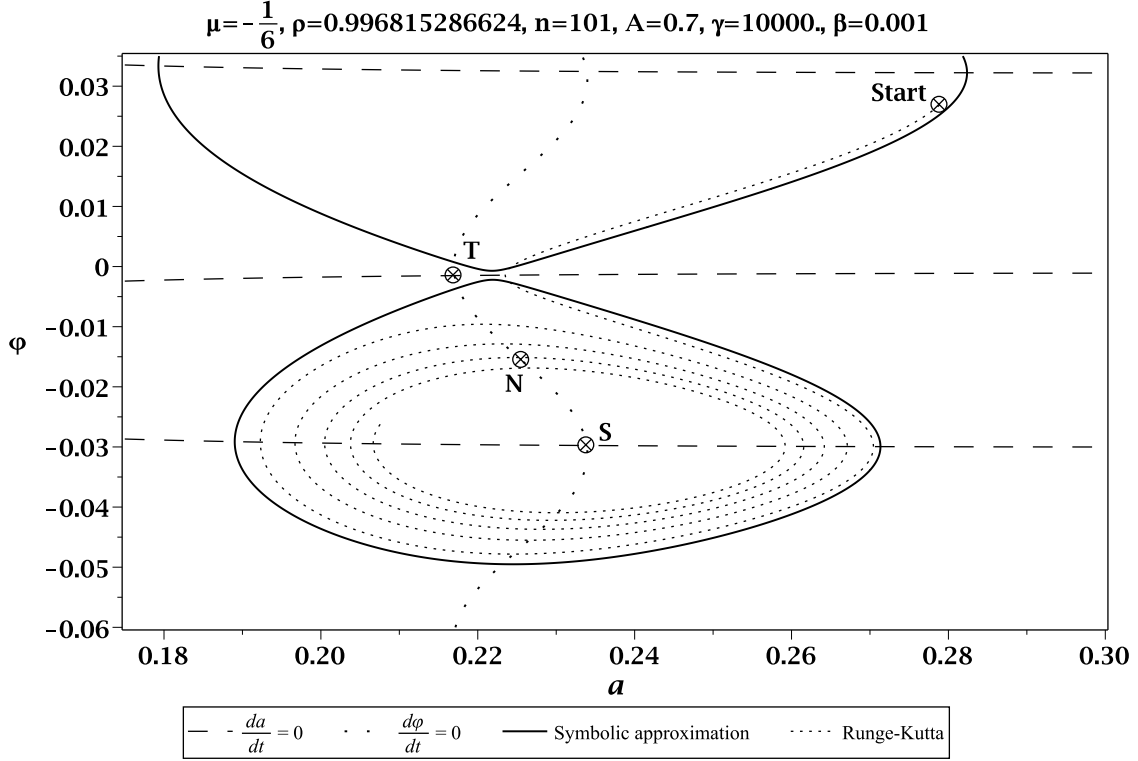


Figure 8: Symbolic approximation vs numeric (Runge-Kutta) solution to the averaged system. Parameters and initial conditions: same as for Fig. 4.

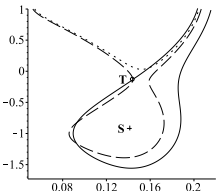
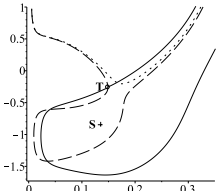
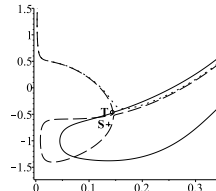
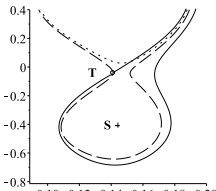
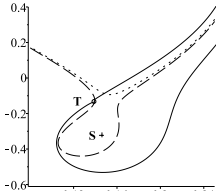
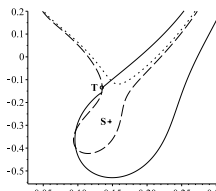
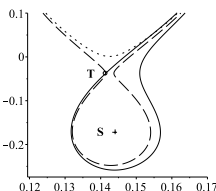
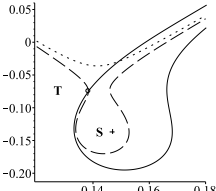
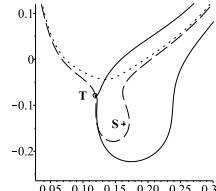
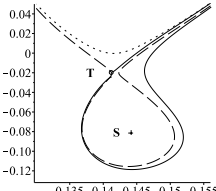
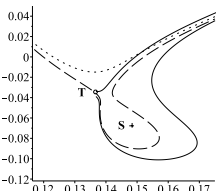
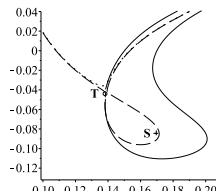
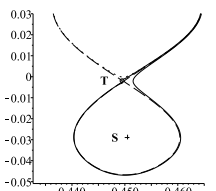
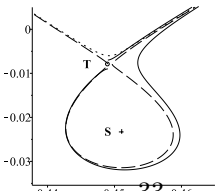
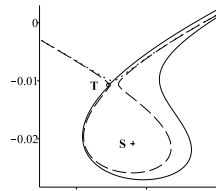
slightly above, the other slightly below. For the implicit equation of the integral curves, two curves are obtained, each representing the oscillator before and after passing near point T. Only the parts representing states before passing near point T are to be kept to build the separatrix. For the numerical calculus, both curves are calculated with a starting point near point T, in reverse time.

Results The results show that for $\gamma = 1000$, $\mu = -1/6$ and $\rho = 0.99873$, the implicit equation is good for $\beta \leq 10^{-4}$, fair for $\beta = 10^{-3}$, and rough for $\beta > 10^{-3}$. The results are better when n increases.

7 Conclusion

An analytic expression of the amplitude $A(a_S)$ of the external excitation as a function of the oscillator's stable-state amplitude a_S has been used to bring out a multiple-bifurcation system. A simple analytic expression of the system's stability criterion has been given, which reduces to a test on the value of a_S versus one parameter a_{flip} and the direction of variation of $A(a_S)$. Attractors have been identified, which duplicate in a rotational symmetry figure.

Table 5: Quality of the symbolic approximation. The plots show φ (in ordinates) versus a (in abscissae). The numerically-calculated separatrix is represented as a solid line, while the curves obtained by a symbolical formula to approximate the separatrix are a dotted line and a dashed line. Common parameter values, unless otherwise noted: $\gamma = 1000, \mu : -1/6, \rho = 6.272/6.28$.

n	$\beta = 10^{-4}$	$\beta = 10^{-3}$	$\beta > 10^{-3}$
3	 $A = 0.0005$	 $A = 0.003$	 $\beta = 0.002, A = 0.004$
7	 $A = 0.0007$	 $A = 0.0025$	 $\beta = 0.002, A = 0.0045$
15	 $A = 0.001$	 $A = 0.006$	 $\beta = 0.005, A = 0.03$
31	 $A = 0.015$	 $A = 0.1$	 $\beta = 0.002, A = 0.2$
101	 $A = 0.5, \rho = 6.2/6.28$	 $A = 1.5, \rho = 6.2/6.28$	 $\beta = 10^{-2}, A = 5.5, \rho = 6.15/6.28$

Using an integrating factor, an approximate implicit analytic solution to the averaged system has been given. Using said approximate analytic solution, it is possible to symbolically assess the capture probability by an attractor by calculus of various areas in the Van der Pol representations [4]. Cases have been discussed, in which integral curves pass nearby the origin before leading to an attractor corresponding to a motion with non-negligible amplitude.

References

- [1] M.J. Béthenod. Sur l’entretien du mouvement d’un pendule au moyen d’un courant alternatif de fréquence élevée par rapport à sa fréquence propre. *Comptes rendus hebdomadaires de l’Académie des sciences*, 207(19):847–849, November 1938. (in French).
- [2] N. Bogolioubov and I. Mitropolski. *Les méthodes asymptotiques en théorie des oscillations non linéaires*. Gauthiers-Villars, 1962.
- [3] D. Cintra and P. Argoul. Nonlinear argumental oscillators: A few examples of modulation via spatial position. *Journal of Vibration and Control*, 2016. (online publication, pre-printing).
- [4] Daniel Cintra and Pierre Argoul. Attractors capture probability in nonlinear argumental oscillators. *Communications in Nonlinear Science and Numerical Simulation*, 48:150 – 169, 2017.
- [5] B. Cretin and D. Vernier. Quantized amplitudes in a nonlinear resonant electrical circuit. In *2009 Joint Meeting of the European Frequency and Time Forum and the IEEE International Frequency Control Symposium, vols 1 and 2*, volume 1 & 2, pages 797–800, Besançon, France, April 2009. Joint Meeting of the 23rd European Frequency and Time Forum/IEEE International Frequency Control Symposium.
- [6] D.B. Doubochinski and J.B. Doubochinski. Amorçage argumentaire d’oscillations entretenues avec une série discrète d’amplitudes stables. *E.D.F. Bulletin de la direction des études et recherches, série C mathématiques, informatique*, 3:11–20, 1991. (in French).
- [7] I. S. Gradshteyn and I. M. Ryzhik. *Table of Integrals, Series, and Products, Seventh Edition*. Alan Jeffrey and Daniel Zwillinger, 2007.
- [8] W. Lacarbonara, D. Bernardini, and F. Vestroni. Nonlinear thermomechanical oscillations of shape-memory devices. *International Journal of Solids and Structures*, 41(56):1209 – 1234, 2004.
- [9] D. I. Penner, D. B. Doubochinski, M. I. Kozakov, A. S. Vermel, and Yu. V. Galkin. Asynchronous excitation of undamped oscillations. *Soviet Physics Uspekhi*, 16(1):158–160, July-August 1973.
- [10] G. Rega and F. Benedettini. Planar non-linear oscillations of elastic cables under subharmonic resonance conditions. *Journal of Sound and Vibration*, 132(3):367–381, 1989.
- [11] J.P. Treilhou, J. Coutelier, J.J. Thocaven, and C. Jacquez. Payload motions detected by balloon-borne fluxgate-type magnetometers. *Advances in Space Research*, 26(9):1423–1426, 2000.

Attractor's capture probability in nonlinear argumental oscillators

Daniel Cintra (corresponding author)
Université Paris-Est, Laboratoire Navier (UMR 8205),
CNRS, Ecole des Ponts ParisTech, IFSTTAR,
F-77455 Marne La Vallée, France.
email: daniel.cintra@enpc.fr

and

Pierre Argoul
Université Paris-Est, MAST, SDOA, IFSTTAR,
F-77447 Marne La Vallée, France
email: pierre.argoul@ifsttar.fr

Abstract

The behaviour of a space-modulated, so-called “argumental” Duffing oscillator, is studied. Starting from a known analytic implicit solution to the equations of motion, and using a Van der Pol representation in the (amplitude, phase)-space, the shape and distribution of the attractors’ upstream basins are discussed, and various capture probabilities by the attractors are assessed under symbolic form. The expressions obtained can help in the design of structures in mechanical engineering, where most often the argumental phenomenon is to be avoided.

Keywords— argumental oscillator; spatial modulation; capture probability; attractor

Contents

1	Introduction	3
1.1	Argumental oscillators: overview	3
1.2	Prior knowledge	3
1.3	Second-order equation	3
1.4	Averaged system of equations	4
1.5	The number n	5
1.6	Forced-oscillation regime	5
1.7	Excitation amplitude A against stable steady-state amplitude a_S	6
1.8	Examples of S and D functions.	6
2	Definitions.	6
2.1	Upstream basin	6
2.2	Ovoid	7
2.3	Tail	7
2.4	Capture probability	7
2.5	Polar Van der Pol representation.	8
2.6	Annulus	9
3	A few geometric properties of the ovoid.	10
3.1	Approximate implicit equation.	10
3.2	Angular and radial diameters.	12
3.3	Angular positions of points S and T.	13
3.4	Angular diameter of the ovoid.	15
	Angular position of point B	15
	Approximating the transcendent equation	16
	A critical parameter	17
3.5	Radial diameter of the ovoid.	18
	Radial positions of points L and R	18
3.6	Area of the ovoid.	19
4	Attractor's capture probabilities.	19
4.1	Capture probability with initial condition $a = a_n$	20
4.2	Capture probability with initial condition on a circle concentric with the annuli. . .	21
4.3	Capture probability with initial condition inside the annulus tangent to the ovoid. .	24
4.4	Capture probability with initial condition inside the whole annulus of rank n	27
4.5	Capture probability with initial condition inside a circle concentric to the annuli. . .	28
5	Conclusion	30

1 Introduction

The objective of this paper is to study a so-called argumental oscillator, and to present attractors and symbolic formulas giving the capture probabilities by attractors under various conditions. In this introduction, argumental oscillators are presented, and some known symbolic results are recalled. In section 2, definitions are given, and the attractor's upstream basin is introduced. In section 3, geometric properties of the basins are studied, which allow to derive symbolic formulae used in section 4, yielding, under symbolic form, various capture probabilities of the attractor.

1.1 Argumental oscillators: overview

Under suitable conditions, the so-called “argumental oscillator” can enter a stable motion at a frequency next to its natural frequency, and much lower than the excitation frequency. The actual motion frequency is generally a sub-multiple of the excitation frequency. For this phenomenon to arise, the interaction between the excitation source and the oscillator must be space-dependent; for instance, it may be maximum when the oscillator is in mid-position, and decrease when the oscillator goes away from said mid-position. The motion can maintain a large amplitude indefinitely. This behaviour may be hazardous, because it is often unexpected. Thus, it appears of interest to assess the probability to enter such a regime.

1.2 Prior knowledge

Pendulums maintained in a steady state by high-frequency sources are described in [1,2]. A pendulum with a discrete series of steady amplitudes, as well as mathematical developments based on the averaging method [3], are described in [4]. Modelling and experimental results about six argumental oscillators are given in [5]. A symbolic stability criterion and an approximate implicit analytic solution to the motion equation are given in [6]. Such argumental oscillators are encountered in various domains: in a weather balloon [7], in an electronic circuit [8].

Oscillations at a frequency which is a sub-multiple of the excitation frequency in a system whose motion equation contains a product of a function of a space variable by an harmonic signal are studied in [9, p. 3085]. Basins of attraction in a system whose motion equation contains a product of the sinus of the space variable by an harmonic signal are studied in [10, p. 73].

1.3 Second-order equation

A 1-degree-of-freedom Duffing-type argumental oscillator [1, 2, 5] obeys a second-order differential equation as follows:

$$\ddot{\alpha}(\tau) + 2\beta\dot{\alpha}(\tau) + \alpha(\tau) + \mu\alpha^3(\tau) = AH(\alpha)E(\tau) \quad (1)$$

where α is the space-position variable, $\tau = \omega_0 t$ is the reduced time, t is the real time, ω_0 is the oscillator's natural angular frequency, β is the damping ratio, μ is the coefficient representing the Duffing non-linearity, A is a constant, H is a non-constant function of α whose absolute value is less than or equal to 1, and which takes the value 1 at least once, E is an harmonic function of τ with amplitude 1 and angular velocity ν , i.e. $E(\tau) = \cos(\nu\tau)$, and the dot notation refers to the differentiation with respect to τ . H is a space-modulation function, while E represents the harmonic excitation. A is the amplitude of the harmonic excitation. The right-hand member of Eq.(1) can also be made of

a H - and a E -function entangled into one function, e.g. $A \cos(k\alpha - \nu\tau)$, where k and ν are constants.

In this paper, an example model of argumental oscillator is used, called "Type B" in [5], representing a pendulum submitted to a space-localized harmonic electromagnetic excitation. It is characterized by the H and E functions as follows:

$$H(\alpha) = \frac{1 - \gamma\alpha^2}{(1 + \gamma\alpha^2)^2} \quad (2)$$

$$E(\tau) = \cos\left(\frac{\nu}{\omega_0}\tau\right) \quad (3)$$

where γ is a constant depending on the system's geometrical properties (usually $10^3 \leq \gamma \leq 10^5$), ν is the angular frequency of the external force, and ω_0 is the natural angular frequency of the oscillator.

1.4 Averaged system of equations

Eq. (1) is classically [3,4] transformed into a pair of first-order equations, by first defining a change of variables, introducing two new variables a and φ , by putting:

$$\begin{cases} \alpha(\tau) = a(\tau) \sin(\rho\tau + \varphi(\tau)) \\ \dot{\alpha}(\tau) = a(\tau)\rho \cos(\rho\tau + \varphi(\tau)). \end{cases} \quad (4)$$

where ρ is a constant to be determined. $a(\tau)$ is the slowly-varying amplitude and $\varphi(\tau)$ is the slowly-varying phase. "Slowly-varying" means here that the frequencies of the a and φ signals are low versus the excitation frequency, i.e. $\rho \ll \frac{\nu}{\omega_0}$.

Besides, putting $\theta = \rho\tau + \varphi$ and knowing that H is, in the example, an even function of θ having a period of π , the Fourier series of $H(a \sin(\theta))$ is introduced, namely

$$H(a \sin(\theta)) = \sum_{q=0}^{+\infty} c_q(a) \cos(2q\theta) \quad (5)$$

with

$$c_q(a) = \frac{2}{\pi} \int_0^\pi H(a \sin(\eta)) \cos(2q\eta) d\eta, \quad (6)$$

Then, after a few transformations, applying the averaging method [3,4] to system (4), and denoting \bar{u} for the averaged value of a variable u , a for \bar{a} , \dot{a} for $\dot{\bar{a}}$, and the same for φ , one gets:

$$\begin{cases} \dot{a} &= -\frac{A}{4\rho} S(a) \sin(n\varphi) - \beta a \\ \dot{\varphi} &= \frac{3\mu}{8\rho} (a^2 - a_n^2) - \frac{A}{4a\rho} \cos(n\varphi) D(a) \end{cases} \quad (7)$$

where n is an odd integer, while λ and a_n are defined by

$$\lambda = \frac{\nu}{\omega_0} \quad (8)$$

$$\rho = \frac{\lambda}{n} = \sqrt{\frac{3\mu a_n^2}{4} + 1} \quad (9)$$

and two functions S and D of a are introduced as follows: $S(a) = c_m(a) + c_p(a)$ and $D(a) = c_m(a) - c_p(a)$, with $m = \frac{n-1}{2}$, $p = \frac{n+1}{2}$, and c_m as given in Eq. (6). As ρ depends on n , it will be denoted ρ_n from now on.

ν , ω_0 and μ are parameters of the system, while n is a mathematical parameter linked to the averaging method, which must be an odd integer in the example used in this paper.

1.5 The number n

n can be seen as setting up a "window" into the system, allowing the application of the averaging method, and giving a view valid in a limited range of amplitudes of the oscillator. It turns out that n is the ratio of the external excitation frequency to the actual period of the oscillator at steady state. As the actual period depends on the amplitude, there is a plurality of possible values for n [4]. In our example, where $\mu < 0$ and n is odd, it can be seen from Eq. (9) that there is a minimum possible value n_{min} for n , with $n_{min} > \lambda$, so that a_n can be computed and does not vanish. It holds:

$$\begin{cases} n_{min} = [\lambda] + 1 & \text{if } [\lambda] \text{ even} \\ n_{min} = [\lambda] + 2 & \text{if } [\lambda] \text{ odd} \end{cases} \quad (10)$$

where $[]$ denotes the "integer part of".

1.6 Forced-oscillation regime

If n is not an odd integer, one has:

$$\begin{cases} \dot{a} = -\beta a \\ \dot{\varphi} = \frac{3\mu}{8\rho}(a^2 - a_n^2) \end{cases} \quad (11)$$

That is, in this case, the averaged system (11) is the same as (7) (where n is an odd integer), except that one must make $A = 0$: for this value of n , the resolution of System(7) by the averaging method considers that the system is disconnected from the external excitation source and ends up either in another region where one must use a different value of n to search for a solution, either near $a = 0$, where it enters the forced-oscillation regime. To calculate the system behaviour in this region, classically consider that $|\alpha(\tau)| \ll 1$, and then that $|\alpha(\tau)| \ll |\mu\alpha^3(\tau)|$. Consider also that $H(\alpha) \approx h_0 = \text{Constant}$, usually with $h_0 = 1$ most of the times if H is an even function. Then linearize the system based on Eq. (1), writing it as follows, with $E(\tau) = \cos\left(\frac{\nu}{\omega_0}\tau\right)$:

$$\ddot{\alpha}(\tau) + 2\beta\dot{\alpha}(\tau) + \alpha(\tau) = Ah_0 \cos\left(\frac{\nu}{\omega_0}\tau\right) \quad (12)$$

Then search for a particular solution to Eq. (12) of the form

$$\alpha(\tau) = a_S \sin(\rho\tau + \varphi_S) \quad (13)$$

where a_S is the constant amplitude and φ_S is the constant phase with respect to the excitation signal, and $\rho = \nu/\omega_0$. Deduce that

$$a_S = \frac{Ah_0}{\sqrt{(\rho^2 - 1)^2 + 4\rho^2\beta^2}} \approx \frac{Ah_0}{\rho^2 - 1}$$

and

$$\varphi_S = \arctan\left(\frac{1 - \rho^2}{2\beta\rho}\right) \approx \arctan\left(\frac{-\rho}{2\beta}\right)$$

with $0 < \beta \ll 1$ and $\rho \gg 1$.

The general solution to Equ.12 is the sum of a transitory solution to the excitationless oscillator, which is a damped sinusoid, and of expression (13). Hence, after the first part vanishes, the amplitude of the steady-state is a_S and the phase is φ_S . The values (a_S, φ_S) define a point representing a steady-state condition in a Van der Pol representation. This point is usually very close to the origin of coordinates and is an attractor, because it is the solution satisfying Eq. (1) with an oscillator frequency equal to the excitation frequency, whatever initial condition is chosen with an amplitude small enough so as to satisfy condition $|\alpha(\tau)| \ll 1$.

1.7 Excitation amplitude A against stable steady-state amplitude a_S .

Fig. 1 shows a typical curve of A against a_S for the steady-state condition ($\dot{a} = 0, \dot{\varphi} = 0$) of Eq. (7), obtained by eliminating φ between the two equations of system (7). The averaging method being a perturbative method, the value of A in Eq. (1) must not be too large. Therefore, for a given value of n , the value of a_S can be symbolically calculated only in a limited interval around a_n [6]. Parameter a_n will be used extensively in this paper: it is a value close to the amplitude of the steady state, defined as a function of ν , ω_0 and n .

1.8 Examples of S and D functions.

With the H function as given in Eq. (2), the symbolic expressions for $S(a)$ and $D(a)$ are as follows [6]:

$$\begin{cases} S(a) &= \frac{4n}{a\sqrt{\gamma}\sqrt{1+\gamma a^2}} \left(\frac{\sqrt{1+\gamma a^2}-1}{a\sqrt{\gamma}} \right)^n \\ D(a) &= \frac{n\sqrt{1+\gamma a^2}-\gamma a^2}{n(1+\gamma a^2)} S(a) \end{cases} \quad (14)$$

where γ is a parameter representing spatial characteristics of the system.

Fig. 2 presents functions S and D for the parameters mentioned in Fig. 1.

2 Definitions.

2.1 Upstream basin

Define an attractor's "upstream basin" as the set of points representing initial conditions ending up in the attractor. Fig. 3 presents an attractor denoted S and the separatrix delimiting the attractor's upstream basin. The separatrix is constructed in two parts, by numerically solving system (7) with two initial conditions close to point T, and computing in reverse time.

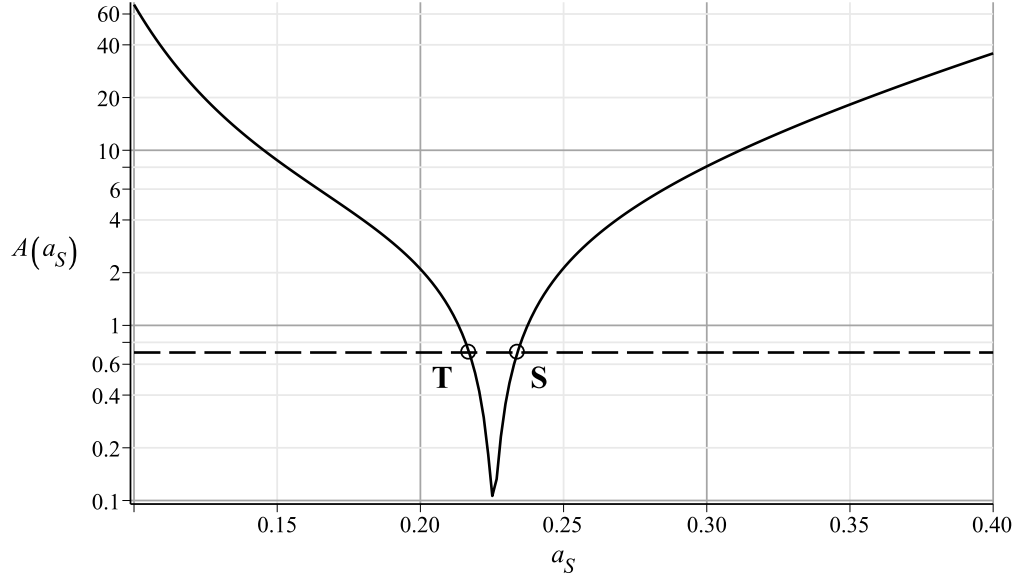


Figure 1: Typical aspect of curve A against a_S . Points S and T correspond to points S and T shown in Fig. 8. Parameters: $n = 101$, $\omega_0 = 6.28$, $\nu = 632.26$, $\beta = 0.001$, $A = 0.7$, $\mu = -1/6$, $\gamma = 10000$.

2.2 Ovoid

Define an "ovoid" as the largest convex set containing the attractor. Define an ovoid's "upstream basin" as the set of points representing initial conditions ending up inside the ovoid. In Fig. 8, one ovoid is represented in Cartesian Van der Pol representation, using a symbolic implicit solution.

2.3 Tail

Define an ovoid's "tail" as the part of the attractor's upstream basin located outside the ovoid. It can be seen in Figs. 3, 5 and 6 that the ovoid's tail has a small area compared to the attractor's upstream basin. In this paper, only cases where the tail's area can be neglected compared to the ovoid's area are studied. Thus it will be considered that the attractor's upstream basin has an area approximately equal to the area of the ovoid containing the attractor. However, in certain cases, for instance when γ is low (less than 100), when n is low (less than 11) or when β is low (less than 10^{-4}), the tail's area can become non-negligible.

2.4 Capture probability

Based on Fig. 4, in Cartesian Van der Pol representation, define as "Starting set" the set of all possible points representing initial conditions in a given experiment. Define as "Attracted starting set" the set of those possible starting points belonging to the Starting set and which are included in the attractor's upstream basin. Define an attractor's "capture probability" as the ratio of the area of the Attracted starting set to the area of the corresponding Starting set.

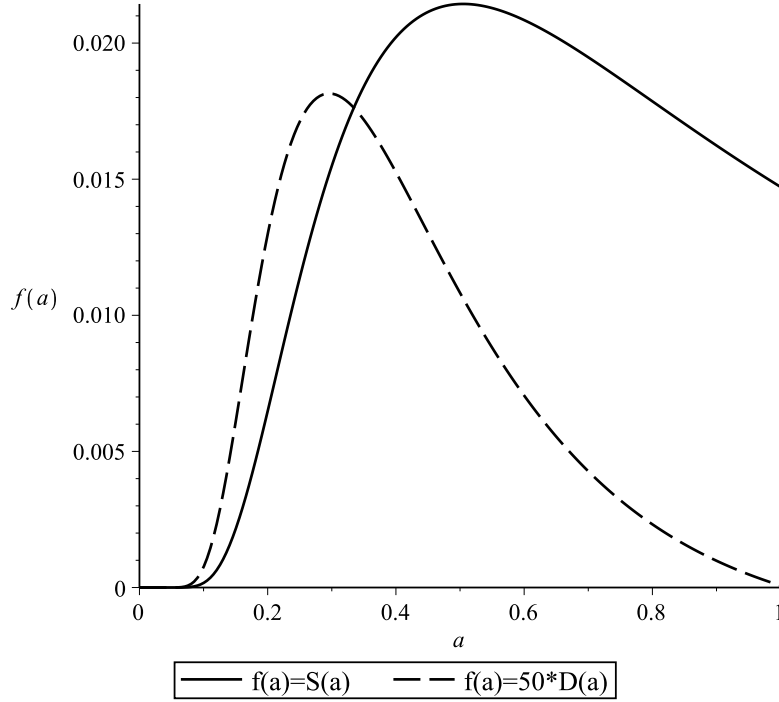


Figure 2: Typical aspect of curves S and D against a . Parameters are the same as for Fig. 1.

2.5 Polar Van der Pol representation.

Besides the Cartesian Van der Pol representation, a polar Van der Pol representation may also be used, i.e. with a as radius and φ as angle. This polar representation is useful to represent plots having a periodicity with respect to φ and plots in which φ can vary by large amounts. In particular, the averaged system of equations (7) is invariant by the transformation $\varphi \rightarrow \varphi + \frac{2\pi}{n}$. Therefore, in the polar Van der Pol representation, the plot of the integral curves and of the ovoids is invariant by a rotation of angle $\frac{2\pi}{n}$, and the entirety of the plot can be obtained by duplication and rotation of only one set of solution curves and ovoids, located in a given circle sector. The invariance by rotation is illustrated in Figs. 5 and 6.

This representation is used herein for the plots of the attractors and the flows. Variable a is called “radius” or “amplitude”; angle φ is called “angular position” or “phase”.

The study is limited to $a + \mu a^3 \geq 0$, i.e. $a \leq \sqrt{-1/\mu}$. As the numerical examples in this paper use $\mu = -1/6$, this means that $a \leq \sqrt{6} \approx 2.45$.

The probability to find the initial-conditions representative point is uniformly distributed against the abscissa (amplitude) and the ordinates (phase). So, in the Cartesian representation, the calculus of areas can be carried out without any risk of giving an excessive weight to a given region. Had the calculus of probabilities been made in a polar Van der Pol representation, it would have given too large an importance to the external regions of the circle for a given phase range delimiting a

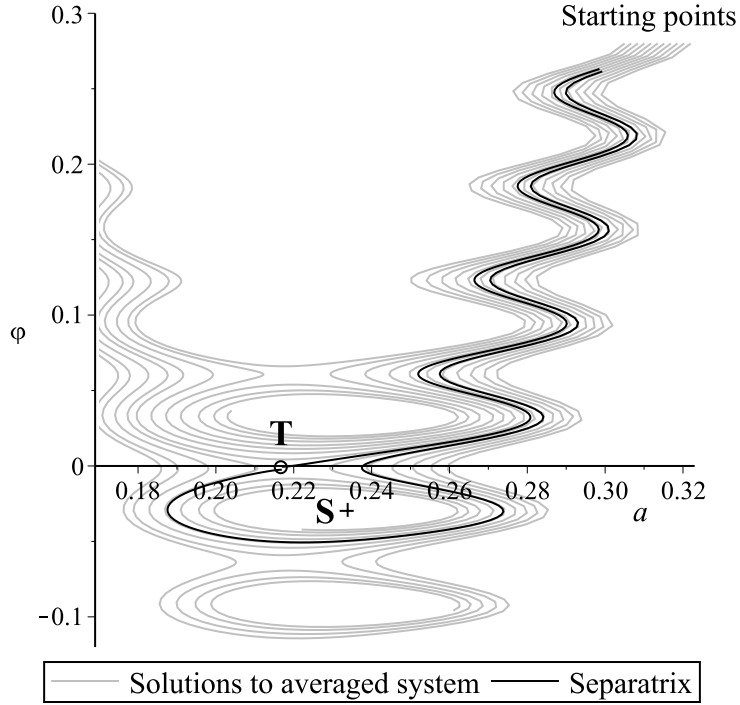


Figure 3: Separatrix and attractor's upstream basin. Point S is the stable steady-state representative point, while point T is the unstable one. Parameters are the same as for Fig. 1.

given angular sector: a given angular region next to the centre of coordinates would have been less probably hit than the same kind of region located far from the centre.

2.6 Annulus

It has been shown above that for a given value of n , the value of a_S can be symbolically calculated only in a limited interval around a_n . In the polar Van der Pol representation, this interval defines an annulus for each value of n . Define this annulus as "annulus of rank n ", or "rank- n annulus". Parameter a_n is approximately the mean radius of the annulus of rank n . Although for a given n , the representative point of the system state can have an amplitude outside this annulus, the trajectories' parts studied in this paper are within this annulus. In Fig. 7, the ovoids located in six adjacent annuli are represented. The annuli are linked to successive odd values of n . When the oscillator does not fall into the argumental regime inside annulus of rank n , it enters another adjacent annulus of lower rank, if said annulus exists, where it can be captured by an attractor located in said annulus. And so on, until the oscillator reaches the lowest annulus, which is a disk centred at the origin. If it is not captured by an attractor of an argumental regime in this last annulus, it ends up in a region located near the center of coordinates, as can be seen in Figs. 5 and 6. This is the forced-oscillation regime discussed above.

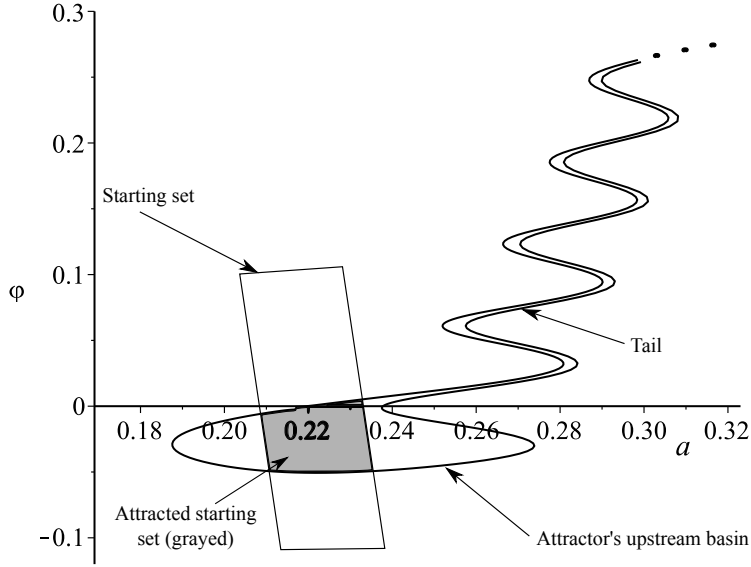


Figure 4: The areas defining the capture probability. The dots above the tail mean that the tail extends beyond the figure.

3 A few geometric properties of the ovoid.

In this section, a closed-form implicit equation constituting an approximate solution to System (7) will be used to assess various geometric properties of the ovoid, leading to an evaluation of the area of the ovoid. This will allow to derive symbolic formulas giving the capture probability for various initial conditions.

3.1 Approximate implicit equation.

Using $\frac{1}{a}$ as an integrating factor [6] applied to System (7), one obtains the approximate implicit equation of the integral curve going through point (a_0, φ_0) for a given n :

$$\beta(\varphi - \varphi_0) - \frac{A}{4n\rho_n} \left(\frac{S(a) \cos(n\varphi)}{a} - \frac{S(a_0) \cos(n\varphi_0)}{a_0} \right) + \frac{3}{8} \frac{\mu}{\rho_n} \left(\frac{a^2 - a_0^2}{2} - a_n^2 (\ln(a) - \ln(a_0)) \right) = 0 \quad (15)$$

with $\rho_n = \frac{1}{n} \frac{\nu}{\omega_0}$.

Fig. 8 is a Cartesian Van der Pol diagram, with a as abscissa and φ as ordinates, representing the implicit approximate equation (15) by a dashed line, with a typical set of system parameters. The corresponding numeric solution is represented as a solid line. Depending on the initial conditions, the symbolic approximation (15) is composed of either a single curve surrounding the ovoid region, or two disconnected curves, like in Fig. 8, one of which surrounds the ovoid region, the other following the numeric solution before arriving at the ovoid, and then going away from the ovoid. In

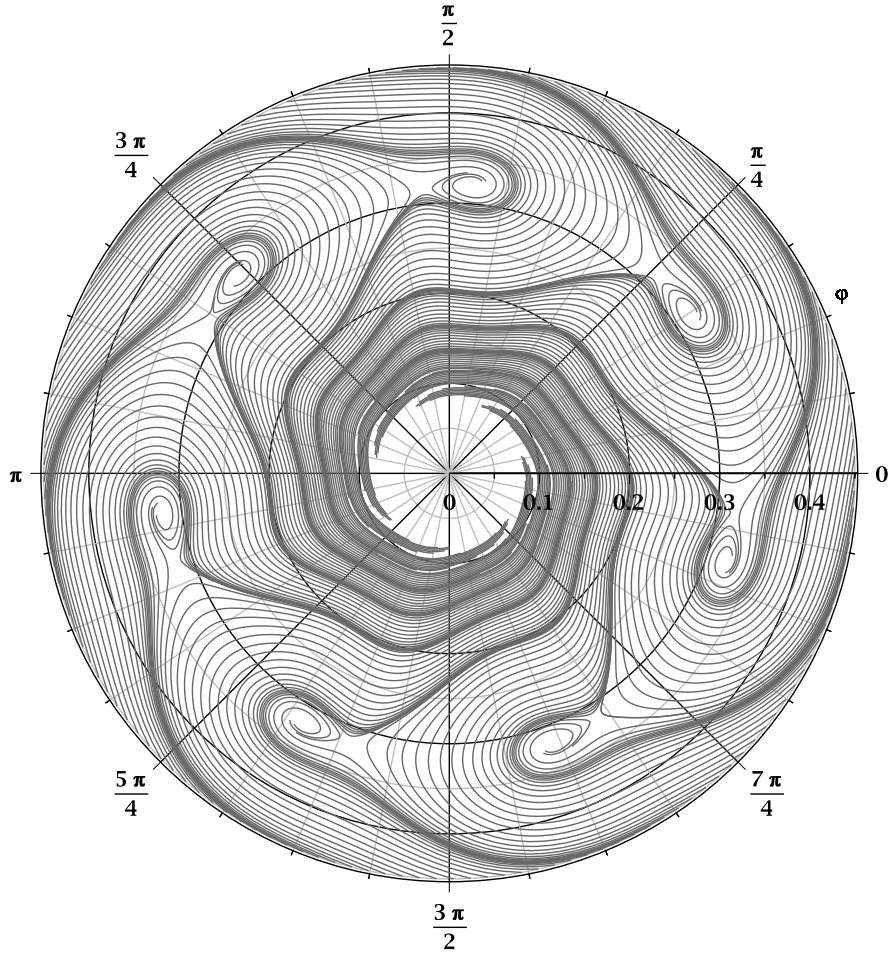


Figure 5: Flows in polar Van der Pol representation. Parameters are: $n = 7$, $\nu = 43.68 \text{ rad/s}$, $\omega_0 = 6.28 \text{ rad/s}$, $\beta = 10^{-3}$, $A = 0.005$, $\mu = -\frac{1}{6}$, $\gamma = 100$ and $\tau_{max} = 1500$. The 150 starting points are uniformly distributed on the circle of radius 0.45. This is the rank-7 annulus, whose upper bound is outside the figure. The lower bound is near 0.

Fig. 8 are also represented a number of points which will be discussed in the next sections. Denote a_B and φ_B the coordinates of point B, and similarly for the other points. The Cartesian representation will be useful hereafter to assess various probabilities in terms of areas in the plane.

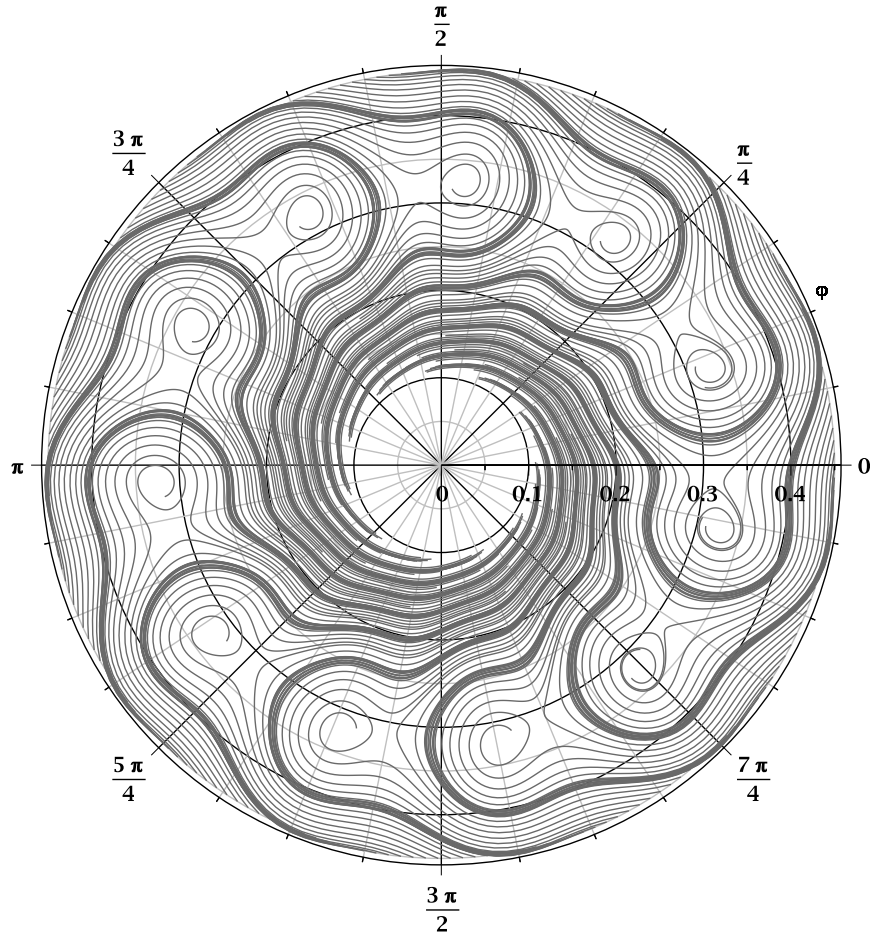


Figure 6: Flows in polar Van der Pol representation. Parameters are the same as for Fig. 5, except $n = 11$, $\nu = 68.64 \text{ rad/s}$, $A = 0.015$, and $\tau_{max} = 1200$. The 200 starting points are uniformly distributed on the circle of radius 0.47. The upper bound of annulus of rank 11 is outside the figure. The lower bound is at 0.

3.2 Angular and radial diameters.

Call “angular diameter” the maximum angular distance between two points of the ovoid, said points having the same radius in the polar Van der Pol representation. And call “radial diameter” the maximum distance between two points of the ovoid, said points having the same angle. Said “angular distance” is in radian unit, while the radial diameter is in the same unit as the oscillator’s amplitude a . In this section, those two diameters will be calculated, based on the positions of remarkable points, and an approximate value of the ovoid’s area will be deduced.

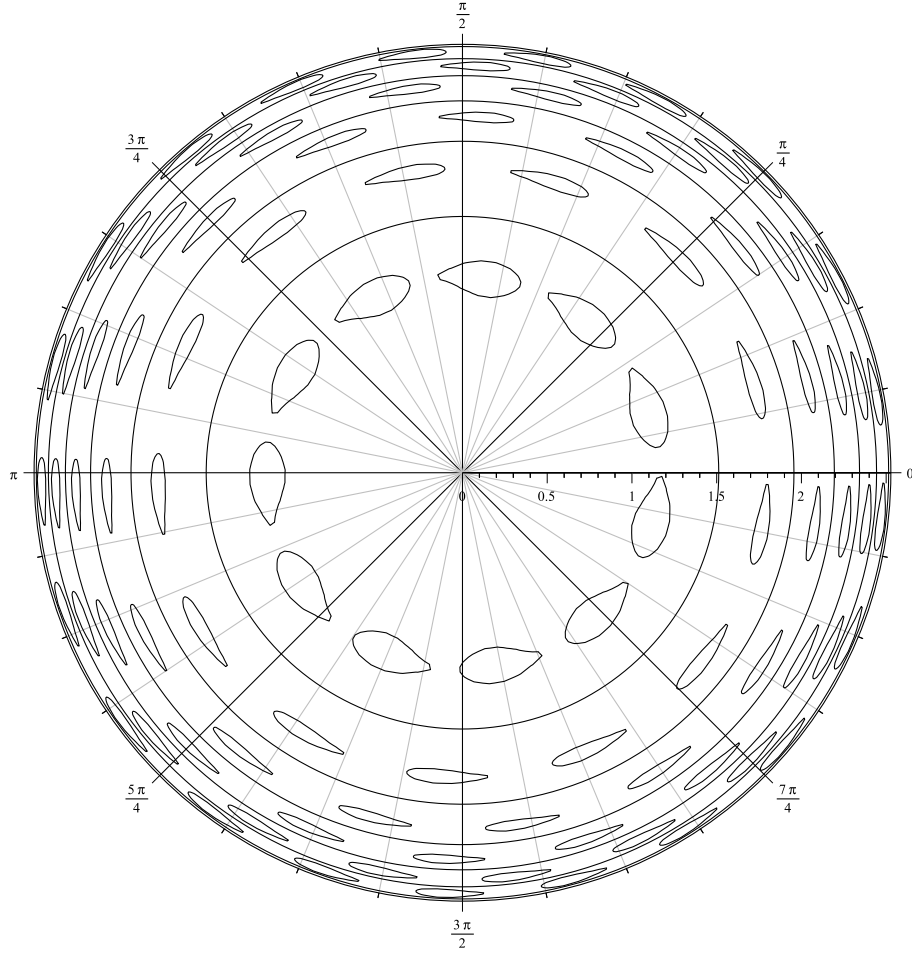


Figure 7: Multiple ovoids in 6 consecutive annuli. Parameters are: $\beta = 10^{-3}$, $A = 1.0$, $\gamma = 10^3$, $\nu = 63.024$, $\omega_0 = 6.28$ and $n = 11$ to 21 . There is one annulus for each value of n , n being an odd integer. The lowest value of n corresponds to the innermost annulus, which is a disk.

3.3 Angular positions of points S and T.

In Fig. 8, four points are represented around the ovoid region. They are called T (at coordinates (a_T, φ_T)) at the top, R (at coordinates (a_R, φ_R)) at the right, B (at coordinates (a_B, φ_B)) at the bottom, and L (at coordinates (a_L, φ_L)) at the left. T and B correspond to $\frac{d\varphi}{dt} = 0$, while L and R correspond to $\frac{da}{dt} = 0$. As shown in Fig. 8, those points are not exactly on the perimeter of the ovoid, because their location is calculated in an approximate way, as described hereafter. A point S is also represented (at coordinates (a_S, φ_S)), which is the stable steady-state solution to the averaged system (7), while point T represents the unstable steady-state solution. Points S and

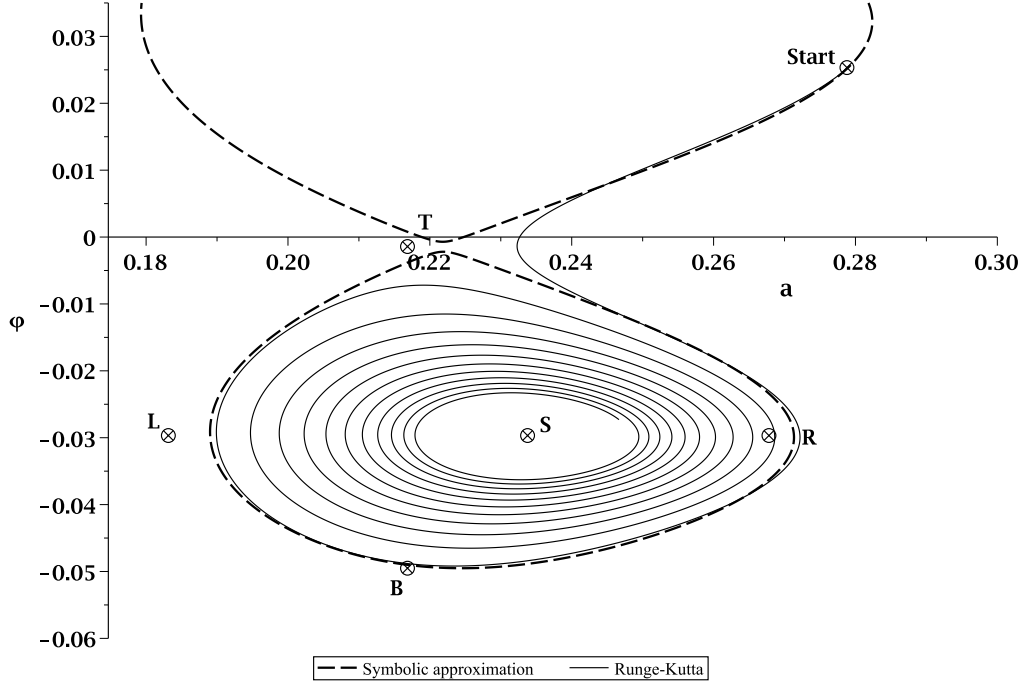


Figure 8: Symbolic approximation vs numeric solution to the averaged system (fifth-order Runge-Kutta Fehlberg method), in Cartesian Van der Pol representation. Integral curve starting at point “Start”, winding up around a stable steady-state solution represented as point S. Point T is the unstable steady-state solution. The other points represented are discussed in the text. Parameters: same as for Fig. 1, plus $a_0 = 0.318$ (initial value for a), $\varphi_0 = 0.392$ (initial value for φ). The ovoid is approximately the dashed closed curve surrounding point S.

T are also the stable (resp. unstable) steady-state solutions to original equation (1). As T and S both satisfy the steady-state condition ($\dot{a} = 0, \dot{\varphi} = 0$) along the integral curve they belong, the positions of these points can be calculated by getting back to the averaged system (7) with $a = a_S$, $\varphi = \varphi_S$, $\dot{a} = 0$ and $\dot{\varphi} = 0$. It holds, with a_n as given in (9):

$$\begin{cases} 0 &= -\frac{A}{4\rho_n} S(a_S) \sin(n\varphi_S) - \beta a_S \\ 0 &= \frac{3\mu}{8\rho_n} (a_S^2 - a_n^2) - \frac{A}{4a_S\rho_n} \cos(n\varphi_S) D(a_S) \end{cases} \quad (16)$$

and similarly for point T:

$$\begin{cases} 0 &= -\frac{A}{4\rho_n} S(a_T) \sin(n\varphi_T) - \beta a_T \\ 0 &= \frac{3\mu}{8\rho_n} (a_T^2 - a_n^2) - \frac{A}{4a_T\rho_n} \cos(n\varphi_T) D(a_T) \end{cases}$$

Hence, with $a_S \approx a_n$, $S(a_S) \approx S(a_n)$, $D(a_S) \approx D(a_n)$, $\sin(n\varphi_S) = -\frac{4\rho_n\beta a_S}{AS(a_S)}$, and similarly for point T:

$$\begin{cases} a_S & \approx a_n \approx a_T \\ \sin(n\varphi_S) & \approx -\frac{4\rho_n\beta a_n}{AS(a_n)} \approx \sin(n\varphi_T) \end{cases} \quad (17)$$

Putting $S_n = S(a_n)$, one gets, in the interval $\left[-\frac{\pi}{n}, \frac{\pi}{n}\right]$, two possible values for φ_S and φ_T : $-\frac{1}{n} \arcsin\left(\frac{4\beta\rho_n a_n}{AS_n}\right)$ and $-\frac{\pi}{n} + \frac{1}{n} \arcsin\left(\frac{4\beta\rho_n a_n}{AS_n}\right)$. Consider the case of the example system, where $a_T < a_n < a_S$ and $\varphi_S < \varphi_T$. It then holds:

$$\begin{cases} \varphi_S & \approx -\frac{\pi}{n} + \frac{1}{n} \arcsin\left(\frac{4\beta\rho_n a_n}{AS_n}\right) \\ \varphi_T & \approx -\frac{1}{n} \arcsin\left(\frac{4\beta\rho_n a_n}{AS_n}\right). \end{cases} \quad (18)$$

3.4 Angular diameter of the ovoid.

Consider the points T and B in Fig. 8. Those two points delimit the angular extension of the ovoid. As an expression for the angular diameter of the ovoid is researched, i.e. $\varphi_T - \varphi_B$, and the expression of φ_T is known, an expression for φ_B remains to be found.

Angular position of point B Assume that, in the Cartesian Van der Pol representation, the ovoid has a shape approximately symmetric with respect to the vertical. Hence it holds:

$$a_B \approx a_T, \quad (19)$$

and consequently, $S(a_B) \approx S(a_T)$. Point B is on the integral curve passing through point T. The equation of this integral curve is Eq. (15), where (a_0, φ_0) is replaced by (a_T, φ_T) . Write that point B is on this curve. Substituting the coordinates of point B for the current coordinates (a, φ) in this equation, and taking (19) into account, it holds, with $a_B \approx a_T$:

$$\beta(\varphi_B - \varphi_T) - \frac{AS(a_T)}{4n\rho_n a_T} (\cos(n\varphi_B) - \cos(n\varphi_T)) \approx 0. \quad (20)$$

Then, considering that $\frac{S(a_T)}{a_T} \approx \frac{S(a_n)}{a_n}$ and substituting $\frac{1}{\sin(n\varphi_T)}$ from Eq. (17) for $-\frac{AS(a_T)}{4\rho_n\beta a_T}$ in Eq. (20), one gets:

$$n\varphi_B - n\varphi_T + \frac{1}{\sin(n\varphi_T)} (\cos(n\varphi_B) - \cos(n\varphi_T)) \approx 0. \quad (21)$$

φ_T being known, this is a transcendent equation in φ_B , which is solved approximately as follows.

Approximating the transcendent equation Put $x = n\varphi_B$ and $x_0 = n\varphi_T$. Due to Eq. (18) with S_n being always positive as given in Eq. (14), x_0 is in the limited range $[-\pi/2, 0]$. Eq. (21) becomes :

$$\sin(x_0) (x - x_0) = \cos(x) - \cos(x_0). \quad (22)$$

This can be interpreted as the intersection of the curve $y(x) = \cos(x)$ with the line $y(x) = \sin(x_0) (x - x_0) + \cos(x_0)$. Fig. 9 shows said curve and said line, intersecting at points M (of abscissa x_0) and J (of abscissa x_J). The line is the tangent to the curve at point M. A first solution to Eq. (22) is $x = x_0$. What is wanted is the next solution, i.e. x_J .

Over the range of x_0 , Eq. (22) defines a transcendent implicit relation between x and x_0 . This

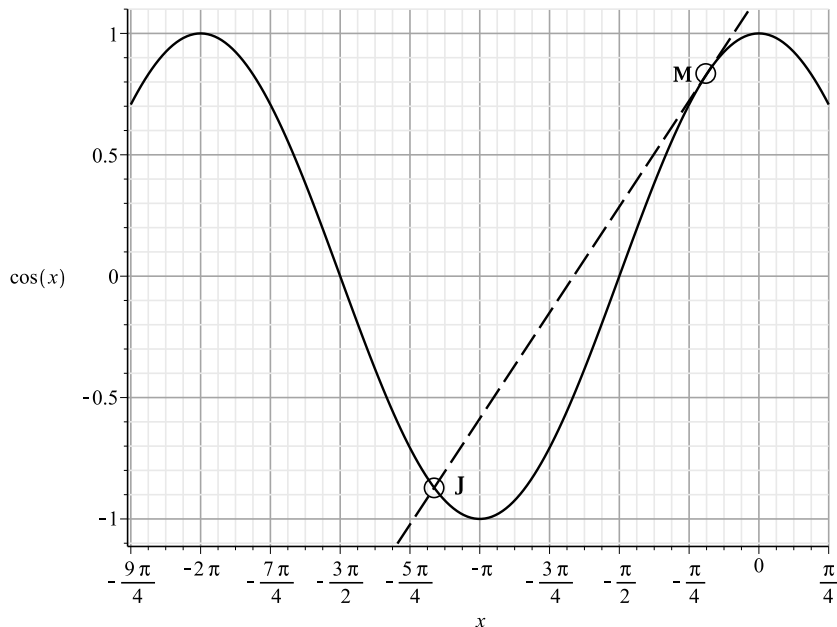


Figure 9: Tangent intersecting sinusoid. Example point M is at $x_0 = -3\pi/16$.

relation is numerically solved, and plotted in Fig. 10 as a solid line. Approximate this curve by using a curve giving x explicitly as a function of x_0 as follows:

$$x(x_0) = -\frac{\pi}{2} - 3 \arcsin \left(1 + \frac{2}{\pi} x_0 \right).$$

This explicit approximation is represented in Fig. 10 as a dotted line. It can be seen that the approximation is of good quality. The slopes of the exact and the approximated curves are identical at $x_0 = 0$. At $x_0 = -\pi/2$, a local calculus yields a slope of -2 for the exact implicit curve, while a direct derivative calculus gives $-6/\pi$ for the approximating curve. The overall maximum absolute error in x amounts to 0.05 over an x -range of $3\pi/2$, around $x_0 = -3\pi/16$. Getting back to the initial problem, where one had put $x = n\varphi_B$ and $x_0 = n\varphi_T$, one gets:

$$\varphi_B \approx -\frac{1}{n} \left(\frac{\pi}{2} + 3 \arcsin \left(1 + \frac{2n}{\pi} \varphi_T \right) \right).$$

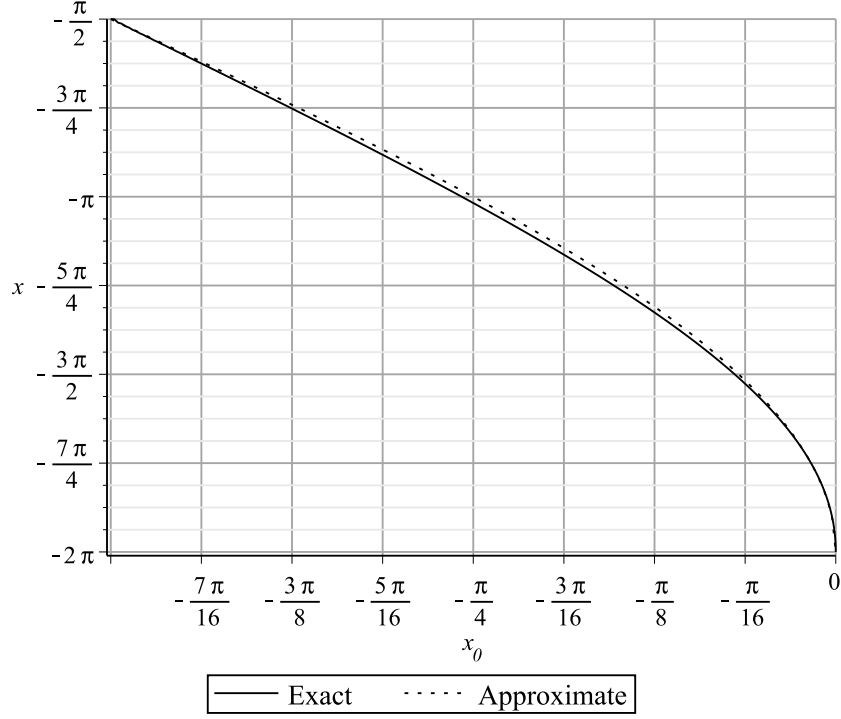


Figure 10: Transcendent equation (22), exact and approximate solutions.

It can be mentioned that if $n\varphi_T = -\frac{\pi}{2}$, then $n\varphi_B = -\frac{\pi}{2}$. In this case, both solutions φ_B and φ_T are identical, and the ovoid is reduced to a single point.

Now that the expression giving φ_B is known, the angular diameter D_{ang} of the ovoid is expressed as an angular value in radian unit:

$$D_{ang} = TB = \varphi_T - \varphi_B \approx \frac{\pi}{2n} + \varphi_T + \frac{3}{n} \arcsin \left(1 + \frac{2n}{\pi} \varphi_T \right), \quad (23)$$

with (assuming that $a_S \approx a_n$)

$$\varphi_T = -\frac{1}{n} \arcsin \left(\frac{4\beta\rho_n a_T}{A S(a_T)} \right) \approx -\frac{1}{n} \arcsin \left(\frac{4\beta\rho_n a_n}{A S(a_n)} \right). \quad (24)$$

A critical parameter Introduce two new parameters r and b_{crit} , with

$$r = \frac{4\beta\rho_n a_n}{A S(a_n)} \quad (25)$$

$$b_{crit} = \frac{S(a_n)}{4\rho_n a_n} \quad (26)$$

Hence $r = \frac{\beta}{b_{crit}}$, and Eq. (24) gives $\varphi_T = -\frac{1}{n} \arcsin(r)$, while Eq. (23) becomes

$$D_{ang} \approx \frac{1}{n} \left(\frac{\pi}{2} - \arcsin(r) + 3 \arcsin \left(1 - \frac{2}{\pi} \arcsin(r) \right) \right), \quad (27)$$

For a given n , b_{crit} represents a critical value for β/A : when $\beta/A > b_{crit}$, i.e. $r > 1$, the angular diameter vanishes, and there is no ovoid, which means that the argumental phenomenon cannot exist. The r parameter is used hereafter as abscissa in some capture probability plots.

Depending on the form of function $S(a)$, i.e. depending on the Fourier decomposition of the function $H(asin(\theta))$ with respect to variable θ , there is a value n_1 of n for which b_{crit} is maximum. If the argumental phenomenon is to be avoided for any value of n , this maximum value indicates the minimum value which β/A is to satisfy. Conversely, if the phenomenon is desired, one should arrange the initial condition so as to maximize the attractor's capture probability in the annulus of rank n_1 . It will be showed hereafter that this can be done by making $a_0 = a_n$, i.e. by having the initial amplitude equal to the expected amplitude of the stable steady-state.

3.5 Radial diameter of the ovoid.

In this section, the radial diameter of the ovoid will be discussed. Knowing the angular diameter, one will be able to assess the ovoid's area for a given value of n , and then the capture probability with various initial conditions.

Radial positions of points L and R To calculate the radial diameter of the ovoid, write the equation giving a_L and a_R . This will lead to a second-degree equation in a , whose solutions are a_L and a_R . The difference of the roots of said equation is the radial diameter $D_{rad} = a_R - a_L$. Assuming that the angular position of points L, S, and R are identical, i.e. $\varphi_L = \varphi_S = \varphi_R$, and that, over the ovoid region, $S(a)$ and $D(a)$ are constants respectively denoted S and D, write that points T, L and R belong to the same integral curve, as given by Eq. (15):

$$\beta(\varphi - \varphi_T) - \frac{AS}{4n\rho_n} \left(\frac{\cos(n\varphi)}{a} - \frac{\cos(n\varphi_T)}{a_T} \right) + \frac{3}{8} \frac{\mu}{\rho_n} \left(\frac{a^2}{2} - \frac{a_T^2}{2} - a_n^2 (\ln(a) - \ln(a_T)) \right) = 0. \quad (28)$$

with (a, φ) being the unknown polar coordinates of points L and R.

Besides, due to system (16), it holds $\cos(n\varphi_S) \approx -\cos(n\varphi_T) = -\frac{a}{AD} \frac{3\mu(a_T^2 - a_n^2)}{2}$.

From Eq. (17), one has $\sin(n\varphi_T) \approx -\frac{4\rho_n\beta a_n}{AS(a_n)}$. Consequently, the coefficient $\frac{AS}{4n\rho_n}$ from Eq. (28)

is approximated by $-\frac{1}{n} \frac{\beta a_n}{\sin(n\varphi_T)}$, and one can write, putting $\eta = \frac{\beta}{n} \cot(n\varphi_T)$ and $\zeta = \frac{3}{8} \frac{\mu}{\rho_n} a_n^2$:

$$\beta(\varphi_S - \varphi_T) - a_n \eta \left(\frac{1}{a_n} + \frac{1}{a_T} \right) + \frac{\zeta}{a_n^2} \left(\frac{a^2}{2} - \frac{a_T^2}{2} - a_n^2 (\ln(a) - \ln(a_T)) \right) = 0. \quad (29)$$

In this equation, only a remains as an unknown. This equation will be studied in the neighbourhood of a_n , and solutions will be searched in a to the equation $y(a) = 0$, denoting by $y(a)$ the left member of Eq. (29).

Putting $a = a_n(1 + \epsilon)$, make a second-order Taylor development of $y(a)$ in the neighbourhood of

a_n . One has: $y(a) \approx y(a_n) + \epsilon a_n y'(a_n) + \frac{(\epsilon a_n)^2}{2} y''(a_n)$. Replacing η and ζ by their definition expressions and ordering with respect to ϵ , one gets:

$$(\zeta + \eta)\epsilon^2 - \eta\epsilon + \beta(\varphi_S - \varphi_T) + 2\eta = 0.$$

The discriminant is $\Delta = \eta^2 - 4(\zeta + \eta)(\beta(\varphi_S - \varphi_T) + 2\eta)$. Let ϵ_L and ϵ_R denote the roots of this second-degree equation. One has, a_R and a_L denoting the values of a at points R and L: $D_{rad} = a_R - a_L = a_n(1 + \epsilon_R) - a_n(1 + \epsilon_L) = a_n(\epsilon_R - \epsilon_L) = a_n \frac{\sqrt{\Delta}}{|\zeta + \eta|}$. Knowing that $\varphi_T - \varphi_S = \frac{\pi}{n} + 2\varphi_T$, one finally gets the expression of the radial diameter D_{rad} :

$$D_{rad} = a_n \frac{\sqrt{\eta^2 + 4(\zeta + \eta) \left(\beta \left(\frac{\pi}{n} + 2\varphi_T \right) + 2\eta \right)}}{|\zeta + \eta|}, \quad (30)$$

with $\varphi_T \approx -\frac{1}{n} \arcsin\left(\frac{4\beta\rho_n a_n}{AS(a_n)}\right)$, $\eta = \frac{\beta}{n} \cot(n\varphi_T)$ and $\zeta = \frac{3}{8} \frac{\mu}{\rho_n} a_n^2$.

3.6 Area of the ovoid.

Knowing the angular and radial diameters of the ellipse which approximates the ovoid, calculate the ovoid's area in Cartesian Van der Pol representation:

$$S = \frac{\pi}{4} D_{ang} D_{rad} \quad (31)$$

where D_{ang} is in radian unit and D_{rad} is in the same unit as the oscillator's amplitude. This area is to be seen as an integral against $d\varphi da$. This result holds as long as the ovoid's radial diameter is less than the annulus' width. This is why one cannot have n grow indefinitely in these formulae.

4 Attractor's capture probabilities.

In this section, various capture probabilities by an attractor will be studied in the Cartesian Van der Pol representation, depending on the initial condition, which will be determined by the initial radius, which corresponds to the energy, regardless of the phase φ . So the initial condition with a given energy will be represented in the polar representation by a circle centred at the coordinates origin, which may go through the points representing the stable steady-state condition, while the initial condition within an energy range will be represented by an annulus, which may be tangent to the ovoids. Finally, the initial condition with a given maximum energy will be represented by a disk centred at the origin. The annulus tangent to the ovoids has the advantage of leading to a simple symbolic formula to express the capture probability. It is always assumed that when the capture has not been made inside an annulus, the probability for the system to be captured inside another annulus is negligible, which could be deduced by the assumption that the intersection of an ovoid's tail with the circle constituting the upper bound of the annulus is negligible as compared to the perimeter of said circle divided by n .

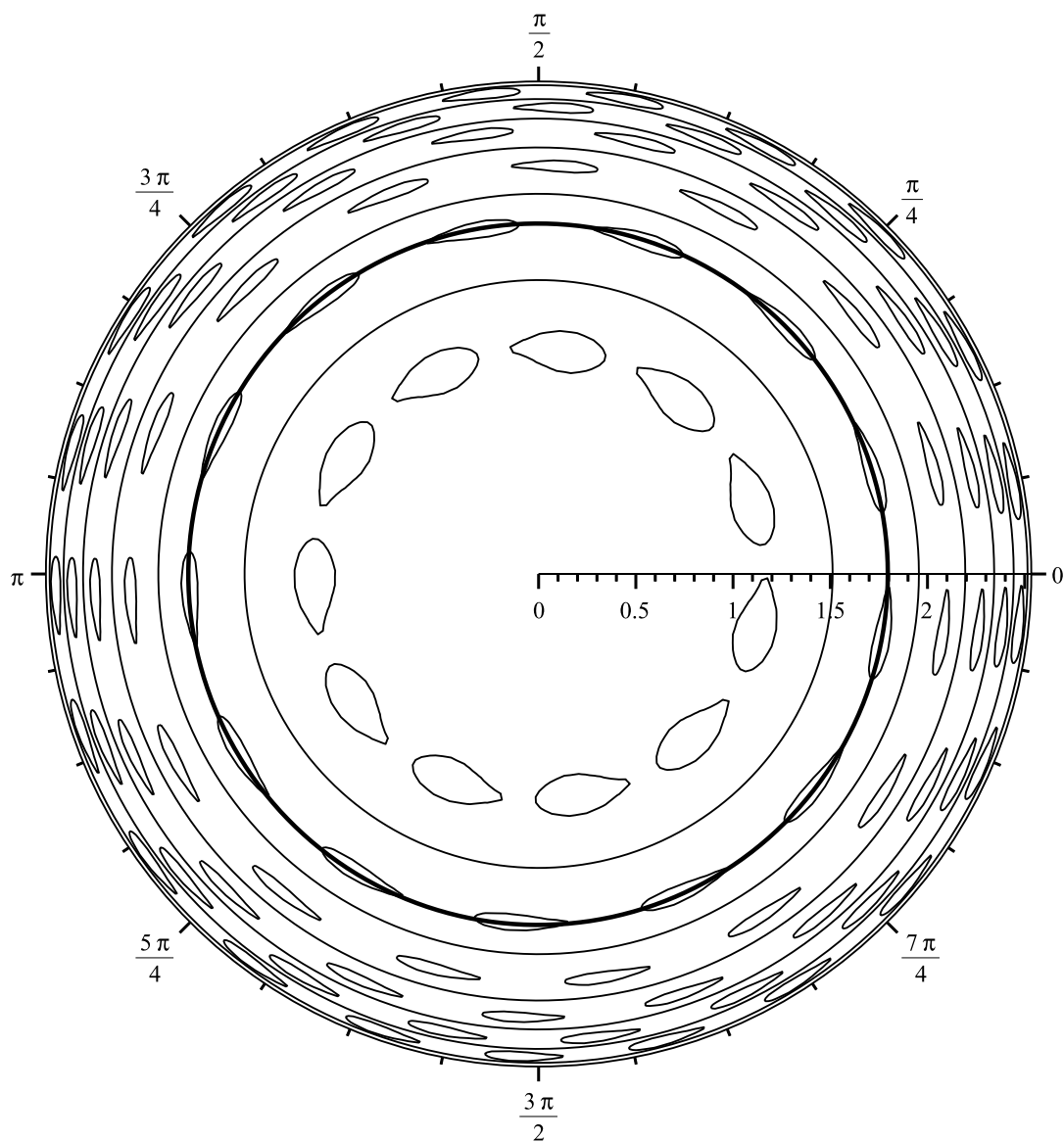


Figure 11: Initial condition on a circle going through the centres of the ovoids in annulus of rank 13 (in bold). The parameters are the same as in Fig. 7.

4.1 Capture probability with initial condition $a = a_n$.

Fig. 11 shows this kind of initial condition. To assess this probability, the angular diameter of the ovoid, that is the distance TB, will be calculated in the Cartesian Van der Pol representation, and the ratio of this distance to the distance between the centres of two contiguous ovoids will be formed.

It has been shown above, in paragraph 2.5, that the averaged system is invariant by a rotation of angle $\frac{2\pi}{n}$. That is, two ovoids having the same radius a_S have their centres S located $\frac{2\pi}{n}$ apart along the line $a = a_S$. Hence, to evaluate the probability for a given point of this line to be in the ovoid, operate in the Cartesian Van der Pol representation, and write that the capture probability P is the ratio of the angular diameter of the ovoid to the distance between the centres of two contiguous ovoids. Using Eq. (27), one gets, when $r < 1$:

$$P = \frac{D_{ang}}{\frac{2\pi}{n}} = \frac{1}{4} + \frac{1}{2\pi} \left(-\arcsin(r) + 3 \arcsin \left(1 - \frac{2}{\pi} \arcsin(r) \right) \right) \quad (32)$$

for initial condition ($a = a_n$, $\varphi = \text{random value}$).

And for $r > 1$, it holds $P = 0$.

Fig. 12 shows P against r . The value $r = 0$ corresponds to the case where the ovoids are in

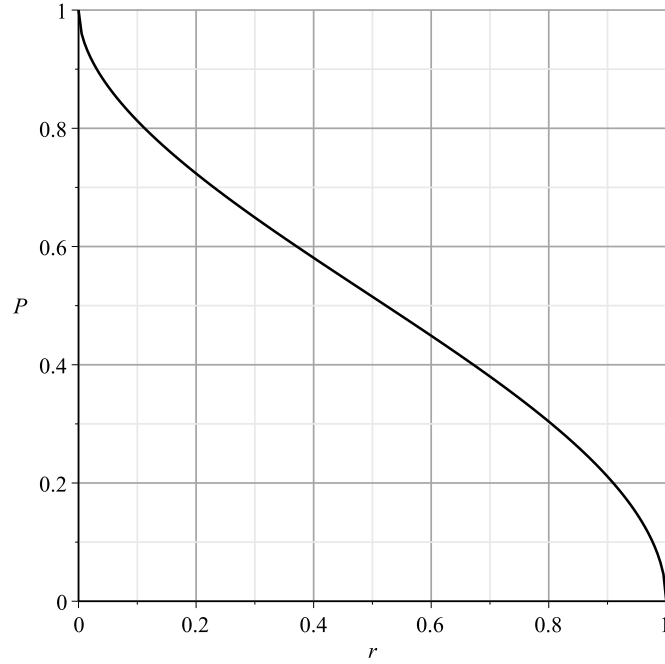


Figure 12: Capture probability P against parameter r , as per Eq. (32), with initial condition $a = a_n$.

contact with each other inside a given annulus.

4.2 Capture probability with initial condition on a circle concentric with the annuli.

In this section, the initial condition, in the polar Van der Pol representation, is on a circle concentric with the annuli; this circle may have any radius, and is not only a circle tangent to the ovoids or to the border of a given annulus. This kind of initial condition is represented in Fig. 13. The study

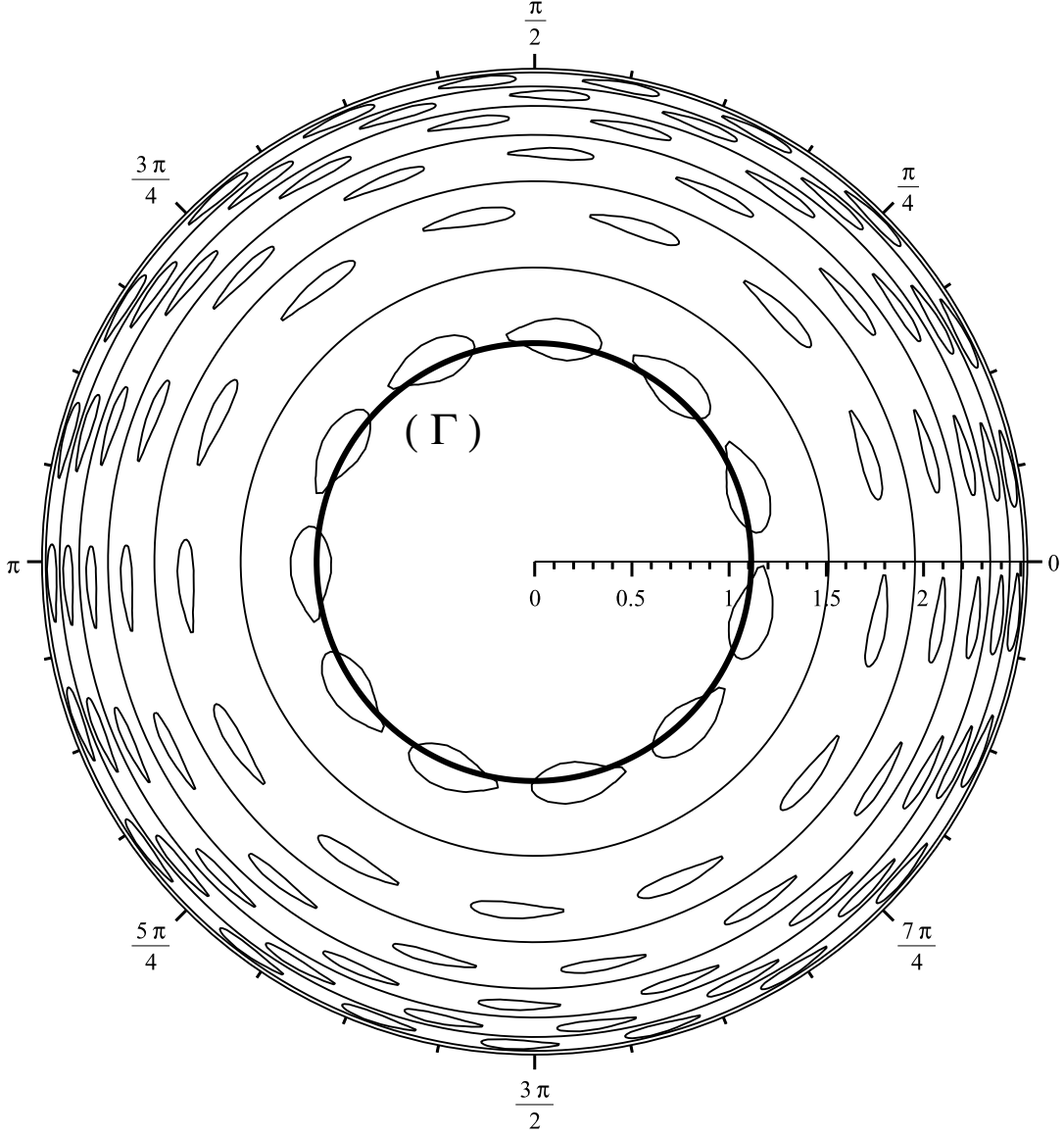


Figure 13: Initial condition on a circle (Γ) (in bold). The parameters are the same as in Fig. 7.

is carried out in the Cartesian Van der Pol representation, as shown in Fig. 14. Vertical lines (D_2) and (D_3) are the borders of the annulus of rank n , in which n ovoids are located, represented as ellipses arranged according to a periodic pattern. Denote by $a_{n-2,n}$ and $a_{n,n+2}$ the abscissae of lines (D_2) and (D_3) from the origin. The ellipses have a vertical diameter D_{ang} and an horizontal diameter D_{rad} . The distance between the centres of two contiguous ellipses is d . This is also the period of the pattern. It holds $d = \frac{2\pi}{n}$. Consider a variable vertical line (D_1) at abscissa x_0 as

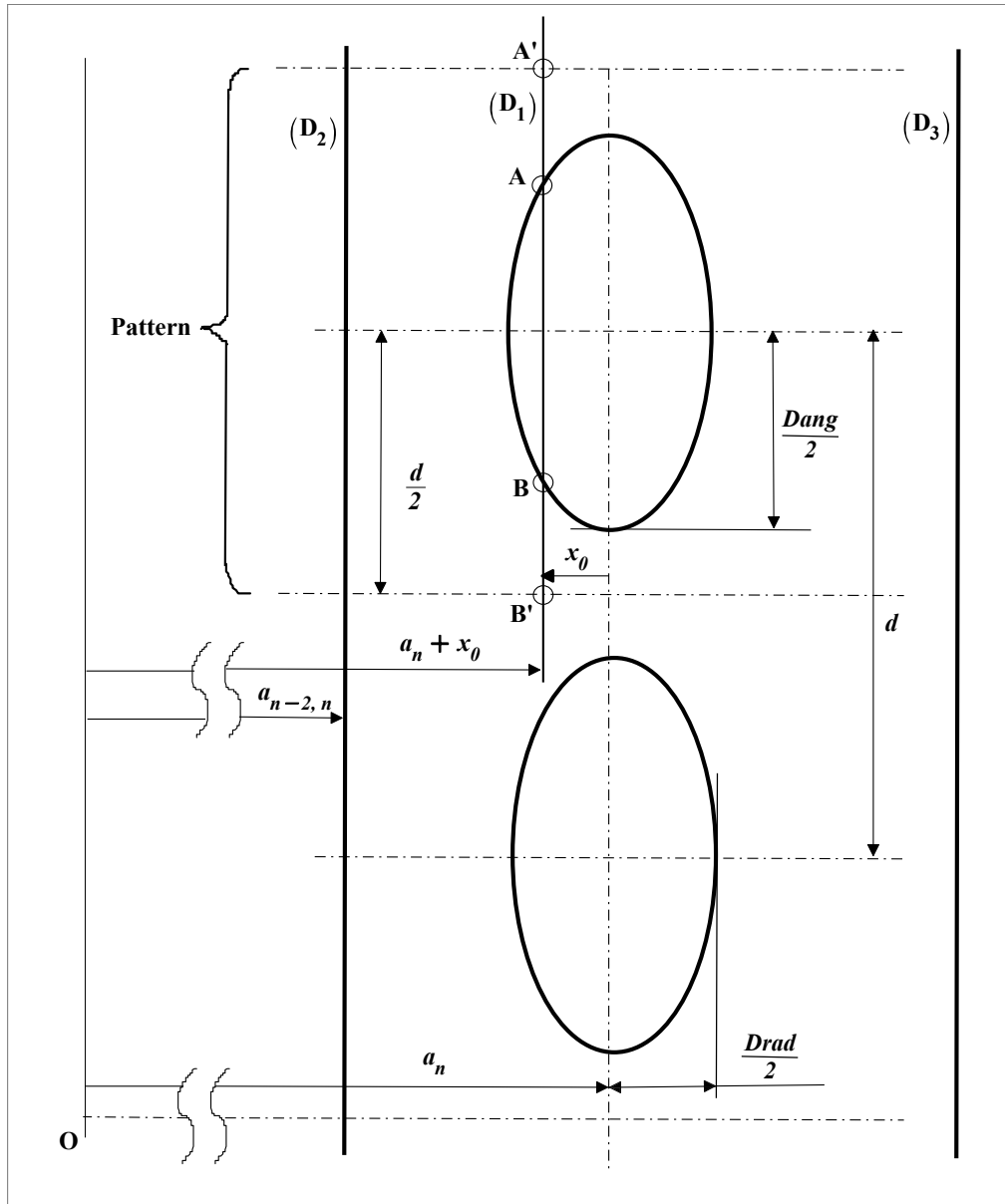


Figure 14: Ovoids approximated by ellipses.

counted from the vertical symmetry axis of the ellipses. This axis is located at abscissa a_n from the origin. The abscissa x of line D_1 from the origin is thus $x = a_n + x_0$. Line D_1 intersects the ellipse at points A and B , and the pattern's horizontal borders at points A' and B' .

Inside the annulus containing the ellipses, if line D_1 intersects the ellipse, i.e. if $a_n - D_{rad}/2 \leq x \leq a_n + D_{rad}/2$, the capture probability $P(x)$ with an initial condition on the circle of radius x is

assessed as the ratio $P(x) = \frac{AB}{A'B'} = \frac{D_{ang} \sqrt{1 - \frac{(x-a_n)^2}{\left(\frac{D_{rad}}{2}\right)^2}}}{d}$. Otherwise, said probability is considered approximately null. Fig. 15 shows $P(x)$ against x in an example using the H and E functions as given in Eqs. (2) and (3).

In the special case where $x = a_n$, one gets $P(x) = \frac{D_{ang}}{d} = \frac{D_{ang}}{\frac{2\pi}{n}}$. This case has been studied above.

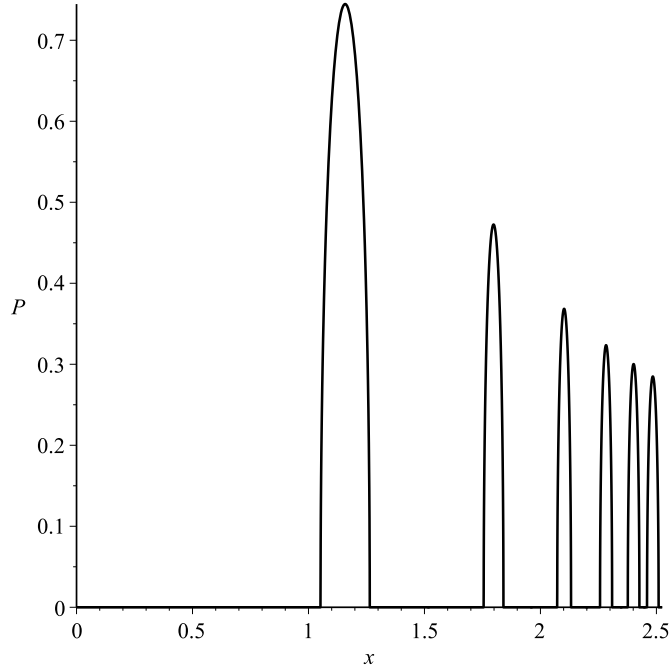


Figure 15: Capture probability P against x , with initial amplitude $a_0 = x$. The parameters are the same as in Fig. 7.

4.3 Capture probability with initial condition inside the annulus tangent to the ovoid.

This kind of initial condition is represented in Fig. 16. To assess this probability, the area of the ovoid will be calculated, and then the ratio of this area to the area of the rectangle delimited by the left and right tangents to the ovoid (at points L and R in Fig. 8), and by the centres (points S

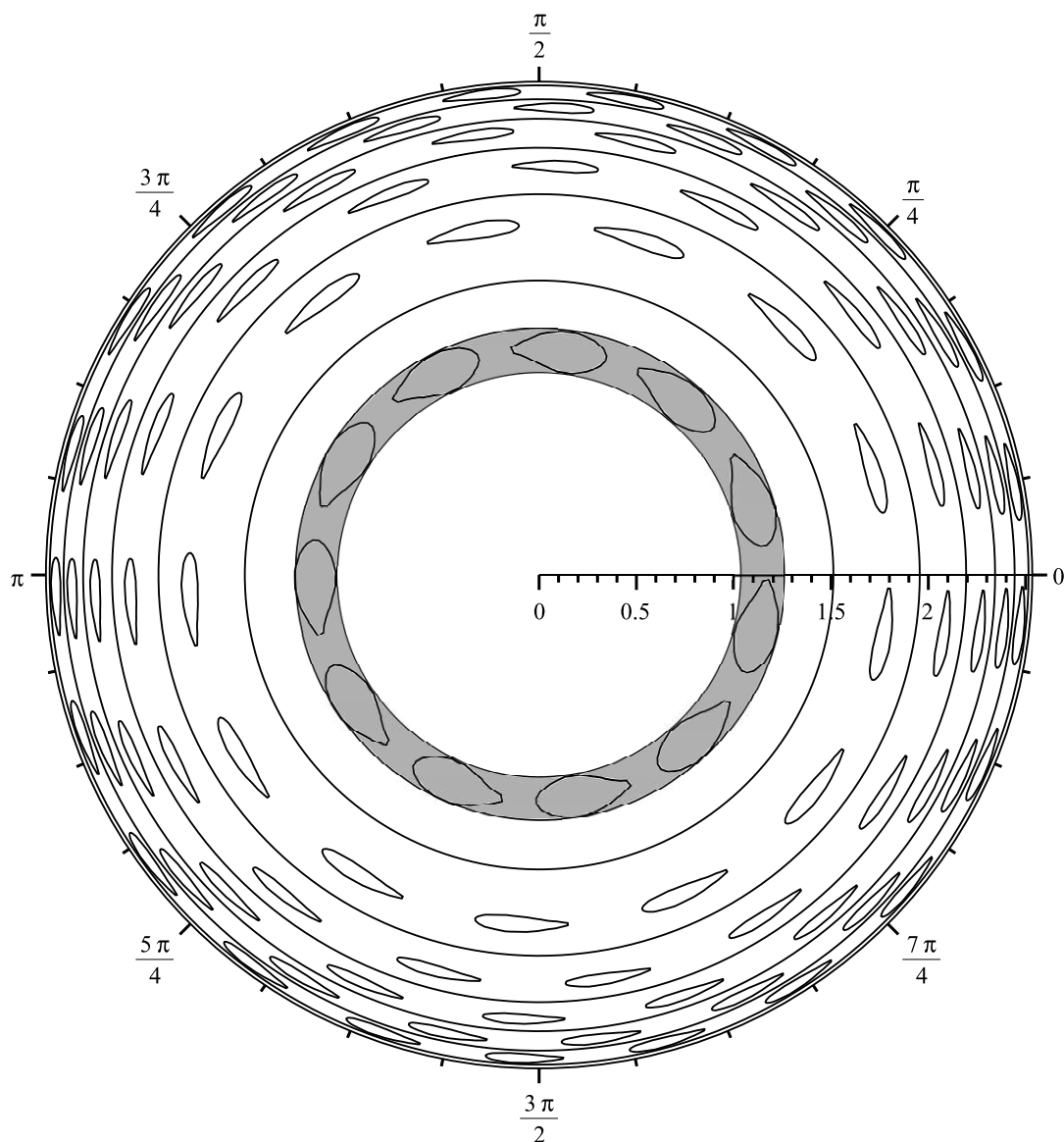


Figure 16: Initial condition inside annulus tangent to the ovoids of annulus of rank 11 (in grey). The parameters are the same as in Fig. 7.

in said figure) of two contiguous ovoids. With the same notations as in Paragraph 4.2 and Fig. 14, the area S_{rect} of said rectangle is $S_{rect} = \frac{2\pi}{n} D_{rad}$.

To calculate the area of the ovoid, approximate it by an ellipse having axes TB and LR as shown in Fig. 8. One has $TB = Dang = \varphi_T - \varphi_B$ and $LR = D_{rad} = a_R - a_L$. The ovoid area is

$$S_{ov} = \frac{\pi}{4} D_{ang} D_{rad}.$$

Hence the capture probability with initial condition inside the annulus tangent to the ovoids of rank- n annulus is

$$P = \frac{S_{ov}}{S_{rect}} = \frac{\pi \frac{D_{ang}}{2} \frac{D_{rad}}{2}}{\frac{2\pi}{n} D_{rad}} = \frac{n D_{ang}}{8}. \quad (33)$$

It can be seen that this expression does not depend on D_{rad} . This is because the ovoid has been approximated by an ellipse, and the annulus tangent to the ovoid has been taken as a delimiting area for the initial condition.

It can be seen that, as the maximal possible value for D_{ang} is $\frac{2\pi}{n}$, in which case two contiguous ovoids are in contact, the maximal possible value for P is $\frac{n}{8} \frac{2\pi}{n} = \frac{\pi}{4}$, independent of n .

Using the same parameter r than for the discussion of the probability with initial condition $a = a_n$, it holds:

$$P = \frac{1}{8} \left(\frac{\pi}{2} - \arcsin(r) + 3 \arcsin \left(1 - \frac{2}{\pi} \arcsin(r) \right) \right),$$

with $r = \frac{\beta}{b_{crit}}$.

It can be noted that, as P does not depend on D_{rad} , its symbolic expression is simple. Fig. 17

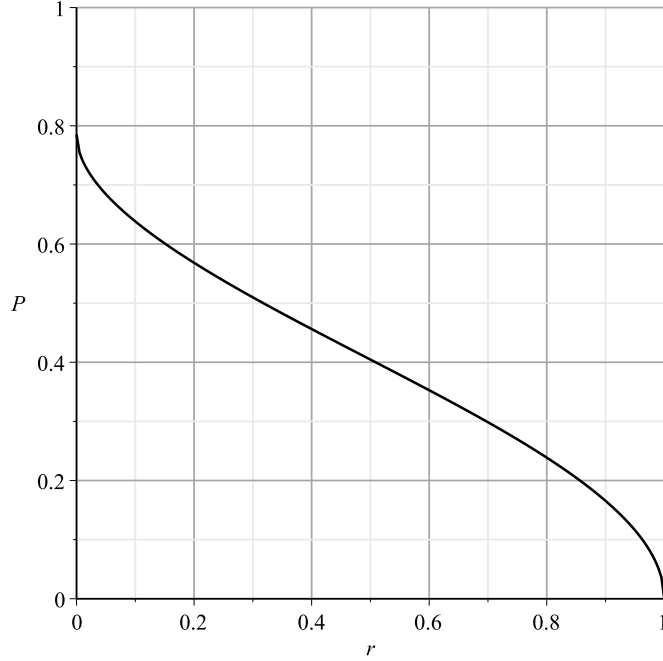


Figure 17: Capture probability P against ratio r with initial amplitude inside the annulus tangent to the ovoids.

shows P against r .

4.4 Capture probability with initial condition inside the whole annulus of rank n .

This kind of initial condition is represented in Fig. 18. Denote $a_{n-2,n}$ and $a_{n,n+2}$ the values of a

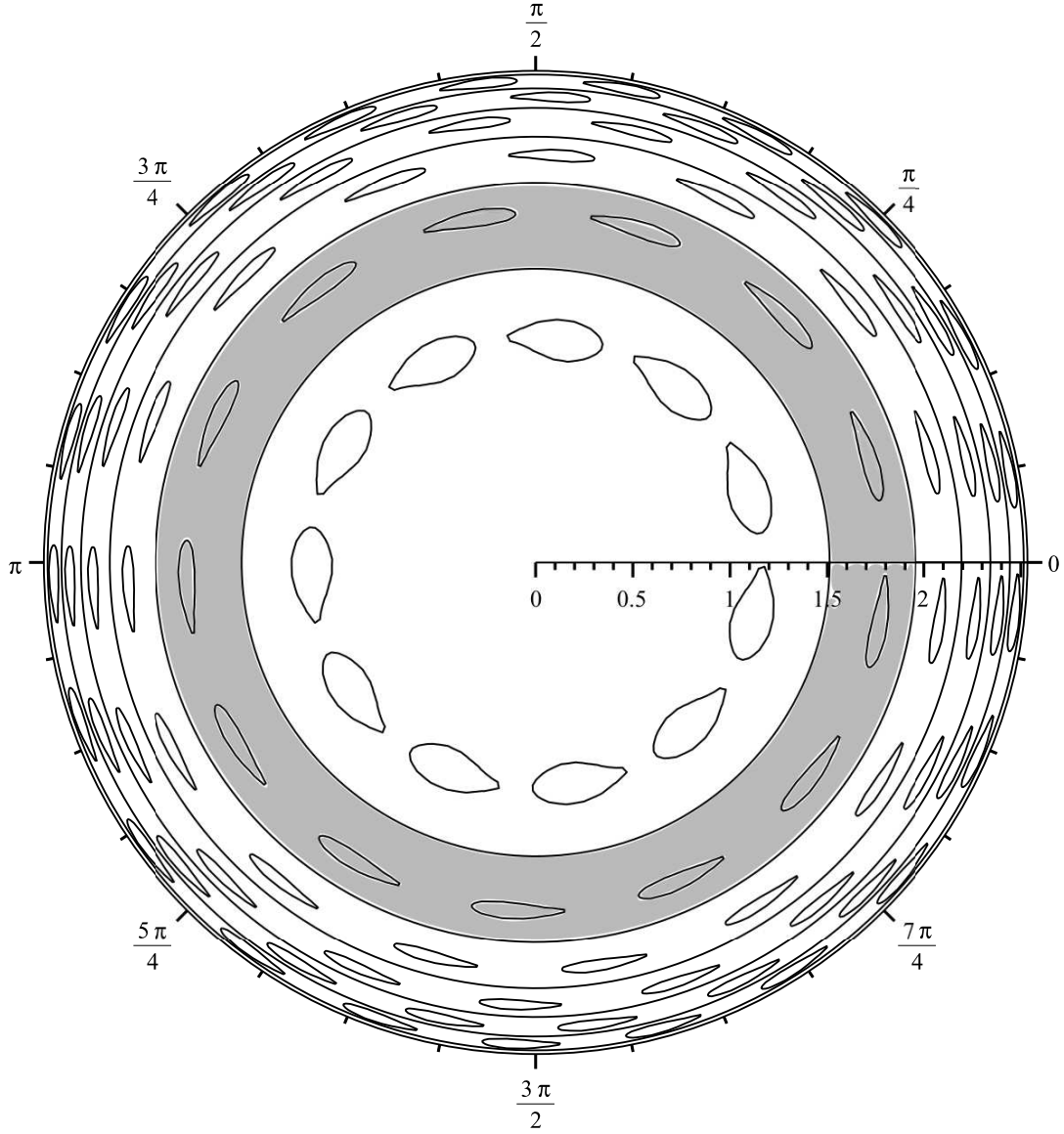


Figure 18: Initial condition inside annulus of rank 13 (in grey). The parameters are the same as in Fig. 7.

corresponding to the lower and upper bounds of said validity region. It has been shown [6] that

$$a_{n,n+2} = \sqrt{\frac{a_n^2 + a_{n+2}^2}{2} + \frac{8}{3\mu} \lambda^2 \beta^2 \left(\frac{D(\xi)}{S(\xi)} \right)^2} \quad (34)$$

where $\lambda = \nu/\omega_0$, a_n is defined as given in (9) as a function of ν , ω_0 and n , and $\xi = \frac{a_n + a_{n+2}}{2}$. Generally, the last term under the radix is negligible versus the first two ones. So it holds: $a_{n,n+2} \approx \sqrt{\frac{a_n^2 + a_{n+2}^2}{2}}$, and the total area of annulus of rank n is

$$2\pi(a_{n,n+2} - a_{n-2,n}) \approx 2\pi \left(\sqrt{\frac{a_n^2 + a_{n+2}^2}{2}} - \sqrt{\frac{a_{n-2}^2 + a_n^2}{2}} \right) \approx \pi(a_{n+2} - a_{n-2})$$

The total area of the n ovoids belonging to that annulus is $nS_{ov} = n\frac{\pi}{4}D_{ang}D_{rad}$. Hence, neglecting, inside the annulus, the area of the ovoids' tails, the capture probability with initial condition in said annulus is $P = \frac{n}{4} \frac{D_{ang}D_{rad}}{a_{n+2} - a_{n-2}}$. Replacing a_{n-2} and a_{n+2} by their developed expressions as given in Eq. (9), one gets:

$$P = \sqrt{-3\mu} \frac{n(n^2 - 4)\sqrt{n^2 - \lambda^2}}{32\lambda^2} D_{ang}D_{rad}, \quad (35)$$

with λ as given in Eq. (8), D_{ang} given by Eq. (23), and D_{rad} given by Eq. (30). Fig. 19 shows probability P against r for the rank-13 annulus of the example.

If n is the minimum possible value n_{min} as defined by Eqs. (10), the system state is in the central disk, and, putting $a_{n-2,n} = 0$, the area of the central annulus writes: $2\pi a_{n,n+2} \approx 2\pi \sqrt{\frac{a_n^2 + a_{n+2}^2}{2}}$.

The formula is then:

$$P = \frac{\sqrt{-3\mu}}{16} \frac{n^2}{\sqrt{n^2 - \lambda^2 \frac{(n+1)^2 + 1}{(n+2)^2}}} D_{ang}D_{rad} \quad (36)$$

4.5 Capture probability with initial condition inside a circle concentric to the annuli.

This kind of initial condition is represented in Fig. 20. In this section, the initial condition is anywhere on a disk centred at the origin. The disk border is anywhere among the ovoids, and can intersect a series of ovoids. To assess the capture probability, first calculate the total area S_1 of the part of the ovoids inside the disk; then, divide this result by the disk area S_2 . Here, it is supposed that the capture probability is negligible when the initial condition is outside any ovoid, i.e. it is supposed that the ovoids' tail area is negligible.

Consider that an integral curve ending up near the origin in the forced-oscillation regime contributes for zero to the capture probability by an attractor of the argumental regimes. Hence, the first annulus from the origin can be considered with its lower border extended down to $x=0$, when one

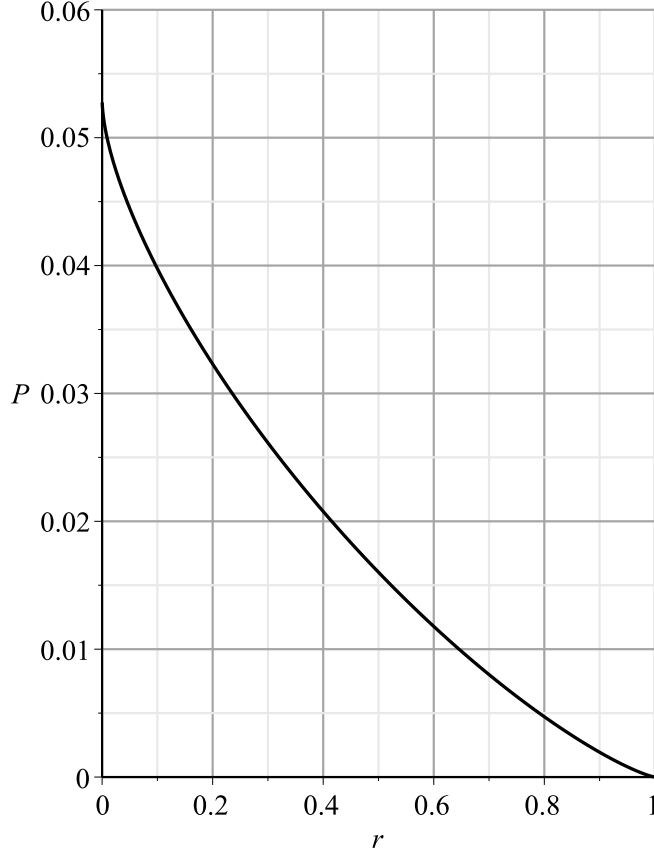


Figure 19: Capture probability as per Eq. (35), with initial condition inside whole rank-13 annulus. The parameters are the same as in Fig. 7.

restricts the scope of interest to the argumental phenomenon. So, if n_{min} is the lowest value for n , put $a_{n_{min}-2, n_{min}} = 0$. Based on Fig. 14, a classical geometry calculus gives the area $S_1(n)$ in annulus n , if $a_n - D_{rad}/2 \leq x \leq a_n + D_{rad}/2$:

$$S_n(x) = \frac{n}{4} D_{rad}(n) D_{ang}(n) \left(\pi - \arccos \left(2 \frac{x - a_n}{D_{rad}(n)} \right) \right) + 2 \frac{x - a_n}{D_{rad}(n)} \sqrt{1 - 4 \frac{(x - a_n)^2}{D_{rad}^2(n)}} \quad (37)$$

Then, calculating the sum of the areas $S(n_k)$ for all annuli of rank n_k comprised entirely or partially in the disk of the initial condition, a plot can be drawn of the capture probability $P(x)$ with initial condition on a disk of radius x , as shown in Fig. 21.

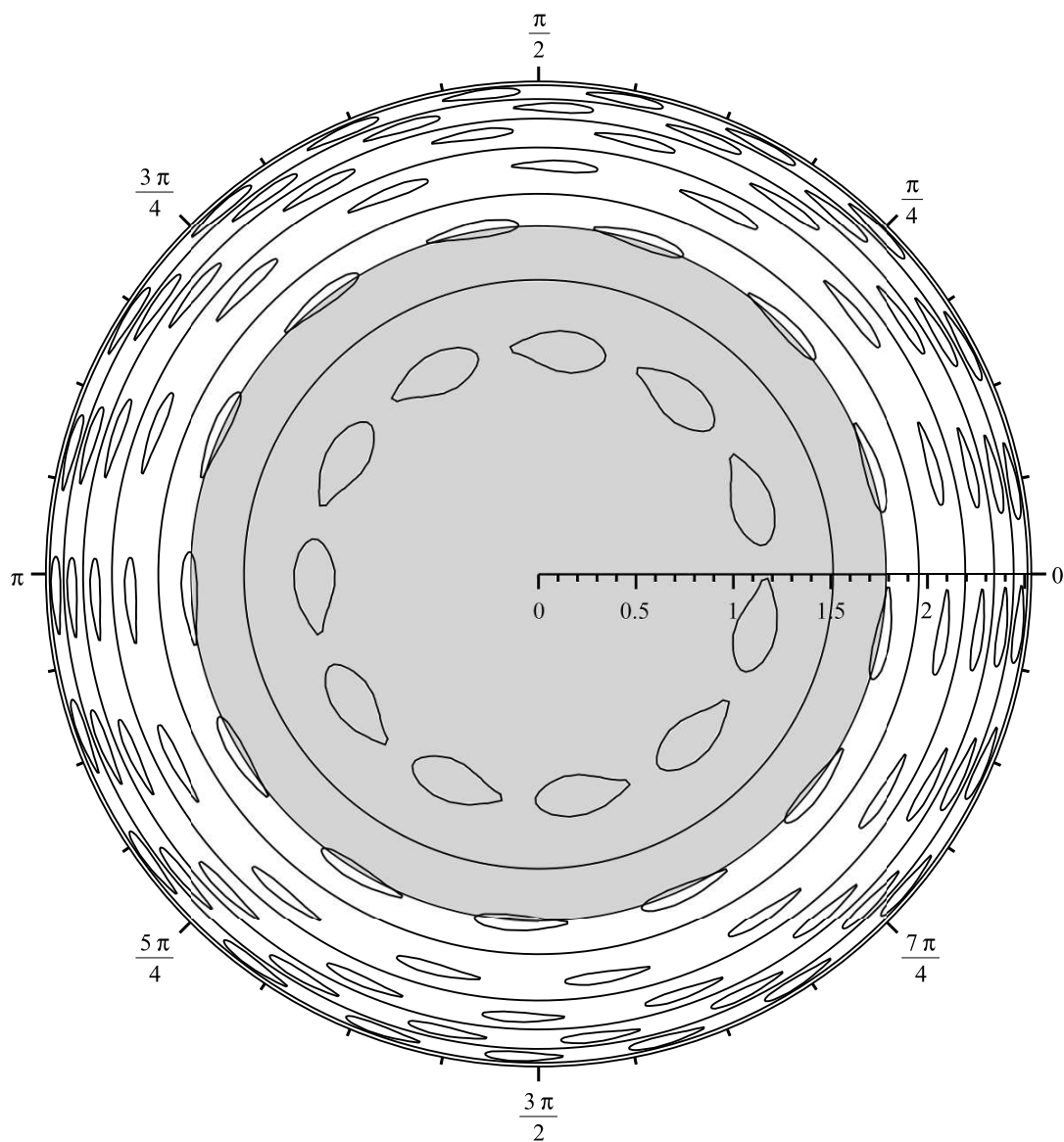


Figure 20: Initial condition on a disk (in grey) covering part of annulus of rank 13 and the entirety of annulus of rank 11. The parameters are the same as in Fig. 7.

5 Conclusion

An approximate analytic implicit equation of the integral curves has been used to assess the shape and area of the attractor's upstream basin in an example 1-DOF argumental Duffing oscillator. Capture probabilities have been evaluated for various initial conditions. It has been shown that

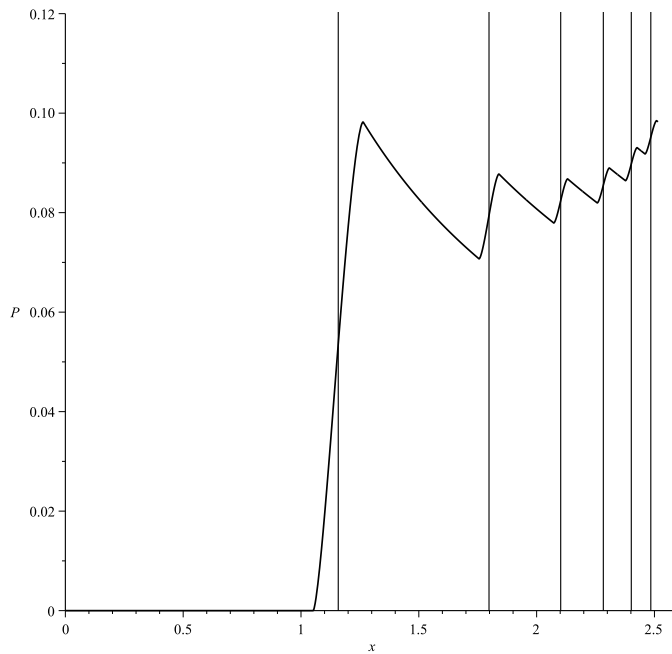


Figure 21: Capture probability P against x , with initial amplitude a_0 in a disk of radius x . The vertical lines are at abscissae a_n (centres of the ovoids in the successive annuli). The parameters are the same as in Fig. 7.

the expression $\frac{\beta}{A}$ plays an important role to assess the capture probability. This expression is the ratio of the damping ratio to the harmonic excitation's amplitude. When this expression is above a critical value, the argumental phenomenon cannot exist.

In this paper, the tail's area has been neglected to assess the area of the whole upstream basin of the attractor in the Van der Pol diagrams. In some cases, in particular when n , β or γ is small, the tail may have an area which cannot be neglected. Calculus is currently being developed to assess the tail's area.

An interesting question to investigate is about systems with more than one minimum in the A -function, and therefore with more complicated implicit solutions and ovoid figures. These systems are important, because in them, the capture phenomenon can be initiated at surprisingly low amplitudes, and evolve into high-amplitude oscillations, taking advantage of the energy provided by the external harmonic excitation source. This kind of argumental oscillations is of interest to further delimit the hazardous parameter domains in mechanical engineering.

The symbolic quantification of the capture probability can help in assessing the risk of occurrence of the argumental phenomenon when it is to be avoided, for instance in mechanical engineering, when designing a structure. Usually, designers will want to avoid harmonic excitation sources

whose frequency is close to the first modal frequency of any part of the structure. This paper shows that, if suitable conditions are met, steady-state condition probability can be symbolically assessed when the excitation frequency is far from modal resonance frequencies, provided there is an integer ratio between the excitation frequency and the structure modal frequencies, and there exists a space-modulating function governing the energy transfer from the excitation source to the structure. In a future work, it will be shown that this kind of space-modulating function can arise due to damaged links in the structure, for instance if a link at one end of a clamped-clamped beam becomes intermittent, and thus dependent on the beam's transverse deformation.

References

References

- [1] Béthenod M. Sur l'entretien du mouvement d'un pendule au moyen d'un courant alternatif de fréquence élevée par rapport à sa fréquence propre. Comptes rendus hebdomadaires de l'Académie des sciences 1938;207(19):847–9. Available from: <http://gallica.bnf.fr/ark:/12148/bpt6k31590>;[accessed 21.11.16]. French.
- [2] Penner DI, Doubochinski DB, Kozakov MI, Vermel AS, Galkin YV. Asynchronous excitation of undamped oscillations. Sov. Phys.-Usp. 1973;16(1):158–60. Available from: doi:10.1070/PU1973v016n01ABEH005156;[accessed 21.11.16].
- [3] Bogolioubov N, Mitropolski I. Les méthodes asymptotiques en théorie des oscillations non linéaires. Gauthiers-Villars, 1962. French.
- [4] Doubochinski D, Doubochinski J. Amorçage argumentaire d'oscillations entretenues avec une série discrète d'amplitudes stables. E.D.F. Bulletin de la direction des études et recherches, série C mathématiques, informatique 1991;3:11–20. French.
- [5] Cintra D, Argoul P. Nonlinear argumental oscillators: A few examples of modulation via spatial position. J Vib Control 2016. Available from: doi:10.1177/1077546315623888;[accessed 21.11.16].
- [6] Cintra D, Argoul P. Nonlinear argumental oscillators: Stability criterion and approximate implicit analytic solution. Epub 2016. Available from arXiv:1606.08993;[accessed 21.11.16].
- [7] Treilhou J, Coutelier J, Thocaven J, Jacquez C. Payload motions detected by balloon-borne fluxgate-type magnetometers. Adv Space Res 2000;26(9):1423–6.
- [8] Cretin B, Vernier D. Quantized amplitudes in a nonlinear resonant electrical circuit. In 2009 Joint Meeting of the European Frequency and Time Forum and the IEEE International Frequency Control Symposium, vols 1 and 2, volume 1 & 2, pages 797–800, Besançon, France, 2009. Joint Meeting of the 23rd European Frequency and Time Forum/IEEE International Frequency Control Symposium. Available from: arXiv:0801.1301;[accessed 21.11.16].
- [9] Abobda L, Wofo P. Subharmonic and bursting oscillations of a ferromagnetic mass fixed on a spring and subjected to an AC electromagnet. Commun Nonlinear SCI 2012;17(7):3082 – 91. Available from: doi:10.1016/j.cnsns.2011.10.037;[accessed 21.11.16].

- [10] Wright JA, Deane JH, Bartuccelli M, Gentile G. Basins of attraction in forced systems with time-varying dissipation. *Commun Nonlinear SCI* 2015;29(13):72 – 87. Available from: doi:10.1016/j.cnsns.2015.04.021;[accessed 21.11.16].

Modeling and numerical results for the argumental transverse vibration of a beam excited through permanent or intermittent elastic contact by a harmonic axial motion

Daniel Cintra · Gwendal Cumunel · Pierre Argoul

Received: date / Accepted: date

Abstract The argumental transverse vibration of a beam excited axially by an harmonic motion transmitted through intermittent or permanent elastic contact is studied. It is shown that this vibration is governed by a nonlinear argumental equation, namely that a vibration in the fundamental transverse mode of the beam can occur when the frequency of the excitation is many times the frequency of the fundamental transverse mode. Two cases are considered : the hinged-(hinged-guided) case and the clamped-(clamped-guided) case. A “natural” model is given and an approached smooth model is derived. The averaging method yields a standard system of differential equations for the smooth model. The stationary condition is represented and studied in the (excitation amplitude, oscillator amplitude)-plane. Stability is studied under symbolic form, and a simple criterion, applicable in said plane, is brought out. With the help of the Van der Pol representation, numeric simulations allow a comparison between the natural model and the smooth model, leading to clues about the natural model obtained from symbolic relations obtained from the smoothed model.

Keywords nonlinear dynamics; argumental oscillator; beam transverse vibration; axial excitation; spatial modulation; Van der Pol representation.

Keywords argumental oscillator · beam · axial excitation · transverse vibration · spatial modulation · Van der Pol representation.

Daniel Cintra (corresponding author), Gwendal Cumunel
Université Paris-Est,
Laboratoire Navier (UMR 8205), CNRS, ENPC, IFSTTAR,
6 et 8, avenue Blaise Pascal,
Cité Descartes, Champs-sur-Marne,
F-77455 Marne La Vallée Cedex 2, France.
email: daniel.cintra@enpc.fr, gwendal.cumunel@enpc.fr
Tel.: +33 1 64 15 37 08

Pierre Argoul
IFSTTAR, Laboratoire MAST-SDOA,
F-77455 Marne La Vallée, Cedex 2, France
email: pierre.argoul@ifsttar.fr

Contents

1	Introduction.	3	12.1	Case $n = 4$	19
2	System configuration.	3	12.2	Case $n = 6$	20
3	Modeling	3	12.3	Discussion.	21
3.1	Expression of the abscissa of the right-hand end of the beam.	4	13	Conclusion.	22
	Hinged-(hinged-guided) case.	4	14	Appendix A: Approximation to a truncated parabola.	23
	Clamped-(clamped-guided) case.	4		Single-parabola case.	23
	Conclusion about both cases.	4		Plateau case.	23
3.2	Natural model of the external force.	5		Composite-parabola case.	23
	Upper bound for a_A	5	15	Appendix B: a stability criterion.	25
	Case of permanent contact.	5		Horizontal tangent.	25
3.3	Smooth model of the external force.	5			
3.3.1	High line and Low line.	5			
3.3.2	Approximation to the amplitude of function y_{approx}	6			
	Case $a_A > a_{Acrit}$	6			
	Case $a_A \leq a_{Acrit}$	7			
	Conclusion for the expression of \hat{y}_{approx}	7			
3.3.3	Approximation to the mean value of function y_{approx}	7			
	Case $a_A > a_{Acrit}$	7			
	Case $a_A < a_{Acrit}$	8			
	Conclusion for the expression of \bar{y}_{approx}	8			
	Approximation to the F function.	8			
4	Second-order differential equation of motion.	8			
4.1	Classical transverse motion of an axially-excited beam.	8			
4.2	Projection onto the first mode.	9			
4.3	Equation of motion with the natural model.	9			
4.4	Equation of motion with the smooth model.	9			
5	Averaging method on the smooth model of the dynamical system.	10			
5.1	Reduced time.	10			
5.2	Standard system.	10			
5.3	Averaged system.	11			
	Averaged expression relative to function G	11			
	Decomposing function $H(a \sin(\theta))$ into a Fourier series of variable θ	11			
	Calculus of $H(a \sin(\theta))E(\tau) \cos(\theta)$	11			
	Calculus of $H(a \sin(\theta))E(\tau) \sin(\theta)$	11			
	Symbolic expressions of functions S_n and D_n	11			
	Parameters ω_{00} and ρ_{00}	11			
	Averaged standard system.	12			
6	Stationary condition.	12			
	β -curve, G-curve and stationary-solutions curve.	12			
	Excitation threshold.	12			
	Graphic representation of the stationary solutions in the (a_S, a_A) -plane.	12			
7	Stability.	13			
7.1	Case $a_A < a_{Acrit}$	13			
7.2	Case $a_A > a_{Acrit}$	14			
8	Frequency response.	15			
9	Comparison of two resolution methods for the smooth model of the external force.	16			
9.1	Smooth model of the external force and averaging method.	16			
9.2	Smooth model of the external force and original second-order equation.	17			
9.3	Conclusion.	17			
10	Natural model of the external force.	17			
	Construction of the Van der Pol plots.	17			
	Construction of the stable and unstable stationary-regime representative points.	17			
11	Other cases with the smooth model.	17			
11.1	A case where $n = 14$	17			
11.2	Cases with permanent contact.	18			
12	Model comparison.	19			

1 Introduction.

The so-called argumental oscillator is a mechanical system which has a stable motion consisting of a periodic motion at a frequency next to its natural frequency when submitted to an external force whose frequency is close to a multiple of said natural frequency. One necessary condition for the phenomenon to arise is that the external force be dependent on the space coordinate of the oscillator. An oscillator exhibiting such characteristics has been described in 1928 [1]; this oscillator was a pendulum fitted with a steel sphere at the tip of the rod, submitted to a harmonic magnetic field spatially localized at the bottom of the sphere's course.

The word "argumental" was forged in 1973 [12], where a pendulum is submitted to an electric field spatially localized at the bottom of the pendulum's course.

Further developments were carried out [9, 10], particularly the "multiple resonance" and the "quantum effect". The multiple resonance is a phenomenon in which a number of oscillators, each having its own resonance frequency, submitted to a unique common excitation frequency, can oscillate simultaneously. This is possible if each oscillator has an actual frequency which is a sub-multiple of the excitation frequency, and if the interaction zone between each oscillator and the excitation source is spatially localized. The quantum effect is when an oscillator can oscillate at a number of stable amplitudes whose frequencies are sub-multiples of a fixed excitation frequency. This is possible if the oscillator's actual frequency depends on its amplitude, which is the case for a classical pendulum, and if the excitation source is spatially localized.

Argumental oscillations have also been observed and described in balloon-borne magnetometer measurements [14] and in an electrical circuit [8]. A few examples of argumental oscillators, consisting of six variations of a pendulum excited by magnetic forces, have been modeled and experimented [5]. A stability criterion in symbolic form and an approximate analytic solution for an argumental oscillator have been given [4]. Capture probabilities by an attractor in an argumental oscillator have been given in symbolic form [3].

As for the beams receiving axial excitation, a cantilever beam submitted to a harmonic force through its base and to a pulsating axial force through its tip, and carrying a payload at its tip, has been studied in [13].

A typical second-order ordinary differential equation for a one-degree-of-freedom argumental oscillator is:

$$\ddot{x} + 2\beta\omega_0\dot{x} + \omega_0^2x = g_1(x) + g_2(x)\cos(\omega_{exc}t), \quad (1)$$

where x is the space coordinate, β is the damping ratio, ω_0 is the natural angular velocity of the oscillator, g_1 and g_2 are functions of x , and ω_{exc} is the angular velocity of the excitation.

In this paper, a beam submitted to an axial harmonic excitation is studied. When near its rectilinear resting position, the beam "senses" the excitation, and when in a sufficiently bended position, it does not sense the excitation any more. This is realized by way of an intermittent contact. It will be shown that this system obeys an argumental equation. This configuration should allow to study the behavior of a structure when two elements are in contact with each other, but can become disconnected, depending on their instantaneous transverse deformation. This situation can occur either by design or after damaging.

Two models are studied, called "natural model" and "smooth model". The natural and the smooth models are studied by way of numerical simulations carried out on a classical second-order equation of motion. A solution of the differential equations pertaining to the smooth model is carried out, using the averaging method. A comparison is made between numerical simulations on the natural model and the solution provided by the averaging method. In [7], these results are used to establish symbolic properties of the stationary regime, and experimental results are given in [6].

2 System configuration.

The schematic system configuration is as shown in Fig. 1. A beam is represented, with its left end S and right end M, in a clamped-(clamped-guided) configuration. At the point M's side, the clamp is carried out by way of a massless trolley. Point M is intermittently pushed to the left by a plate C, which is linked to a point A via a massless spring. $\mathbf{F} = F\mathbf{i}$, where \mathbf{i} is the unit vector along the abscissae axis, is the force intermittently applied by plate C to the beam's right end at M. F is negative when the beam is in compression. In the figure, point A moves horizontally with an harmonic motion, in such a manner that the contact between plate C and point M be intermittent when the beam and point A are vibrating. When the beam is in resting (i.e. rectilinear) position and point A is in center position, the force applied to point M is denoted by F_0 .

3 Modeling

In this section, a first model is studied, called "natural model" because it is deduced directly from simple physical laws and the arrangement of the constituting components: beam,

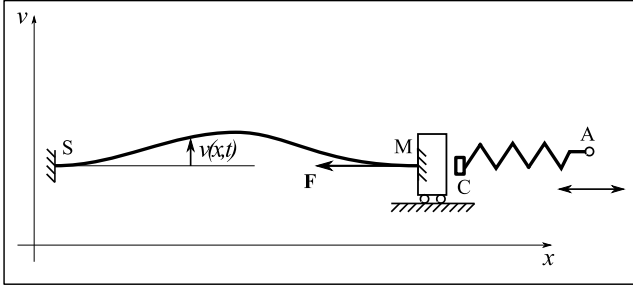


Fig. 1 System configuration. x is the horizontal abscissa, v is the transverse displacement, t is the time, and \mathbf{F} is the force applied by plate C to the beam at point M. Point M moves freely horizontally, but is clamped vertically. There is no rotation at S and M.

spring, and points M and A. This leads to a discontinuous model, involving a C^0 -class function for the external force, due to the intermittent nature of the contact at point M.

Then, a second model is studied, called “smooth model” because it is an approximation to the natural model. This model is not as close to physical reality as the natural model, but, in exchange, involves a C^∞ -class function for the external force, easier to manipulate.

3.1 Expression of the abscissa of the right-hand end of the beam.

In this section, an expression of point M’s abscissa x_M is calculated. This expression will be needed to calculate the force F . As the beam bends, point M moves to the left. Define L the beam’s length and x_M the point M’s abscissa. Along the beam, define the curvilinear abscissa from point S to current point (x, v) as $s(x, v, t)$. A classical method to calculate x_M is as follows.

As the beam is considered inextensible, point M’s curvilinear abscissa is always equal to L , i.e.

$$s(x_M, v, t) = L = \int_0^{x_M} \sqrt{1 + \left(\frac{\partial v(x, t)}{\partial x} \right)^2} dx. \quad (2)$$

Then, using the 2nd-order Taylor polynomial

$$\sqrt{1 + \left(\frac{\partial v(x, t)}{\partial x} \right)^2} \approx 1 + \frac{1}{2} \left(\frac{\partial v(x, t)}{\partial x} \right)^2 \text{ inside Eq. (2), and considering that } \int_0^{x_M} \left(\frac{\partial v(x, t)}{\partial x} \right)^2 dx \approx \int_0^L \left(\frac{\partial v(x, t)}{\partial x} \right)^2 dx, \text{ obtain:}$$

$$x_M(t) \approx L - \frac{1}{2} \int_0^L \left(\frac{\partial v(x, t)}{\partial x} \right)^2 dx. \quad (3)$$

Then, consider that the transverse motion is projected on the beam’s first mode shape $\tilde{\phi}(x)$, and expressed as

$$v(x, t) = q_1(t) \tilde{\phi}(x) = L q_1(t) \frac{\tilde{\phi}(x)}{L} = L q_1(t) \phi_1(x), \quad (4)$$

where $\phi_1(x)$ is the beam’s first mode shape, adimensioned by L , so chosen as to have $\|\phi_1\|_\infty = 1$, and $q_1(t)$ is the modal coordinate as a function of time.

Hinged-(hinged-guided) case. In this case, consider that the first mode is

$$\phi_1(x) = \sin\left(\pi \frac{x}{L}\right). \quad (5)$$

Clamped-(clamped-guided) case. In this case, consider that the mode shape of the first mode shape is (as per classical textbooks):

$$\phi_1(x) = B_1 [\sin(ax) - 1.0178 \cos(ax) - \sinh(ax) + 1.0178 \cosh(ax)]$$

with $aL \approx 4.730$ and $B_1 = 0.6024$ so as to have $\|\phi_1\|_\infty = 1$.

Approach this mode shape with

$$\phi_1(x) = \frac{1}{2} \left(1 - \cos\left(\frac{2\pi x}{L}\right) \right). \quad (6)$$

It can be seen in Fig. 2 that the approaching curve is close to the exact curve.

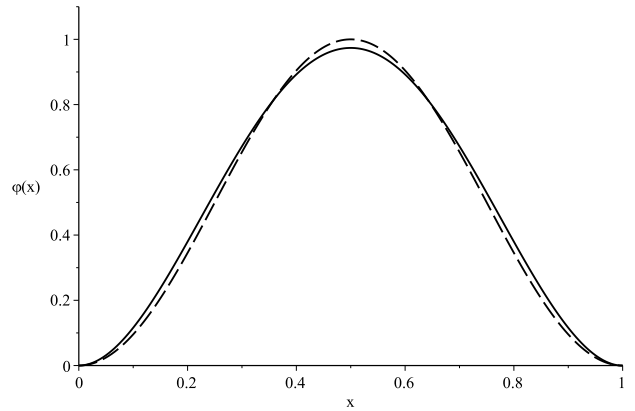


Fig. 2 Approached mode shape for a clamped-(clamped-guided) mode shape: exact (solid line), approached (dashed line).

Conclusion about both cases. Substituting expression (5) or (6) into Eq. (4), then $v(x, t)$ into (3), obtain:

$$x_M(t) \approx L \left(1 - \frac{\pi^2}{4} q_1^2(t) \right) \quad (7)$$

for both the hinged-(hinged-guided) case and the clamped-(clamped-guided) case.

From this point on, for the sake of clarity, time will be omitted in the notation of $q_1(t)$.

3.2 Natural model of the external force.

In this section, an expression of the external force F will be calculated. Define x_A the point A's abscissa and $x_{A0} = \overline{x_A}$, where the overline notation means the averaging operation versus time. Considering that when there is contact between C and M, those two points have the same abscissa, it can be seen from Fig. 1 that, provided there is contact between C and M, and denoting by F_0 (which is negative) the force F when $x_A = x_{A0} = x_A(0)$ and $x_M = L$:

$$F - F_0 = k(x_A - x_{A0} + L - x_M), \quad (8)$$

where F is the force, k is the spring's stiffness, L is the beam's length, and x_M is point M's abscissa.

Define a_A as the amplitude of A's harmonic motion, normalized by L , i.e. $x_A(t) = x_{A0} + La_A \cos(\omega_{exc}t)$. Hence, Eq. (8) writes, taking (7) into account:

$$F(q_1) = F_0 + kL \left(a_A \cos(\omega_{exc}t) + \frac{\pi^2}{4} q_1^2 \right), \quad (9)$$

where F is denoted $F(q_1)$ because it depends on q_1 and t .

If the contact is intermittent, i.e. if, from time to time, points M and A become sufficiently distant from each other, so as to yield a positive value for the right-hand member of (9), it holds:

$$\begin{cases} F(q_1) = K(q_1) & \text{if } K(q_1) \leq 0 \\ F(q_1) = 0 & \text{otherwise} \end{cases} \quad (10)$$

$$\text{with } K(q_1) = F_0 + kL \left(a_A \cos(\omega_{exc}t) + \frac{\pi^2}{4} q_1^2 \right).$$

This constitutes the natural model of force F .

Upper bound for a_A . In this paper, the critical buckling force F_B on the beam is considered never being reached nor exceeded. Therefore, it is necessary that $|F(q_1)| < F_B$ at all times, which, knowing that $|F(q_1)| \leq |F(0)|$ for any q_1 (and that the equality occurs), translates to $|F(0)| < F_B$ at all times, i.e. $-F_0 + kLa_A < F_B$. Finally, the upper bound of a_A can be expressed as:

$$a_A < \frac{F_B + F_0}{kL} = \frac{F_B - |F_0|}{kL}. \quad (11)$$

This value is referred to in this paper as the ‘‘Buckling limit’’.

Case of permanent contact. Putting $F < 0$ in Eq. (9), deduce that the condition for the contact to be permanent is:

$$a_A \cos(\omega_{exc}t) + \frac{\pi^2}{4} q_1^2 < -F_0/(kL) \text{ at all times. The worst case is when } \cos(\omega_{exc}t) = 1, \text{ which leads to:}$$

$$a_A < -\frac{F_0}{kL} - \frac{\pi^2}{4} q_1^2. \quad (12)$$

This relation will be used hereinafter.

3.3 Smooth model of the external force.

In this section, a smooth model of the external force F is presented. A truncated sinusoid is approximated by a sinusoid of same frequency and of lower or equal amplitude, whose extremums are adjusted in reference to the truncated sinusoid, as in Fig. 4. In addition, a truncated parabola is approximated by a smooth function, as showed in Appendix A. The combination of those two approximations leads to a continuous model.

3.3.1 High line and Low line.

An approaching function F_{approx} for $F(q_1)$ will be defined below. For the sake of clarity, define y_{exact} and y_{approx} by $y_{exact}(q_1) = F(q_1)/(kL)$ and $y_{approx}(q_1) = F_{approx}(q_1)/(kL)$. y_{exact} and y_{approx} are expressions of force F adimensioned by kL .

The case where $F_0/(kL) < 0$ when $q_1 = 0$ will be studied. That is, when point A is in its center position and the beam is at rest, there is contact between points M and C. In Figs. 3 to 6, various plots of y_{approx} and y_{exact} are represented. The values of the parameters are as follows: $F_0/(kL) = -2 \cdot 10^{-3}$, $a_A = 1.8 \cdot 10^{-3}$.

The case represented in Fig. 3 is when $\frac{F_0}{kL} + a_A < 0$, i.e. when the beam is at rest and the excitation is on, the contact between points M and C is never disrupted.

The plot of y_{exact} is a sinusoid, which may be truncated or not, represented in Figs. 3 to 6 by a solid line, along with the plot of y_{approx} in dashed line, and dotted construction lines showing the entirety of the sinusoid before truncation, as well of various indications.

As soon as the sinusoid crosses the line $y = 0$, it gets truncated, and the only remaining part is located below said line. Knowing that the excitation frequency is significantly greater than the beam's frequency (at least four times greater), make the hypothesis that during one period of the excitation, the value of q_1 is approximately constant, and the force F can be represented as a pure sinusoid, possibly truncated. From Eq. (10), it can be seen that, for a given value of q_1 , the dotted horizontal marker line labeled $F_0/(kL) + a_A + \pi^2 q_1^2/4$ locates the top of the un-truncated sinusoid, while the marker line labeled $F_0/(kL) - a_A + \pi^2 q_1^2/4$ locates the bottom of said sinusoid. The dotted horizontal markers labeled ‘‘High line’’ and ‘‘Low line’’ locate the highest (resp. lowest) point of the remaining part of the sinusoid after truncation. It can be seen that the more q_1 increases, the more the plot of y_{exact} (solid line) moves to the line $y = 0$, and the less the remaining part of the sinusoid is significant.

Denoting by H_l and L_l the High line's and Low line's ordi-

nates, it holds:

$$\begin{cases} H_l(q_1) = \frac{F_0}{kL} + a_A + \frac{\pi^2 q_1^2}{4} & \text{if } \frac{F_0}{kL} + a_A + \frac{\pi^2 q_1^2}{4} < 0 \\ H_l(q_1) = 0 & \text{otherwise} \end{cases}$$

and

$$\begin{cases} L_l(q_1) = \frac{F_0}{kL} - a_A + \frac{\pi^2 q_1^2}{4} & \text{if } \frac{F_0}{kL} - a_A + \frac{\pi^2 q_1^2}{4} < 0 \\ L_l(q_1) = 0 & \text{otherwise.} \end{cases}$$

The method employed in this section consists in approximating the exact function y_{exact} by a full sinusoid y_{approx} located between the High line and the Low line. It holds:

$$\begin{aligned} y_{approx} &= \frac{H_l + L_l}{2} + \frac{H_l - L_l}{2} \cos(\omega_{exc} t) \\ &= \bar{y}_{approx} + \hat{y}_{approx} \cos(\omega_{exc} t) \end{aligned} \quad (13)$$

where the overline notation denotes the mean value of function y_{approx} over one period of the excitation source and \hat{y}_{approx} denotes the amplitude of function y_{approx} , i.e. half the difference between the maximum and minimum values of y_{approx} over one said period.

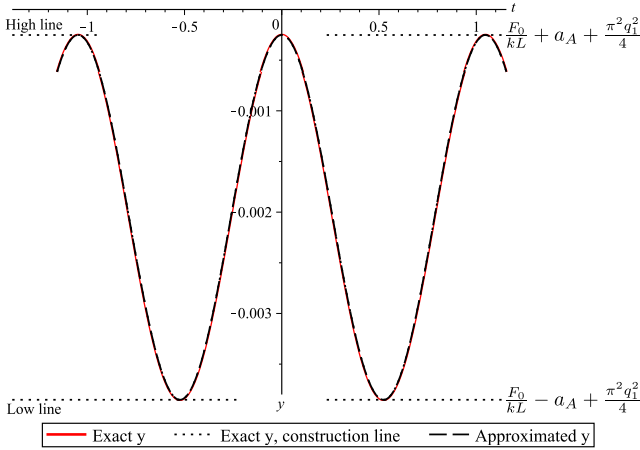


Fig. 3 Exact (solid line) and approached (dashed line) adimensioned axial force $y = F/(kL)$, with $q_1 = 0.0$, $F_0/(kL) = -2 \cdot 10^{-3}$, and $a_A = -0.9 \frac{F_0}{kL}$.

3.3.2 Approximation to the amplitude of function y_{approx} .

Define $a_{Acrit} = \left| \frac{F_0}{kL} \right| = -\frac{F_0}{kL}$, and form the expression of $\hat{y}_{approx} = (H_l - L_l)/2$:

$$\begin{cases} \hat{y}_{approx} = a_A & \text{if } \frac{\pi^2}{4} q_1^2 \leq a_{Acrit} - a_A \\ \hat{y}_{approx} = 0 & \text{if } a_{Acrit} + a_A < \frac{\pi^2}{4} q_1^2 \\ \hat{y}_{approx} = K_1 & \text{otherwise} \end{cases} \quad (14)$$

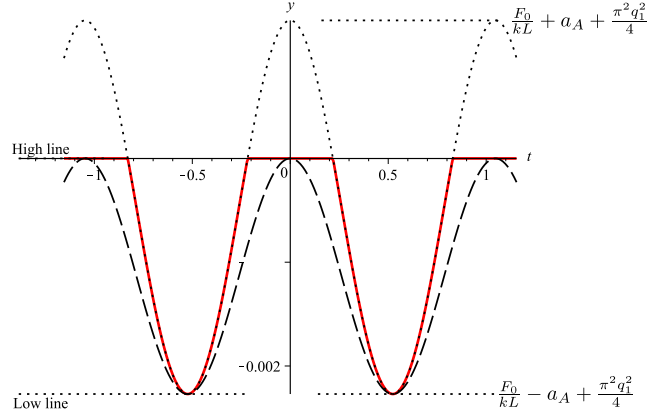


Fig. 4 Exact (solid line) and approached (dashed line) adimensioned axial force $y = F/(kL)$, with $q_1 = 0.015$, $F_0/(kL) = -2 \cdot 10^{-3}$, and $a_A = -0.9 \frac{F_0}{kL}$. The truncated exact curve is part of the complete dotted curve.

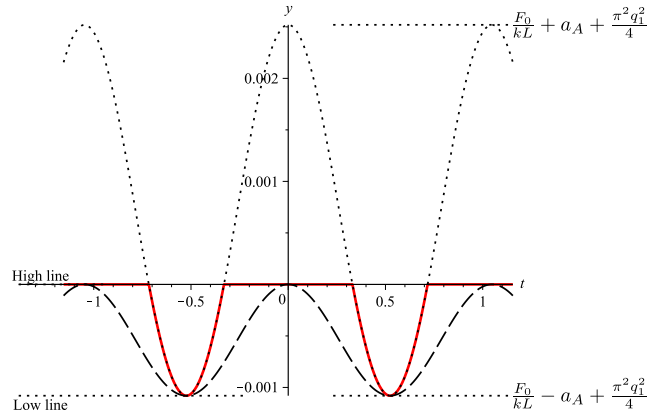


Fig. 5 Exact (solid line) and approached (dashed line) adimensioned axial force $y = F/(kL)$, with $q_1 = 0.02$, $F_0/(kL) = -2 \cdot 10^{-3}$, and $a_A = -0.9 \frac{F_0}{kL}$. The truncated exact curve is part of the complete dotted curve.

$$\text{with } K_1 = -\frac{1}{2} \left(\frac{F_0}{kL} - a_A + \frac{\pi^2}{4} q_1^2 \right).$$

From the piecewise definition of \hat{y}_{approx} in Eq. (14), search a C^∞ approximation to \hat{y}_{approx} . Two cases must be distinguished, depending on the position of a_A versus a_{Acrit} .

Case $a_A > a_{Acrit}$. In this case, the first case of Eqs. (14) cannot exist. It follows that this is a “single-parabola case” as per Appendix A.

The parabola's vertex is at ordinate $\frac{1}{2} \left(-\frac{F_0}{kL} + a_A \right)$. With the notations of Appendix A, $\alpha = \frac{1}{2} \left(-\frac{F_0}{kL} + a_A \right)$, $\beta = -\frac{\pi^2}{8}$, and $x = q_1$. Hence the function J_{approx} approaching \hat{y}_{approx} writes

$$J_{approx}(q_1) = \frac{\frac{1}{2} \left(-\frac{F_0}{kL} + a_A \right)}{1 - \frac{\pi^2}{4} \frac{\lambda}{\left(-\frac{F_0}{kL} + a_A \right)} q_1^2}. \quad (15)$$

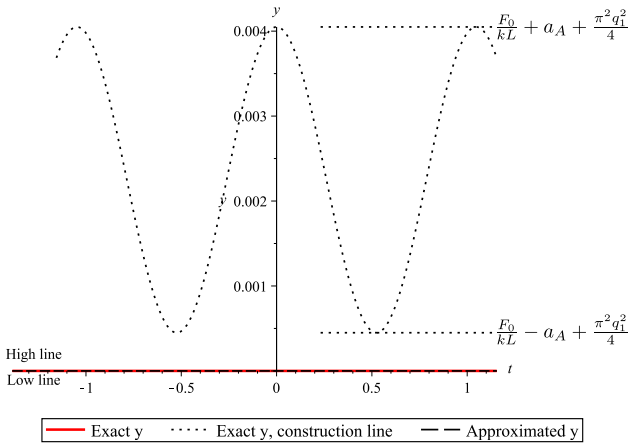


Fig. 6 Exact (solid line, $y = 0$ and approached (dashed line, identical to exact curve) adimensioned axial force $y = F/(kL)$, with $q_1 = 0.025$, $F_0/(kL) = -2 \cdot 10^{-3}$, and $a_A = -0.9 \frac{F_0}{kL}$. The dotted curve is the original y before truncation.

At this point, it would be nice to have a value of λ such that the denominator in expression (15) be independant of a_A . Knowing that λ must be comprised between -2 and -8 (see Appendix A), this is possible if $\lambda = -\frac{F_0}{kL} - a_A$ and $a_A < 7a_{Acrit}$, which is physically within reason. With this expression for λ , it holds

$$J_{approx}(q_1) = \frac{\frac{1}{2} \left(-\frac{F_0}{kL} + a_A \right)}{1 + Bq_1^2}, \quad (16)$$

$$\text{with } B = -\frac{\pi^2 kL}{4F_0} = \frac{\pi^2}{4 a_{Acrit}}.$$

Case $a_A \leq a_{Acrit}$. In this case, all three cases of Eqs. (14) are valid. It follows that this is a “plateau case” as per Appendix A. The plateau is at ordinate a_A . Using Eq. (69) of Appendix A with $J_{pl} = a_A$, $\alpha = \frac{1}{2} \left(-\frac{F_0}{kL} + a_A \right)$, $\beta = -\frac{\pi^2}{8}$, and $x = q_1$, this can be approximated by:

$$J_{approx} = \frac{a_A}{1 + Eq_1^2}, \quad (17)$$

with

$$E = -\frac{\pi^2}{4} \frac{1 + \lambda}{\left(\frac{2}{\lambda} + 1 \right) a_A - \frac{F_0}{kL}}. \quad (18)$$

Notice that if $\lambda = -2$, expression E is independant of a_A . Therefore, in this case, this value of λ is chosen, and it follows that $E = -\frac{\pi^2 kL}{4F_0}$, which is the same value as B in the case $a_A > a_{Acrit}$.

Conclusion for the expression of \hat{y}_{approx} . Finally:

$$\begin{cases} \hat{y}_{approx} \approx \frac{a_A}{1 + Bq_1^2} & \text{if } a_A < a_{Acrit} \\ \hat{y}_{approx} \approx \frac{1}{2} \frac{-\frac{F_0}{kL} + a_A}{1 + Bq_1^2} & \text{otherwise} \end{cases} \quad (19)$$

$$\text{with } B = -\frac{\pi^2 kL}{4F_0} = \frac{\pi^2}{4 a_{Acrit}}.$$

3.3.3 Approximation to the mean value of function y_{approx} .

Form the expression of $\bar{y}_{approx} = (H_l + L_l)/2$:

$$\begin{cases} \bar{y}_{approx} = \frac{F_0}{kL} + \frac{\pi^2}{4} q_1^2 & \text{if } \frac{\pi^2}{4} q_1^2 \leq a_{Acrit} - a_A \\ \bar{y}_{approx} = 0 & \text{if } a_{Acrit} + a_A < \frac{\pi^2}{4} q_1^2 \\ \bar{y}_{approx} = K_2 & \text{otherwise} \end{cases} \quad (20)$$

$$\text{with } K_2 = \frac{1}{2} \left(\frac{F_0}{kL} - a_A + \frac{\pi^2}{4} q_1^2 \right).$$

Notice that $K_2 = -K_1$.

From the piecewise definition of \bar{y}_{approx} in Eq. (20), search a C^∞ approximation to \bar{y}_{approx} . Two cases must be distinguished, depending on the position of a_A versus a_{Acrit} .

Case $a_A > a_{Acrit}$. In this case, the first case of Eq. (20) cannot exist. It follows that this is a single-parabola case as per Appendix A. The parabola's equation is $J(q_1) = K_2$, and the vertex is at ordinate $\frac{1}{2} \left(\frac{F_0}{kL} - a_A \right)$, which is negative. Noticing that, excepted for the sign, these parameters are the same as for the approximation of \hat{y}_{approx} for $a_A > a_{Acrit}$, and using the same method as for obtaining Eq. (16), put

$$\lambda = -\kappa \frac{\frac{F_0}{kL} - a_A}{\frac{F_0}{kL}} = -\kappa \frac{a_{Acrit} + a_A}{a_{Acrit}},$$

with $\kappa = 2$ to ensure continuity of expression C (defined below) with case $a_A < a_{Acrit}$, and obtain

$$J_{approx}(q_1) = \frac{\frac{1}{2} \left(\frac{F_0}{kL} - a_A \right)}{1 + Cq_1^2} \quad (21)$$

$$= \frac{1}{2} \left(\frac{F_0}{kL} - a_A \right) \left(1 - \frac{Cq_1^2}{1 + Cq_1^2} \right), \quad (22)$$

with $C = -\frac{\pi^2 kL}{2F_0} = \frac{\pi^2}{2 a_{Acrit}}$. It can be seen that the model is limited to $a_A < 3a_{Acrit}$ to ensure that $-8 < \lambda < -2$.

Case $a_A < a_{Acrit}$. In this case, all three cases of Eq. (20) are valid. This is a composite-parabola case as per Appendix A. Here $\alpha_1 = F_0/(kL)$, $\beta = \pi^2/4$, and $\alpha_2 = F_0/((kL) - a_A)$. Using Eq. (70) of Appendix A, \bar{y}_{approx} can be approximated by: $\frac{F_0}{kL} \frac{1}{1+Cq_1^2}$, with

$$C = -\lambda \frac{\pi^2}{4} \frac{1}{\sqrt{(-\frac{F_0}{kL})(-\frac{F_0}{kL} + a_A)}}.$$

However, this expression depends on a_A , while, in the other cases, it does not. The idea is to choose λ so as to have C independant of a_A , after noticing that λ needs not be a constant, but only needs to be between -8 and -2 (see Appendix A).

Put

$$\lambda = \kappa \frac{\sqrt{(-\frac{F_0}{kL})(-\frac{F_0}{kL} + a_A)}}{\frac{F_0}{kL}}, \quad (23)$$

where κ is a coefficient to be determined. After a few calculus, condition $-4 \leq \lambda \leq -2$ leads to

$$\frac{4}{\kappa^2} - 1 \leq \frac{a_A}{|\frac{F_0}{kL}|} \leq \frac{16}{\kappa^2} - 1. \quad (24)$$

Since here $a_A < a_{Acrit} = \left| \frac{F_0}{kL} \right|$, it holds $0 < \frac{a_A}{|\frac{F_0}{kL}|} < 1$. It follows that the value $\kappa = 2$ satisfies (24). Finally, C writes:

$$C = -\frac{\pi^2 kL}{2 F_0} = \frac{\pi^2}{2 a_{Acrit}}. \quad (25)$$

Then

$$\bar{y}_{approx} \approx \frac{F_0}{kL} \frac{1}{1+Cq_1^2} = \frac{F_0}{kL} \left(1 - \frac{Cq_1^2}{1+Cq_1^2} \right). \quad (26)$$

Conclusion for the expression of \bar{y}_{approx} . Finally, the mean value of function y_{approx} writes:

$$\begin{cases} \bar{y}_{approx} \approx \frac{F_0}{kL} \left(1 - \frac{Cq_1^2}{1+Cq_1^2} \right) & \text{if } a_A < a_{Acrit} \\ \bar{y}_{approx} \approx \frac{1}{2} \left(\frac{F_0}{kL} - a_A \right) \left(1 - \frac{Cq_1^2}{1+Cq_1^2} \right) & \text{otherwise,} \end{cases} \quad (27)$$

with $C = -\frac{\pi^2 kL}{2F_0} = \frac{\pi^2}{2 a_{Acrit}}$ and $a_A < 3a_{Acrit}$.

Therefore, recalling that a_A must never exceed the Buckling limit, one is leaded to introduce a parameter called the “Model validity upper limit”, equal to

$$\text{Model validity upper limit} = \min(\text{Buckling limit}, 3a_{Acrit}). \quad (28)$$

This is a value which a_A must never exceed to ensure that the model is not a priori invalid.

Approximation to the F function. Substituting Eqs. (19) and (27) into Eq. (13), and substituting F_{approx} for kLy_{approx} , obtain:

$$F_{approx}(q_1) = C_1 + f_1(q_1) + f_2(q_1) \cos(\omega_{exc} t) \quad (29)$$

with, if $a_A < a_{Acrit}$:

$$\begin{cases} C_1 = F_0, \\ f_1(q_1) = -C_1 \frac{Cq_1^2}{1+Cq_1^2}, \\ f_2(q_1) = \frac{kLa_A}{1+Bq_1^2}, \end{cases} \quad (30)$$

and otherwise:

$$\begin{cases} C_1 = \frac{1}{2}(F_0 - kLa_A), \\ f_1(q_1) = -C_1 \frac{Cq_1^2}{1+Cq_1^2}, \\ f_2(q_1) = -C_1 \frac{1}{1+Bq_1^2}, \end{cases} \quad (31)$$

with a_A the point A's adimensioned amplitude, F_0 the axial force applied to the beam when it is rectilinear and point A is in central position, k the spring's stiffness, L the beam's length, and $C = 2B = -\frac{\pi^2 kL}{2F_0} = \frac{\pi^2}{2 a_{Acrit}}$.

4 Second-order differential equation of motion.

Eq. (7) gives x_M as a function of q_1 , while Eqs. (30) and (31) give an approximated expression of the external force as a function of q_1 . Substituting these expressions into the general equation in the modal coordinates which will be brought out in this section, it is possible to obtain a second-order ordinary differential equation in q_1 (which is a function of time).

4.1 Classical transverse motion of an axially-excited beam.

The classical equation of motion of an axially-excited Euler-Bernoulli beam with non rotating and planar motion and neglecting stretching is [11, Chap. 14]:

$$\begin{aligned} \frac{\partial^2}{\partial x^2} \left(EI(x) \frac{\partial^2 v(x,t)}{\partial x^2} \right) + \frac{\partial}{\partial x} \left(F(x) \frac{\partial v(x,t)}{\partial x} \right) \\ + m(x) \frac{\partial^2 v(x,t)}{\partial t^2} = p(x,t), \end{aligned} \quad (32)$$

where $v(x,t)$ is the transverse displacement, E is Young's modulus, $I(x)$ is the second moment of area of the beam's cross-section, $F(x)$ is the axial force (positive in case of compression), $m(x)$ is the mass per unit length, and $p(x,t)$ is a transverse distributed force.

Consider herein that $p = \mu Sg$, where g is the acceleration of gravity, μ is the mass density, and S is the beam's cross-section area. Next, consider that the axial force F depends only on the beam's actual deformation state q_1 (as defined in Section 3) and on time, which does not change the form of Eq. (32). Denote said force by $-F$, so that $F < 0$ in case of compression, to be consistent with convention of Section 3. Also, consider that the flexural rigidity $EI(x)$ and the transverse distributed force are constant over the beam. Moreover, consider that μ and S are constant over the beam. Finally, use the dot notation to denote differentiation with respect to time, and classically introduce a damping effect as $2\beta'\dot{v}$ to obtain

$$\mu S \ddot{v}(x, t) + EI \frac{\partial^4 v(x, t)}{\partial x^4} - F \frac{\partial^2 v(x, t)}{\partial x^2} = \mu Sg \quad (33)$$

4.2 Projection onto the first mode.

Putting $v(x, t) = \sum_{k=1}^{+\infty} q_k(t) \phi_k(x)$ and projecting Eq. (33) onto the first mode, and classically adding a modal damping ratio to take the damping into account, obtain, for the hinged-(hinged-guided) case and the mode shape as per Eq. (5):

$$\ddot{q}_1 + \frac{2\beta'}{\mu S} \dot{q}_1 + \left(\frac{\pi}{L}\right)^4 \frac{EI}{\mu S} q_1 + \left(\frac{\pi}{L}\right)^2 \frac{F(q_1)q_1}{\mu S} - \frac{4g}{\pi L} = 0, \quad (34)$$

and for the clamped-(clamped-guided) case and the mode shape as per Eq. (6):

$$\ddot{q}_1 + \frac{2\beta'}{\mu S} \dot{q}_1 + \left(\frac{2\pi}{L}\right)^4 \frac{EI}{3\mu S} q_1 + \frac{4}{3} \left(\frac{\pi}{L}\right)^2 \frac{F(q_1)q_1}{\mu S} - \frac{4g}{3L} = 0. \quad (35)$$

Introduce the beam's critical buckling force

$$F_B = \frac{\pi^2 EI}{a_3^2 L^2}, \quad (36)$$

where L is the beam's length and a_3 is a coefficient equal to 1 in the hinged-(hinged-guided) case and to 1/2 in the clamped-(clamped-guided) case.

Equations (34) and (35) can be rewritten into a unique expression:

$$\ddot{q}_1 + \frac{2\beta'}{\mu S} \dot{q}_1 + a_1 \left(\frac{\pi}{L}\right)^2 \frac{F_B}{\mu S} q_1 + a_1 \left(\frac{\pi}{L}\right)^2 \frac{F(q_1)q_1}{\mu S} - a_2 \frac{g}{L} = 0, \quad (37)$$

with $a_1 = 1$ and $a_2 = 4/\pi$ in the hinged-(hinged-guided) case, and with $a_1 = 4/3$ and $a_2 = 4/3$ in the clamped-(clamped-guided) case.

Transforming Eq. (37), obtain:

$$\ddot{q}_1 + 2\beta \omega_0 \dot{q}_1 + \omega_0^2 q_1 = -\omega_0^2 \frac{q_1}{F_B + C_2} (-C_2 + F(q_1)) + a_2 \frac{g}{L},$$

with $\omega_0^2 = a_1 \left(\frac{\pi}{L}\right)^2 \frac{F_B + C_2}{\mu S}$, $\beta \omega_0 = \frac{\beta'}{\mu S}$, and $C_2 =$ arbitrary constant.

Then, choosing $C_2 = F_0$ to have ω_0 consistent with its natural value when $F_0 = 0$, obtain:

$$\ddot{q}_1 + 2\beta \omega_0 \dot{q}_1 + \omega_0^2 q_1 = -\omega_0^2 \frac{q_1}{F_B + F_0} (-F_0 + F(q_1)) + a_2 \frac{g}{L} \quad (38)$$

$$\text{with } \omega_0^2 = a_1 \left(\frac{\pi}{L}\right)^2 \frac{F_B + F_0}{\mu S}.$$

4.3 Equation of motion with the natural model.

By implementing the natural model of the external force, this second-order differential equation will be of use below, to assess the quality of the smooth approximated model which is given in Section 3. In the natural model, force $F(q_1)$ is as follows:

$$\begin{cases} F(q_1) = K(q_1) & \text{if } K \leq 0 \\ F(q_1) = 0 & \text{otherwise} \end{cases} \quad (39)$$

$$\text{with } K(q_1) = F_0 + kL \left(a_A \cos(\omega_{exc} t) + \frac{\pi^2}{4} q_1^2 \right).$$

Substituting $F(q_1)$ as given by Eqs. (39) into Eq. (38) yields the equation of motion with the natural model.

4.4 Equation of motion with the smooth model.

By implementing the smooth model of the external force into the second-order differential equation (38), it will be possible to use the averaging method, and then to derive symbolic relations.

Recall that $a_{Acrit} = \left| \frac{F_0}{kL} \right| = -\frac{F_0}{kL}$. Because the expression of force F in Eq. (37) differs depending on the sign of $a_A - a_{Acrit}$, two cases must be distinguished here, depending on said sign.

Obtain, substituting F_{approx} as given in Eqs. (29), (30) and (31) into Eq. (38):

– If $a_A < a_{Acrit}$, and then $C_1 = F_0$:

$$\begin{aligned} \ddot{q}_1 + 2\beta \omega_0 \dot{q}_1 + \omega_0^2 q_1 = & -\omega_1^2 \frac{Cq_1^3}{1 + Cq_1^2} + a_2 \frac{g}{L} \\ & + \omega_1^2 \frac{a_A}{\frac{F_0}{kL}} \frac{q_1}{1 + Bq_1^2} \cos(\omega_{exc} t). \end{aligned} \quad (40)$$

– If $a_A \geq a_{Acrit}$, and then $C_1 = \frac{1}{2}(F_0 - kLa_A)$:

$$\ddot{q}_1 + 2\beta\omega_0\dot{q}_1 + \omega_0^2 q_1 = -\omega_2^2 \frac{Cq_1^3}{1+Cq_1^2} + a_2 \frac{g}{L} - \omega_2^2 \frac{q_1}{1+Bq_1^2} \cos(\omega_{exc}t). \quad (41)$$

With

$$\omega_0^2 = a_1 \left(\frac{\pi}{L}\right)^2 \frac{F_B + F_0}{\mu S}, \quad \omega_1^2 = -\frac{F_0}{F_B + F_0} \omega_0^2, \quad \omega_2^2 = -\frac{F_0 - a_A kL}{2F_B + F_0 - a_A kL} \omega_0^2, \quad (42)$$

$$C = 2B = -\frac{\pi^2 kL}{2F_0} = \frac{\pi^2}{2a_{Acrit}}. \quad (43)$$

This can be summarized by introducing functions $g_1(q_1)$ and $g_2(q_1)$, and writing:

$$\ddot{q}_1 + 2\beta\omega_0\dot{q}_1 + \omega_0^2 q_1 = g_1(q_1) + g_2(q_1) \cos(\omega_{exc}t),$$

$$\text{with } g_1(q_1) = -\frac{\omega_0^2}{F_B + C_1} q_1 f_1(q_1) + a_2 \frac{g}{L},$$

$$g_2(q_1) = -\frac{\omega_0^2}{F_B + C_1} q_1 f_2(q_1),$$

f_1 and f_2 as per Eqs. (29), (30) and (31),

$$\omega_0^2 = a_1 \left(\frac{\pi}{L}\right)^2 \frac{F_B + C_1}{\mu S}, \quad \beta\omega_0 = \frac{\beta'}{\mu S}, \quad F_B = \frac{\pi^2 EI}{a_3^2 l^2},$$

$a_1 = 1$, $a_2 = 4/\pi$, and $a_3 = 1$ in the hinged-(hinged-guided) case,

$a_1 = 4/3$, $a_2 = 4/3$, and $a_3 = 1/2$ in the clamped-(clamped-guided) case,

and g the acceleration of gravity.

Those equations are argumental equations similar to Eq. (1).

5 Averaging method on the smooth model of the dynamical system.

The averaging method, studied in [2] and used in an argumental-oscillator context [4, 10], is applied to the second-order differential equation of motion in q_1 , i.e. Eq. (40) or (41), with the approximated smooth form of the external force, to obtain a standard system of two first-order differential equations in amplitude and phase.

5.1 Reduced time.

Introducing the reduced time τ , classically defined as $\tau = \omega_0 t$, and using from now on the dot notation to denote differentiation with respect to τ , obtain

$$\ddot{z} + 2\beta\dot{z} + z = \frac{g_1(z)}{\omega_0^2} + \frac{g_2(z)}{\omega_0^2} \cos\left(\frac{\omega_{exc}}{\omega_0} \tau\right), \quad (44)$$

with $z(\tau) = q_1$ and

– If $a_A < a_{Acrit}$:

$$g_1(z) = -\omega_1^2 \frac{Cz^3}{1+Cz^2} + a_2 \frac{g}{L} \quad \text{and} \quad g_2(z) = -\omega_{11}^2 \frac{z}{1+Bz^2},$$

with $\omega_1^2 = -\frac{F_0}{F_B + F_0} \omega_0^2$ and $\omega_{11}^2 = \frac{a_A kL}{F_B + F_0} \omega_0^2$.

– Otherwise:

$$g_1(z) = -\omega_2^2 \frac{Cz^3}{1+Cz^2} + a_2 \frac{g}{L} \quad \text{and} \quad g_2(z) = -\omega_2^2 \frac{z}{1+Bz^2},$$

with $\omega_2^2 = -\frac{F_0 - a_A kL}{2F_B + F_0 - a_A kL} \omega_0^2$.

It should be noted that ω_{11} and ω_2 depend on the excitation's amplitude a_A , and that it is assumed that $|F_0 - a_A kL| < 2F_B$. Then, to use the classical averaging method's results, in which the second-order reduced-time differential equation in z writes

$$\ddot{z} + z = -2\beta\dot{z} - g(z) + AH(z)E(\tau), \quad (45)$$

identify (44) with (45), obtaining

$$\begin{cases} g(z) = -\frac{g_1(z)}{\omega_0^2} \\ AH(z) = \frac{g_2(z)}{\omega_0^2} \\ E(\tau) = \cos\left(\frac{\omega_{exc}}{\omega_0} \tau\right) \end{cases}$$

with $H(z) = -\frac{z}{1+Bz^2}$ and

$$\begin{cases} A(a_A) = \frac{kLa_A}{F_B + F_0} & \text{if } a_A < a_{Acrit} \\ A(a_A) = -\frac{F_0 - a_A kL}{2F_B + F_0 - a_A kL} & \text{otherwise.} \end{cases} \quad (46)$$

It can be noted that A is in both cases a positive, monotonic increasing function of a_A .

The expression for $H(z)$ is the same in both cases: this allows to carry out only one calculus when it comes to Fourier decomposition below. Because A depends on a_A , it will be denoted from now on as $A(a_A)$.

5.2 Standard system.

Searching for a solution $z(\tau)$ close to a slowly-varying sinusoid, carry out the classical averaging method, beginning by a change of variables as follows, introducing variables a and φ :

$$\begin{cases} z(\tau) = a(\tau) \sin(\rho\tau + \varphi(\tau)) \\ \dot{z}(\tau) = a(\tau) \rho \cos(\rho\tau + \varphi(\tau)), \end{cases}$$

where ρ is a mathematical parameter to be determined later, a is the slowly-varying amplitude of the solution, and φ is the slowly-varying phase of the solution w.r.t. the excitation.

Obtain the standard system involving variables a and φ , which is the system which will be averaged:

$$\begin{cases} \dot{a} = \frac{\cos(\theta)}{\rho} [-2\beta\rho a \cos(\theta) - g(a \sin(\theta)) \\ \quad + A(a_A)H(a \sin(\theta))E(\tau) + a \sin(\theta)(\rho^2 - 1)] \\ \dot{\varphi} = -\frac{\sin(\theta)}{\rho a} [-2\beta\rho a \cos(\theta) - g(a \sin(\theta)) \\ \quad + A(a_A)H(a \sin(\theta))E(\tau) + a \sin(\theta)(\rho^2 - 1)] \end{cases} \quad (47)$$

with $\theta = \rho\tau + \varphi$, $\rho = \frac{\omega}{\omega_0}$, ω a constant to be determined (close to ω_0), $A(a_A)$ according to Eq. (46), and $E(\tau) = \cos\left(\frac{\omega_{exc}}{\omega_0}\tau\right)$.

The reciprocal relations are as follows, knowing that $a(\tau)$ is always positive:

$$\begin{cases} a(\tau) = \sqrt{z^2(\tau) + \left(\frac{\dot{z}(\tau)}{\rho}\right)^2} \\ \varphi(\tau) = \arctan\left(\rho \frac{\dot{z}(\tau)}{z(\tau)}\right) - \rho\tau [2\pi]. \end{cases} \quad (48)$$

These relations are of use to interpret the results of a solution to the second-order equation of the natural or smooth model in terms of Van der Pol representation, to afterwards compare them to the solution given by the averaged smooth model, which is natively in Van der Pol coordinates.

5.3 Averaged system.

The averaging method involves time-averaging of the terms of Eq. (47).

Averaged expression relative to function G. Putting $G(a, a_A) = \overline{\sin(\theta)g(a \sin(\theta))}$, where the overline notation denotes averaging with respect to time over one period of the solution, and neglecting gravity, obtain:

– If $a_A < a_{Acrit}$:

$$G(a) = -\frac{1}{2} \frac{F_0}{F_B + F_0} a \left(1 - \frac{2}{Ca^2} + \frac{1}{Ca^2} \frac{2}{\sqrt{1 + Ca^2}}\right). \quad (49)$$

– Otherwise:

$$G(a, a_A) = -\frac{1}{2} \frac{F_0 - a_A kL}{2F_B + F_0 - a_A kL} a \left(1 - \frac{2}{Ca^2} + \frac{1}{Ca^2} \frac{2}{\sqrt{1 + Ca^2}}\right) \quad (50)$$

Decomposing function $H(a \sin(\theta))$ into a Fourier series of variable θ . This decomposition will allow an averaging of $H(a \sin(\theta))$ hereinafter.

$H(a \sin(\theta))$ being an odd function of variable θ , and being of period π , define its Fourier series coefficients h_q by

$$H(a \sin(\theta)) = \sum_{q=1, q \text{ odd}}^{+\infty} h_q \sin(q\theta).$$

Then a calculus yields:

– If $a_A < a_{Acrit}$:

$$h_q = -a_A kL \frac{2}{B^{\frac{q+1}{2}}} \frac{(\sqrt{1 + Ba^2} - 1)^q}{\sqrt{1 + Ba^2} a^q},$$

– Otherwise:

$$h_q = \frac{F_0 - a_A kL}{2} \frac{2}{B^{\frac{q+1}{2}}} \frac{(\sqrt{1 + Ba^2} - 1)^q}{\sqrt{1 + Ba^2} a^q}.$$

Calculus of $\overline{H(a \sin(\theta))E(\tau)\cos(\theta)}$. If $\frac{\omega_{exc}}{\rho\omega_0}$ is an even integer (denoted by n), obtain

$$\overline{H(a \sin(\theta))E(\tau)\cos(\theta)} = \frac{1}{4} S_n \sin(n\varphi),$$

with $S_n = h_{n-1} + h_{n+1}$.

Otherwise, $\overline{H(a \sin(\theta))E(\tau)\cos(\theta)} = 0$.

Calculus of $\overline{H(a \sin(\theta))E(\tau)\sin(\theta)}$. If $\frac{\omega_{exc}}{\rho\omega_0}$ is an even integer (denoted by n), obtain

$$\overline{H(a \sin(\theta))E(\tau)\sin(\theta)} = -\frac{1}{4} D_n \cos(n\varphi),$$

with $D_n = h_{n-1} - h_{n+1}$.

Otherwise, $\overline{H(a \sin(\theta))E(\tau)\sin(\theta)} = 0$.

Symbolic expressions of functions S_n and D_n . A calculus gives

$$S_n = -\frac{4}{a^{n+1}} \frac{(\sqrt{1 + Ba^2} - 1)^n}{B^{\frac{n}{2} + 1}}, \quad (51)$$

$$D_n = \frac{S_n}{\sqrt{1 + Ba^2}}. \quad (52)$$

Parameters ω_{00} and ρ_{00} . Recall that $\omega_0^2 = a_1 \left(\frac{\pi}{L}\right)^2 \frac{F_B + F_0}{\mu S}$.

Put $\omega_{00} = \omega_0|_{F_0=0}$, and $f_{00} = \omega_{00}/(2\pi)$, herein called “free-running frequency”, i.e. the beam’s fundamental frequency for small amplitudes and no axial force applied. It follows that, for a given value of n , ω_{00} is a constant parameter of the physical system if ω_{exc} is considered constant. Then, recalling that $\rho = \frac{\omega_{exc}}{n\omega_0}$ and introducing parameter $\rho_{00} = \frac{\omega_{exc}}{n\omega_{00}}$, obtain :

$$\begin{cases} \omega_0 = \omega_{00} \sqrt{\frac{F_B + F_0}{F_B}} \\ \rho = \rho_{00} \sqrt{\frac{F_B}{F_B + F_0}} \end{cases} \quad (53)$$

It can be seen that ρ_{00} is also a constant parameter of the physical system. Because $F_0 \leq 0$, it holds $\rho \geq \rho_{00}$.

Averaged standard system. The classical averaging calculus yields the following system, if ρ is chosen so that $n = \frac{\omega_{exc}}{\rho\omega_0}$ is an even integer:

$$\begin{cases} \dot{a} = \frac{A(a_A)}{4\rho} S_n(a) \sin(n\varphi) - \beta a \\ \dot{\varphi} = \frac{G(a, a_A)}{\rho a} + \frac{A(a_A)}{4\rho a} D_n(a) \cos(n\varphi) - \frac{\rho^2 - 1}{2\rho}, \end{cases} \quad (54)$$

with $A(a_A)$ defined as per Eq. (46), C by Eq. (43) and G per Eqs. (49) and (50).

If $n = \frac{\omega_{exc}}{\rho\omega_0}$ is not an even integer, it holds:

$$\begin{cases} \dot{a} = -\beta a \\ \dot{\varphi} = \frac{G(a, a_A)}{\rho a} - \frac{\rho^2 - 1}{2\rho}, \end{cases}$$

that is, the motion equations are the same as if the system were disconnected from the excitation source.

Thus, the choice of parameter ρ allows to bring out a differential system of equations. Then, if this system has solutions, the argumental phenomenon can arise. However, there are often more than one unique possible value for ρ . Generally choose the value closest to 1. For each value of ρ , a different system holds. And for each of these systems, a set of solutions may exist.

6 Stationary condition.

Setting $\dot{a} = 0$ and $\dot{\varphi} = 0$ in system (54) constitutes the equations of the stationary condition:

$$\begin{cases} \frac{A(a_A)}{4\rho} S_n(a_S) \sin(n\varphi_S) - \beta a_S = 0 \\ G_1(a_S, a_A) + \frac{A(a_A)}{4a_S} D_n(a_S) \cos(n\varphi_S) - \frac{\rho^2 - 1}{2} = 0, \end{cases} \quad (55)$$

where a_S is the stationary-motion's amplitude and φ_S is the phase shift of said motion with respect to the excitation force, and function G_1 is defined as

$$G_1(a_S, a_A) = G(a_S, a_A)/a_S. \quad (56)$$

β -curve, G -curve and stationary-solutions curve. Writing that $\sin^2(n\varphi_S) + \cos^2(n\varphi_S) = 1$, obtain from Eqs. (55):

$$(4\rho\beta)^2 + 4 \frac{S_n^2(a_S)}{D_n^2(a_S)} (2G_1(a_S, a_A) - (\rho^2 - 1))^2 = \frac{A(a_A)^2 S_n^2(a_S)}{a_S^2}. \quad (57)$$

This can then be written:

$$F_\beta(a_S) + 4 \frac{S_n^2(a_S)}{D_n^2(a_S)} F_G^2(a_S) = 0, \quad (58)$$

with

$$F_\beta(a_S) = (4\rho\beta)^2 - \left(\frac{A(a_A) S_n(a_S)}{a_S} \right)^2$$

and

$$F_G(a_S, a_A) = 2G_1(a_S, a_A) - (\rho^2 - 1).$$

Define the “ β -curve” as the curve representing the solution to equation $F_\beta(a_S) = 0$. Also, define the “ G -curve” as the curve representing the solution to equation $F_G(a_S, a_A) = 0$. Finally, define the “stationary-solutions curve” as the curve whose each point represents one stationary solution to Eq. (57).

Excitation threshold. It is of interest to be able to assess the minimum value of a_A versus a_S along a stationary-solutions curve, because this value of a_A is the excitation threshold allowing the argumental phenomenon to arise with given parameters $n, \beta, F_B, F_0, L, k, f_{00}$, and ρ_{00} . The numerical plots show that the minimum of a_A seems to be close to an intersection point of the β -curve and the G -curve. Therefore, it is natural to carry out a local study around said intersection point to confirm this impression. Said local study, along with other symbolic calculus, is carried out in [7].

Graphic representation of the stationary solutions in the (a_S, a_A) -plane. Fig. 7 shows the implicit stationary-solutions curve, obtained numerically, giving a_A against a_S for the values of parameters given in the figure's legend. The solid-line curve is the stationary-solutions curve, with a minimum at point A_{min} . Observation of Fig. 7 shows that, due to the distinction pertaining to the position of a_A against a_{Acrit} , the stationary-solutions curve can be seen as a set composed of two parts, depending on the position of the current stationary-solution's representative point with respect to the horizontal line $a_A = a_{Acrit} = |F_0|/(kL)$, herein called the “critical line”:

- An upper part (above said line) composed of two arcs, in contact at their higher extremities at one point, and at their lower extremities at said line.
- A lower part, constituted by a V-shaped curve, presenting a minimum at point A_{min} .

The upper and lower parts are connected at the critical line. The right (resp. left) arc and the right (resp. left) part of the V-shaped curve represent the stable (resp. unstable) stationary solutions. For a given value of the excitation, i.e. a given amplitude a_A , there are two possible values for a_S , represented by points S and U . Point S is the stable stationary condition, while point U is the unstable one. The V-shaped curve represents cases where there is permanent contact between the beam and the excitation source when the beam is in rectilinear position. In these cases, the contact may or may not remain permanent when the beam enters a transversal vibration, depending on the spring's stiffness, the initial

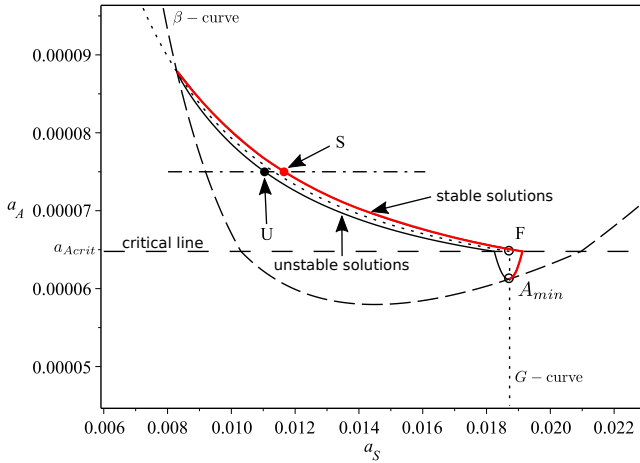


Fig. 7 An example of stationary conditions for the averaged system with the smooth model of the external force. a_S is the stationary-motion's amplitude, a_A is the excitation's amplitude. The dash-dotted line shows the value of a_A which is used for the Van der Pol representation of Fig. 15. The dotted line is the G-curve. The solid line is the stationary-solutions curve. The dashed line is the β -curve. S and U respectively represent the stable and unstable stationary conditions. They are located at the intersection of the stationary-solutions curve and the dash-dotted line. The space-dashed horizontal line is the "critical line". A_{min} is at the minimum of the stationary-solutions curve. Parameter values are: $n = 6$, $\beta = 2.4 \cdot 10^{-3}$, $F_B = 51N$, $F_0 = -8N$, $L = 0.95m$, $k = 130 kN/m$, $f_{00} = 6.615Hz$, $f_{exc} = 39.500711Hz$, $\rho_{00} = 0.9952308$. Model validity upper limit $= 1.94 \cdot 10^{-4}$.

force F_0 , and the amplitudes of transversal vibration of the beam and of the excitation source.

Fig. 8 shows the layout of the curves for another set of parameters. In this case, the intersection between the G -curve and the β -curve never exists under the critical line, and therefore, the V-shaped part of the stationary-solutions curve never shows up.

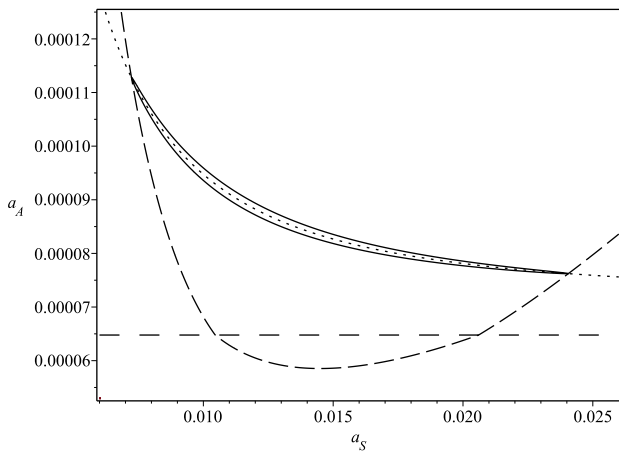


Fig. 8 Stationary conditions in the case $\rho_{00} > 1$ for the averaged system with the smooth model of the external force. The graphical-elements' descriptions and parameter values are the same as for Fig. 7, except $f_{exc} = 39.88845Hz$ and $\rho_{00} = 1.005$.

7 Stability.

In this section, the stability of the stationary condition is studied for the smooth model.

7.1 Case $a_A < a_{Acrit}$.

Symbolic relations have been given in [4], starting from following averaged system:

$$\begin{cases} \dot{a} = A(a_A)f(a)\sin(n\varphi) + g(a) \\ \dot{\varphi} = A(a_A)j(a)\cos(n\varphi) + h(a), \end{cases}$$

where $A(a_A)$ depends only on the excitation amplitude a_A . Putting $\dot{a} = 0$ and $\dot{\varphi} = 0$, obtain the following system in a_S and φ_S , representing the locus of the stationary-state in the (a_S, a_A) -plane, parameterized by φ_S :

$$\begin{cases} A(a_A)f(a_S)\sin(n\varphi_S) + g(a_S) = 0 \\ A(a_A)j(a_S)\cos(n\varphi_S) + h(a_S) = 0, \end{cases} \quad (59)$$

where a_S and φ_S are the amplitude and phase of the stationary regime.

It has been shown in said paper that the stability criterion for this system consists of two inequalities as follows, along said locus in the (a_S, a_A) -plane, after elimination of φ_S , and considering now that $A(a_A)$ is a function of a_S :

$$f \frac{d}{da_S} \left(\frac{g}{f} \right) + n j \frac{g}{f} < 0 \quad (60)$$

and

$$j f \frac{dA^2(a_A)}{da_S} > 0. \quad (61)$$

(a_S is omitted in the expressions of functions f , g , and j).

In the smooth model, in the case $a_A < a_{Acrit}$, $G(a)$ indeed does not depend on a_A , as can be seen per Eq. (49). Thus it is possible to identify Eq. (59) with Eq. (55), by doing $f(a_S) = \frac{S_n(a_S)}{4\rho}$, $g(a_S) = -\beta a_S$, $j(a_S) = \frac{D_n(a_S)}{4a_S}$, and $h(a_S) = \frac{G(a_S)}{a_S} - \frac{\rho^2 - 1}{2}$. Then, substituting these expressions into Eqs. (60) and (61), obtain following first and second inequalities:

$$\begin{cases} -2\beta < 0 \\ \frac{D_n(a_S)}{4a_S} \frac{S_n(a_S)}{4a_S} \frac{dA^2(a_A)}{da_S} > 0. \end{cases}$$

The first inequality is always true, and the second one, knowing that S_n and D_n are negative functions, and that A is always positive, amounts to $\frac{dA(a_A)}{da_S} > 0$. And as A is a monotonic increasing function of a_A , as per Eq. (46), a_A varies in

the same direction as A . Consequently, the stability criterion in the case $a_A < a_{Acrit}$ is that along the stationary-solutions curve (V-shaped part), the representative point is located in a region where function $A(a_S)$ is increasing. This is visible on numerical simulations as shown in Figs. 26 and 29.

7.2 Case $a_A > a_{Acrit}$.

In this case, relations (59) are not relevant. The calculus which led to these relations must be redone on the basis of the averaged system (54), whose general form is:

$$\begin{cases} \dot{a}_S = Af(a_S)\sin(n\varphi) + g(a_S) \\ \dot{\varphi} = Aj(a_S)\cos(n\varphi) + h(a_S) + Ak(a_S), \end{cases} \quad (62)$$

where A is a constant representative of the excitation's amplitude.

The system representing the locus of the stationary-state in the (a_S, a_A) -plane is, like previously:

$$\begin{cases} Af(a_S)\sin(n\varphi) + g(a_S) = 0 \\ Aj(a_S)\cos(n\varphi) + h(a_S) + Ak(a_S) = 0. \end{cases} \quad (63)$$

Define function $J(a_S)$ by $G(a_S, a_A) = \frac{A(a_A)}{2}J(a_S)$, and identify systems (55) and (63) to obtain $f(a_S) = \frac{S_n(a_S)}{4\rho}$, $g(a_S) = -\beta a_S$, $j(a_S) = \frac{D_n(a_S)}{4a_S}$, $h(a_S) = -\frac{\rho^2 - 1}{2}$, and $k(a_S) = \frac{J(a_S)}{2a_S}$. Then use the results of Appendix B to obtain, along the locus of the stationary-regime representative points in the (a_S, a_A) -plane:

- A first inequality identical to Eq. (60), which is always verified for the same reasons than in the case $a_A > a_{Acrit}$.
- A second inequality as follows:

$$A' \left(A - \frac{h + Ak}{j} \frac{k}{j} \right) > 0, \quad (64)$$

with $A' = \frac{dA(a_A)}{da_S}$. Substitute the expressions of f, g, h, j, k into Eq. (64) to obtain, after some classical calculus and with $G_1(a_S) = G(a_S)/a_S$:

$$A' \left(\frac{A^2}{16} \frac{D_n^2(a_S)}{a_S^2} + G_1(a_S) \left(\frac{\rho^2 - 1}{2} - G_1(a_S) \right) \right) > 0, \quad (65)$$

which is the expression of the second inequality characterizing a stable stationary regime. It can be noticed that the G-curve's equation is $G_1(a_S, a_A) = \frac{\rho^2 - 1}{2}$, which may help to graphically interpret Eq. (65), as follows. In the (a_A, a_S) plane, take a point V (a_V, a_{AV}) on the G-curve (see Fig. 9). Draw a horizontal line going through point V. This line intersects the stationary-solutions curve at two points P (to the

left of point V) and P' (to the right of V). Suppose that $A' < 0$ at point P. As function G_1 is positive, monotonic increasing, it can be seen that Eq. (65) cannot be verified if $a_S < a_V$, which means that point P, at the left of point V, is an unstable stationary regime. By contrast, Eq. (65) may be verified at point P', where $a_S > a_V$, if $A' < 0$ at P'. The conclusions are reversed if $A' > 0$.

In reference to Eq. (65), Figs. 9 and 10 shows a shaded area above the critical line, representing the region where

$$\frac{A^2}{16} \frac{D_n^2(a_S)}{a_S^2} + G_1(a_S) \left(\frac{\rho^2 - 1}{2} - G_1(a_S) \right) < 0.$$

In Fig. 10, it can be seen, above the critical line, that function $a_A(a_S)$ is decreasing on both the left and the right arcs constituting the solutions curve, and so is function $A(a_S)$, because A is a monotonic increasing function of a_A . It can be seen that the right arc of the solutions curve is located in the shaded region. Hence, the stationary regime is stable on the right arc of the solutions curve and unstable on the left arc. In Fig. 11, points P and Q, on the solutions

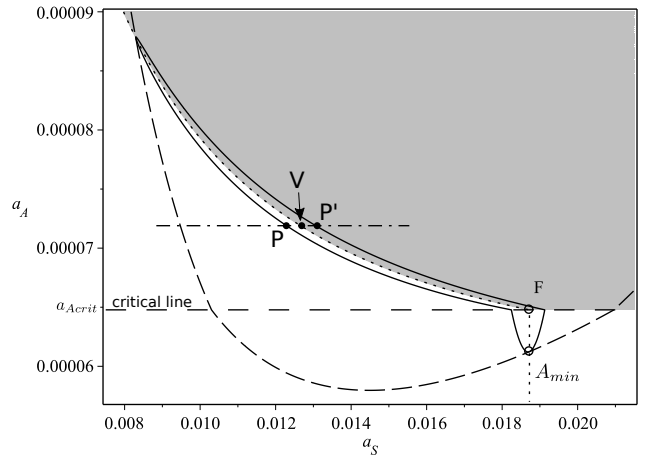


Fig. 9 An example of stability region, with same parameters and graphic elements as Fig. 7.

curve, are respectively located at the minimum of a_A and at the maximum of a_S . Appendix B shows, in paragraph “Horizontal tangent”, that point Q is located at the border of the shaded region. Consequently, in the lower right part of the solutions curve which is represented in Fig. 11, the stable part of the stationary-solutions curve is constituted by the part above points Q plus the part between point P and point Q, because between points P and Q, it holds $A' > 0$, and therefore the non-shaded area should be used to have Eq. (65) verified. Applying the same reasoning to the upper part of the stationary-solutions curve shows that there is a top horizontal-tangency point P' like point P in Fig. 11. Points P and P' constitute the border of the stable and unstable regions along the stationary-solutions curve, the stable

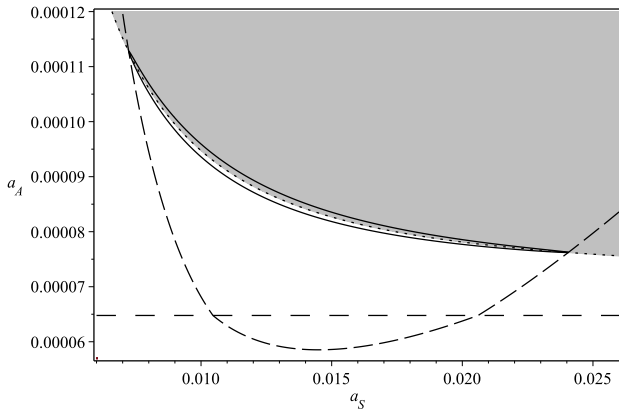


Fig. 10 An example of stability region, with same parameters and graphic elements as Fig. 8.

part of said curve being the right part of the curve between said points.

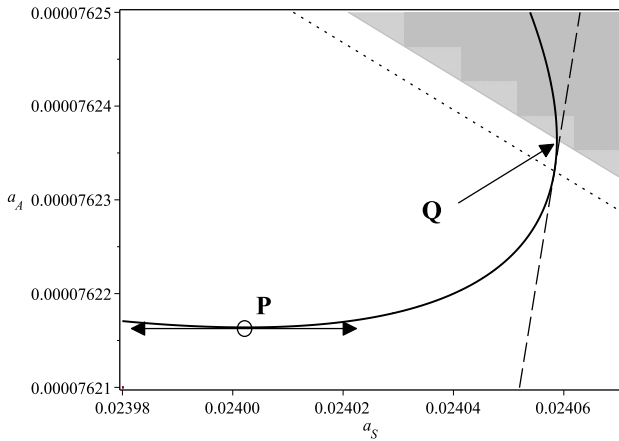


Fig. 11 Detail of Fig. 10.

8 Frequency response.

When the parameters are appropriate, the argumental phenomenon may arise, depending on the initial conditions, as can be seen in Fig. 16. The stationary-regime's amplitude can be plotted against frequency, taking into account the cases where a stationary regime establishes. When the stationary regime does not establish, a forced regime prevails. However, this is not the classical frequency-response study, because here the system needs an initial impulse to get to the stationary regime. The system evolves from the initial condition, which most often must be different of zero, towards either a stationary regime or zero. In Fig. 13, for a given fixed excitation amplitude, both stable and unstable stationary response amplitudes are plotted against excitation frequency.

The excitation amplitude has been chosen close to the Model validity upper limit so as to obtain three curves. In Fig. 12, the excitation amplitude is lower, the number of curves decreases, and the normalized response frequency gets closer to n times the fundamental free-running frequency f_{00} for low amplitudes. In Fig. 14, the damping is very low; it follows that there are more curves (the plot represents only the first six curves), and the normalized response frequency also gets closer (w.r.t. Fig. 13) to n times the fundamental free-running frequency f_{00} for low amplitudes.

For each value in abscissa, when a curve exists, two points can be seen: a lower point representing the unstable stationary amplitude, and an upper point representing the stable stationary amplitude, as has been shown in Fig. 7.

The calculus is as follows. First choose f_{00} , which is the

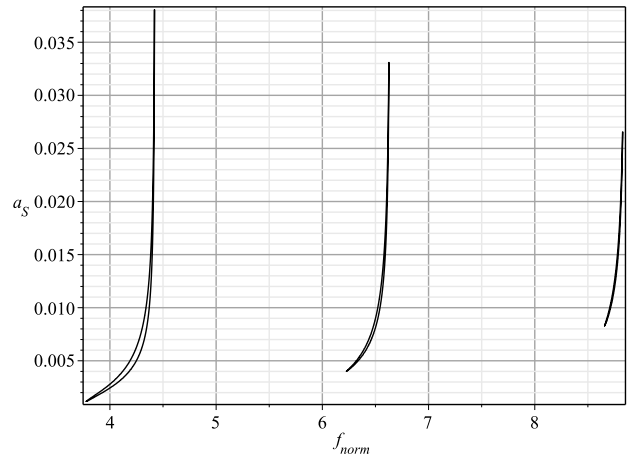


Fig. 12 An example of frequency response: beam's transverse stationary amplitude a_s against normalized excitation frequency f_{exc} (normalized by $f_{00} = 6.615$ Hz). Parameter values are: $n = 4, 6, 8$ (from left to right), $\beta = 2.4 \cdot 10^{-3}$, $F_B = 51$ N, $F_0 = -8.0$ N, $L = 0.95$ m, $k = 250$ kN/m, $f_{00} = 6.615$ Hz, and $a_A = 1.0 \cdot 10^{-4}$. Model validity upper limit = $1.01 \cdot 10^{-4}$.

fundamental frequency of the beam (an invariable system parameter), the excitation amplitude a_A , and the initial force F_0 . The independant variable is the normalized beam's frequency f_{norm} , with

$$f_{norm} = \frac{f_{exc}}{f_{00}},$$

where f_{exc} is the shaker frequency (the excitation frequency), and f_{00} is the beam's free-running frequency as defined in Section 5.3, paragraph "Parameters ω_{00} and ρ_{00} ."

It holds:

$$\rho = \rho_{00} \sqrt{\frac{F_B}{F_B + F_0}} = \frac{f_{norm}}{n} \sqrt{\frac{F_B}{F_B + F_0}}. \quad (66)$$

Substitute this last expression for ρ in Eq. (57) to obtain an implicit equation with f_{norm} as independant variable and a_s

as dependant variable, and plot the results for each successive value of n . Finally, accumulate the curves for the various values of n inside the same plot with f_{norm} as abscissa and a_S as ordinate.

It turns out that, for a given ρ , there are either zero or two solutions in a_S to Eq. (57).

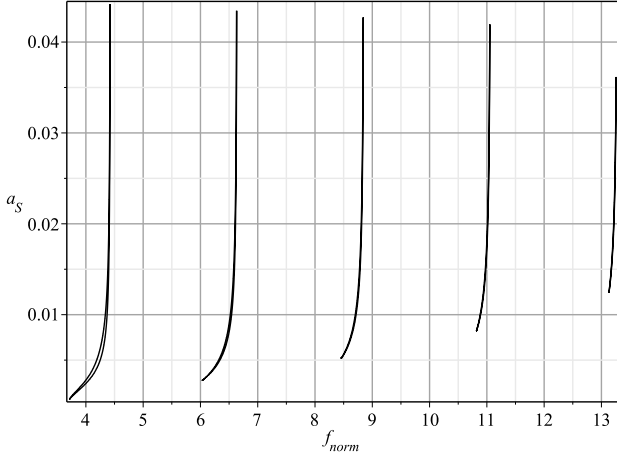


Fig. 13 An example of frequency response: beam's transverse stationary amplitude a_S against normalized excitation frequency f_{exc} (normalized by $f_{00} = 6.615 \text{ Hz}$). Parameter values are the same as for Fig. 12, except $n = 4, 6, 8, 10, 12$ (from left to right) and $\beta = 1.0 \cdot 10^{-3}$.

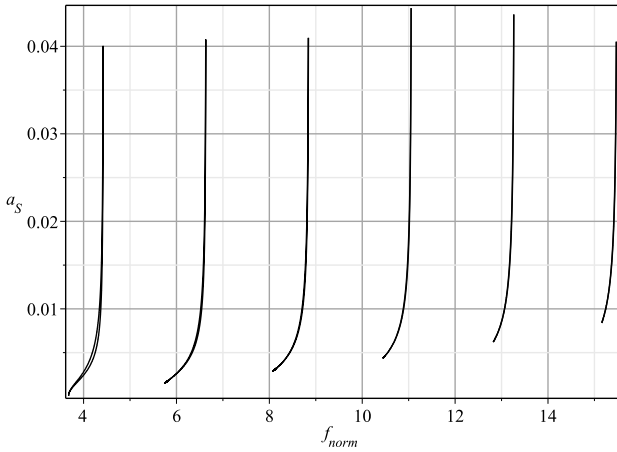


Fig. 14 An example of frequency response with almost no damping: beam's transverse stationary amplitude a_S against normalized excitation frequency f_{exc} (normalized by $f_{00} = 6.615 \text{ Hz}$). Parameter values are the same as in Fig. 13, except $n = 4, 6, 8, 10, 12, 14$ (from left to right) and $\beta = 1.0 \cdot 10^{-6}$. Not all the relevant values of n are represented: relevant values go beyond $n = 14$.

9 Comparison of two resolution methods for the smooth model of the external force.

In this section, the smooth model is studied. A comparison between the numerical solutions to the averaged system (54) and the numerical solutions to the original second-order equation (40) or (41) will test the validity of the averaging method. The numerical solver used is the Runge-Kutta solver of the Maple 18 software.

9.1 Smooth model of the external force and averaging method.

Figure 7 shows a plot of the numerical solutions to System (55), giving the stationary solutions to System (54). The parameters are those of a typical experimental setup. Each point of the plot represents a stationary motion, i.e. a motion with constant amplitude and constant phase. The abscissae are the beam's motion amplitude, while the ordinates are the excitation's, i.e. the motion amplitude of Point A represented in Fig. 1. An example of Van der Pol plot representing the solutions to the averaged system (54) with the smooth model is given in Fig. 15 for $n = 6$. When an attractor center or a saddle point is identifiable, it is one of the points of a stationary-solutions curve in the (a_S, a_A) -plane.

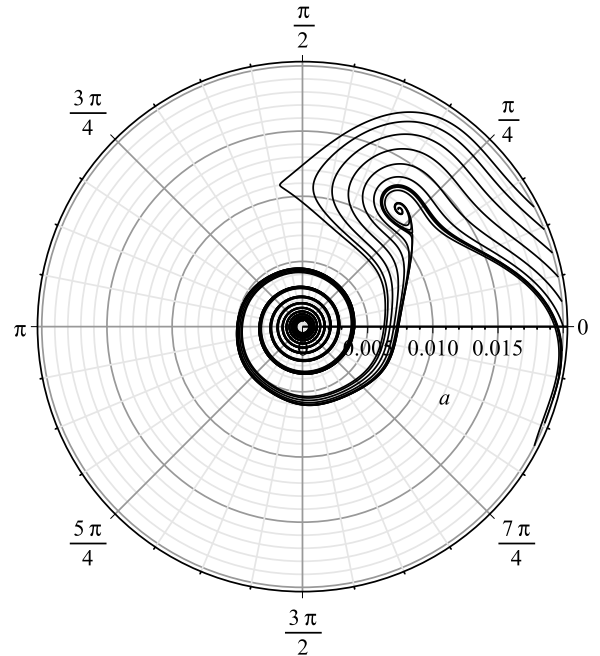


Fig. 15 Van der Pol plot, averaged system with the smooth model of the external force. a is the motion's amplitude, φ is the motion's phase. The value of a_A which is used is $7.5 \cdot 10^{-5}$. The initial values are 0.02 for a and $-0.475 \dots 0.491$ for φ . The parameter values are the same as in Fig. 7.

9.2 Smooth model of the external force and original second-order equation.

An example of Van der Pol plot representing solutions to the original second-order equation (41) with the smooth model is given in Fig. 16, to be compared to Fig. 15. It can be seen that the curves are very close to each other.

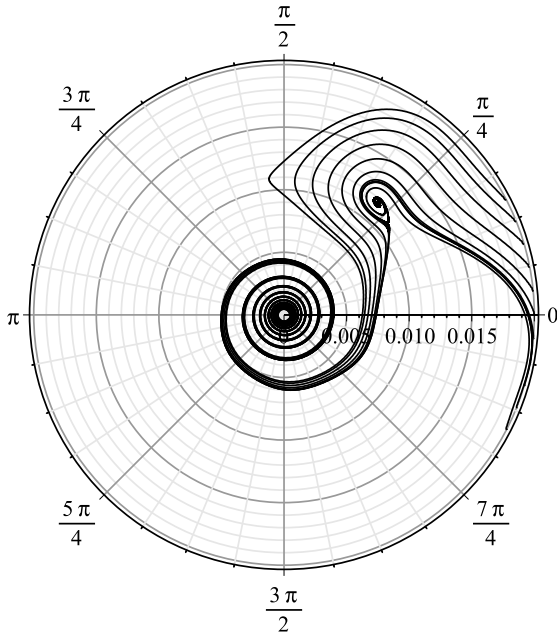


Fig. 16 Van der Pol plot, original second-order equation with the smooth model of the external force. a is the motion's amplitude, φ is the motion's phase. The parameter values and initial values are the same as in Fig. 15.

9.3 Conclusion.

With the smooth model, the comparison between the results of the original second-order equation and those of the averaged system shows that there is almost no difference between them. Therefore from now on, consider that the comparison between the smooth model and the natural model will be carried out by comparing the results of the averaged system for the smooth model and the results of the original second-order equation for the natural model.

The main advantage in using the averaged model, besides a reduction of the computing time, is that it gives access to all the symbolic relations and properties. The disadvantage is that the averaged model is based on an approximate model transforming the C^0 -class original expression of the external excitation force into an approximating C^∞ -function, more appropriate for applying the averaging method.

10 Natural model of the external force.

Having carried out the calculus about the smooth model, the calculus about the natural model remains to be done. In this section, the natural model of the external force as given by Eq. (10) is studied using a numerical solution of the original second-order equation (38). The solutions are obtained by the Runge-Kutta solver, giving q_1 as a function of t .

Construction of the Van der Pol plots. To construct the corresponding Van der Pol plots, first convert the solution into reduced-time, and then use the reciprocal relations (48), with $\rho = \omega_{exc}/(\omega_0 n)$, to obtain $a(\tau)$ and $\varphi(\tau)$. Finally, apply a low-pass filter on $a(\tau)$ and $\varphi(\tau)$ to partially cancel out the oscillations of the curves about the mean trajectory, owing to the external excitation force. An example of Van der Pol plot obtained by this method is given in Fig. 17, to be compared with Figs. 15 and 16. Here the comparison shows that the curves are similar, but not identical. This is not surprising, because the smooth model is built upon approximations. Particularly, with the help of Fig. 29, it can be seen that between the two models, offsets can be expected on the stationary amplitude a_S and on the stationary phase φ_S . In the Van der Pol plots, these offsets are visible in the positions of the attractors' centers and of the saddle points. In the (a_S, a_A) -plane, the amplitude offsets are directly identifiable as the abscissa difference between two distinct points, one on a stationary-solutions curve, the other as a discrete point resulting from a numerical calculus yielding a Van der Pol plot, followed by a manual identification on said plot.

Construction of the stable and unstable stationary-regime representative points. In the averaged smooth model, those two points are calculated for a given excitation a_A , using Eq. (55). In the natural model, they are determined graphically by observation of the Van der Pol plots obtained for a given excitation amplitude a_A . The points representing a stable stationary condition are the centers of spirals, while those corresponding to an unstable condition are the saddle type. For instance, in Fig. 17, the stable S point is at radius 0.0115 and angle $5\pi/16$, while the unstable U point is locatable at the peak of the curve near the point at radius 0.008 and angle $\pi/2 + 0.6\pi/16$, and then, knowing the problem's invariance through a rotation of $2\pi/n$, duplicated 6 times around the circle of radius 0.008, yielding a point U' at $\pi/2 + 0.6\pi/16 - 2\pi/6 \approx 3.26\pi/16$.

11 Other cases with the smooth model.

11.1 A case where $n = 14$.

To illustrate that the argumental phenomenon can arise for values of n greater than 4 or 6, a plot of the averaged-system's

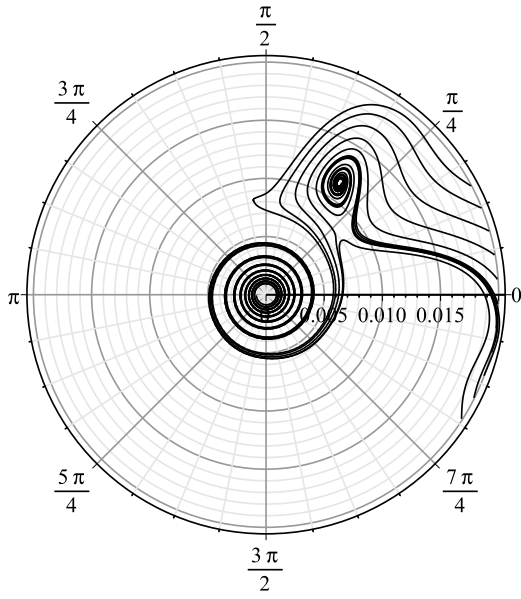


Fig. 17 Van der Pol plot, original second-order equation with the natural model of the external force. The radius is the motion's amplitude, the angle is the motion's phase. The parameter values are the same as in Fig. 16, except $a_A = 6.5 \cdot 10^{-5}$.

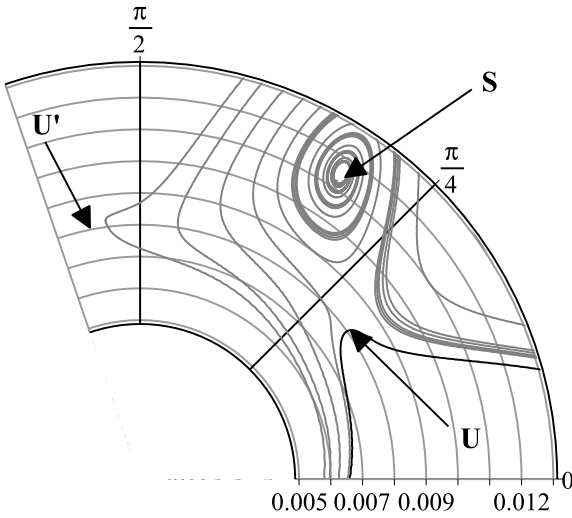


Fig. 18 Detailed view of Fig. 17. S is a stable stationary point, while U and U' are unstable ones.

stationary solutions for the smooth model with $n = 14$ is showed in Figs. 19, 20, and 21.

11.2 Cases with permanent contact.

In this paragraph, it will be shown, using the smooth model, that in certain cases, the argumental phenomenon can exist while the contact between the excitation source and the

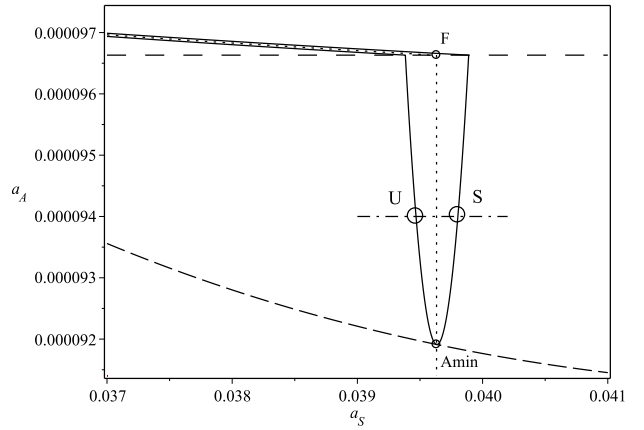


Fig. 19 Stationary condition, averaged system with the smooth model of the external force. a_S is the stationary-motion's amplitude, a_A is the excitation's amplitude. S and U are the stable and unstable stationary solutions to the averaged system when $a_A = 0.094 \cdot 10^{-3}$. Parameter values are: $n = 14$, $\beta = 1.6 \cdot 10^{-3}$, $F_B = 51 \text{ N}$, $F_0 = -22.95 \text{ N}$, $L = 0.95 \text{ m}$, $k = 250 \text{ kN/m}$, $f_{00} = 6.615 \text{ Hz}$, $f_{exc} = 92.14695 \text{ Hz}$, $\rho_{00} = 0.995$, and Model validity upper limit (in ordinate a_A) = $1.18 \cdot 10^{-4}$.

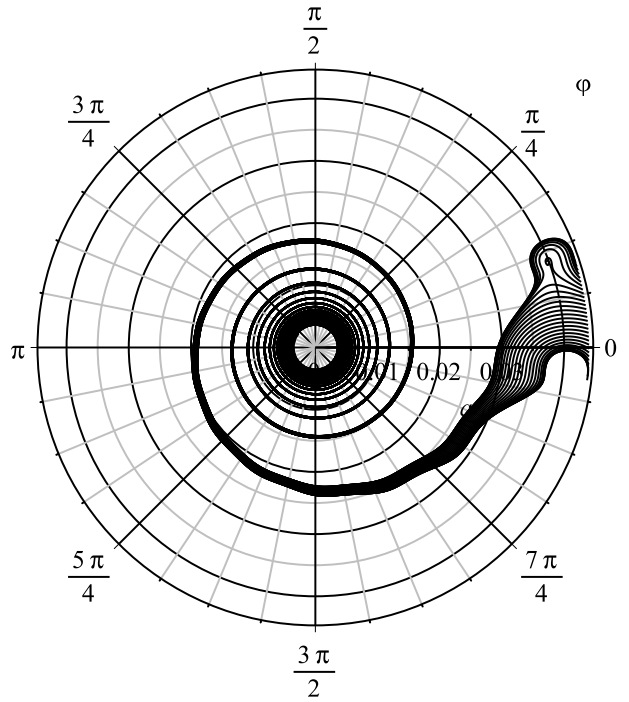


Fig. 20 Van der Pol representation for Fig. 19 when $a_A = 0.094 \cdot 10^{-3}$. The zoomed view in Fig. 21 shows more trajectories to bring out the stationary points.

beam remains permanent. Eq. (12), gives, in the (a_S, a_A) -plane, the equation defining the region where the contact is permanent:

$$a_A < -\frac{F_0}{kL} - \frac{\pi^2}{4} a_S^2 = a_{Acrit} - \frac{\pi^2}{4} a_S^2 \quad (67)$$

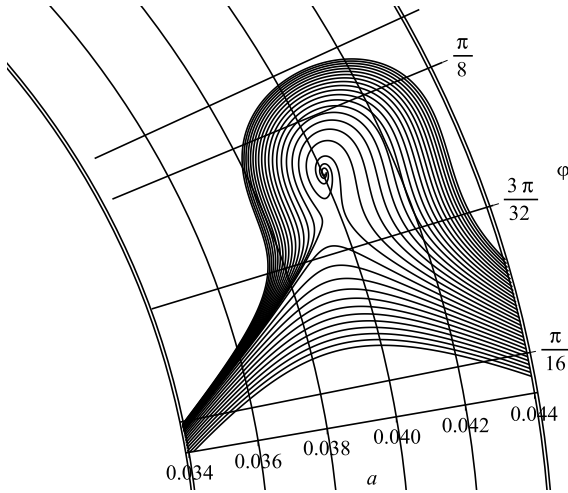


Fig. 21 Zoomed view of Fig. 20, with more trajectories to bring out the stationary points.

This is an arc of parabola with vertex at $(a_S = 0, a_A = a_{Acrit})$, and intersecting the abscissae axis at $a_S = \frac{2}{\pi} \sqrt{a_{Acrit}}$. Two examples of argumental phenomenon for a beam with permanent contact are given, in the (a_S, a_A) -plane, in Figs. 22 and 25. Fig. 23 is a Van der Pol representation in rectangular coordinates (due to visualization limits in Maple), of the motion yielded by the smooth model with the parameters of Fig. 22 and $a_A = 5.0 \cdot 10^{-5}$ (i.e. about half the Model validity upper limit). A number of threads can be seen, each thread corresponding to given initial conditions. Fig. 24 is the same, but with the natural model. For clarity's sake, there are less threads represented in Fig. 24 than in Fig. 23. It can be seen that each thread is shaky (although some filtering has been applied to enhance readability); this is because the natural model is based on the second-order initial equation of motion, whose solution renders every detailed motion due to the external force's action. The smooth model, after application of the averaging method, cancels out all tiny vibrations around the slowly-varying sinusoid which is the solution to the averaged system of equations (54), and it follows that the threads in the Van der Pol representation for this model are smooth. Comparison of Figs. 23 and 24 shows that the attractors' centers are localized in the neighborhood of each other.

12 Model comparison.

In this section, using the results from sections above, a comparison between the exact and the approximated forms of the external force will test the validity of the smooth model versus the natural model.

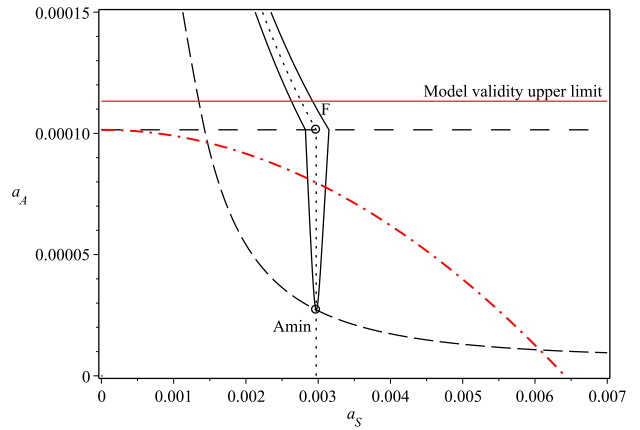


Fig. 22 A case of permanent contact with the smooth model with $n = 4$. The region where the contact is permanent is below the dash-dotted line. Parameters: $n = 4$, $F_B = 51N$, $F_0 = -24.1N$, $\rho_{00} = 0.8$, $\beta = 0.0024$, $k = 250kN/m$, $L = 0.95m$, $f_{exc} = 21.168Hz$, $f_{00} = 6.615Hz$, and Model validity upper limit $= 1.1326 \cdot 10^{-4}$. Only the part of the stationary-solutions curve (solid line) located below this limit is relevant.

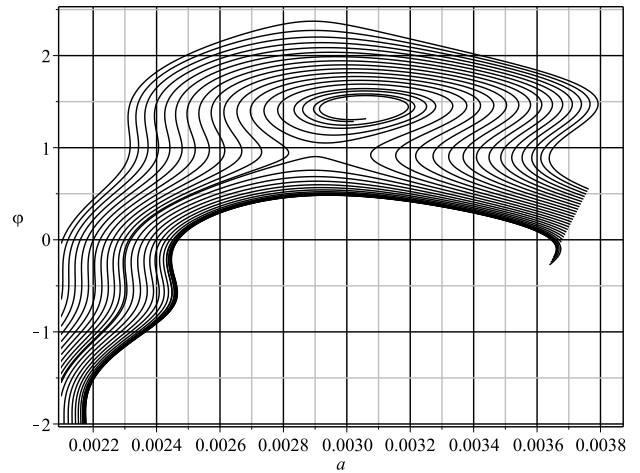


Fig. 23 Smooth-model Van der Pol simulation in rectangular coordinates. Parameters are those of Fig. 22, plus $a_A = 5.0 \cdot 10^{-5}$.

12.1 Case $n = 4$.

Figs. 26 and 27 show a comparison between the smooth model (with the averaged system) and the natural model (with the second-order equation) for $n = 4$. It can be seen that, for this set of parameters, the smooth model gives results very close to those of the natural model for low values of the excitation's amplitude a_A . In the natural model, the "V" part of the curve is skewed, while it is not in the smooth model. This is because of an approximation made in the smooth model, namely in the expression of B . A model using the expression $B = -\frac{\pi^2}{2} \frac{1}{\frac{F_0}{kL} - a_A}$ instead of $B = -\frac{\pi^2}{4} \frac{kL}{F_0}$ yields this skewed layout of the "V" part of the stationary-solutions curve. However, for simplification purposes, and

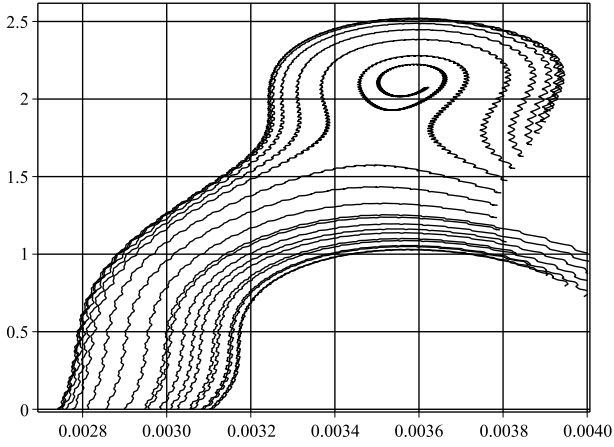


Fig. 24 Natural-model Van der Pol simulation in rectangular coordinates. Parameters are those of Fig. 23.

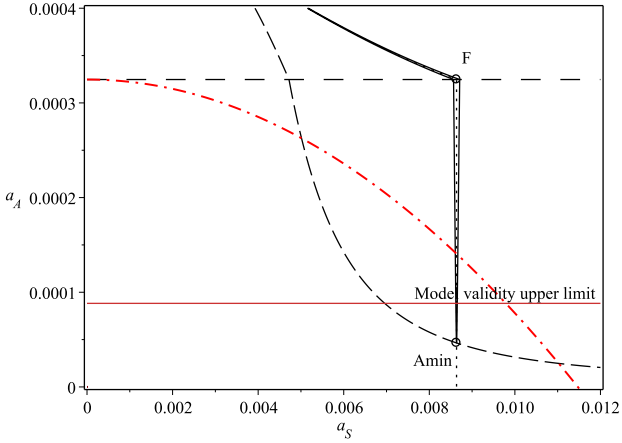


Fig. 25 A case of permanent contact with the smooth model for $n = 6$. The dash-dotted line is the border of the region where the contact is permanent. Parameters: $n = 6$, $F_B = 51N$, $F_0 = -40.1N$, $\rho_{00} = 0.75$, $\beta = 0.0008$, $k = 130kN/m$, $L = 0.95m$, and Model validity upper limit $= 8.8 \cdot 10^{-5}$. Only the part of the stationary-solutions curve (solid line) located below this limit is relevant with this model.

to allow analytical expression to be brought out, it has been decided to rather use the expression $B = -\frac{\pi^2 kL}{4 F_0}$. It can be seen that for high values of a_A , the smooth model gives solutions which do not exist in the natural model. It can be noticed that the region where the natural model and the smooth model are in good agreement is below the Model validity upper limit. As a conclusion, there is a fair agreement between smooth and natural models except in the higher region. Fig. 28 gives a few stationary-solutions curves, with parameters of Fig. 26, for various values of F_0 .

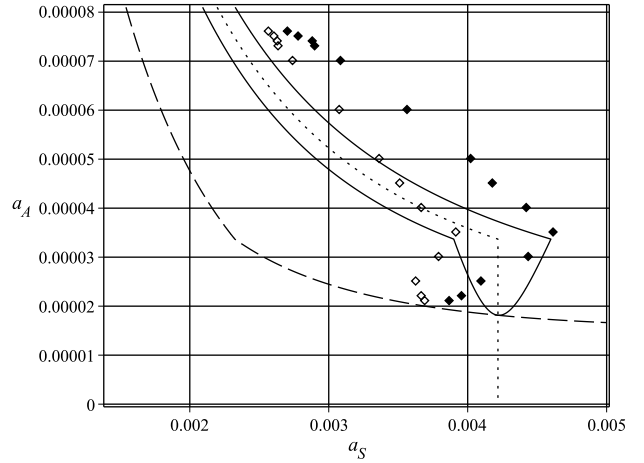


Fig. 26 Stationary condition, a_A (point A's amplitude) against a_S (stationary motion's amplitude). Comparison between natural model (with second-order equation), represented as diamonds, and smooth model (with averaged system), represented as a solid line. The G -curve is the dotted line, while the β -curve is the dashed line. Parameters are: $n = 4$, $F_B = 51N$, $F_0 = -6.4N$, $f_{00} = 6.615Hz$, $\beta = 2.4 \cdot 10^{-3}$, $L = 0.95m$, $k = 200 \cdot 10^3 N/m$, $f_{exc} = 25.849813$, and $\rho_{00} = 0.976939$. In the same way as in Fig. 7, where stable and unstable stationary solutions are represented as an infinity of points belonging to solid lines, a discrete series of stable (solid diamonds) and unstable (diamonds) stationary points are represented here. Model validity upper limit $= 1.01 \cdot 10^{-4}$.

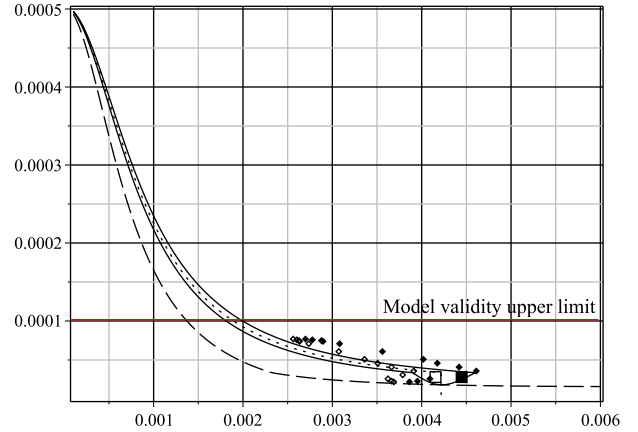


Fig. 27 This view shows the whole picture containing Fig. 26.

12.2 Case $n = 6$.

For $n = 6$, Fig. 29 uses the same parameters as Fig. 7, except $F_0 = -7.2N$, to plot the stationary solutions to the smooth model with addition of points representing the stationary results of the natural-model simulations. The full range of values for parameter a_A yielding a stationary condition in the natural model have been explored for the parameters mentioned in Fig. 7. Here the value of F_0 is close to the lower limit where the argumental phenomenon disappears. It can be seen that in this case, the results of the smooth model are not as close to the natural model as in Fig. 26, but still give

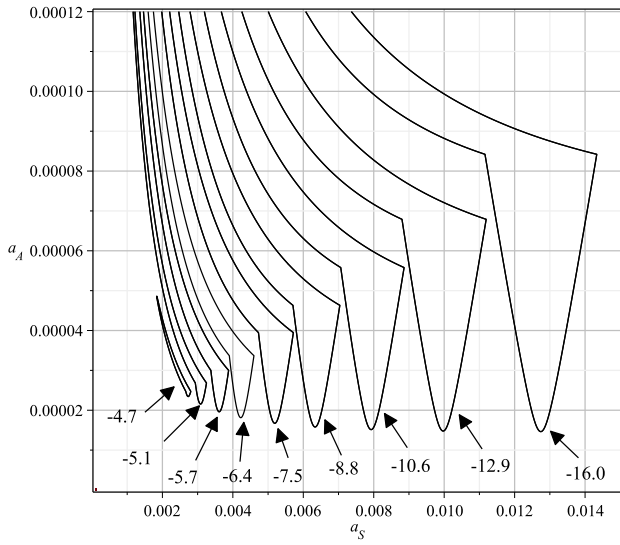


Fig. 28 Stationary condition, a_A (point A's amplitude) against a_S (stationary motion's amplitude). A few stationary-solutions curves for the smooth model, for various values of F_0 , denoted by arrows in the graph. Parameter values are the same as in Fig. 26. Worst-case (i.e. for $F_0 = -16.0$) Buckling limit $= 1.84 \cdot 10^{-4}$, and Model validity upper limit depending on F_0 , as per Equ. (28).

a fair assessment.

Given the high sensitivity of the system response versus a number of parameters, Fig. 29 shows that the curves are located in the same region of parameters a_S and a_A , although the global shape of the averaged-system curve and the natural-model curve are different. Hence the knowledge of the symbolic formulas of the smooth model constitute a guide to the choice of parameters for the natural model, which is closer to physical reality. The comparison of the curves in Figs. 15 and 16 shows that the averaging method, for the parameters used, yields very good results. The curves in Fig. 17 are fairly close to those in Figs 15 and 16. This must be viewed in the global context of Fig. 29, where it can be seen that the parameter windows for the argumental phenomenon to arise are narrow with respect to the possible parameter ranges.

12.3 Discussion.

The necessity that the parameters be located in a narrow window explains why argumental phenomenons arise rarely in the context of structure vibration. Said windows are even narrower as n increases. The example used in Figs. 7 to 17 is for $n = 6$, but Figs. 19 and 20, to be compared with Fig. 7, show how the situation evolves when $n = 14$. In this case, the windows for a_A and a_S are respectively about 30% and 3% of the central values of a_A and a_S for $n = 14$, against 45% and 70% for $n = 6$; the ratio F_0/F_B is 78% for $n = 14$, against 10% for $n = 6$, which means that, for $n = 14$, F_0

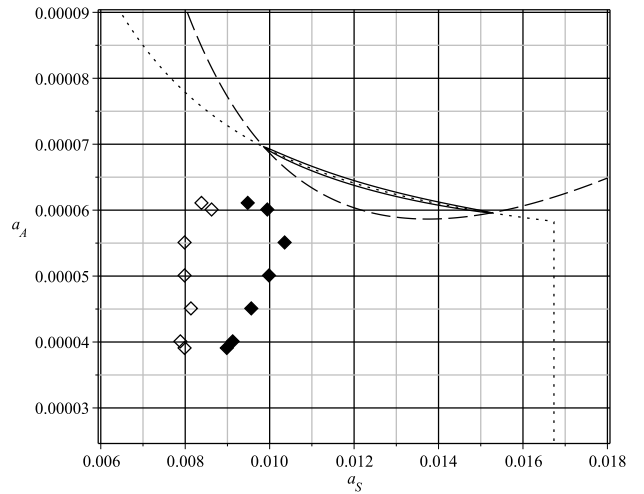


Fig. 29 Stationary condition, a_A (point A's amplitude) against a_S (stationary motion's amplitude). Comparison between second-order equation (with natural model) and averaged system (with smooth model). Parameters are the same as in Fig. 7, except $F_0 = -7.2N$, i.e.: $n = 6$, $\beta = 2.4 \cdot 10^{-3}$, $F_B = 51N$, $F_0 = -7.2N$, $L = 0.95m$, $k = 130 \text{ kN/m}$, $f_{00} = 6.615Hz$, $f_{exc} = 39.500711Hz$, $\rho_{00} = 0.9952308$. Model validity upper limit $= 3.48 \cdot 10^{-4}$. In the same way as in Fig. 7, stable and unstable stationary points are represented. Results of numerical simulations using the natural model are represented as diamonds (unstable points) and solid diamonds (stable points). Model validity upper limit $= 1.74 \cdot 10^{-4}$.

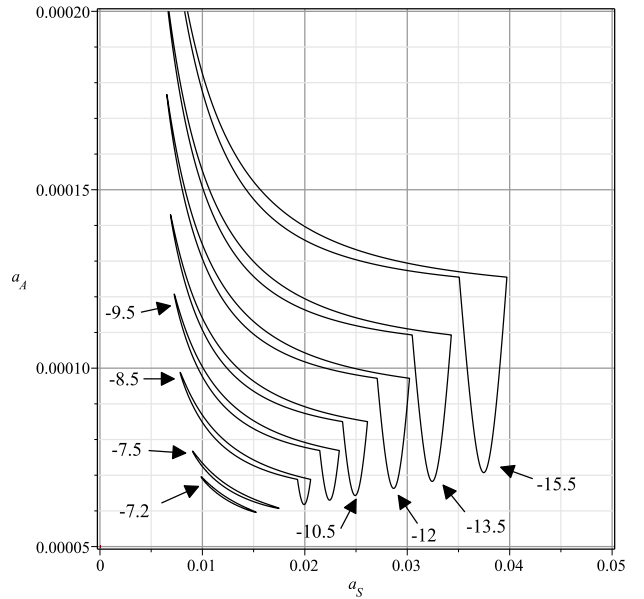


Fig. 30 Stationary condition, a_A (point A's amplitude) against a_S (stationary motion's amplitude). A few stationary-solutions curves for the smooth model, for various values of F_0 , denoted by arrows in the graph. Parameter values are the same as in Fig. 29. Worst-case (i.e. for $F_0 = -15.5$) Buckling limit $= 1.94 \cdot 10^{-4}$, and Model validity upper limit depending on F_0 , as per Equ. (28).

needs to be much higher than for the case $n = 6$ for the ar-

gumentary phenomenon to be possible.

It can be seen in the Van der Pol plots that if the right amplitude excitation (a_A) is applied and the beam is given an initial amplitude (preferably slightly larger than the expected stationary amplitude a_S), the system's trajectory will either end up into an attractor or decrease to zero due to damping, depending on initial conditions. A study of the capture probability by the attractor (the spiral) is given in [3].

Figure 30 gives some stationary-solutions curves with same parameters as Fig. 29, except for F_0 , which takes a set of values.

The coordinates of points representing stable and unstable stationary-motion conditions show that, given the high sensitivity of the Van der Pol representation and the zoom window used, the results of the smooth-model simulation are indeed a good guide to those of the natural model. They allow to numerically explore the natural model with more efficiency.

13 Conclusion.

It has been shown that when a beam under test is submitted, through a permanent or an intermittent elastic contact, to an harmonic axial excitation which is a multiple (greater than 1) of twice the beam's fundamental transverse frequency, it can enter a stationary regime, where its transverse vibration has a frequency which is the beam's fundamental transverse frequency. Besides the classical resonant case, where the axial excitation is twice the fundamental frequency of the beam, and the aforesaid multiple is equal to 1, this constitutes an argumental phenomenon.

This situation can be encountered when two beams are placed head-to-head, in axial contact, permanent or intermittent. It could seem intuitive that the argumental phenomenon is due to the intermittent contact. It has been shown that the phenomenon can also arise when the contact is permanent. Therefore, to avoid the argumental phenomenon, it is not sufficient to arrange the system so as to maintain a permanent contact.

It has also been showed that the smooth model and the natural model are sufficiently close to each other to allow to use the symbolic formulas of the smooth model to constitute a guide to the choice of parameters for the natural model, which is closer to physical reality.

14 Appendix A: Approximation to a truncated parabola.

In this Appendix, an approximation to a C^0 -class function J is studied.

Single-parabola case. Define function $J(x)$ as follows:

$$\begin{cases} J(x) = \alpha + \beta x^2 & \text{if } \alpha + \beta x^2 \leq 0 \\ J(x) = 0 & \text{otherwise} \end{cases}$$

with $\alpha < 0$ and $\beta > 0$. This is a C^0 -class function. Consider

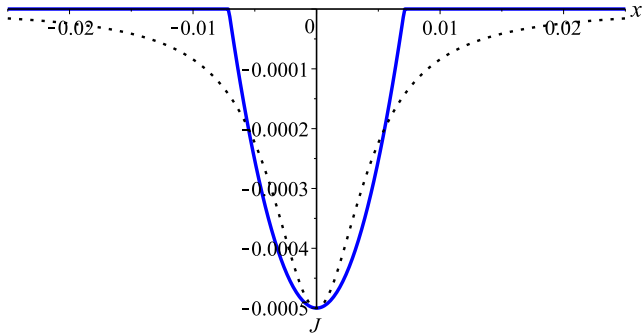


Fig. 31 Exact truncated parabola $J(x)$ (solid line) and approaching function $J_{approx}(x)$ (dotted line) J , with $\alpha = J(0) = -5 \cdot 10^{-4}$, $\beta = 10$, and $\lambda = -2.5$.

(see Fig. 31) that function

$$J_{approx}(x) = \frac{\alpha}{1 + \lambda \beta / \alpha x^2}, \quad (68)$$

with $-8 \leq \lambda \leq -2$, is a fair approximation to $J(x)$. J_{approx} is of class C^∞ .

By construction, the exact and the approached curves coincide at $(x = 0, J(0) = \alpha)$.

Parameter λ can be determined by choosing a coincidence point common to the exact and the approached curves. If the desired coincidence point is determined by its abscissa x_1 , then take: $\lambda = \frac{-\alpha}{\alpha + \beta x_1^2}$, so that

$$J_{approx}(x) = \frac{\alpha}{1 - \frac{\beta}{\alpha + \beta x_1^2} x^2}.$$

Now, if the coincidence point is determined by its ordinate

$J_{co} = J(x_1)$, take $\lambda = -\frac{J(0)}{J_{co}}$, so that

$$J_{approx}(x) = \frac{\alpha}{1 - \frac{J(0)}{J_{co}} \frac{\beta}{\alpha} x^2}.$$

Plateau case. In case the vertex of parabola $J(x) = \alpha + \beta x^2$ is truncated, the function J to be approximated shows a plateau, as can be seen in Fig. 32. Let J_{pl} be the plateau's

ordinate, and J_{co} the coincidence point's ordinate. Then, as previously, $\lambda = -\frac{J_{pl}}{J_{co}}$. Searching an approximating function

under the form $J_{approx}(x) = \frac{J_{pl}}{1 + \zeta x^2}$, search for the expression of ζ by writing that functions J (truncated parabola) and J_{approx} coincide at ordinate $J_{pl}/(-\lambda)$. Obtain $\zeta = \beta \frac{1 + \lambda}{\alpha + \frac{J_{pl}}{\lambda}}$, and therefore

$$J_{approx}(x) = \frac{J_{pl}}{1 + \beta \frac{1 + \lambda}{\alpha + \frac{J_{pl}}{\lambda}} x^2} \quad (69)$$

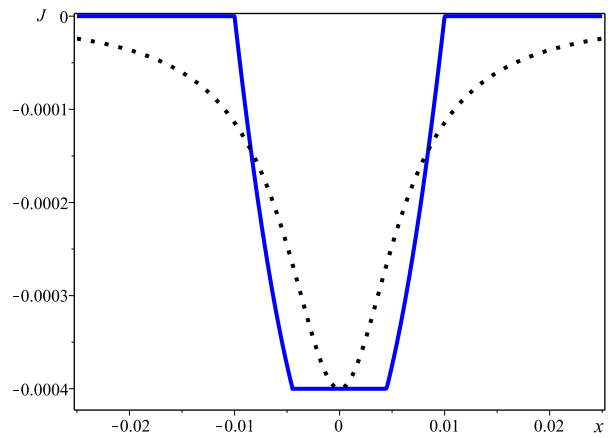


Fig. 32 Exact truncated parabola J (solid line) and approaching function J_{approx} (dotted line), with $\alpha = -5 \cdot 10^{-4}$, $\beta = 5$, $\lambda = -2$, and a plateau at ordinate $-4 \cdot 10^{-4}$.

Composite-parabola case. In this case, function $J(x)$ consists of two connected parabola arcs, intersecting at point I, as shown in Fig. 33. First parabola (left of point I) is $J(x) = \alpha_1 + \beta x^2$, with vertex at V_1 , while second one (right of point I) is $J(x) = (\alpha_2 + \beta x^2)/2$, with vertex at V_2 . The idea is to use the mean parabola to approximate the two parabola arcs. Let P and Q be the respective points of the higher and lower parabola located at ordinate zero. Let T be the geometric mean of points P and Q, and let the vertical-axis parabola passing through T and having vertex V_1 be called “mean parabola”, with equation $J(x) = \alpha_1 + \xi x^2$, with ξ being a parameter to be determined. It holds $x_Q = \sqrt{-\alpha_1/\beta}$, $x_P = \sqrt{-\alpha_2/\beta}$, and $x_T^2 = x_P x_Q = \sqrt{\alpha_1 \alpha_2}/\beta$. Obtain $\xi = \beta \sqrt{\frac{\alpha_1}{\alpha_2}}$. Now to approximate the mean parabola representing equation $J(x) = \alpha_1 + \xi x^2$, use function $J_{approx}(x) = \frac{\alpha_1}{1 + \lambda \frac{\beta_{app}}{\alpha_1} x^2}$,

where β_{app} is a coefficient to be determined. Obtain

$$J_{approx}(x) = \frac{\alpha_1}{1 - \frac{\lambda \beta}{\sqrt{\alpha_1 \alpha_2}} x^2}. \quad (70)$$

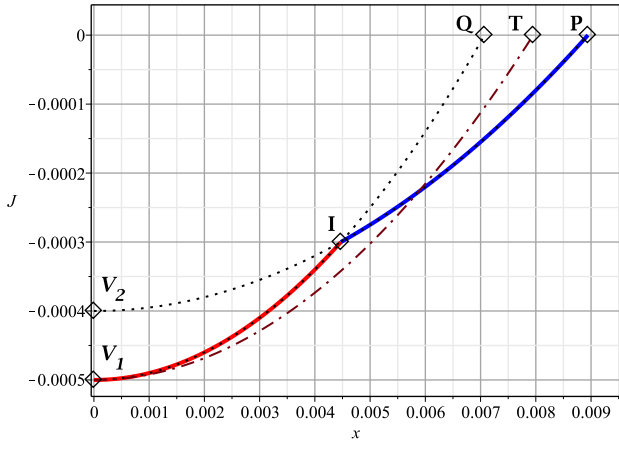


Fig. 33 J function consisting of two parabola arcs (solid lines), one at left of point I with vertex V_I at α_1 , and one at right of point I with vertex V_2 at $\alpha_2/2$. Construction lines for the rest of the parabolas are in dotted lines. The “mean” parabola representing J_{approx} is the dash-dotted line. Parameters: $\alpha_1 = -5 \cdot 10^{-4}$, $\alpha_2 = -8 \cdot 10^{-4}$, and $\beta = 10$. For clarity’s sake, only the positive abscissae are represented.

15 Appendix B: a stability criterion.

In this Appendix, it is brought out a stability criterion of a differential-equations system which is encountered in a number of argumental physical setups after applying the averaging method. This is an extension to the stability criterion given in [4].

Consider a differential system as follows:

$$\begin{cases} \dot{a} = Af(a) \sin(n\varphi) + g(a) = F(a, \varphi) \\ \dot{\varphi} = Aj(a) \cos(n\varphi) + h(a) + Ak(a) = G(a, \varphi), \end{cases} \quad (71)$$

where A is a constant representative of the excitation's amplitude, and the dot notation represents the differentiation w.r.t. (with respect to) reduced time τ . This kind of system is obtained when a solution of the form $a(\tau) \sin(\rho\tau + \varphi(\tau))$ is tested, where a and φ are slowly-varying quantities (slowly is meant with reference to the excitation source) and ρ is a parameter to be determined.

To bring out a stability criterion, use the same process than in [4], using the same notations.

From condition $F'_a + G'_\varphi < 0$, a first inequality is obtained, which is the same as in [4], as follows:

$$f \frac{d}{da} \left(\frac{g}{f} \right) + nj \frac{g}{f} < 0,$$

where a quote applied to a lowercase letter denotes the differentiation w.r.t. a , while the quote applied to an uppercase letter denotes the differentiation w.r.t. the index of said letter.

Then, recalling that the second inequality characterizing a stable stationary condition writes

$$F'_a G'_\varphi - F'_\varphi G'_a > 0, \quad (72)$$

obtain

$$\begin{aligned} \frac{F'_a G'_\varphi - F'_\varphi G'_a}{n} = \\ -f' j \frac{g^2}{f^2} + g' j \frac{g}{f} - j' f \frac{(h+Ak)^2}{j^2} + \frac{f}{j} (h+Ak)(h'+Ak'). \end{aligned} \quad (73)$$

In system (71), make $\dot{a} = 0$ and $\dot{\varphi} = 0$, then eliminate φ , to obtain a system which represents the locus of the stationary condition expressed in the coordinates (A, a_S) :

$$A^2 = \frac{g^2}{f^2} + \frac{(h+Ak)^2}{j^2}. \quad (74)$$

Then, along said locus, consider A as a function of a_S and differentiate Equ (74) w.r.t. a_S to obtain:

$$A' = \frac{\frac{gg'}{f^2} - \frac{g^2 f'}{f^3} + \frac{(h+Ak)(h'+Ak')}{j^2} - \frac{(h+Ak)^2 j'}{j^3}}{A - \frac{h+Ak}{j} \frac{k}{j}}.$$

Compare with Eq. (73) to deduce, after a few transformations, a relation along the locus of the stationary condition:

$$F'_a G'_\varphi - F'_\varphi G'_a = \frac{1}{2} j f \frac{dA^2}{da} \left(A - \frac{h+Ak}{j} \frac{k}{j} \right) \frac{n}{A}. \quad (75)$$

Use Equ (72) and substitute $2AA'$ for $\frac{dA^2}{da}$ in Eq. (75) to obtain the second inequality characterizing the stable stationary condition:

$$j f A' \left(A - \frac{h+Ak}{j} \frac{k}{j} \right) > 0. \quad (76)$$

Horizontal tangent. Notice that this inequality vanishes when $A' = 0$, i.e. when the locus of the stationary condition has a horizontal tangent. Now differentiate Eq. (74) w.r.t. A and a , to obtain

$$2 \left(\frac{(h+Ak)k}{j^2} - A \right) dA + \frac{\partial}{\partial a} \left(\frac{g^2}{f^2} + \frac{(h+Ak)^2}{j^2} \right) da = 0,$$

which shows that expression

$$\frac{(h+Ak)k}{j^2} - A \quad (77)$$

vanishes at points where the locus of the stationary condition defined by Eq. (74) has a vertical tangent. It follows that inequality (76) vanishes at points where the tangent to said locus has a horizontal or a vertical tangent. And when both A' and (77) change sign at the same point, the validity of the stability criterion (76) remains when going through said point. This situation occurs when the vertical tangent is at a point where the locus curve is convex. Conversely, if the vertical tangent is an inflexion point, only (77) changes sign, and consequently the stability criterion toggles.

The rules regarding tangents also hold in the (a_A, a_S) – plane defined in this paper, because $A(a_A)$ is a monotonic increasing function of a_A .

References

1. Béthenod, M.: Sur l'entretien du mouvement d'un pendule au moyen d'un courant alternatif de fréquence élevée par rapport à sa fréquence propre. *Comptes rendus hebdomadaires de l'Académie des sciences* **207**(19), 847–849 (1938). URL <http://gallica.bnf.fr/ark:/12148/bpt6k31590>. (in French)
2. Bogolioubov, N., Mitropolski, I.: *Les méthodes asymptotiques en théorie des oscillations non linéaires*. Gauthiers-Villars (1962)
3. Cintra, D., Argoul, P.: Attractors capture probability in non-linear argumental oscillators. *Communications in Nonlinear Science and Numerical Simulation* **48**(Supplement C), 150 – 169 (2017). DOI <https://doi.org/10.1016/j.cnsns.2016.12.023>. URL <http://www.sciencedirect.com/science/article/pii/S1007570416305159>
4. Cintra, D., Argoul, P.: Non-linear argumental oscillators: Stability criterion and approximate implicit analytic solution. *International Journal of Non-Linear Mechanics* **94**(Supplement C), 109 – 124 (2017). DOI <https://doi.org/10.1016/j.ijnonlinmec.2017.03.013>. URL <http://www.sciencedirect.com/science/article/pii/S0020746217301981>. A Conspectus of Nonlinear Mechanics: A Tribute to the Oeuvres of Professors G. Rega and F. Vestroni
5. Cintra, D., Argoul, P.: Nonlinear argumental oscillators: A few examples of modulation via spatial position. *Journal of Vibration and Control* **23**(18), 2888–2911 (2017). DOI [10.1177/1077546315623888](https://doi.org/10.1177/1077546315623888). URL <https://doi.org/10.1177/1077546315623888>
6. Cintra, D., Cumunel, G., Argoul, P.: Experimental study of the argumental transverse vibration of a beam excited through permanent or intermittent elastic contact by a harmonic axial motion. *Journal to be determined* (2017)
7. Cintra, D., Cumunel, G., Argoul, P.: A few properties in symbolic form for the argumental transverse vibration of a beam excited through permanent or intermittent elastic contact by a harmonic axial motion. *Journal to be determined* (2017)
8. Cretin, B., Vernier, D.: Quantized amplitudes in a nonlinear resonant electrical circuit. In: 2009 Joint Meeting of the European Frequency and Time Forum and the IEEE International Frequency Control Symposium, vols 1 and 2, vol. 1 & 2, pp. 797–800. Joint Meeting of the 23rd European Frequency and Time Forum/IEEE International Frequency Control Symposium, Besançon, France (2009). URL <http://arxiv.org/ftp/arxiv/papers/0801/0801.1301.pdf>
9. Doubouchinski, D.: Argumental oscillations. Macroscopic quantum effects. *SciTech Library* (2015). URL <http://www.sciteclibrary.ru/rus/catalog/pages/15207.html>
10. Doubouchinski, D., Doubouchinski, J.: Amorçage argumentaire d'oscillations entretenues avec une série discrète d'amplitudes stables. *E.D.F. Bulletin de la direction des études et recherches, série C mathématiques, informatique* **3**, 11–20 (1991). (in French)
11. Humar, J.: *Dynamics of Structures*. A.A. Balkema (2001)
12. Penner, D.I., Duboshinskii, D.B., Kozakov, M.I., Vermel, A.S., Galkin, Y.V.: Asynchronous excitation of undamped oscillations. *Phys. Usp.* **16**(1), 158–160 (1973). DOI [10.1070/PU1973v016n01ABEH005156](https://doi.org/10.1070/PU1973v016n01ABEH005156). URL <https://ufn.ru/en/articles/1973/1/m/>
13. Pratiher, B., Dwivedy, S.K.: Nonlinear response of a flexible cartesian manipulator with payload and pulsating axial force. *Nonlinear Dynamics* **57**(1), 177–195 (2009). DOI [10.1007/s11071-008-9431-6](https://doi.org/10.1007/s11071-008-9431-6). URL <https://doi.org/10.1007/s11071-008-9431-6>
14. Treilhou, J., Coutelier, J., Thocaven, J., Jacquez, C.: Payload motions detected by balloon-borne fluxgate-type magnetometers. *Advances in Space Research* **26**(9), 1423–1426 (2000)

Experimental study of the argumental transverse vibration of a beam excited through permanent or intermittent elastic contact by a harmonic axial motion

Daniel Cintra (corresponding author), Gwendal Cumunel
Université Paris-Est,
Laboratoire Navier (UMR 8205), CNRS, ENPC, IFSTTAR,
6 et 8, avenue Blaise Pascal,
Cité Descartes, Champs-sur-Marne,
F-77455 Marne La Vallée Cedex 2, France.
email: daniel.cintra@enpc.fr, gwendal.cumunel@enpc.fr
and

Pierre Argoul
IFSTTAR, Laboratoire MAST-SDOA,
F-77455 Marne La Vallée, Cedex 2, France
email: pierre.argoul@ifsttar.fr

Abstract

The transverse vibration of a beam excited axially by a harmonic motion transmitted through intermittent elastic contact is experimentally studied. The beam's configuration is clamped-(clamped-guided). It is shown that this vibration is in the fundamental transverse mode of the beam, and can occur when the frequency of the excitation is four or six times the frequency of the fundamental transverse mode. The energy transfer between the excitation source and the beam occurs only when the beam is in certain spatial configurations. This constitutes an argumental phenomenon. Experimental results are given and compared to models.

Keywords— nonlinear dynamics; argumental oscillator; beam transverse vibration; axial excitation; spatial modulation; Van der Pol representation.

Contents

1	Introduction.	3
2	System configuration.	4
	Notations:	5
3	Experimental setup.	6
3.1	Description.	6
	Remark.	7
3.2	Spectral-purity monitoring.	8
3.3	Calibration for the case $n = 4$	11
3.4	Calibration for the case $n = 6$	14
4	Experimental results.	16
4.1	Frequency ratio: $n = 4$	16
4.2	Frequency ratio: $n = 6$	21
5	Conclusion.	25

1 Introduction.

The so-called argumental oscillator is a mechanical system which has a stable motion consisting of a periodic motion at a frequency next to its natural frequency when submitted to an external force whose frequency is close to a multiple of said natural frequency. One necessary condition for the phenomenon to arise is that the external force be dependent on the space coordinate of the oscillator. An oscillator exhibiting such characteristics has been described in 1928 [1]; this oscillator was a pendulum fitted with a steel sphere at the tip of the rod, submitted to a harmonic magnetic field spatially localized at the bottom of the sphere's course.

The word “argumental” was forged in 1973 [10], where a pendulum is submitted to an electric field spatially localized at the bottom of the pendulum's course.

Further developments were carried out [8,9], particularly the “multiple resonance” and the “quantum effect”. The multiple resonance is a phenomenon in which a number of oscillators, each having its own resonance frequency, submitted to a unique common excitation frequency, can oscillate simultaneously. This is possible if each oscillator has an actual frequency which is a sub-multiple of the excitation frequency, and if the interaction zone between each oscillator and the excitation source is spatially localized. The quantum effect is when an oscillator can oscillate at a number of stable amplitudes whose frequencies are sub-multiples of a fixed excitation frequency. This is possible if the oscillator's actual frequency depends on its amplitude, which is the case for a classical pendulum, and if the excitation source is spatially localized.

Argumental oscillations have also been observed and described in balloon-borne magnetometer measurements [12] and in an electrical circuit [7]. A few examples of argumental oscillators, consisting of six variations of a pendulum excited by magnetic forces, have been modeled and experimented [6]. A stability criterion in symbolic form and an approximate analytic solution for an argumental oscillator have been given [5]. Capture probabilities by an attractor in an argumental oscillator have been given in symbolic form [4].

As for the beams receiving axial excitation, a cantilever beam submitted to a harmonic force through its base and to a pulsating axial force through its tip, and carrying a payload at its tip, has been studied in [11].

A typical second-order ordinary differential equation for a one-degree-of-freedom argumental oscillator is:

$$\ddot{x} + 2\beta\omega_0\dot{x} + \omega_0^2x = g_1(x) + g_2(x)\cos(\omega_{exc}t), \quad (1)$$

where x is the space coordinate, β is the damping ratio, ω_0 is the natural angular velocity of the oscillator, g_1 and g_2 are functions of x , and ω_{exc} is the angular

velocity of the excitation.

The classical averaging calculus makes the hypothesis that the solution has the form $x(t) = a(t)\sin(\rho\omega_0 t + \varphi(t))$, where $a(t)$ and $\varphi(t)$ are slowly-varying functions of time, “slowly” being with respect to the excitation’s signal. This yields the following system, if ρ is chosen so that $n = \frac{\omega_{exc}}{\rho\omega_0}$ is an even integer:

$$\begin{cases} \dot{a} &= \frac{A(a_A)}{4\rho} S_n(a) \sin(n\varphi) - \beta a \\ \dot{\varphi} &= \frac{G(a, a_A)}{\rho a} + \frac{A(a_A)}{4\rho a} D_n(a) \cos(n\varphi) - \frac{\rho^2 - 1}{2\rho}, \end{cases} \quad (2)$$

with $A(a_A)$ representing the excitation amplitude a_A , S_n and D_n being two functions of a , G being a function of a and the excitation amplitude a_A .

In this paper, the transverse vibration of a beam excited axially by a harmonic motion transmitted through intermittent elastic contact is experimentally studied. The beam’s configuration is clamped-(clamped-guided) (see Fig. 1). It has been shown [3] that this system obeys an argumental equation, and that two models can be devised:

- A discontinuous “natural model”, deduced directly from simple physical laws and the arrangement of the constituting components: beam, spring, and points M and A, leading to numerical simulations.
- A continuous “smooth model”, approximation to the natural model, allowing a solution using the averaging method [5].

Using experimental results, a comparison is made in this paper with the numerical simulations on the natural model and with the solution provided by the smooth model, using the averaging method. In [2], a few symbolic properties of this system are given.

2 System configuration.

The schematic system configuration is as shown in Fig. 1. A beam is represented, with its left end S and right end M, in a clamped-(clamped-guided) configuration. At the point M’s side, the clamp is carried out by way of a massless trolley. Point M is intermittently pushed to the left by a plate C, which is linked to a point A via a massless spring. $\mathbf{F} = F\mathbf{i}$, where \mathbf{i} is the unit vector along the abscissae axis, is the force intermittently applied by plate C to the beam’s right end at M. F is negative when the beam is in compression. In the figure, point A moves horizontally with a harmonic motion, in such a manner that the contact between plate C and point M be intermittent when the beam and point A are vibrating. When the beam is in resting (i.e. rectilinear) position and point A is in center position, the force applied to point M is denoted

by F_0 .

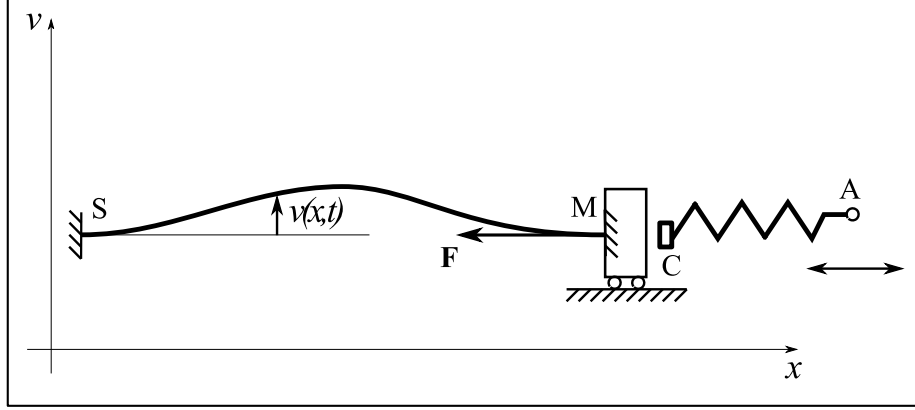


Figure 1: System configuration. x is the horizontal abscissa, v is the transverse displacement, t is the time, and \mathbf{F} is the force applied by plate C to the beam at point M. Point M moves freely horizontally, but is clamped vertically. There is no rotation at S and M.

Notations:

- ω_{exc} is the angular frequency of the excitation source at point A,
- F_0 is the force F when the beam is at rest and point A is at rest in central position,
- F_B is the beam's critical buckling force,
- ω_0 is the beam's natural angular frequency when point A is at rest in its central position, with $\omega_0^2 = a_1 \left(\frac{\pi}{L}\right)^2 \frac{F_B + F_0}{\mu S}$, where $a_1 = 1$ in the hinged-(hinged-guided) case, and $a_1 = 4/3$ in the clamped-(clamped-clamped) case, μ = mass per volume unit of the beam, S = section of the beam,
- n is an even integer roughly equal to $\frac{\omega_{exc}}{\omega_0}$,
- ρ is a parameter, generally close to 1, chosen so as to have $\frac{\omega_{exc}}{\rho\omega_0} = n$,
- k is the spring's stiffness,
- L is the beam's length,
- aL is the amplitude of the beam's motion (a is adimensioned),

- $a_S L$ is the amplitude of the beam's stationary-motion (a_S is adimensioned),
- $a_A L$ is the amplitude of the excitation at point A (a_A is adimensioned),
- ρ_{00} is defined as $\rho \sqrt{\frac{F_B}{F_B + F_0}}$,
- β is the experimentally-measured beam's damping ratio,
- A is a function of a_A characterizing the excitation amplitude,
- S_n and D_n are two functions of a characterizing the spectral components of the interaction between the BUT and the external excitation,
- G is a function of a and a_A characterizing the spatial localization of the interaction between the BUT and the external excitation.

3 Experimental setup.

Define n the frequency ratio of the excitation frequency to the beam's transverse motion frequency. In this section, the experimental setup which has been used to test the cases $n = 4$ and $n = 6$ is presented, along with its calibration procedure.

3.1 Description.

To implement the arrangement shown in Fig. 1, a “beam under test” (BUT) is placed at the left-hand of the experimental setup, while the spring and point A of Fig. 1 are embodied by a second beam, called “control beam”, which is excited transversally by a shaker (see Fig. 2). The point A of Fig. 1 is embodied by the junction point between the control beam and the shaker's rod, while the spring of Fig. 1 is embodied by the control beam. Thus, the elasticity of the spring is embodied by the bending elasticity of the control beam. Although the bending elasticity of the control beam is not strictly constant, the experiments and calibrations show that it can be considered constant over the displacement range of the shaker for the experiments which were carried out. Both beams are made of aluminum. The boundary conditions of the BUT are: clamped at the left end and clamped-guided at the right end, where the translational joint is achieved by means of two thin spring steel strips (0,4 mm thickness), as seen in Fig. 3, in a parallelogram configuration allowing the translation of the beam attached to them. As for the control beam, the left end is a clamped-guided joint and the right end is a decentered revolute joint. The decentered revolute joint consists of a cylinder, the circumference of which the end of the beam is attached to, and of two bearings, as illustrated in Fig. 4. To minimize the rotation at the left end of the control beam, due to its small length, the distance between the strips is increased, compared to the configuration of the right end

of the BUT (see Fig. 3).

In order to limit the occurrence of high-frequency modes of the BUT, its first resonance frequency is lowered by addition of local masses. Stiffeners are added to isolate the first mode by pushing aside the higher modes. The same procedure is done on the control beam. A steel ball is machined and glued on the edge of the BUT so as to provide a punctual (sphere-plane) contact between the two beams. To adjust the intermittent contact of the two beams, allowing the occurrence of the researched phenomenon, a steel spring strip (thickness of 0,1 to 0,3 mm) can be added, if necessary, between the ball and the control beam (see Fig. 3).

The measurements are carried out by two laser displacement sensors (Keyence IL-030, around $1\mu m$ resolution, time step of 0,33 ms): one near the left end of the BUT to measure its deflection (see Fig. 5), and the other one, located near the center of the control beam and in front of the shaker, to measure the deflection of the control beam. The shaker (Modalshop model 2004E), driven by a power amplifier (B&K 2719), is used to transversally excite the control beam. The connection between the shaker and the beam is made by way of a centered revolute joint (see Fig. 6).

As the position of point A of Fig. 1 must be precisely commanded, the shaker's position is controlled by a feedback loop. The global synoptic diagram is in Fig. 7. A CompactRIO controller (NI 9076) with two CompactDAQ modules (NI 9234 for the measurements acquisition and NI 9263 for the excitation signal generation) is used to carry out the active control of the shaker. Except for the feedback-control part of this diagram, the system's principle and logic implementation is the same as described in [6].

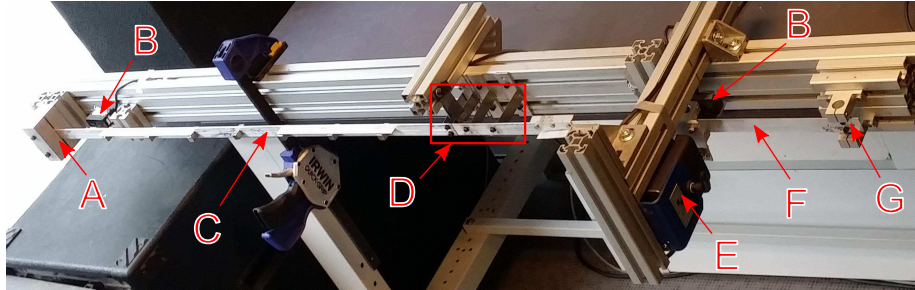


Figure 2: Experiment's global view. A: clamped joint, B: position sensor, C: beam under test (BUT), D: spring steel strips region (detailed in Fig. 3), E: shaker, F: control beam, G: decentered revolute joint.

Remark. In this paper, the experiments are made with two beams so arranged that the head of the control beam has a motion frequency the same as the control beam's transverse motion, because the control beam's position at rest is offset from the rectilinear position (see Fig. 8).

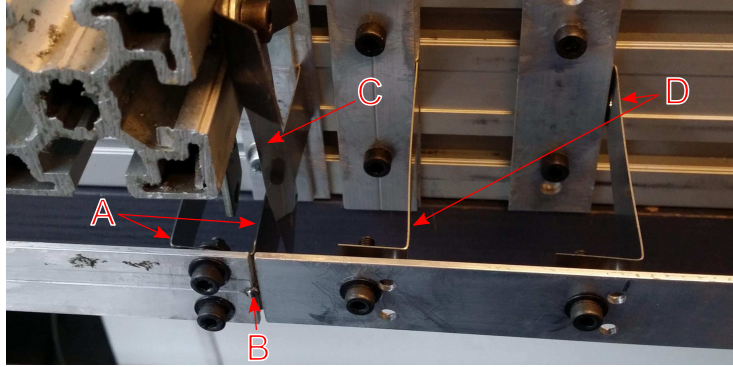


Figure 3: Contact point's environment. A: spring steel strips of the beam under test (BUT), B: steel ball at the contact point between the two beams, C: contact-adjustment spring steel strip, D: spring steel strips of the control beam.

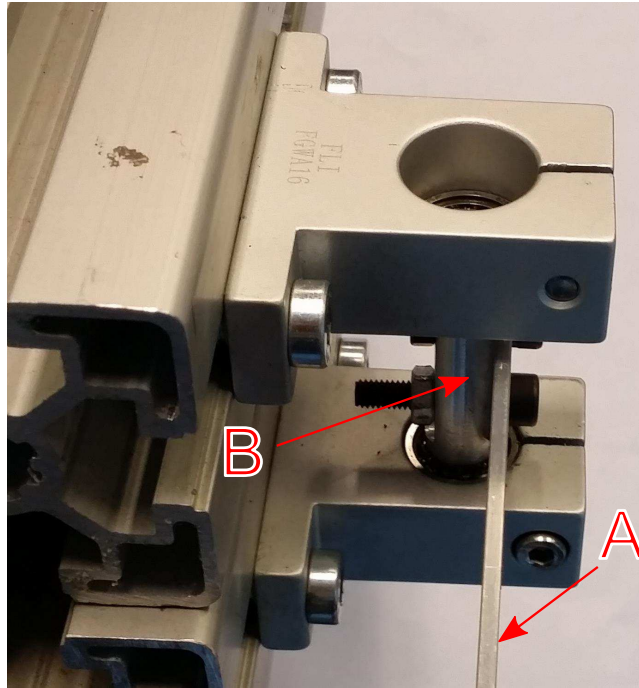


Figure 4: Control beam's pivot joint. A: control beam, B: decentered revolute joint.

3.2 Spectral-purity monitoring.

To ensure that the shaker does not introduce signals into the beam under test (BUT) which induce a classical resonance of the BUT, the spectral contents

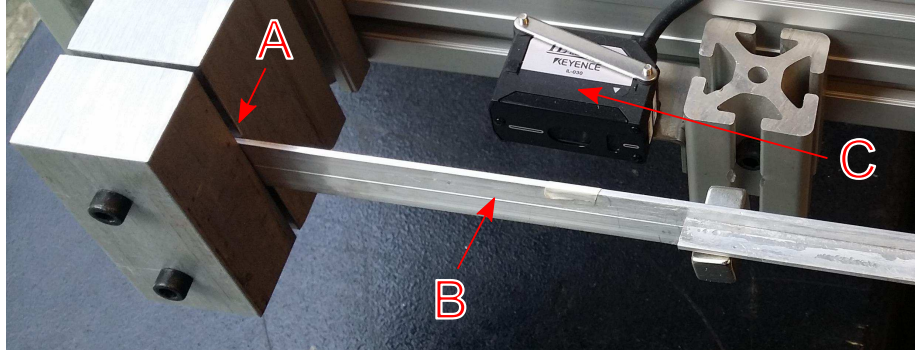


Figure 5: BUT's deflection measurement. A: clamped joint, B: BUT, C: position sensor.

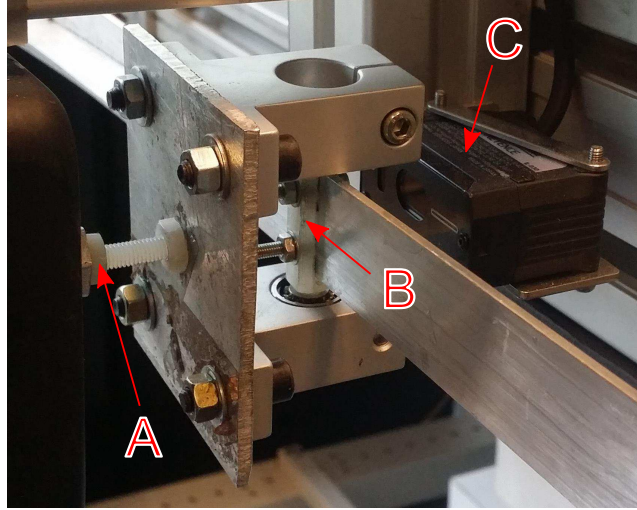


Figure 6: Shaker. A: nylon rod and nuts, B: axis of the revolute joint, C: control beam's position sensor.

of the motion of point A must be monitored. As only the first mode of the BUT is considered in this paper, the classical beam resonance of said first mode arises when point A's frequency is twice the BUT's resonant frequency f_0 . So, measurements of the amplitudes of point A's motion and the corresponding transverse motion of the BUT have been carried out at an excitation frequency of $2f_0$. Moreover, the frequency f_0 has been investigated too. The results are in Table 1. Point A's peak-to-peak amplitude (in mm) versus the shaker's peak-to-peak amplitude (in mm) is obtained from the data in Fig. 9, which yield a slope of $0.04mm/mm$. One must then divide by 2 to obtain the classical amplitude from the peak-to-peak amplitude. The BUT's adimensioned amplitude

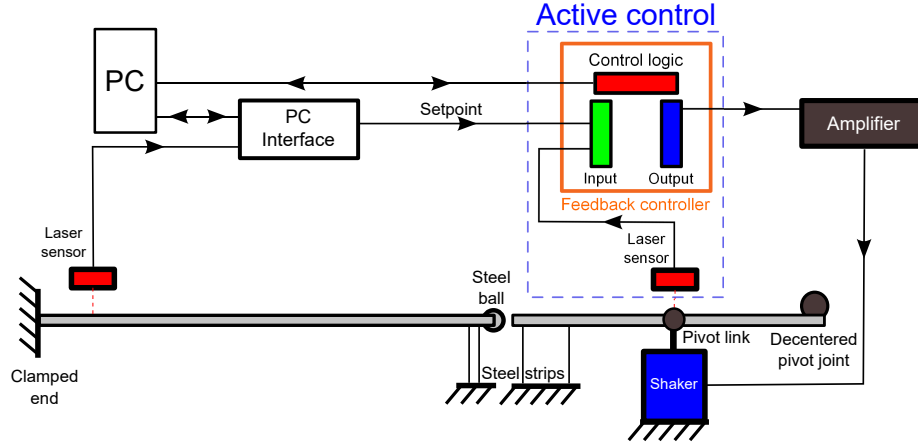


Figure 7: Global synoptic diagram.

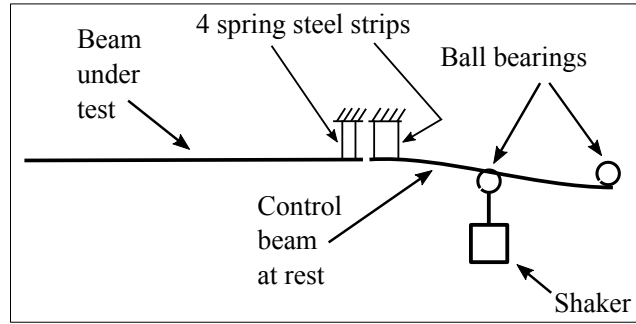


Figure 8: Offset position of the control beam at rest.

(in mm/m) is obtained by dividing the BUT's amplitude (in mm) by L , where L is the length of the BUT. The values of the shaker's spectrum components are in arbitrary unit of power.

It can be seen that if the shaker's unwanted power spectrum components corresponding to the frequencies f_0 and $2 f_0$ are kept under $3.5 \cdot 10^{-5}$, then the corresponding unwanted BUT amplitudes are kept under $0.063 \text{ mm/m} = 0.063 \cdot 10^{-3}$. The hypothesis is herein made, that the order of magnitude of the BUT's response due to these unwanted components at f_0 and $2 f_0$ is still valid when these components are mixed with high-amplitude components at $4 f_0$ or $6 f_0$ during the experiments.

Table 1: Amplitude of the BUT's transverse motion in response to axial excitations at f_0 and $2f_0$, for various amplitudes of point A, f_0 being the BUT's resonant frequency.

Shaker's and point A's frequency	Shaker's pk-pk amplitude (mm)	Point A's amplitude (mm)	Beam's amplitude (mm/m)	Shaker's Power spectrum component
f_0	0.62	0.012	1.2	$20 \cdot 10^{-3}$
f_0	0.38	0.0076	0.99	$8.3 \cdot 10^{-3}$
f_0	0.19	0.0037	0.28	$1.8 \cdot 10^{-3}$
f_0	0.024	0.00048	0.039	$1.9 \cdot 10^{-5}$
f_0	0.012	0.00024	0.024	$1.8 \cdot 10^{-6}$
$2 f_0$	0.57	0.011	1.4	$5.1 \cdot 10^{-3}$
$2 f_0$	0.19	0.0038	0.47	$5.6 \cdot 10^{-3}$
$2 f_0$	0.09	0.0018	0.19	$1.3 \cdot 10^{-3}$
$2 f_0$	0.015	0.0003	0.063	$3.5 \cdot 10^{-5}$
$2 f_0$	0.005	0.0001	0.009	$3.9 \cdot 10^{-6}$

3.3 Calibration for the case $n = 4$.

Due to the very small displacements at the contact point between the BUT and the control beam, the position of the tip of the control beam has to be derived from its transverse displacement, and therefore a calibration has to be made.

First, the static position of point A is measured as a function of the shaker's static position, given by a position sensor. To do this, the resonant frequency of the BUT is measured for various thicknesses of spring steel strips inserted between the two beams; by comparing the frequencies, it is possible to establish reference points and to determine, step by step, the points of Fig. 9. Then, by measuring the resonant frequency under various static positions of the shaker, an empirical relation between the static position of point A and the static axial force F_0 can be established. The results are given in Fig. 10. Then, by taking the numerical derivative of F_0 with respect to x_A , the local value of the stiffness k is obtained. The results are given in Fig. 11. Finally, the value of the stiffness k retained for the experiment is obtained using a value of k obtained in the region corresponding to the mean value of x_A of this figure. The value retained for k is $k = 200 \text{ kN/m}$.

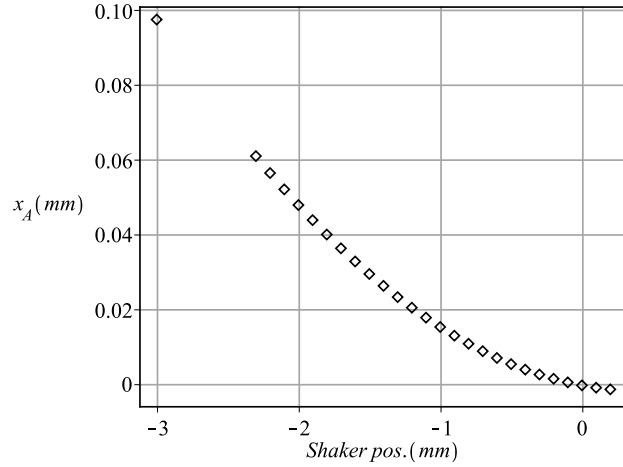


Figure 9: Point A's peak-to-peak amplitude against shaker's peak-to-peak amplitude for the case $n = 4$, with contact adjustment carried out by adding a $0.1mm$ spring steel strip in the experiments. Measured points are represented as diamonds.

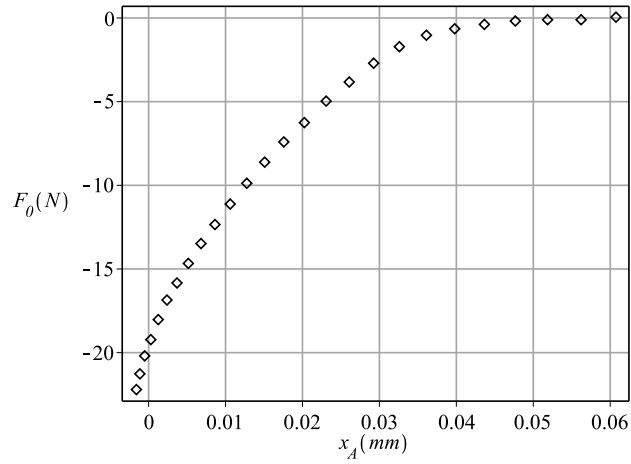


Figure 10: Static axial force F_0 against point A's static position for the case $n = 4$, with contact adjustment carried out by adding a $0.1mm$ spring steel strip in the experiments. Measured points are represented as diamonds.

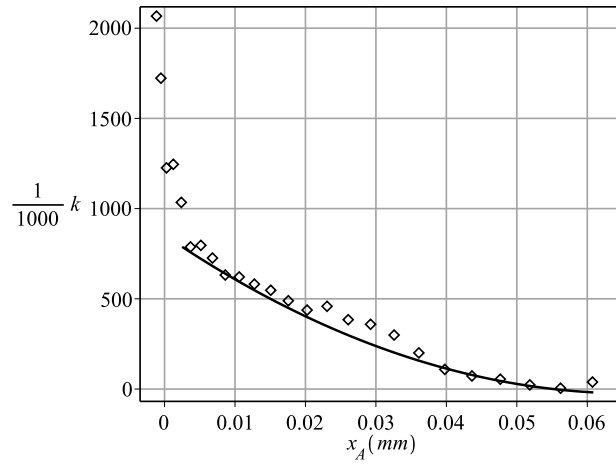


Figure 11: Stiffness k against point A's static position for the case $n = 4$, and trend curve in the region of interest (solid line), with contact adjustment carried out by adding a $0.1mm$ spring steel strip in the experiments. Measured points are represented as diamonds.

3.4 Calibration for the case $n = 6$.

For the case $n = 6$, it was necessary to add a stiffener on the control beam to avoid a mode between point C and the shaker head. So the value of k changed, as well as the relationship between the shaker's position and x_A . The value retained for k is now $k = 130 \text{ kN/m}$. The calibration procedure is the same as for the case $n = 4$.

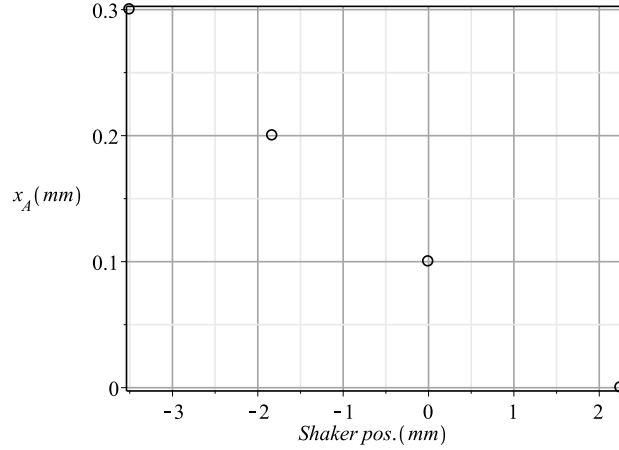


Figure 12: Point A's static position against shaker's static position for the case $n = 6$, with contact adjustment carried out by adding a 0.1mm spring steel strip in the experiments. Measured points are represented as circles.

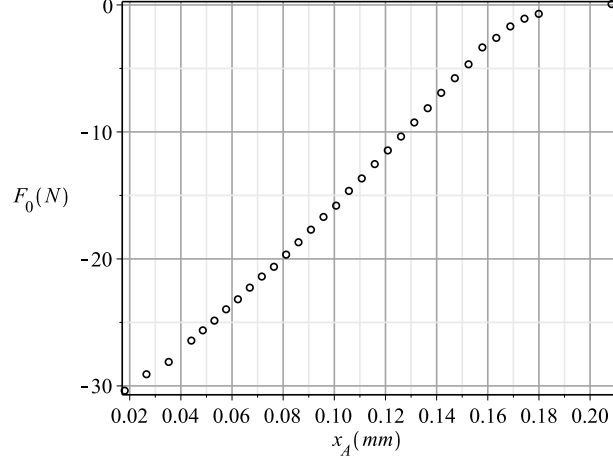


Figure 13: Static axial force F_0 against point A's static position for the case $n = 6$, with contact adjustment carried out by adding a $0.1mm$ spring steel strip in the experiments. Measured points are represented as circles.

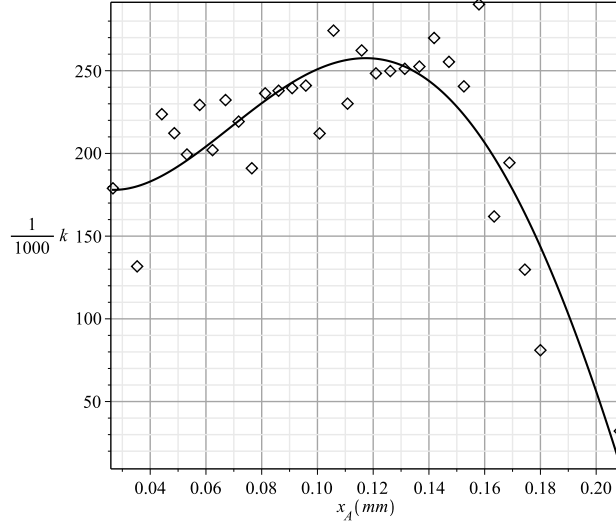


Figure 14: Stiffness k against point A's static position for the case $n = 6$, and trend curve (solid line), with contact adjustment carried out by adding a $0.1mm$ spring steel strip in the experiments. Measured points are represented as diamonds.

4 Experimental results.

In this section, the experimental results are presented in Van der Pol plots, along with other detailed data about the motion and spectral purity. Those Van der Pol plots are polar plots with a as modulus and φ as argument, with reference to Equ. (2). The damping ratio β has been determined experimentally.

4.1 Frequency ratio: $n = 4$

Fig. 15 shows the experimental Van der Pol curves obtained with a frequency ratio $n = 4$. Fig. 16 shows the detail of one curve from Fig. 15. This curve lasted for 40s.

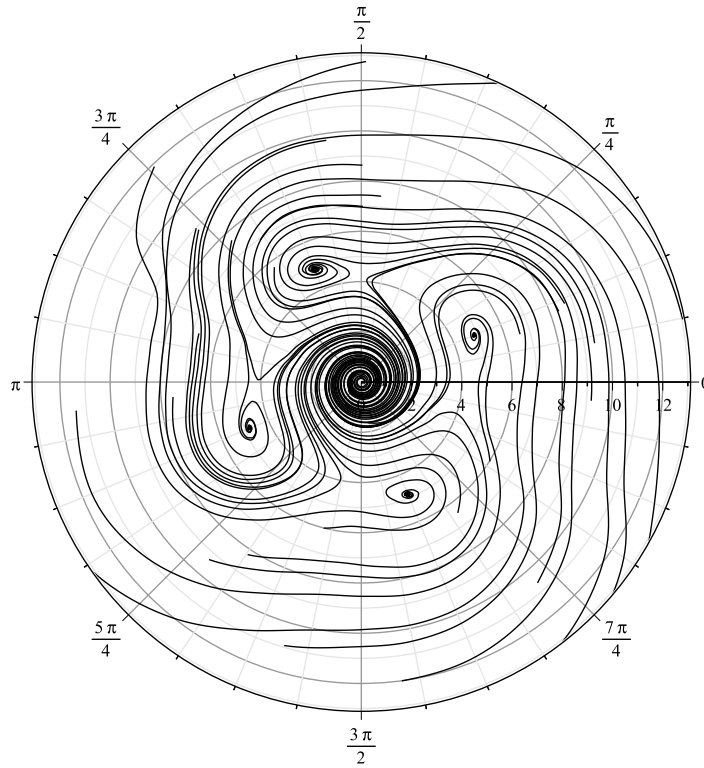


Figure 15: Experimental Van der Pol curves for $n=4$. The adimensioned amplitude is in mm/m. Parameters are: $n = 4$, $F_B = 51N$, $F_0 = -5.0N$, $f_{00} = 6.615Hz$, $\beta = 2.4 \cdot 10^{-3}$, $L = 0.95m$, $k = 200 \cdot 10^{-3}N/m$, $f_{exc} = 25.849813Hz$, $\rho_{00} = 0.976939$. The high number of decimal positions is to allow one to reproduce numerical results.

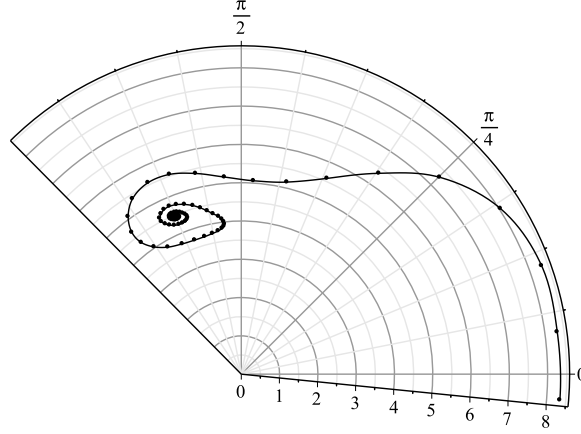
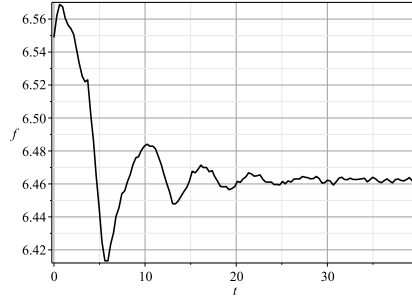


Figure 16: Detail of one curve from Fig. 15. There is one dot embedded on the curve every two periods of the beam's motion.

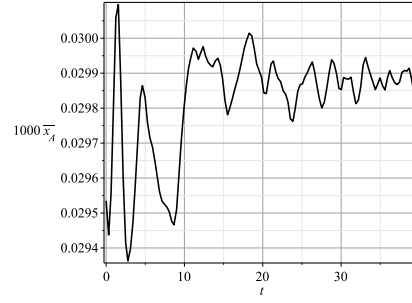
As can be seen in Fig. 17 (c) and (d), the point A's power spectrum components relative to the frequencies f_0 and $2 f_0$ are kept respectively under $1.5 \cdot 10^{-6}$ and $2 \cdot 10^{-5}$.

Fig. 18 gives numerical simulation results and experimental results relative to stationary regimes. Referring to [2,3], results of the numerical simulations on the averaged system (with smooth model) are given. The smooth model yields a curve with a crescent-shaped top part and a V-shaped bottom part, curve whose right part constitutes the stable stationary regimes, and the left part the unstable ones. Parameter values for the smooth model are the same as for Fig. 15, except $F_0 = -6.4N$. Other experimental results are also represented, with the same parameters as for Fig. 15 and various values of the excitation a_A . It can be seen that the experimental data are in good agreement with the smooth model in the whole region where experimental data are available. The "Model upper validity limit" as defined in [3] is outside the figure, which means that the smooth model is valid on the whole figure.

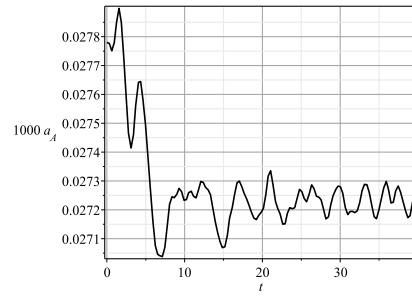
Fig. 19 shows that, for $n = 4$, and given the high sensitivity of the results against parameter values, the smooth model and the natural model are in good agreement with each other. It can be noticed that the skewed form of the V-shaped part of the stationary-solutions curve in the experimental data is better modeled by the natural model than by the smooth model, as can be seen in Fig. 19. This is due to a specific approximation in the smooth model, as explained in [3]. In conclusion, for $n = 4$, the experimental data are in good agreement with both the natural and the experimental models.



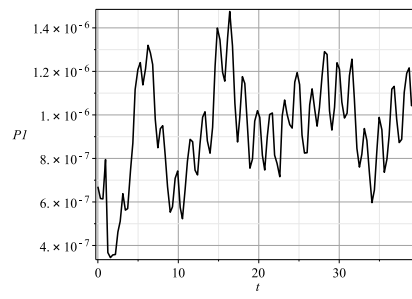
(a)



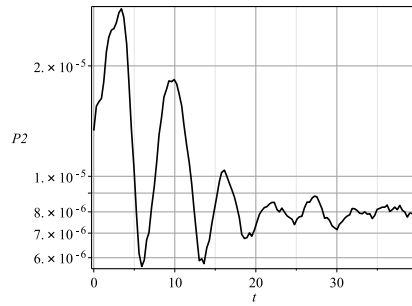
(b)



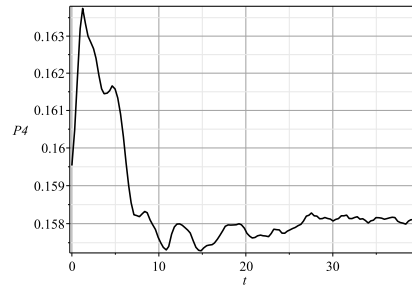
(c)



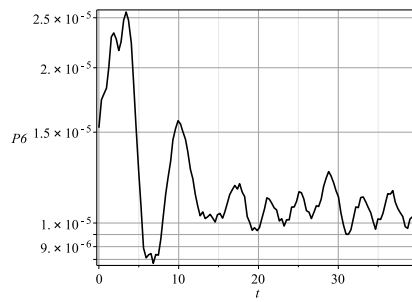
(d)



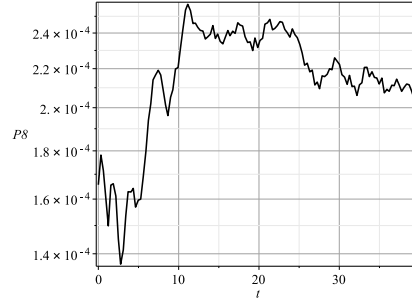
(e)



(f)



(g)



(h)

Figure 17: Details of the thread of Fig. 16: BUT frequency (BF) (a), point A's mean position (b), point A's amplitude (c), and point A's spectral components at: 1 x BF (d), 2 x BF (e), 4 x BF (f), 6 x BF (g), 8 x BF (h).

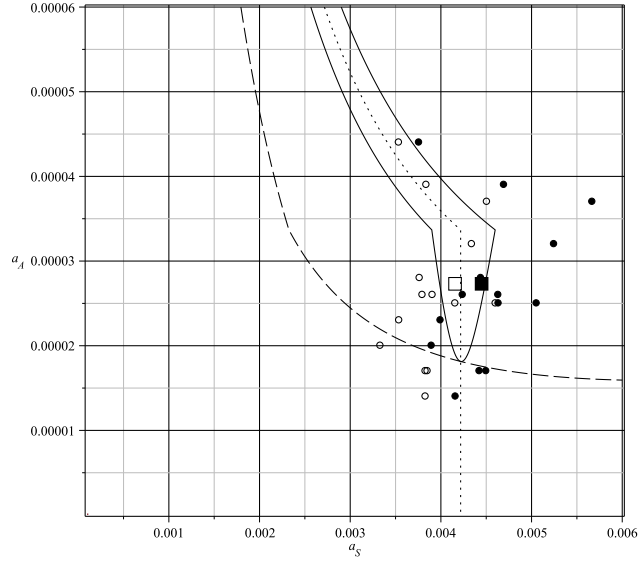


Figure 18: Stationary regimes, a_A (point A's amplitude) against a_S (stationary motion's amplitude) for $n = 4$. Comparison between smooth model and experimental results. The smooth model is represented as a solid line. The dashed line and the dotted line are the β -curve and the G -curve as described in [3]. The experimental results of Fig. 15 are represented as a solid square (stable point) and a hollow square (unstable point). Other stationary experimental points: unstable points (circles) and stable points (solid circles). The parameters are those of Fig. 15, except $F_0 = -6.4N$.

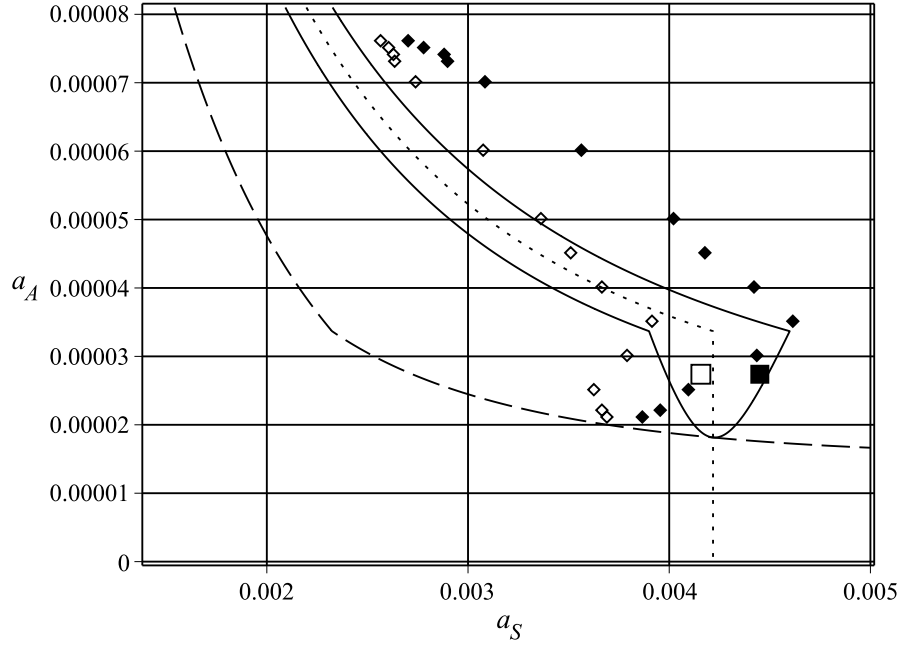


Figure 19: Stationary condition, a_A (point A's amplitude) against a_S (stationary motion's amplitude). Comparison between natural model (with second-order equation), represented as diamonds, and smooth model (with averaged system), represented as a solid line. The G -curve is the dotted line, while the β -curve is the dashed line. Parameters are those of Fig. 18. For the smooth model, stable and unstable stationary solutions are represented as an infinity of points belonging to solid lines, while for the natural model, a discrete series of stable (solid diamonds) and unstable (hollow diamonds) stationary points are represented.

4.2 Frequency ratio: $n = 6$

Fig. 20 shows the experimental Van der Pol curves obtained with a frequency ratio $n = 6$. Fig. 21 shows the detail of one curve from Fig. 20. This curve lasted for 60s.

As can be seen in Fig. 22 (c) and (d), the shaker's components relative to

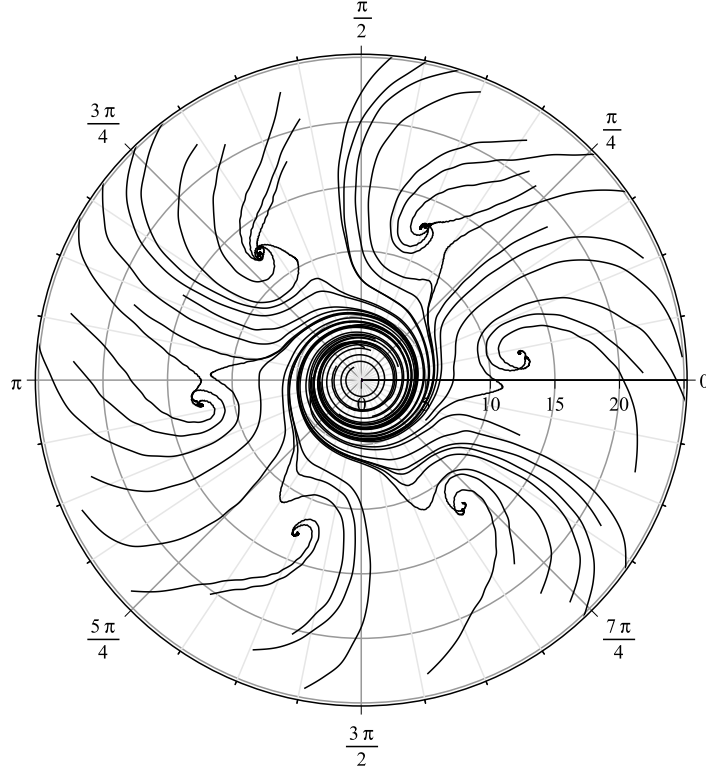


Figure 20: Experimental Van der Pol curves for $n=6$. The adimensioned amplitude is in mm/m. Parameter values are: $n = 6$, $\beta = 2.4 \cdot 10^{-3}$, $F_B = 51N$, $F_0 = -5.0N$, $L = 0.95m$, $k = 130 \text{ kN/m}$, $f_{00} = 6.615Hz$, $f_{exc} = 39.500711Hz$, $\rho_{00} = 0.9952308$.

the frequencies f_0 and $2f_0$ are kept respectively under $3.5 \cdot 10^{-5}$ and $1.6 \cdot 10^{-5}$. Fig. 23 gives numerical simulation results and experimental results relative to stationary regimes. Referring to [2,3], results of the numerical simulations on the averaged system (with smooth model) and results of numerical simulations on the second-order equation (using the natural model) are given. The smooth model yields a crescent-shaped curve whose right part is the stable regimes, and the left part the unstable regimes. Parameter values for natural and smooth model are the same as for Fig. 20, except $F_0 = -7.2N$. Experimental results

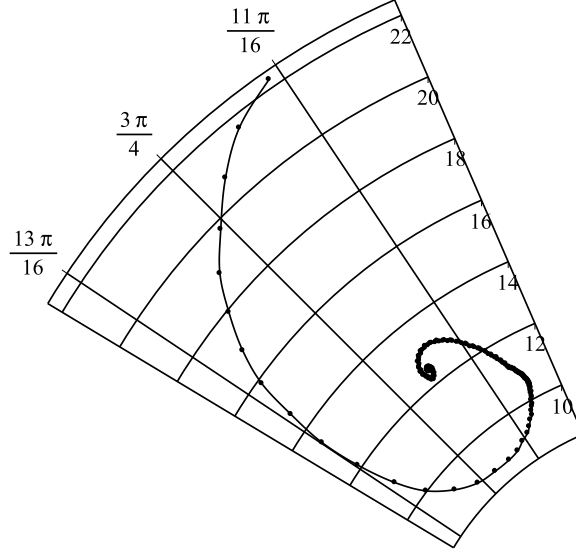
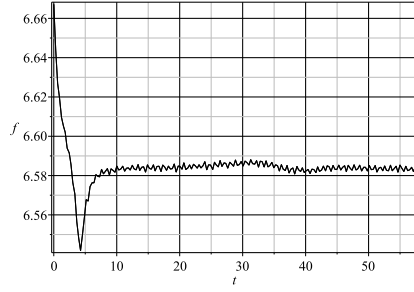


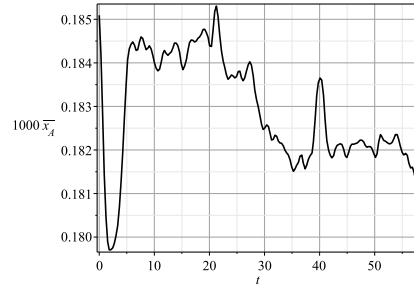
Figure 21: Detail of one curve from Fig. 20. There is one dot embedded on the curve every two periods of the beam's motion.

relative to Fig. 20 are also represented, along with other experimental results representing stable stationary regimes for the same parameters as for Fig. 20 and various values of the excitation a_A . In this last case (asterisk on Fig. 23), only stable stationary regimes are represented, because there were not enough experimental data to correctly identify the position of the unstable stationary representative points.

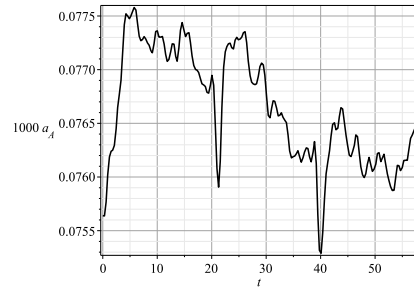
It can be seen that the agreement between experimental data and natural model is good, but that it is only fair between experimental data and smooth model. This is in all likelihood due to the approximations built into the smooth model and to the proximity to the vanishing of the argumental phenomenon for the parameters of Fig. 23. Indeed, the smooth model can be expected to be less performing when the truncated sinusoids used in [3] are about to vanish, due to the method employed to build the smooth model. However, given the sensitivity of the system to its parameters, the presence of the experimental data in the vicinity to the smooth model stationary-solutions curve can be considered a fair result.



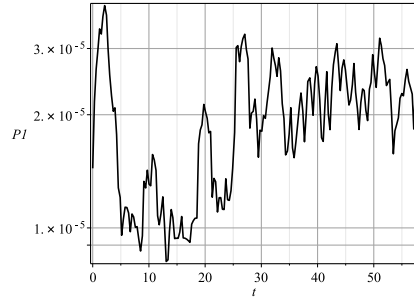
(a)



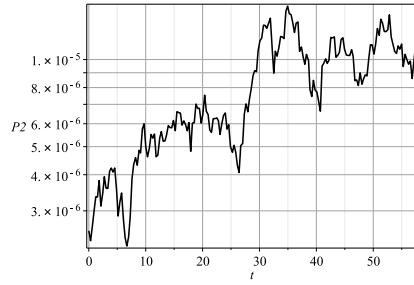
(b)



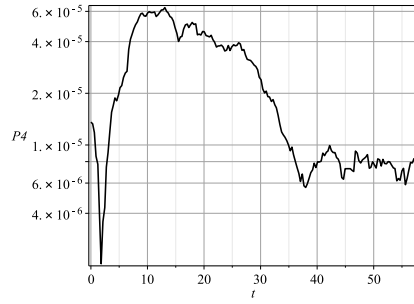
(c)



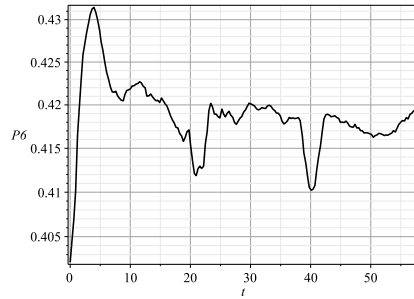
(d)



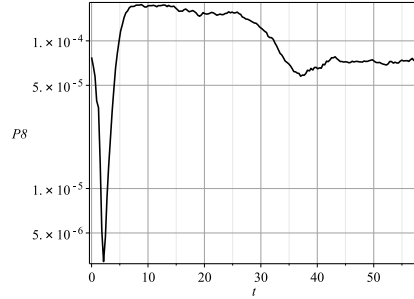
(e)



(f)



(g)



(h)

Figure 22: Details of the thread of Fig. 21: BUT frequency (BF) (a), point A's mean position (b), point A's amplitude (c), and point A's spectral components at: 1 x BF (d), 2 x BF (e), 4 x BF (f), 6 x BF (g), 8 x BF (h).

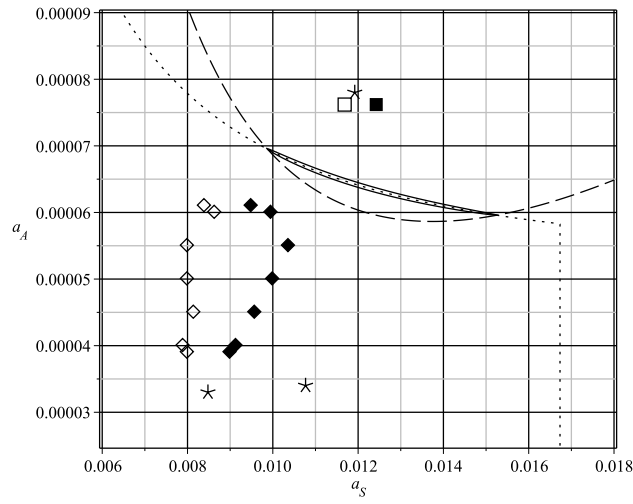


Figure 23: Stationary regimes, a_A (point A's amplitude) against a_S (stationary motion's amplitude) for $n = 6$. Comparison between models and experimental results. The smooth model is represented as a solid line. The dashed line and the dotted line are the β -curve and the G -curve as described in [3]. The natural model is represented as solid diamonds (stable points) and hollow diamonds (unstable points). The experimental results of Fig. 20 are represented as a solid square (stable point) and a hollow square (unstable point). Other experimental results (stable points only) are represented as asterisks.

5 Conclusion.

Experiments have been carried out with two beams placed head-to-head. The beam under test (BUT) was in a clamped-(clamped-guided) configuration. The second beam was controlled so as to provide an elastic intermittent contact with the BUT. It has been experimentally shown that a beam under test submitted to a harmonic axial excitation through an intermittent elastic contact can enter a stationary regime where its transverse vibration has a frequency which is the beam's fundamental frequency, and equal to a sub-multiple (other than one) of half the frequency of the axial excitation. The axial excitation was four or six times the fundamental frequency of the beam. These conditions constitute an argumental phenomenon.

In the case $n = 4$, the experimental data are in good agreement with both the natural and the smooth models. In the case $n = 6$, the experimental data are in good agreement with the natural model, and in fair agreement with the smooth model.

The experiments described herein have been carried out to the power limit of the shaker. To explore greater values of n , a more powerful shaker should be used. Also, lower values of the damping ratio could be employed. Finally, a more efficient device to convert the high-amplitude, low-force of the shaker into a low-amplitude, high-force excitation could be considered.

References

- [1] M.J. Béthenod. Sur l’entretien du mouvement d’un pendule au moyen d’un courant alternatif de fréquence élevée par rapport à sa fréquence propre. *Comptes rendus hebdomadaires de l’Académie des sciences*, 207(19):847–849, November 1938. (in French).
- [2] D. Cintra, G. Cumunel, and P. Argoul. A few properties in symbolic form for the argumental transverse vibration of a beam excited through permanent or intermittent elastic contact by a harmonic axial motion. *Journal to be determined*, 2017.
- [3] D. Cintra, G. Cumunel, and P. Argoul. Modeling and numerical results for the argumental transverse vibration of a beam excited through permanent or intermittent elastic contact by a harmonic axial motion. *Journal to be determined*, 2017.
- [4] Daniel Cintra and Pierre Argoul. Attractors capture probability in nonlinear argumental oscillators. *Communications in Nonlinear Science and Numerical Simulation*, 48(Supplement C):150 – 169, 2017.
- [5] Daniel Cintra and Pierre Argoul. Non-linear argumental oscillators: Stability criterion and approximate implicit analytic solution. *International Journal of Non-Linear Mechanics*, 94(Supplement C):109 – 124, 2017. A Conspectus of Nonlinear Mechanics: A Tribute to the Oeuvres of Professors G. Rega and F. Vestroni.
- [6] Daniel Cintra and Pierre Argoul. Nonlinear argumental oscillators: A few examples of modulation via spatial position. *Journal of Vibration and Control*, 23(18):2888–2911, 2017.
- [7] B. Cretin and D. Vernier. Quantized amplitudes in a nonlinear resonant electrical circuit. In *2009 Joint Meeting of the European Frequency and Time Forum and the IEEE International Frequency Control Symposium, vols 1 and 2*, volume 1 & 2, pages 797–800, Besançon, France, April 2009. Joint Meeting of the 23rd European Frequency and Time Forum/IEEE International Frequency Control Symposium.
- [8] D. Doubochinski. *Argumental oscillations. Macroscopic quantum effects*. SciTech Library, August 2015.
- [9] D.B. Doubochinski and J.B. Doubochinski. Amorçage argumentaire d’oscillations entretenues avec une série discrète d’amplitudes stables. *E.D.F. Bulletin de la direction des études et recherches, série C mathématiques, informatique*, 3:11–20, 1991. (in French).
- [10] D. I. Penner, D. B. Duboshinskii, M. I. Kozakov, A. S. Vermel, and Yu. V. Galkin. Asynchronous excitation of undamped oscillations. *Phys. Usp.*, 16(1):158–160, 1973.

- [11] Barun Pratiher and Santosha Kumar Dwivedy. Nonlinear response of a flexible cartesian manipulator with payload and pulsating axial force. *Non-linear Dynamics*, 57(1):177–195, Jul 2009.
- [12] J.P. Treilhou, J. Coutelier, J.J. Thocaven, and C. Jacquez. Payload motions detected by balloon-borne fluxgate-type magnetometers. *Advances in Space Research*, 26(9):1423–1426, 2000.

A few properties in symbolic form for the
argumental transverse vibration of a beam
excited through permanent or intermittent elastic
contact by a harmonic axial motion

Daniel Cintra (corresponding author), Gwendal Cumunel
Université Paris-Est,
Laboratoire Navier (UMR 8205), CNRS, ENPC, IFSTTAR,
6 et 8, avenue Blaise Pascal,
Cité Descartes, Champs-sur-Marne,
F-77455 Marne La Vallée Cedex 2, France.
email: daniel.cintra@enpc.fr, gwendal.cumunel@enpc.fr

and

Pierre Argoul
IFSTTAR, Laboratoire MAST-SDOA,
F-77455 Marne La Vallée, Cedex 2, France
email: pierre.argoul@ifsttar.fr

Abstract

The transverse argumental vibration of a beam excited axially by a harmonic motion transmitted through intermittent or permanent elastic contact is studied. Previous results have shown, using a smooth model and the averaging method, that a vibration in the fundamental transverse mode of the beam can occur when the frequency of the excitation is an even multiple (greater than 2) of the frequency of the fundamental transverse mode. In this paper, a few properties of the smooth model are brought out in symbolic form, namely the conditions of occurrence of the stationary regime, formulas pertaining to the excitation threshold, and the precision of the assessment of said thresholds. An all-case upper bound of the relative error about the value of the excitation threshold is given.

Keywords— nonlinear dynamics; argumental oscillator; beam transverse vibration; axial excitation; spatial modulation; Van der Pol representation.

Contents

1	Introduction.	3
2	System configuration.	4
3	Stationary condition.	4
	Notations:	4
	Results of the averaging method.	7
	Basic equation of the amplitude in stationary condition.	7
	β -curve, G -curve and stationary-solutions curve.	7
	Excitation threshold.	8
	Stationary-solutions curve.	8
	Restriction on ρ_{00}	8
3.1	Intersection of the β -curve and the G -curve.	9
	Case $\rho_{00} > 1$	11
	Case $\rho_{00} < 1$	13
	A simple criterion to compare a_T and a_0	14
3.2	Graphical representation of the argumental phenomenon's possibility of existence.	15
3.3	Approximate symbolic solution for the intersection above the critical line.	20
4	Conclusion.	21
5	Appendix A: tangency condition between the upper β-curve and the upper G-curve.	22
	Equation of the intersection between $a_{A1}(a)$ and $a_{A2}(a)$	22
	Function $y_1(z) = E \left(1 - \frac{1}{z} + \frac{1}{z\sqrt{2z+1}} \right)$	22
	Function $y_2(z) = \frac{1}{z} \left(\frac{\sqrt{1+z}-1}{\sqrt{z}} \right)^n$	22
	Tangency of functions $y_1(z)$ and $y_2(z)$	23
	Basis for a numerical study.	24
6	Appendix B: position of the G-curve versus the critical line.	27
	Notation	27
	Definition domain.	27
	Limit at 0 and at $+\infty$	27
	Direction of variation.	28
	Intersection with the critical line.	28
	Allowed values for ρ and ρ_{00}	28
	Conclusion.	29

1 Introduction.

The so-called argumental oscillator is a mechanical system which has a stable motion consisting of a periodic motion at a frequency next to its natural frequency when submitted to an external force whose frequency is close to a multiple of said natural frequency. One necessary condition for the phenomenon to arise is that the external force be dependent on the space coordinate of the oscillator. An oscillator exhibiting such characteristics has been described in 1928 [1]; this oscillator was a pendulum fitted with a steel sphere at the tip of the rod, submitted to a harmonic magnetic field spatially localized at the bottom of the sphere's course.

The word “argumental” was forged in 1973 [10], where a pendulum is submitted to an electric field spatially localized at the bottom of the pendulum's course.

Further developments were carried out [8,9], particularly the “multiple resonance” and the “quantum effect”. The multiple resonance is a phenomenon in which a number of oscillators, each having its own resonance frequency, submitted to a unique common excitation frequency, can oscillate simultaneously. This is possible if each oscillator has an actual frequency which is a sub-multiple of the excitation frequency, and if the interaction zone between each oscillator and the excitation source is spatially localized. The quantum effect is when an oscillator can oscillate at a number of stable amplitudes whose frequencies are sub-multiples of a fixed excitation frequency. This is possible if the oscillator's actual frequency depends on its amplitude, which is the case for a classical pendulum, and if the excitation source is spatially localized.

Argumental oscillations have also been observed and described in balloon-borne magnetometer measurements [12] and in an electrical circuit [7]. A few examples of argumental oscillators, consisting of six variations of a pendulum excited by magnetic forces, have been modeled and experimented [4]. A stability criterion in symbolic form and an approximate analytic solution for an argumental oscillator have been given [3]. Capture probabilities by an attractor in an argumental oscillator have been given in symbolic form [2].

As for the beams receiving axial excitation, a cantilever beam submitted to a harmonic force through its base and to a pulsating axial force through its tip, and carrying a payload at its tip, has been studied in [11].

A typical second-order ordinary differential equation for a one-degree-of-freedom argumental oscillator is:

$$\ddot{x} + 2\beta\omega_0\dot{x} + \omega_0^2x = g_1(x) + g_2(x)\cos(\omega_{exc}t), \quad (1)$$

where x is the space coordinate, β is the damping ratio, ω_0 is the natural angular velocity of the oscillator, g_1 and g_2 are functions of x , and ω_{exc} is the angular

velocity of the excitation.

In this paper, the transverse argumental vibration of a beam excited axially by a harmonic motion transmitted through intermittent or permanent elastic contact is studied. Previous results [6] have shown that this system obeys an argumental equation, and, using a discontinuous natural model with numerical calculus, as well as a smooth continuous model with the averaging method, that a vibration in the fundamental transverse mode of the beam can occur when the frequency of the excitation is an even multiple (greater than 2) of the frequency of the fundamental transverse mode. Experimental results pertaining to this configuration are given in [5].

2 System configuration.

The schematic system configuration is as shown in Fig. 1. A beam is represented, with its left end S and right end M, in a clamped-(clamped-guided) configuration. At the point M's side, the clamp is carried out by way of a massless trolley. Point M is intermittently pushed to the left by a plate C, which is linked to a point A via a massless spring. $\mathbf{F} = F\mathbf{i}$, where \mathbf{i} is the unit vector along the abscissae axis, is the force intermittently applied by plate C to the beam's right end at M. F is negative when the beam is in compression. In the figure, point A moves horizontally with a harmonic motion, in such a manner that the contact between plate C and point M be intermittent when the beam and point A are vibrating. When the beam is in resting (i.e. rectilinear) position and point A is in center position, the force applied to point M is denoted by F_0 .

3 Stationary condition.

The argumental transverse vibration of an axially-excited beam has been modeled and studied via the averaging method [6], with the help of a smooth model, to derive the results summarized below.

Notations:

- ω_{exc} is the angular frequency of the excitation source at point A,
- F_0 is the force F when the beam is at rest and point A is at rest in central position,
- F_B is the beam's critical buckling force,
- ω_0 is the beam's natural angular frequency when point A is at rest in its central position, with $\omega_0^2 = a_1 \left(\frac{\pi}{L}\right)^2 \frac{F_B + F_0}{\mu S}$, where $a_1 = 1$ in the hinged-

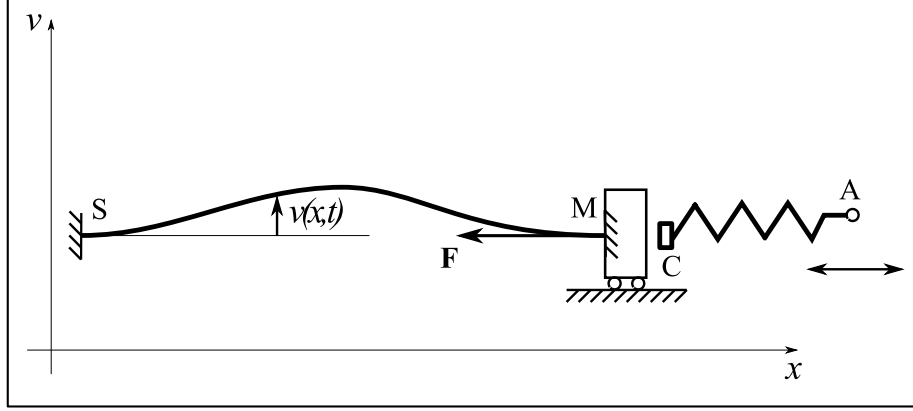


Figure 1: System configuration. x is the horizontal abscissa, v is the transverse displacement, t is the time, and \mathbf{F} is the force applied by plate C to the beam at point M. Point M moves freely horizontally, but is clamped vertically. There is no rotation at S and M.

(hinged-guided) case, and $a_1 = 4/3$ in the clamped-(clamped-clamped) case, μ = mass per volume unit of the beam, S = section of the beam,

- ω_{00} is the value of ω_0 when $F_0 = 0$,
- n is an even integer roughly equal to $\frac{\omega_{exc}}{\omega_0}$,
- ρ is a parameter, generally close to 1, chosen so as to have $\frac{\omega_{exc}}{\rho\omega_0} = n$,
- k is the spring's stiffness,
- L is the beam's length,
- aL is the amplitude of the beam's motion (a is adimensioned),
- $a_S L$ is the amplitude of the beam's stationary-motion (a_S is adimensioned),
- $a_A L$ is the amplitude of the excitation at point A (a_A is adimensioned),
- ρ_{00} is defined as $\rho \sqrt{\frac{F_B}{F_B + F_0}}$,
- β is the experimentally-measured beam's damping ratio,
- a_{Acrit} is a parameter defined as $a_{Acrit} = -\frac{F_0}{kL} = \frac{|F_0|}{kL}$ (if $a_A < a_{Acrit}$, when the beam is at rest and the excitation is on, the contact between points M and C is never disrupted),

- B and C are constants defined as $B = -\frac{\pi^2}{4} \frac{kL}{F_0} = \frac{\pi^2}{4 a_{Acrit}}$ and $C = 2 B$,
- The “Buckling limit” is the value which a_A must not exceed for the buckling force never to be exceeded [6], i.e. $\min\left(\frac{F_B + F_0}{kL}, 3a_{Acrit}\right)$.
- The “Model validity upper limit” is the value which a_A must not exceed for the buckling force never to be exceeded and for the conditions built into the smooth model to be verified [6], i.e. $\min\left(\frac{F_B + F_0}{kL}, 3a_{Acrit}\right)$,
- A is a function of a_A defined as

$$\begin{aligned} & - \text{ If } a_A < a_{Acrit}: \\ & \quad A(a_A) = \frac{kLa_A}{F_B + F_0} \end{aligned} \quad (2)$$

which, in this case, is actually independent of a_A .

$$\begin{aligned} & - \text{ Otherwise:} \\ & \quad A(a_A) = -\frac{F_0 - a_A kL}{2F_B + F_0 - a_A kL} \end{aligned} \quad (3)$$

- S_n and D_n are two functions of a defined as

$$S_n(a) = \frac{4}{a^{n+1}} \frac{(\sqrt{1 + Ba^2} - 1)^n}{B^{\frac{n}{2}+1}} \quad (4)$$

$$D_n(a) = \frac{S_n(a)}{\sqrt{1 + Ba^2}} \quad (5)$$

Moreover:

$$\frac{1}{S_n} \frac{\partial S_n}{\partial a} = \frac{1}{a} \left(\frac{n}{\sqrt{1 + Ba^2}} - 1 \right) \quad (6)$$

- G is a function of a and a_A defined as

$$\begin{aligned} & - \text{ If } a_A < a_{Acrit}: \\ & \quad G(a, a_A) = -\frac{1}{2} \frac{F_0}{F_B + F_0} a \left(1 - \frac{2}{Ca^2} + \frac{1}{Ca^2} \frac{2}{\sqrt{1 + Ca^2}} \right) \end{aligned} \quad (7)$$

which, in this case, is actually independent of a_A .

$$\begin{aligned} & - \text{ Otherwise:} \\ & \quad G(a, a_A) = -\frac{1}{2} \frac{F_0 - a_A kL}{2F_B + F_0 - a_A kL} a \left(1 - \frac{2}{Ca^2} + \frac{1}{Ca^2} \frac{2}{\sqrt{1 + Ca^2}} \right) \end{aligned} \quad (8)$$

Results of the averaging method. The averaging method consists here in searching a solution close to a slowly-varying sinusoid, carrying out the following classic change of variables

$$\begin{cases} z(\tau) &= a(\tau) \sin(\rho\tau + \varphi(\tau)) \\ \dot{z}(\tau) &= a(\tau)\rho \cos(\rho\tau + \varphi(\tau)) \end{cases}$$

where the dot notation denotes the differentiation w.r.t. reduced time τ . With the system configuration studied in this paper, the averaging method yields, among others, the following result: knowing that $n = \frac{\omega_{exc}}{\rho\omega_0}$ is an even integer, then the system obeys the following system of equations:

$$\begin{cases} \dot{a}(\tau) &= \frac{A(a_A)}{4\rho} S_n(a) \sin(n\varphi(\tau)) - \beta a \\ \dot{\varphi}(\tau) &= \frac{G(a, a_A)}{a} + \frac{A(a_A)}{4a} D_n(a) \cos(n\varphi(\tau)) - \frac{\rho^2 - 1}{2} \end{cases} \quad (9)$$

where $\varphi(\tau)$ is the motion's phase shift w.r.t. the excitation force.

Under certain initial conditions, and when some relations between the parameters are satisfied, there is a stationary solution to system (9), namely $z(\tau) = a_S \sin(\rho\tau + \varphi_S)$, where a_S and φ_S are constants, which satisfies the system (9) in which \dot{a} and $\dot{\varphi}$ are set to 0. From this system, a number of symbolic relations will be derived in this paper, which give clues about the stationary condition.

Basic equation of the amplitude in stationary condition. Eliminating φ_S by writing that $\sin^2(n\varphi_S) + \cos^2(n\varphi_S) = 1$, obtain from Eqs (9):

$$(4\rho\beta)^2 + 4 \frac{S_n^2(a_S)}{D_n^2(a_S)} (2G_1(a_S) - (\rho^2 - 1))^2 = \frac{A^2(a_A) S_n^2(a_S)}{a_S^2} \quad (10)$$

where $G_1(a_S, a_A) = G(a_S, a_A)/a_S$.

β -curve, G-curve and stationary-solutions curve. To help visualizing some results hereinafter, define a function F_β by

$$F_\beta(a_S, a_A) = (4\rho\beta)^2 - \left(\frac{A(a_A) S_n(a_S)}{a_S} \right)^2,$$

and define the “ β -curve” as the curve representing the solution to equation $F_\beta(a_S) = 0$. Also, define a function F_G by

$$F_G(a_S, a_A) = 2G_1(a_S) - (\rho^2 - 1),$$

and define the “G-curve” as the curve representing the solution of

$$F_G(a_S) = 0. \quad (11)$$

Finally, define the “stationary-solutions curve” as the curve representing the solution to Eq. (10). Then, Eq. (10) can be written:

$$F_\beta(a_S) + 4 \frac{S_n^2(a_S)}{D_n^2(a_S)} F_G^2(a_S) = 0 \quad (12)$$

Excitation threshold. It is of interest to be able to assess the minimum value a_{Amin} of a_A versus a_S along a stationary-solutions curve, because this value of a_A is the excitation threshold allowing the argumental phenomenon to arise with given parameters n , β , F_B , F_0 , L , k , f_{00} , and ρ_{00} . The numerical plots show that the minimum of a_A is close to an intersection point of the β -curve and the G -curve. This is an hypothesis which is made throughout this paper. Using a classical approach, by differentiation of Eq. (10), leads to an intricate calculus, with no significant simplification in sight. However, this differentiation leads to guess that $F_\beta(a) \approx 0$ and $F_G(a) \approx 0$ at the minimum of the stationary-solutions curve.

Stationary-solutions curve. Figs. 3 and 2 show the implicit stationary-solutions curves, obtained numerically, giving a_A against a_S for the values of parameters given in the figures’ legends. For each figure, the solid-line curve represents the stationary-solutions curve of Eq. (10), with a minimum at point A_{min} , which is close to the calculated point of intersection of the β -curve and the G -curve. The solution to System (9) can be seen as composed of two parts, depending on the position with respect to the horizontal line $a_A = a_{Acrit} = |F_0|/(kL)$, herein called the “critical line”:

- An upper part (above said line) composed of two arcs, in contact at their higher extremities at one point, and at their lower extremities at said line.
- A lower part, constituted by a V-shaped curve, presenting a minimum at point A_{min} .

The upper and lower parts are connected at the critical line. The right (resp. left) arc and the right (resp. left) part of the V-shaped curve represent the stable (resp. unstable) stationary solutions. For a given value of the excitation, i.e. a given amplitude a_A , there are two possible values for a_S , represented by points S and U . Point S is the stable stationary condition, while point U is the unstable one. The V-shaped curve represents cases where there is permanent contact between the beam under test (BUT) and the excitation source when the BUT is in rectilinear position. In these cases, the contact may or may not remain permanent when the BUT enters a transversal vibration, depending on the spring’s stiffness and the amplitudes of transversal vibration of the BUT and of the excitation source.

Restriction on ρ_{00} . Appendix B in Section 6 shows that only the values of ρ_{00}^2 comprised between $1 - \lambda$ and 1 are valid to be in the case where a V-shaped part exists. The calculus below are focused on the case $\rho_{00} < 1$, because when

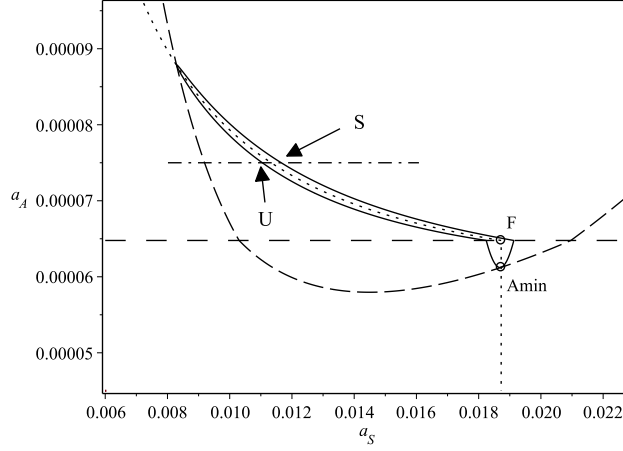


Figure 2: Stationary condition in the case $\rho_{00} < 1$ for the averaged system with the smooth model of the external force. a_S is the stationary-motion's amplitude, a_A is the excitation's amplitude. The dotted line is the G curve. The solid line is the locus of the stationary solutions to the averaged smooth model. The dashed line is the β -curve. S and U respectively represent the stable and the unstable stationary conditions located at the intersection of the stationary-solutions curve and the dash-dotted line representing the excitation level. The space-dashed horizontal line is the "critical line". Below said line, A_{min} is the minimum of the stationary-solutions curve. F is the forking point. Parameter values are: $n = 6$, $\beta = 2.4 \cdot 10^{-3}$, $F_B = 51N$, $F_0 = -8N$, $L = 0.95m$, $k = 130 \text{ kN/m}$, $f_{00} = 6.615Hz$, $f_{exc} = 39.500711Hz$, $\rho_{00} = 0.9952308$, $\lambda = 0.1569$, and Model validity upper limit $= 1.94 \cdot 10^{-4}$.

$\rho_{00} > 1$, there is no V-shaped part of the stationary-solutions curve, which is entirely above the critical line at ordinate a_{Acrit} ; in this case, it is sufficient to take, as a minimum excitation threshold, the asymptotic limit of the G -curve when $a_S \rightarrow +\infty$, given in Appendix A in Section 5 as $2(1 - 1/\rho_{00}^2)(F_B + F_0) - F_0$. Fig. 4 shows the layout of the curves when $\rho_{00} > 1$: as the G -curve (dotted line) never intersects the critical line, the intersection between the G -curve and the β -curve never exists under the critical line, and therefore, the V-shaped part of the stationary-solutions curve never shows up.

3.1 Intersection of the β -curve and the G -curve.

In this section, the intersection conditions of the β -curve and the G -curve will be studied. The primary focus is not to give a general solution for any configuration of the β -curve and the G -curve, but to bring out some limit configurations, i.e. tangency conditions between said curves, corresponding to limit conditions of possibility of existence for the argumental phenomenon. Those curves each

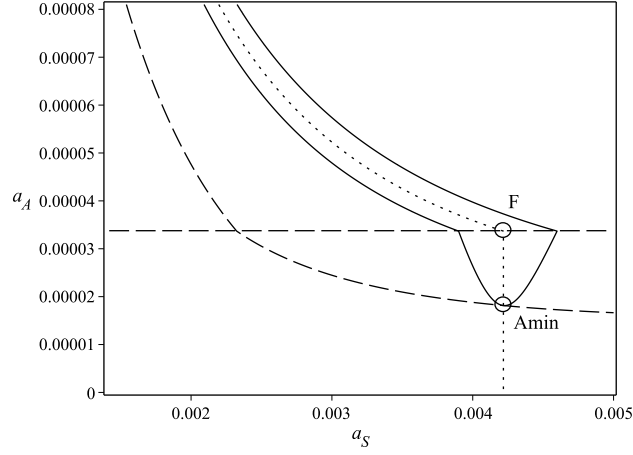


Figure 3: Stationary condition in the case $\rho_{00} < 1$ for the averaged system with the smooth model of the external force. a_S is the stationary-motion's amplitude, a_A is the excitation's amplitude. The graphical-elements descriptions are the same as in Fig. 2. Parameters are: $n = 4$, $F_B = 51N$, $F_0 = -6.4N$, $f_{00} = 6.615Hz$, $\beta = 2.4 \cdot 10^{-3}$, $L = 0.95m$, $k = 200 \cdot 10^3 N/m$, $f_{exc} = 25.849813$, and $\rho_{00} = 0.976939$. Model validity upper limit= $1.01 \cdot 10^{-4}$.

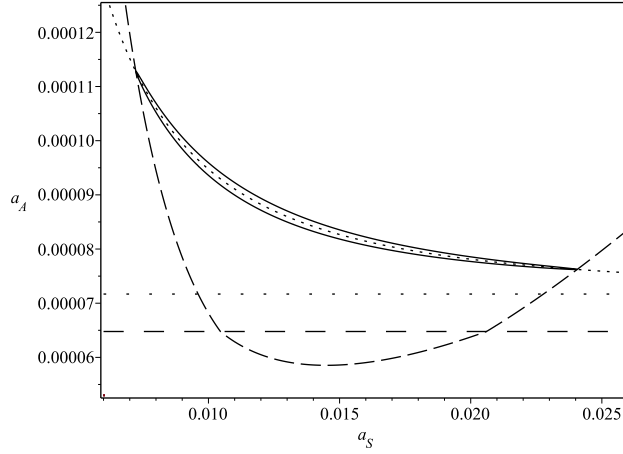


Figure 4: Stationary condition in the case $\rho_{00} > 1$ for the averaged system with the smooth model of the external force. The space-dotted line is the asymptote of the G -curve when $a_S \rightarrow +\infty$. Other graphical-element descriptions and parameter values are the same as for Fig. 2, except $f_{exc} = 39.88845Hz$ and $\rho_{00} = 1.005$.

have two different versions: the upper version and the lower version. The upper (resp. lower) version is applicable when the point representing the stationary condition in the (a_S, a_A) -plane is located above (resp. below) the critical line $a_A = |F_0|/(kL)$. But, for the study in this section, the upper versions will be prolonged in the region located below the critical line, for reasoning purposes only. Call “forking point” F the point of intersection of the G -curve with the critical line (see Figs. 5 and 6). The top of lower G -curve is the said forking point. Define a_0 as the abscissa of said point.

Referring to Figs. 5 and 6, compare the upper versions, including their prolonged parts, and study the tangency condition between the upper β -curve and the upper G -curve. When the tangency point is above the critical line, a slight contraction of the β -curve upon the vertical direction (due to a lower value of β), starting from the tangency condition, will produce two points of intersection between said curve and the G -curve. Those points will both be above the critical line. The rightmost point is close to the minimum of the crescent-shaped stationary-solutions curve representing the stationary conditions of the averaged system. Now if the tangency point is below the critical line, a slight contraction on the β -curve will also produce two points of intersection, but those points will be at the right of the vertical segment constituting the lower G -curve, and therefore, they will not be on the lower G -curve. It will be necessary to apply a stronger contraction on the upper β -curve, until it intersects the G -curve at its forking point. Then, substituting the lower β -curve for the upper β -curve, a slight contraction on the lower β -curve will produce two points of intersection with the G -curve, one located on the upper G -curve, the other on the lower G -curve. This latter point is the point of interest. It is close to the minimum of the V-shaped part of the stationary-solutions curve representing the stationary conditions of the averaged system. Said substitution is legitimate, because the prolonged upper β -curve and the lower β -curve intersect each other at the critical line, so that continuity is preserved.

So, in the upper part of the (a_S, a_A) -plane (above the critical line), the tangency of the β -curve and the G -curve is the limit condition for the intersection of said curves to exist, and then for the existence of solutions to the averaged system. In the lower part of the plane, the limit condition is when the lower β -curve goes through the G -curve’s forking point.

An approaching method is given in Section 3.3 to assess the intersection of the β -curve and the G -curve.

Case $\rho_{00} > 1$. Denote $a_{A1}(a)$ for the upper G -function, which writes:

$$a_{A1}(a) = \frac{F_0}{kL} + 2\frac{F_B}{kL} \frac{(\rho^2 - 1)Ca^2}{\rho^2 Ca^2 - 2 + \frac{2}{\sqrt{Ca^2 + 1}}}$$

and denote $a_{A2}(a)$ for the upper β -function, which writes:

$$a_{A2}(a) = \frac{F_0}{kL} + 2 \frac{F_B}{kL} \frac{1}{1 + \frac{1}{\rho\beta} \frac{1}{Ba^2} \left(\frac{\sqrt{1+Ba^2}-1}{\sqrt{Ba^2}} \right)^n}$$

Using Eq. (27) of Appendix A, the tangency condition between the upper β -curve and the upper G -curve is:

$$\frac{\rho\beta}{\rho^2 - 1} \approx \frac{4n^2}{(n^2 - 4)^2} \left(\frac{n-2}{n+2} \right)^{n/2} \quad (13)$$

Substituting $\rho_{00}^2 \frac{F_B}{F_B + F_0}$ for ρ^2 yields:

$$\frac{\rho_{00}\sqrt{1-\lambda}}{\rho_{00}^2 - 1 + \lambda} \beta < \frac{4n^2}{(n^2 - 4)^2} \left(\frac{n-2}{n+2} \right)^{n/2} \quad (14)$$

with $\lambda = \frac{|F_0|}{F_B} = \frac{-F_0}{F_B}$.

To see how this condition translates in the (λ, ρ_{00}) -plane, carry out some calculus, putting $x = 1 - \lambda$, $y = \rho_{00}^2$, $F = \frac{4n^2}{(n^2 - 4)^2} \left(\frac{n-2}{n+2} \right)^{n/2}$, and $c = 1 + \frac{1}{2F^2}$, to obtain the inequality

$$(y - cx)^2 - (c^2 - 1)x^2 > 0 \quad (15)$$

which in turn yields

$$\begin{cases} y > (c + \sqrt{c^2 - 1})x \\ \text{or} \\ y < (c - \sqrt{c^2 - 1})x \end{cases} \quad (16)$$

Getting back to the original parameters λ and ρ_{00} , obtain:

$$\begin{cases} \lambda > 1 - \frac{\rho_{00}^2}{c + \sqrt{c^2 - 1}} \\ \text{or} \\ \lambda < 1 - \frac{\rho_{00}^2}{c - \sqrt{c^2 - 1}} \end{cases} \quad (17)$$

Because $c > 1$ by definition, the second condition cannot be satisfied if $\rho_{00} > 1$. It remains the first condition, meaning that the representative point in the (λ, ρ_{00}) -plane must be above an horizontal-axis parabola. The condition is expressed by the inequation

$$\lambda > 1 - \frac{\rho_{00}^2}{c + \sqrt{c^2 - 1}} \quad (18)$$

Said point must also be under the parabola of equation $\lambda = 1 - \frac{\rho_{00}^2}{2}$ because of condition (37) given in Appendix B.

Case $\rho_{00} < 1$. Denote a_T for the abscissa of the tangency point between the limit upper β -curve and the upper G -curve. Here two cases must be distinguished, depending on the relative abscissae a_T and a_0 of the tangency point and the G -curve's forking point. The expression of a_0^2 is given in Eq. (22) and the expression for a_T^2 in Eq. (30). A simple criterion to compare a_T and a_0 is given hereinafter.

- If $a_T < a_0$, the intersection points of the limit β -curve and the G -curve are both above the critical line, and consequently are on the upper parts of said curves (see Fig. 5). Therefore, the limit intersection condition of said curves is the same as for the case $\rho_{00} > 1$.
- If $a_0 < a_T$, it has been showed above that the limit intersection condition is constituted by the lower β -curve going through the G -curve's forking point (see Fig. 6). The lower β -function is

$$a_A(a) = \rho_{00}\beta \frac{\sqrt{F_B(F_B + F_0)}}{kL} \frac{1}{\frac{1}{Ba^2} \left(\frac{\sqrt{1+Ba^2}-1}{\sqrt{Ba^2}} \right)^n} \quad (19)$$

The condition for the lower β -curve and the lower G -curve to intersect is

$$a_A(a_0) < a_{Acrit} \quad (20)$$

where a_0 is the forking point's abscissa. Eq. (36) gives the expression of a_0 .

Then substitute a_0 for a in Equ (20) using Eq. (19) to obtain the condition of intersection below the critical line:

$$\beta < \frac{\lambda}{\rho_{00}\sqrt{1-\lambda}} \frac{1}{Ba_0^2} \left(\frac{\sqrt{1+Ba_0^2}-1}{\sqrt{Ba_0^2}} \right)^n \quad (21)$$

Then transform the expression Ba_0^2 using Eqs (36) and the definition of constant B to obtain

$$Ba_0^2 = \frac{\lambda}{1-\rho_{00}^2} - \frac{1}{4} - \frac{1}{4} \sqrt{1 + 8 \frac{\lambda}{1-\rho_{00}^2}} \quad (22)$$

and finally substitute this expression of Ba_0^2 into (21) to obtain a condition based only on parameters λ , ρ_{00} , β and n , valid when $\rho_{00} < 1$ and $a_0 < a_T$.

Finally, conditions (18) and (21) allow to plot in the (λ, ρ_{00}) -plane, for given values of β and n , the regions where the argumental phenomenon can arise.

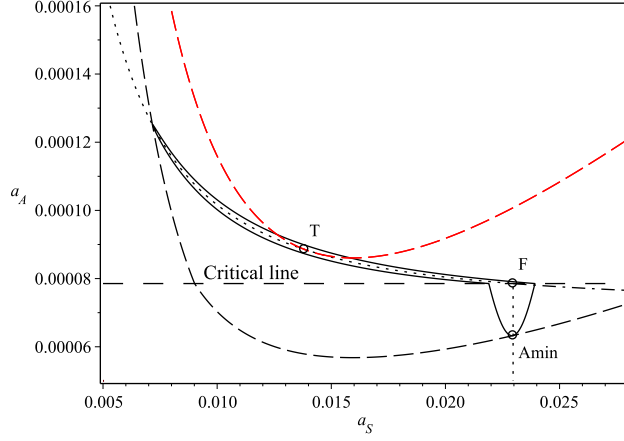


Figure 5: Tangent upper β -curve, case $\rho_{00} < 1$ and $a_T < a_0$. Parameters and description are the same as for Fig. 2, except $F_0 = -9.7N$. The solid curve is the set of stationary solutions curve to the averaged system. F is the forking point. The G -curve is the dotted curve. The upper dashed beta curve is tangent at T to the G -curve. The β -curve giving the minimum value of a_A is the lower dashed curve. The horizontal space-dashed line is the critical line. Model validity upper limit= $2.36 \cdot 10^{-4}$.

A simple criterion to compare a_T and a_0 . Here it is assumed that $\rho_{00} < 1$. To form the criterion, firstly consider the case $a_T < a_0$. Using the expressions of a_0^2 from Eq. (22) and a_T^2 from Eq. (30), transform expression $a_T^2 < a_0^2$ into

$$n^2 - 12 < \frac{4\lambda}{1 - \rho_{00}^2} - 1 - \sqrt{1 + \frac{8\lambda}{1 - \rho_{00}^2}}$$

Then put $u = \frac{4\lambda}{1 - \rho_{00}^2}$ to obtain

$$\sqrt{1 + 2u} < u + 11 - n^2$$

and then, assuming from now on that $u + 11 - n^2 > 0$, obtain

$$u^2 + 2(10 - n^2)u + (10 - n^2)(12 - n^2) > 0 \quad (23)$$

Deduce that u must be outside the interval between the roots, and also greater than $n^2 - 11$, which finally yields:

$$\frac{4\lambda}{1 - \rho_{00}^2} > n^2 - 10 + \sqrt{2(n^2 - 10)} \quad (24)$$

The condition $a_0 < a_T$ yields an inequality opposed to (24).

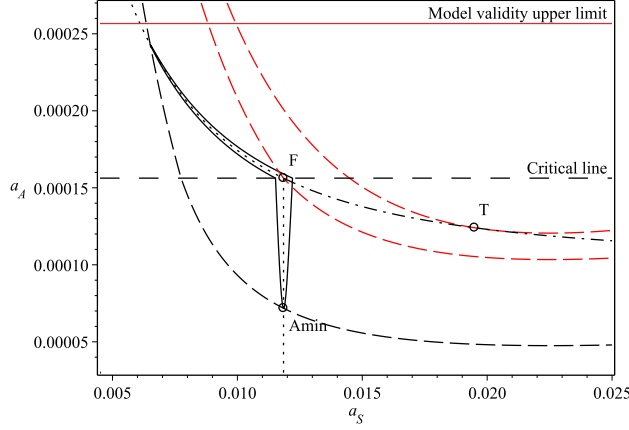


Figure 6: Tangent upper β -curve, case $\rho_{00} < 1$ and $a_0 < a_T$. Parameters and description are the same as for Fig. 2, except $F_0 = -19.3N$, $f_{exc} = 37.7055 Hz$, $\rho_{00} = 0.95$. The solid curve is the set of stationary solutions to the averaged system. F is the forking point. The prolonged G -curve in the domain located below the critical line is the dot-dashed curve. The upper dashed beta curve is tangent to the prolonged G -curve at point T. The dashed β -curve going through point F is the limit β -curve having an intersection with the G -curve. The β -curve giving the minimum value of a_A along the stationary-solutions curve is the lower dashed curve. The horizontal space-dashed line is the critical line. The Model validity upper limit is visible on the graph.

3.2 Graphical representation of the argumental phenomenon's possibility of existence.

In Section 3.1, it has been shown that the condition of intersection of the β -curve and the G -curve depends only on parameters λ , ρ_{00} , β , and n . This condition is the condition of possibility of existence of the argumental phenomenon. Considering that β and f_{00} are fixed for a given configuration of the BUT, and that n is an arbitrary even integer greater or equal to 4 accounting for a first-approximation frequency ratio between the excitation frequency and f_{00} , one is led to use the (λ, ρ_{00}) -plane to represent the regions where the argumental phenomenon can occur. Knowing that $\rho_{00} = f_{exc}/(n f_{00})$, the variability of f_{exc} is accounted for by the variability of ρ_{00} , and the variability of F_0 is accounted for by the variability of λ , with $\lambda = |F_0|/F_B$. Noticing that ρ_{00} appears only as ρ_{00}^2 , preferably use the (λ, ρ_{00}^2) -plane for the graphical representations. By so doing, all parabolas having the axis of abscissae as principal axis become rectilinear lines, so that plots are easier to read and manipulate.

A number of figures represent the possibility of existence of the argumental phenomenon in the (λ, ρ_{00}^2) -plane:

Figs 7 and 8 are for $n = 4$ and $\beta = 0.0024$; Figs 9 and 10 are for $n = 6$ and $\beta = 0.0024$; Figs 11 and 12 are for $n = 14$ and $\beta = 0.0016$.

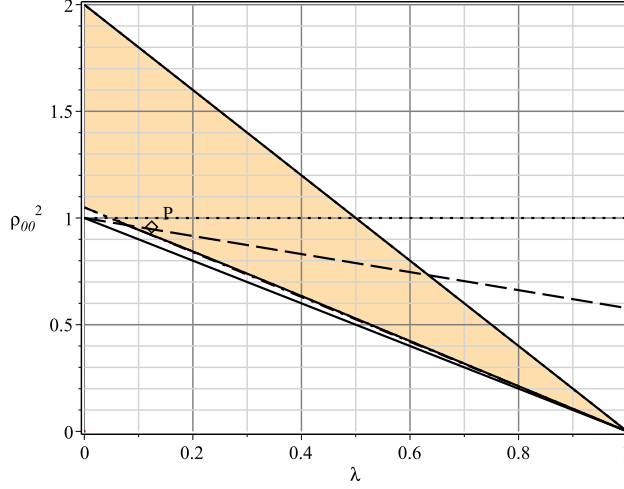


Figure 7: Possibility of existence of the argumental phenomenon (in the shaded region). Parameter values for n , β , F_B , f_{00} , and f_{exc} are the same as for Fig. 3, whose values of λ and ρ_{00} are represented here by point P. The solid lines are the upper and lower limits of the smooth model's validity region. The dotted line is the border between the case $\rho_{00} < 1$ and the case $\rho_{00} > 1$. The dashed line is the border between the case $a_T < a_0$ and the case $a_T > a_0$. The dash-dotted line is the border below which the β -curve and the G -curve don't intersect in the region above the dashed line. The dash-dotted line is not relevant in the region below the dashed line. The solid curve is the curve below which the β -curve and the G -curve don't intersect in the region below the dashed line. It is not relevant above the dashed line.

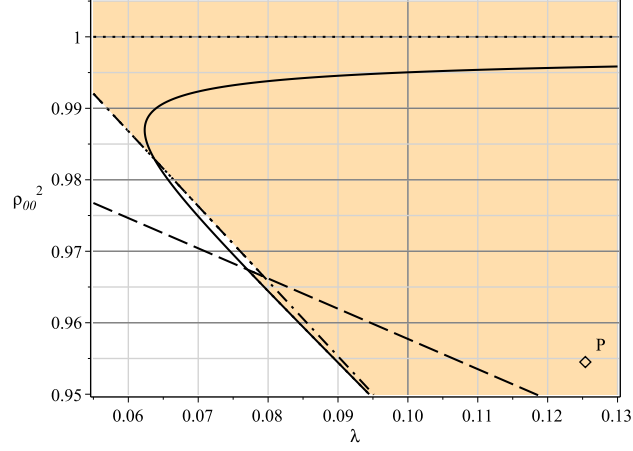


Figure 8: Zoomed view of Fig. 7. The slight offset of the shaded area at $(0.08, 0.967)$ is due to the use of approximated symbolic formulas for a_T and a_0 .

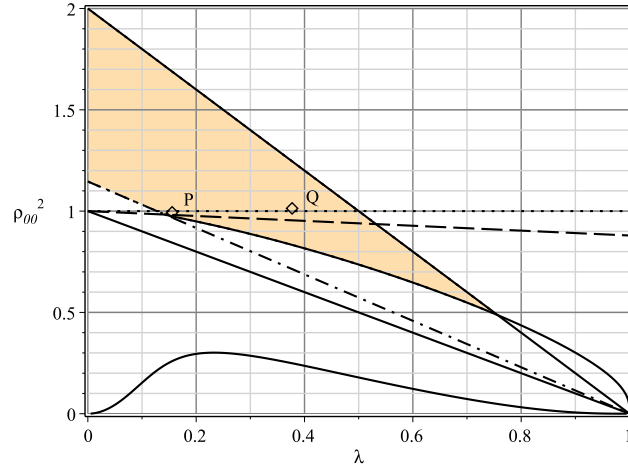


Figure 9: Possibility of existence of the argumental phenomenon (in the shaded region). Parameter values for n , β , F_B , and f_{00} are the same as in Figs. 2 and 4. Point P (resp. Q) represents the values of λ and ρ_{00} in Fig. 2 (resp. Fig. 4). The description of the graphic elements is the same as for Fig. 7.

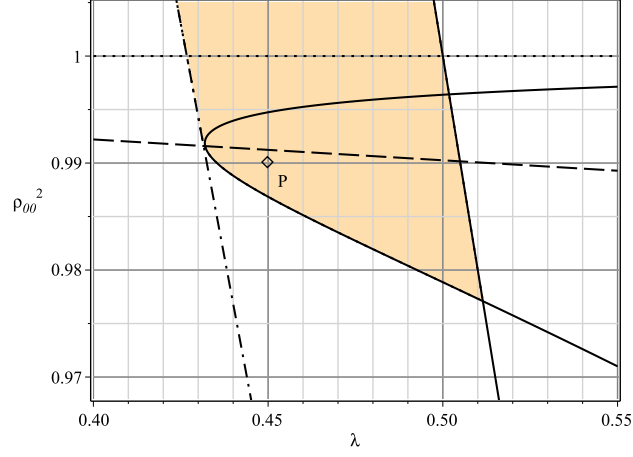


Figure 10: Zoomed view of Fig. 9. The slight offset of the shaded area at $(0.145, 0.983)$ is due to the use of approximated symbolic formulas for a_T and a_0 .

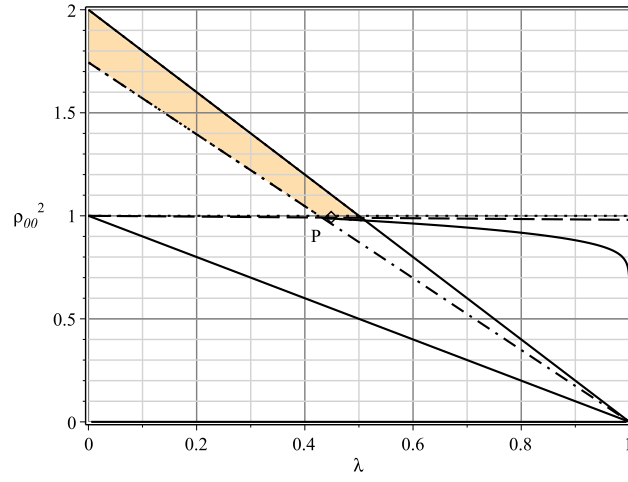


Figure 11: Possibility of existence of the argumental phenomenon (in the shaded region). Parameter values are: $n = 14$, $\beta = 1.6 \cdot 10^{-3}$, $F_B = 51N$, $f_{00} = 6.615Hz$ and $f_{exc} = 92.1495Hz$, $\rho_{00} = 0.995$, $\lambda = 0.45$. Point P represents the values of λ and ρ_{00} . The description of the graphic elements is the same as for Fig. 7.

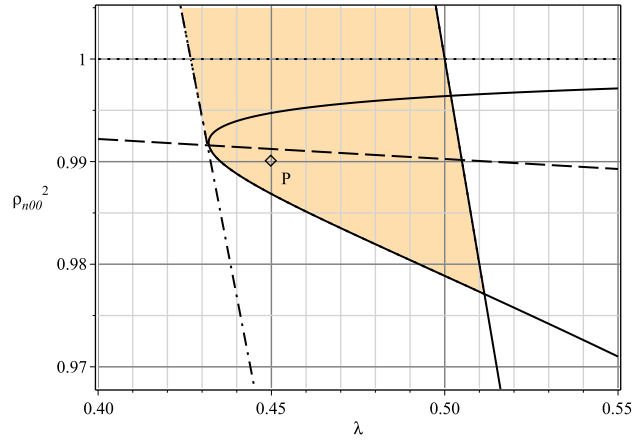


Figure 12: Zoomed view of Fig. 11.

3.3 Approximate symbolic solution for the intersection above the critical line.

In this section, the intersection of the β -curve and the G -curve is assessed when above the critical line. As for the intersection below the critical line, it arises at an abscissa a_0 which is calculated in Appendix B. Then, substituting a_0 for a_S in the lower β -curve's equation (19) yields the ordinate of the intersection point. If the conditions of intersection studied above are satisfied, it is possible to solve approximately Eq. (25) by putting $z = Ba_S^2$ and using the following remarks:

- Function $1 - \frac{1}{z} + \frac{1}{z\sqrt{2z+1}}$ can be approximated by function $\frac{\sqrt{2}z}{1 + \sqrt{2}z}$.
- Function $J(z) = \frac{1}{z} \left(\frac{\sqrt{1+z}-1}{\sqrt{z}} \right)^n$ can be approximated by function

$$K(z) = \frac{hz}{bz^2 + cz + 1},$$

$$\text{with } c = 8 \frac{n^2 + 4}{(n^2 - 4)^2}, b = \frac{16}{(n^2 - 4)^2}, \text{ and } h = \frac{4}{n^2 - 4} \left(\frac{n-2}{n+2} \right)^{n/2} \left(c + \frac{8}{n^2 - 4} \right) = \frac{64n^2}{(n^2 - 4)^3} \left(\frac{n-2}{n+2} \right)^{n/2}.$$

Thus, Eq. (25) becomes:

$$E \frac{\sqrt{2}z}{1 + \sqrt{2}z} = \frac{hz}{bz^2 + cz + 1}$$

$$\text{with } E = \frac{\rho\beta}{\rho^2 - 1}.$$

This is a second-degree equation in z , which, once solved in z , and due to the definition of z by $z = Ba_S^2$, yields the abscissae of points A_{min-} and A_{min+} . This second-degree equation in z is:

$$E\sqrt{2}bz^2 + \sqrt{2}(Ec - h)z + E\sqrt{2} - h = 0$$

The condition to have real roots is: $2(Ec - h)^2 - 4E\sqrt{2}(E\sqrt{2} - h) \geq 0$. Then, using Eq. (25), the ordinates of said points can be calculated. Those points are represented in Fig. 2.

4 Conclusion.

It has been presented a symbolic study of the stationary transverse vibrations of a system consisting of a beam submitted, through a permanent or an intermittent elastic contact, to a harmonic axial excitation which is an even multiple (greater than 2) of the beam's fundamental transverse frequency. This constitutes an argumental phenomenon.

A symbolic-form approximation of the excitation threshold as a function of the physical system's parameters has been given, as the intersection of two curves in the (oscillator's amplitude, excitation's amplitude)-plane, whose symbolic expressions have been brought out.

A study of the symbolic limit conditions for the argumental phenomenon to arise has been given and represented in the (λ, ρ_{00}^2) -plane.

A study of the symbolic limit conditions for permanent contact seems of interest. Numerical simulations show that this case can arise with ordinary parameter values. This seems an important condition to be aware of, because it shows that the argumental phenomenon in this context can occur even if there is permanent contact between the beam and the excitation source, which can be the case when there is no damage to the structure.

5 Appendix A: tangency condition between the upper β -curve and the upper G -curve.

In this Appendix, the tangency condition between the curves representing the upper G -function

$$a_{A1}(a) = \frac{F_0}{kL} + 2 \frac{F_B}{kL} \frac{(\rho^2 - 1)Ca^2}{\rho^2 Ca^2 - 2 + \frac{2}{\sqrt{Ca^2 + 1}}}$$

and the upper beta-function

$$a_{A2}(a) = \frac{F_0}{kL} + 2 \frac{F_B}{kL} \frac{1}{1 + \frac{1}{\rho\beta} \frac{1}{Ba^2} \left(\frac{\sqrt{1+Ba^2}-1}{\sqrt{Ba^2}} \right)^n}$$

will be studied in the (a, a_A) -plane for a real positive and n integer with $n \geq 4$. The equation of the intersection between $a_{A1}(a)$ and $a_{A2}(a)$ will first be formed, then the tangency condition will be studied.

Equation of the intersection between $a_{A1}(a)$ and $a_{A2}(a)$. Write $a_{A1}(a) = a_{A2}(a)$ and substitute the developed expressions of $a_{A1}(a)$ and $a_{A2}(a)$ given above, then carry out basic calculus to obtain, denoting Ba^2 by z for clarity:

$$\frac{1}{z} \left(\frac{\sqrt{1+z}-1}{\sqrt{z}} \right)^n = E \left(1 - \frac{1}{z} + \frac{1}{z} \frac{1}{\sqrt{1+2z}} \right) \quad (25)$$

with $E = \frac{\rho\beta}{\rho^2 - 1}$. The tangency condition between the curves of $a_{A1}(a)$ and $a_{A2}(a)$ for $a > 0$ is the same as the tangency condition between the functions $y_1(z) = E \left(1 - \frac{1}{z} + \frac{1}{z\sqrt{1+2z}} \right)$ and $y_2(z) = \frac{1}{z} \left(\frac{\sqrt{1+z}-1}{\sqrt{z}} \right)^n$ for $z > 0$. What is searched is a condition on E .

So the curves representing function $y_1(z) = E \left(1 - \frac{1}{z} + \frac{1}{z\sqrt{2z+1}} \right)$ and function $y_2(z) = \frac{1}{z} \left(\frac{\sqrt{1+z}-1}{\sqrt{z}} \right)^n$ will be studied for z real positive, $n \geq 4$, and $E = \text{positive constant}$.

Function $y_1(z) = E \left(1 - \frac{1}{z} + \frac{1}{z\sqrt{2z+1}} \right)$. This function is an increasing function for $z > 0$. Near zero, the function is equivalent to $3z/2 - 5z^2/2$. The asymptotic limit for $z \rightarrow +\infty$ is 1. The plot for $E = 1$ is given in Fig. 13.

Function $y_2(z) = \frac{1}{z} \left(\frac{\sqrt{1+z}-1}{\sqrt{z}} \right)^n$. This function is defined for every real positive z , and can be extended to 0 in $z = 0$.

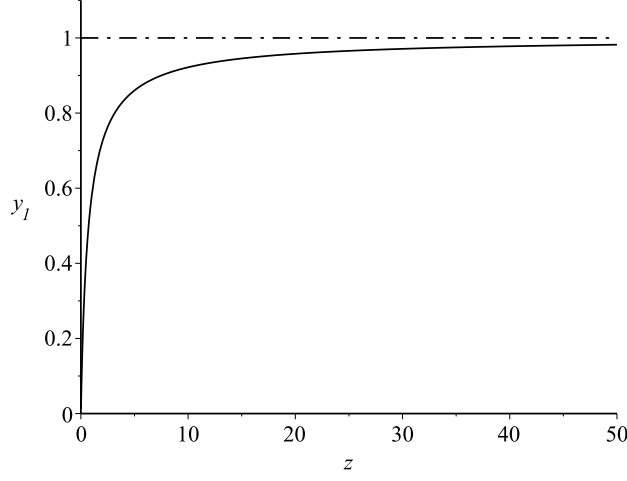


Figure 13: Plot of $y_1(z)$, with $E = 1$.

Near zero, the function is equivalent to $\frac{z^{\frac{n}{2}-1}}{2^n}$.

Near infinity, the function is equivalent to $\frac{1}{x} \left(1 - \frac{n}{\sqrt{z}}\right)$.

The function increases from $z = 0$ to $z_{2max} = \frac{n^2}{4} - 1$, then decreases asymptotically to 0.

The value of the maximum is $y_{2max} = \frac{4}{n^2 - 4} \left(\frac{n-2}{n+2}\right)^{n/2}$.

The plot for $n = 6$ is given in Fig. 14.

Tangency of functions $y_1(z)$ and $y_2(z)$. Knowing the behaviour of functions y_1 and y_2 , one is led to consider that when those curves are tangent, the tangency point is approximately at the maximum of y_2 , provided that $y_1(z_{2max}) = y_{2max}$. Hence the value E_T of E which satisfies this tangency must verify:

$$E_T \left(1 - \frac{1}{z_{2max}} + \frac{1}{z_{2max}\sqrt{2z_{2max} + 1}}\right) = \frac{4}{n^2 - 4} \left(\frac{n-2}{n+2}\right)^{n/2}$$

Using the approximation

$$1 - \frac{1}{z_{2max}} + \frac{1}{z_{2max}\sqrt{2z_{2max} + 1}} \approx 1 - \frac{4}{n^2} \quad (26)$$

for $n \geq 4$, finally obtain:

$$E_T \approx \frac{4n^2}{(n^2 - 4)^2} \left(\frac{n-2}{n+2}\right)^{n/2} \quad (27)$$

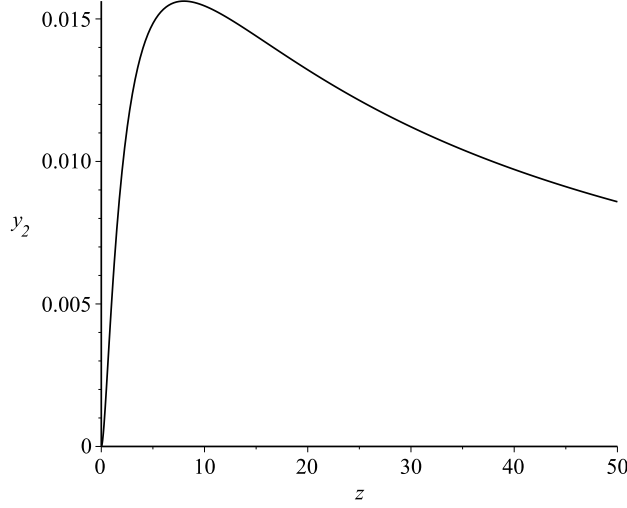


Figure 14: Plot of $y_2(z)$, with $n = 6$.

with $E_T = \frac{\rho\beta}{\rho^2 - 1}$. As for the tangency point's ordinate, assume that it is the same as the maximum of the $y_2(z)$ curve, i.e. y_{2max} . Note that $E_T = \frac{n^2}{n^2 - 4} y_{2max}$.

The following hypothesis are made:

- For $E < E_T$, the curves of y_1 and y_2 intersect at $z = 0$ and at least at two other points, one located at $z < z_{2max}$ and one at $z > z_{2max}$.
- For $E > E_T$, the curves of y_1 and y_2 intersect at $z = 0$.

A typical case is represented in Fig. 15 for $n = 6$ and $E_T = 9/512$, according to Eq. (27). On the plots, it can be seen that the value of y_1 in z_{2max} is slightly greater than expected. This is due to approximation (26), which partially compensates for a better tangency estimate. Other values of n give similarly good results for E_T , except for $n = 4$, where it is better to use a value of $1.03 E_T$.

Basis for a numerical study. To assess the relative error on z_T , form an equation giving the exact value of the tangency abscissa, by putting $y(z) = y_1(z) - y_2(z)$ and writing that both $y(z) = 0$ and $dy/dz = 0$. First transform the equation $y(z) = 0$ to obtain

$$E \left(z - 1 + \frac{1}{\sqrt{1+2z}} \right) = \left(\frac{\sqrt{1+z} - 1}{\sqrt{z}} \right)^n \quad (28)$$

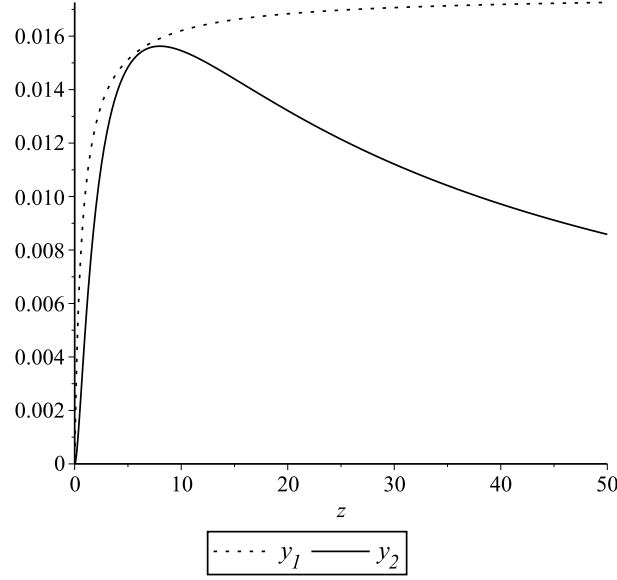


Figure 15: Tangency of $y_1(z)$ and $y_2(z)$, with $n = 6$.

Then calculate $dy/dz(z)$ to obtain

$$\frac{dy}{dz} = \frac{E}{z^2} \left(1 - \frac{1}{\sqrt{2z+1}} - \frac{z}{(2z+1)^{3/2}} \right) + \frac{1}{z^2} \left(\frac{\sqrt{1+z}-1}{\sqrt{z}} \right)^n \left(1 - \frac{n}{2\sqrt{1+z}} \right)$$

and put $dy/dz(z) = 0$. Then write $y(z) = \frac{dy}{dz}(z)$ and, based on Eq. (28), substitute $E \left(z - 1 + \frac{1}{\sqrt{1+2z}} \right)$ for $\left(\frac{\sqrt{1+z}-1}{\sqrt{z}} \right)^n$ to obtain:

$$\sqrt{2z+1} - 1 - \frac{z}{2z+1} = ((z-1)\sqrt{2z+1} + 1) \left(\frac{n}{2\sqrt{1+z}} - 1 \right) \quad (29)$$

On the basis of the study above, which concludes that z_{2max} is a good approximation for the abscissa of the tangency point, try the expression $z_T = \frac{n^2}{4} - 1$ to assess an approximate solution to Eq. (29). A numerical analysis, based on the numerical solutions in z of Eq. (29), shows that this results in a good approximation for z_T , except for the lower values of n . It also shows that if the expression for z_T is changed to become

$$z_T = \frac{n^2}{4} - 3 \quad (30)$$

the approximation is much better for the lower values of n , without being noticeably modified for the higher values. Note that the asymptotic development

(26), which is limited to second-order in $1/n$, is unchanged by this adjustment; the modification shows up only at the fourth-order term. Consequently, the formula giving E is also unchanged. The formula $z_T = \frac{n^2}{4} - 3$ yields a maximum relative error of $+3.25\%$ on E at $n = 4$, and -0.8% at $n = 6$. For the other values of n beyond 6, the relative error is negative and has a magnitude below 0.8% . As a conclusion, the chosen formulas for z_T and E_T are those given in Eqs (27) and (30).

6 Appendix B: position of the G -curve versus the critical line.

In this Appendix, the position of the G -curve versus the critical line is studied, and a simple condition on ρ_{00} is brought out, indicating whether the G -curve is entirely above the critical line or if it intersects said line.

Eqs (7) and (8) show that the G -curve has a different equation, depending on whether the region of interest is above or under the critical line. This appears in Figs. 2 and 4. Therefore, to study the intersection between the G -curve and the critical line, first study the behaviour of the G -curve when the G -function is expressed as in Eq. (8), i.e. when the current point on the G -curve is above the critical line. The equation of the G -curve above the critical line is given by Eq. (8):

$$\frac{G(a, a_A)}{a} = \frac{\rho^2 - 1}{2} = -\frac{1}{2} \frac{F_0 - a_A kL}{2F_B + F_0 - a_A kL} \left(1 - \frac{2}{Ca^2} + \frac{1}{Ca^2} \frac{2}{\sqrt{1 + Ca^2}} \right)$$

which yields $a_A = \frac{y(a)}{kL}$, with

$$y(a) = F_0 + 2F_B \frac{(\rho^2 - 1)Ca^2}{\rho^2 Ca^2 - 2 + \frac{2}{\sqrt{Ca^2 + 1}}} \quad (31)$$

Notation In this Appendix, the value $\frac{|F_0|}{F_B}$ will be denoted by λ .

Definition domain. The definition domain of $y(a)$ is:

- If $\rho^2 < 1$: $\mathbb{R}^+ \setminus \{a_2\}$ and $\lim_{a \rightarrow a_2^-} y(a) = +\infty$, $\lim_{a \rightarrow a_2^+} y(a) = -\infty$
- If $\rho^2 > 1$: \mathbb{R}^+

with

$$a_2 = \sqrt{\frac{2}{\rho^2 C} - \frac{1 + \sqrt{1 + \frac{8}{\rho^2}}}{2C}} \quad (32)$$

Limit at 0 and at $+\infty$. It holds $\lim_{a \rightarrow 0^+} y(a) = F_0 + 2F_B$. The function $y(a)$ can be extended by continuity to $2F_B + F_0$ at $a = 0$. Also:

$$\lim_{a \rightarrow +\infty} y(a) = F_0 + 2F_B \frac{\rho^2 - 1}{\rho^2} = 2 \left(1 - \frac{1}{\rho_{00}^2} \right) (F_B + F_0) - F_0 \quad (33)$$

and therefore:

- If $\rho^2 < 1$, i.e. $\rho_{00}^2 < 1 - \lambda$, this limit is negative.

- If $\rho^2 > 1$, this limit is negative or positive:
 - If $1 - \lambda < \rho_{00}^2 < 1$, this limit is lower than $|F_0|$.
 - If $1 < \rho_{00}^2$, this limit is higher than $|F_0|$.

Direction of variation. The derivative $\frac{dy}{da}$ is the same sign as $1 - \rho^2$. Therefore, if $\rho < 1$, $y(a)$ is increasing.

Intersection with the critical line. Recall that the critical line is $\frac{a_A}{kL} = \frac{|F_0|}{F_B}$, i.e. $y(a) = |F_0| = -F_0$. Substituting this value for $y(a)$ and $\rho_{00}^2 \frac{F_B}{F_B + F_0}$ for ρ^2 in Eq. (31) yields

$$(\rho_{00}^2 - 1)Ca^2 = 2\frac{F_0}{F_B} \left(1 - \frac{1}{\sqrt{Ca^2 + 1}}\right)$$

with $a \neq 0$. Put $x = \sqrt{Ca^2 + 1}$, and rearrange terms to obtain, discarding the case $x = 1$:

$$x^2 + x - 2R = 0 \tag{34}$$

with $R = -\frac{F_0}{F_B(1 - \rho_{00}^2)}$ and therefore, $R > 0$ because $\rho_{00}^2 < 1$ and $F_0 < 0$.

Discard the negative root, and write that the positive root is greater than 1 to obtain the condition $R > 1$, i.e. $\rho_{00}^2 > 1 - \frac{|F_0|}{F_B}$.

Finally, the condition for the intersection of the G -curve and the critical line to exist is

$$1 - \lambda < \rho_{00}^2 < 1 \tag{35}$$

with $\lambda = \frac{|F_0|}{F_B}$.

To calculate the abscissa a_0 of said intersection, use relation $x^2 - 1 = Ca^2$ together with Eq. (34) to obtain

$$a_0^2 = \frac{|F_0|}{\pi^2 kL} \left(\frac{4\lambda}{1 - \rho_{00}^2} - 1 - \sqrt{1 + \frac{8\lambda}{1 - \rho_{00}^2}} \right) \tag{36}$$

Allowed values for ρ and ρ_{00} . It has been shown in [6] that a necessary condition for the smooth model to be valid is that $a_A kL < F_B + F_0$. Therefore:

- If $\rho < 1$, i.e. $\rho_{00}^2 < 1 - \lambda$, and because $y(a)$ is then always increasing and $y(0) = 2F_B + F_0 > F_B + F_0$, it can be seen that $y(a)$ will never go under $F_B + F_0$ for $0 \leq a < a_2$ (a_2 as defined in Eq. (32)), so that said model is not valid over this interval; it is not valid either for $a_2 < a$, because in this case, $y(a) < 0$. As a conclusion, this case must be discarded.

- If $\rho > 1$, i.e. $1 - \lambda < \rho_{00}^2$, and because the G -curve starts at $a_A = 2F_B + F_0$ for $a = 0$ and is always decreasing, it then can enter the validity domain of the smooth model if it crosses the horizontal line $a_A = (F_B + F_0)/(kL)$. However, for this to happen, it is necessary that $\lim_{a \rightarrow +\infty} y(a) < F_B + F_0$, i.e., using Eq. (33): $\rho_{00}^2 < 2(1 - \lambda)$. If this condition is met, $y(a)$ then decreases to a finite value lower than $|F_0| = kLa_{Acrit}$. So:
 - If $1 - \lambda < \rho_{00}^2 < 1$, the function $a_A(a)$ intersects the critical line $a_A = a_{Acrit} = |F_0|/(kL)$ at $a_S = a_0$, then decreases toward a limit lower than a_{Acrit} , which means that the function never intersects again the critical line.
 - If $1 < \rho_{00}^2$, the function $a_A(a)$ is entirely located above the critical line.
 - * If $1 < \rho_{00}^2 < 2(1 - \lambda)$, at least a part of the G -curve is in the validity domain of the smooth model. This condition implies $\lambda < 1/2$.
 - * If $2(1 - \lambda) < \rho_{00}^2$, there is no part of the G -curve is in the validity domain of the smooth model. This condition must be discarded.

Conclusion. The approached smooth model can be studied only if

$$1 - \lambda < \rho_{00}^2 < 2(1 - \lambda)$$

- If $1 - \lambda < \rho_{00}^2 < 1$, the G -curve has an upper part above the critical line, then a lower part consisting of a vertical segment.
- If $1 < \rho_{00}^2 < 2(1 - \lambda)$, the G -curve is entirely located above the critical line.

References

- [1] Béthenod, M.: Sur l'entretien du mouvement d'un pendule au moyen d'un courant alternatif de fréquence élevée par rapport à sa fréquence propre. *Comptes rendus hebdomadaires de l'Académie des sciences* **207**(19), 847–849 (1938). URL <http://gallica.bnf.fr/ark:/12148/bpt6k31590>. (in French)
- [2] Cintra, D., Argoul, P.: Attractors capture probability in non-linear argumental oscillators. *Communications in Nonlinear Science and Numerical Simulation* **48**(Supplement C), 150 – 169 (2017). DOI <https://doi.org/10.1016/j.cnsns.2016.12.023>. URL <http://www.sciencedirect.com/science/article/pii/S1007570416305159>
- [3] Cintra, D., Argoul, P.: Non-linear argumental oscillators: Stability criterion and approximate implicit analytic solution. *International Journal of Non-Linear Mechanics* **94**(Supplement C), 109 – 124 (2017). DOI <https://doi.org/10.1016/j.ijnonlinmec.2017.03.013>. URL <http://www.sciencedirect.com/science/article/pii/S0020746217301981>. A Conspectus of Nonlinear Mechanics: A Tribute to the Oeuvres of Professors G. Rega and F. Vestroni
- [4] Cintra, D., Argoul, P.: Nonlinear argumental oscillators: A few examples of modulation via spatial position. *Journal of Vibration and Control* **23**(18), 2888–2911 (2017). DOI [10.1177/1077546315623888](https://doi.org/10.1177/1077546315623888). URL <https://doi.org/10.1177/1077546315623888>
- [5] Cintra, D., Cumunel, G., Argoul, P.: Experimental study of the argumental transverse vibration of a beam excited through permanent or intermittent elastic contact by a harmonic axial motion. *Journal to be determined* (2017)
- [6] Cintra, D., Cumunel, G., Argoul, P.: Modeling and numerical results for the argumental transverse vibration of a beam excited through permanent or intermittent elastic contact by a harmonic axial motion. *Journal to be determined* (2017)
- [7] Cretin, B., Vernier, D.: Quantized amplitudes in a nonlinear resonant electrical circuit. In: 2009 Joint Meeting of the European Frequency and Time Forum and the IEEE International Frequency Control Symposium, vols 1 and 2, vol. 1 & 2, pp. 797–800. Joint Meeting of the 23rd European Frequency and Time Forum/IEEE International Frequency Control Symposium, Besançon, France (2009). URL <http://arxiv.org/ftp/arxiv/papers/0801/0801.1301.pdf>
- [8] Doubochinski, D.: Argumental oscillations. Macroscopic quantum effects. SciTech Library (2015). URL <http://www.sciteclibrary.ru/rus/catalog/pages/15207.html>
- [9] Doubochinski, D., Doubochinski, J.: Amorçage argumentaire d'oscillations entretenues avec une série discrète d'amplitudes stables. *E.D.F. Bulletin de*

la direction des études et recherches, série C mathématiques, informatique
3, 11–20 (1991). (in French)

- [10] Penner, D.I., Duboshinskii, D.B., Kozakov, M.I., Vermel, A.S., Galkin, Y.V.: Asynchronous excitation of undamped oscillations. *Phys. Usp.* **16**(1), 158–160 (1973). DOI 10.1070/PU1973v016n01ABEH005156. URL <https://ufn.ru/en/articles/1973/1/m/>
- [11] Pratiher, B., Dwivedy, S.K.: Nonlinear response of a flexible cartesian manipulator with payload and pulsating axial force. *Nonlinear Dynamics* **57**(1), 177–195 (2009). DOI 10.1007/s11071-008-9431-6. URL <https://doi.org/10.1007/s11071-008-9431-6>
- [12] Treilhou, J., Coutelier, J., Thocaven, J., Jacquez, C.: Payload motions detected by balloon-borne fluxgate-type magnetometers. *Advances in Space Research* **26**(9), 1423–1426 (2000)